

Oxygen Reduction at Soft Interfaces

THÈSE N° 6428 (2014)

PRÉSENTÉE LE 26 SEPTEMBRE 2014

À LA FACULTÉ SCIENCES DE BASE

LABORATOIRE D'ÉLECTROCHIMIE PHYSIQUE ET ANALYTIQUE

PROGRAMME DOCTORAL EN CHIMIE ET GÉNIE CHIMIQUE

ÉCOLE POLYTECHNIQUE FÉDÉRALE DE LAUSANNE

POUR L'OBTENTION DU GRADE DE DOCTEUR ÈS SCIENCES

PAR

Haiqiang DENG

acceptée sur proposition du jury:

Prof. B. Fierz, président du jury
Prof. H. Girault, directeur de thèse
Prof. G. Laurenczy, rapporteur
Prof. Z. Ding, rapporteur
Prof. Z. Samec, rapporteur



ÉCOLE POLYTECHNIQUE
FÉDÉRALE DE LAUSANNE

Suisse
2014

To my wife and my parents

Acknowledgments

Firstly, I appreciate highly my supervisor Prof. Hubert H. Girault, who gave me the chance to join his group – LEPA four years ago. During my four years’ studies in LEPA, he has devoted his professional guidance, patience, trust, and encouragement to me especially when it goes to very difficult moment with my thesis. It is impossible to finish this thesis without his numerous help.

Secondly, I want to thank Prof. Zhifeng Ding, Prof. Zdeněk Samec, and Prof. Gabor Laurenczy who have kindly accepted to be the jury committee of my defense. Besides, I am thankful to Prof. Béat Fierz for his acceptance of being the president of the jury committee.

I am grateful to Fernando Cortés-Salazar for his guidance during my first year of thesis and I have learned many skills especially the scanning electrochemical microscopy from him. He is always kind and patient and always gives me good suggestions when I have any questions. My special thanks will go to Pekka Peljo for his cordial and countless help during my PhD studies and also for his reading and correcting of my thesis. I really enjoy the collaboration with him who contributed a lot to the work presented here and many discussions with him are fruitful. I also give sincere thanks to T. Jane Stockmann and Dmitry Momotenko who also contributed a lot especially the simulations works presented in this thesis. Discussions with them are quite beneficial to the thesis. I also want to acknowledge Shokoufeh Rastgar who contributed significantly to the fourth chapter of this thesis and Liang Qiao for his kind assistance in mass spectrometry experiments and analysis. Additionally, I would like to thank Micheál D. Scanlon, Manuel A. Méndez, Jonnathan C.A. Hidalgo, Peiyu Ge, Astrid Olaya, Lei Liao, Chenyi Yi, Prof. Bin Su, Prof. Fei Li, Prof. Marcin Opallo, Andreas Lesch, Veronique Amstutz, and Voyame Patrick for their valuable discussions and technical support.

I am indebted to Christophe, Stéphane, Frédéric Gumy, and all the people who work in the mechanical and electronic workshops of ISIC in EPFL. Great thanks belong to our secretary Maria Szuman (former) and Patricia Byron-Exarcos (present) and our former technician Valarie Devaud for their kind help and assistance in administrative and technical issues.

LEPA is a good group where I can work with my colleagues who have diverse backgrounds and interests. I really enjoy the time with them and my sincere gratitude goes to all other members (past and present) in LEPA: Hongyan Bi, Pingping Fang, Kathryn Toghil, Yu Lu, Fang Liu, Xiaojun Bian, Hualan Zhou, Elena Tobolkina, Heron Vrabel, Alexandra Bondarenko, Natalia Gasilova, Lucie Rivier, Evgeny Smirnov, etc. I also take the opportunity to address the special thank to Yu Lu and her husband Cheng Yu who helped me to find a good apartment to live in.

I have a very good time to go travelling, hiking, and skiing with my Chinese friends in Lausanne. They are Zhaolu Diao, Chaobo Huang, Hui Yang, Ke Liu, Yan Yan, Li Jin, Le Chen, Han Wu, Zhen Huang, Chen Yan, Xiaoqin Zhong, Yan Deng, Tzu-En Lin, Zhaoyu Gao, Shuangyi Zhao, Zongzhao Zhai, Xifan Tang, Jian Zhang, Rui Du, Xiaoyun Yu, Tian

Guo, Hongbing Song, Ji Cao, Xin Yang, and Ping Xi, etc. I also acknowledge a good friendship with the boss of the Chinese Restaurant Ning Bo – Chuanjun Sun and his wife for their hospitality and kindness.

Also not forgetting Prof. Lishi Wang of South China University of Technology and Xinjian Huang, my former colleague, for their encouragement and help during my Master studies. I also thank Prof. Lishi Wang and Mingwei Xiao for their kind help in making my studies in Switzerland possible.

Here, I want to express my ocean-deep love to my wife and schoolmate Sumei Wang for her support, encouragement, and devotion during my four years' study abroad. My life will be hard without her. I am also deeply indebted to my parents, Lianxu Deng and Cuilian Pan, for their unconditional love, support and encouragement throughout my life. I also thank my sisters Haiyan Deng and Haixia Deng for their help and encouragement in my life and studies.

Finally, I highly acknowledge the China Scholarship Council (CSC) for financial support.

Abstract

Modern electrochemistry at the liquid/liquid interface, also termed the interface between two immiscible electrolyte solutions (ITIES), has been investigated for more than 40 years due to its importance in mimicking many vital processes, including photosynthesis and cellular respiration (oxygen reduction) occurring at biomembranes. The versatility of ITIES electrochemistry, in terms of reactions that can be studied (such as ion transfer, facilitated ion transfer, as well as heterogeneous electron transfer) has greatly contributed to its success. In this thesis, the oxygen (O_2) reduction reaction (ORR), with multiple electron/proton transfer steps at/near the ITIES, was investigated. Besides the ORR, hydrogen peroxide (H_2O_2) reduction, hydrogen evolution reaction (HER), S_N1 reactions, and photoinduced electron transfer, at the ITIES, were also studied.

ITIES provides a unique platform to study the ORR that has been investigated intensively at the solid electrode/electrolyte interface or in bulk (organic) solution. The ITIES is a so-called soft molecular interface that is intrinsically defect-free, whereby the tedious polishing necessary for preparation of single-crystal and solid electrodes is avoided. Additionally, the voltammetrical results obtained at the ITIES are highly reproducible. This provides a more convenient way to study the ORR that combines the advantages from both solid electrode/electrolyte interface and the bulk phase strategy – aqueous rather than organic acid can be used as the proton source and a lipophilic reductant as the electron donor. The ITIES also facilitates charge/product separation during the photoinduced electron transfer, mimicking biological photosynthesis.

O_2 and H_2O_2 reduction by a multiferrocenyl compound, 1,2-diferrocenylethane (DFcE), was firstly investigated as a model system at the ITIES. The overall reaction is composed of a Galvani potential dependent proton transfer followed by the homogeneous reaction in the organic phase between dissolved O_2 , protons, and a sacrificial electron donor to generate H_2O_2 . However, contradictory to what was expected, the H_2O_2 yield is quite low ($< 6\%$). H_2O_2 reduction that is faster than O_2 reduction accounts for this low yield. Besides, H_2O_2 decomposition catalyzed by this transition metal compound should also be taken into account to calculate the true H_2O_2 yield or selectivity. The rate of ORR by DFcE is slow due to the low thermodynamic driving force, but can be improved dramatically by addition of a molecular catalyst – biscobalt porphyrin.

H_2O_2 , a green oxidant, is currently produced on an industrial scale by the biphasic anthraquinone oxidation (AO) process using an expensive palladium catalyst. A novel methodology employing a metal-free catalyst – reduced graphene oxide (RGO) – generated *in-situ* at the ITIES and subsequently employed in ORR, was developed as an inexpensive replacement for the AO process for H_2O_2 production. The H_2O_2 yield is *ca.* 43% following this methodology. To circumvent the non-ideal H_2O_2 yield in the biphasic RGO catalyzed ORR approach, a novel strategy employing heterogeneous photoinduced ORR with a 55.7% yield in H_2O_2 was demonstrated. This can be improved further if the lipophilic quencher can be recycled, for example by photocatalytic water oxidation.

The mechanistic and kinetic details of O₂ reduction at the ITIES has not been fully evaluated in the literature. This has been successfully elucidated by comparison of experimentally obtained four-electrode cyclic voltammograms (CVs), and approach curves in scanning electrochemical microscopy (SECM), to simulated CVs and approach curves generated through COMSOL Multiphysics software employing the finite element method (FEM). It was shown that the overall reaction is composed of a Galvani potential dependent proton transfer (*i.e.* ion transfer, IT) followed by two homogeneous reactions (C₁C₂) occurring in the organic phase. In this IT-C₁C₂ mechanism an inorganic acid in aqueous phase is used as the proton source and ferrocene derivatives, such as decamethylferrocene (DMFc), in the organic phase as the electron donor. Rate constants were determined with these two methods and they are in a good agreement. Additionally, counter-anions, such as ClO₄⁻, and H₂O can inhibit the ORR kinetics significantly due to ion-pair formation and competition with O₂ in the interaction with the protonated DMFc, respectively.

The ORR by ferrocene derivatives at the ITIES can also be triggered by transfer of hydrophilic metal cations accompanied by their hydration shells into the bulk organic phase. Hydrophilic cations polarize the water molecules in their hydration shells due to electrostatic interactions between the ions and the water dipoles, making the protons more acidic. Then the ORR proceeds just as under acidic conditions; the only difference being that the water molecules of the cations hydration shells are the proton source. This proton source can also be used in HER and, as demonstrated herein, for synthetic reactions such as those incorporating carbocation formation in an S_N1 mechanism. Furthermore, ORR at soft interfaces catalyzed by other cations has also been investigated briefly and their catalytic ability is shown to be correlated to the hydration energy of the cations which are, in turn, directly proportional to the cation charge densities. The rate of the biphasic ORR can be enhanced further in the presence of a cation carrier such as a crown ether in organic phase. Finally, COMSOL simulated four-electrode CVs were employed to elucidate the mechanism and kinetics of O₂ reduction triggered by hydrated cation transfer.

Keywords: liquid/liquid interface, oxygen reduction, H₂O₂, hydrogen evolution, S_N1 reactions, decamethylferrocene, proton, hydrophilic metallic cations.

Résumé

L'électrochimie atuelle à l'interface liquide/liquide, encore appelé l'interface entre deux solutions électrolyte non miscibles (ITIES), a été étudiée depuis plus de 40 ans de par son importance dans l'imitation de beaucoup de processus vitaux. Ces derniers incluent la photosynthèse et la respiration cellulaire (réduction de l'oxygène), qui se produisent toutes deux dans les membranes biologiques. La versatilité de l'électrochimie aux interfaces liquide/liquide, en termes de réaction qui peuvent être étudiées (comme par exemple le transfert d'ion, le transfert d'ion assisté, ou encore le transfert d'électron hétérogène) a grandement contribué à son succès. Dans cette thèse, la réaction de réduction de l'oxygène (ORR), comptant de multiple transferts d'électron/proton à l'interface ou proche de celle-ci, a été étudiée. A côté de cette réaction, la réduction du peroxyde d'hydrogène (H_2O_2), la génération d'hydrogène, les réactions S_N1 , ainsi que les transferts d'électrons photo-induits ont été étudiés, toujours aux ITIES.

Les ITIES offrent une plateforme unique pour l'étude de la réduction de l'oxygène, qui a été intensivement étudiée au préalable à l'interface électrode solide/électrolyte ou en solution (organique). Les ITIES sont des interfaces moléculaires souples, intrinsèquement sans défaut, qui permettent d'éviter le polissage fastidieux nécessaire à la préparation de monocristal et d'électrode solide. En plus, les résultats de voltammetrie obtenus aux ITIES sont largement reproductibles. Elles offrent donc un moyen plus pratique pour étudier l'ORR, qui combine les avantages à la fois des interfaces électrode solide/électrolyte et des stratégies de réactions en solution – des acides aqueux plutôt qu'organiques peuvent être utilisés comme source de protons et des réducteurs lipophiles comme donneurs d'électrons. Les ITIES facilitent également la séparation charge/produit lors de transfert d'électron photo-induit, imitant en cela la photosynthèse.

La réduction d' O_2 et de H_2O_2 par un composé multiferrocenyl, le 1,2-diferrocenylethane (DFcE), a été tout d'abord étudiée comme système modèle aux ITIES. La réaction globale est composée d'un transfert de proton dépendant d'un potentiel de Galvani, suivi par la réaction homogène en phase organique entre l' O_2 dissout, les protons et le donneur sacrificiel d'électrons qui génère finalement du H_2O_2 . Cependant, contrairement à ce qui était attendu, le rendement de production de H_2O_2 est relativement faible (<6%). Le fait que la réduction de H_2O_2 soit plus rapide que la réduction d' O_2 explique ce faible rendement. Par ailleurs, la décomposition de H_2O_2 catalysée par ce composé à base d'un métal de transition doit aussi être prise en compte dans le calcul du rendement et de la sélectivité réels. La vitesse de la ORR par le DFcE est peu élevée du fait de la faible force motrice thermodynamique, mais elle est peut être considérablement améliorée par l'addition de catalyseur moléculaire – la porphyrine de biscobalt.

Le H_2O_2 , un oxydant "green", est couramment produit à l'échelle industrielle par l'oxydation de l'anthraquinone en système biphasique à l'aide d'un catalyseur de palladium coûteux. Une nouvelle méthodologie employant un catalyseur non métallique, l'oxyde de graphène réduit (RGO), généré *in-situ* aux ITIES et utilisé par la suite dans l'ORR, a été développée comme

une alternative peu coûteuse au procédé de production de H_2O_2 par l'oxydation de l'anthraquinone. Le rendement de H_2O_2 obtenu ainsi est d'environ 43%. Afin d'améliorer le rendement de H_2O_2 dans le système RGO biphasique par la ORR, une nouvelle stratégie utilisant une ORR photo-induite, hétérogène, permettant un rendement en H_2O_2 de 55.7% a été démontrée. Ce rendement peut encore être amélioré en recyclant les quencheurs lipophiles, par exemple par l'oxydation photocatalytique de l'eau.

Les mécanismes et les détails cinétiques de la ORR aux ITIES n'ont pas été pleinement évalués dans la littérature. Ceux-ci ont été élucidés avec succès par comparaison de voltammogrammes cyclique (CVs) à quatre électrodes obtenus expérimentalement et de courbes d'approche en microscopie électrochimique à balayage (SECM) à des CVs et des courbes d'approche générées à l'aide du logiciel COMSOL Multiphysics, en employant la méthode des éléments finis (FEM). Il a été démontré que la réaction globale est composée d'un transfert de proton dépendant d'un potentiel de Galvani (*i.e.* transfert de ion IT), suivi par deux réactions homogènes (C_1C_2) survenant dans la phase organique. Dans ce mécanisme IT- C_1C_2 , un acide inorganique dans la phase aqueuse sert de source de protons alors que dans la phase organique un dérivé du ferrocène, comme le decaméthylferrocène (DMFc), sert de donneur d'électrons. Les constantes de vitesse ont été déterminées à l'aide des deux méthodes et montrent une bonne concordance. De plus, des contre-ions, tels que ClO_4^- , ou H_2O peuvent inhiber la cinétique des ORR significativement dû, respectivement, à la formation de paire d'ions et à la compétition avec l' O_2 dans l'interaction avec le DMFc protoné.

L'ORR par les dérivés du ferrocène aux ITIES peut également être provoquée par le transfert de cations métalliques hydrophiles accompagnés de leur sphère d'hydratation dans la phase organique. Les cations hydrophiles polarisent les molécules d'eau de leur sphère d'hydratation du fait des interactions électrostatiques entre les ions et les dipôles de l'eau, rendant les protons plus acides. Ainsi la ORR a lieu exactement comme en condition acide; avec pour seule différence, le fait que l'eau des sphères d'hydratation devienne la source de protons. Cette dernière peut également être utilisée pour la réaction de génération d'hydrogène et, comme démontré ici, pour des réactions de synthèse comme celles incorporant la formation d'un carbocation dans un mécanisme $\text{S}_{\text{N}}1$. Par ailleurs, la ORR aux interfaces souples catalysée par d'autres cations a également été étudiée brièvement et leur capacité catalytique semble corrélée avec l'énergie d'hydratation des cations, qui est, elle, directement proportionnelle à la densité de charge des cations. La ORR biphasique peut être améliorée en présence d'un porteur de cation tel qu'un éther couronne en phase organique. Finalement, des CVs à quatre électrodes simulées sur COMSOL ont été employées pour élucider les mécanismes et la cinétique de la réduction d' O_2 provoquée par transfert de cation hydraté.

Mots-clés: interface liquide/liquide, réduction d'oxygène, H_2O_2 , évolution d'hydrogène, réaction $\text{S}_{\text{N}}1$, decaméthylferrocène, protons, cations métalliques hydrophiles.

List of Symbols

A	electrode surface area
a	activity
c	concentration
$c_i^{0,o}$	initial concentration of the ion i in organic phase
$c_i^{0,w}$	initial concentration of the ion i in aqueous phase
D	diffusion coefficient
e	elementary charge
$E^{\circ'}$	formal redox potential
E°	standard redox potential
F	Faraday constant
g	geometry factor
i	ion or current
i_p	peak current
I_{ss}	steady state current
K	equilibrium constant
k_{et}	bimolecular electron transfer rate constant
k°	standard rate constant
L	neutral carrier
L	normalized distance
M	ionic species or (transition) metal
n	amount of substance or charge number or stoichiometric number
N_A	Avogadro's constant
P	partition coefficient
P_i°	standard partition coefficient of ion i
pH^w	aqueous pH
pK_a	acidity constant
r	radius or radial
R	universal gas constant
RG	ratio between the radius of the insulating sheath plus the active electrode and that of the active electrode
RX	binary electrolyte

T	thermodynamic temperature
U_+	cation-water electrostatic interaction energy
U_-	anion-water electrostatic interaction energy
ν	scan rate
V^o	volume of organic phase
V^w	volume of aqueous phase
z	normal
z_i	charge number of i including the sign
α	phase or charge transfer coefficient
γ	activity coefficient
δ	solvent layer thickness
δ_d	diffusion layer
δ_r	reaction layer
ΔE^o	standard cell potential
ΔE_{ref}	potential difference between the reference electrodes
ΔG^o	standard reaction Gibbs energy change
$\Delta G_{\text{tr},i}^{o,w \rightarrow o}$	standard Gibbs transfer energy of i from w to o
ΔH^o	standard reaction enthalpy change
$\Delta_o^w \phi$	Galvani potential difference
$\Delta_o^w \phi_{1/2}$	half-wave potential
$\Delta_o^w \phi_i^o$	standard transfer potential of i between w and o
$\Delta_o^w \phi_i^{o'}$	formal transfer potential of i between w and o
$\Delta_o^w \phi_{\text{pa}}$	anodic peak potential
$\Delta_o^w \phi_{\text{pc}}$	cathodic peak potential
ε	molar extinction coefficient
ε_0	permittivity of vacuum
ε_o	relative permittivity of oil phase
ε_w	relative permittivity of aqueous phase
η	solvent viscosity
θ	shank angle
Λ	dimensionless substrate kinetics parameter

μ_i^α	chemical potential
$\tilde{\mu}_i^\alpha$	electrochemical potential of charged species i in phase α
$\mu_i^{\circ,\alpha}$	standard chemical potential of i in phase α
ρ	density
σ_i	charge density on the specific layer
ϕ	inner potential
χ	surface potential
ψ	outer potential
∇	gradient operator

List of Abbreviations

ACT	aqueous complexation followed by the transfer of the complex
AO	anthrahydroquinone oxidation
ATP	adenosine triphosphate
BACl	bis(triphenylphosphoranylidene) ammonium chloride
BATB	bis(triphenylphosphoranylidene)ammonium tetrakis(pentafluorophenyl)borate
BATPBCl	bis[triphenylphosphoranylidene]ammonium tetrakis [4-chlorophenyl]borate
CA	chronoamperometric
CE	counter electrode
CNT	carbon nanotube
Co ₂ (DPOx)	Biscobalt2,2'-bis[5-(2,8,13,17-tetraethyl-3,7,12,18-tetramethylporphyrinyl)] diphenylether
Cp	cyclopentadienyl ring
CPET	concerted proton and electron transfer
Cs	spherical aberration coefficient
CV	cyclic voltammetry
DB18C6	dibenzo-18-crown-6
DCE	1,2-dichloroethane
DFc	1,1'-dimethylferrocene
DFcE	1,2-diferrocenylethane
DFT	density functional theory
DMFc	decamethylferrocene
EC	electrochemical-chemical
EC'	catalytic reaction
EELS	electron energy loss spectroscopy
EPPG	edge plane pyrolytic graphite
ESI-MS	electrospray ionization mass spectrometry
ET	electron transfer
Fc	ferrocene
FcCH ₂ OH	ferrocene methanol
FEG	field emission gun

List of Abbreviations

FEM	finite element method
FIT	facilitated ion transfer
FT	Fourier transform
GC	gas chromatography
GCE	glassy carbon working electrode
GE	graphite electrode
GO	graphene oxide
GS	Girault-Schiffrin
HA	hydration asymmetry parameter
HER	hydrogen evolution reaction
IHP	inner Helmholtz plane
INPE	ideally non-polarizable electrode
IPE	ideally polarizable electrode
IR	infra-red
IT	ion transfer
ITIES	interface between two immiscible electrolyte solutions
L/L	liquid/liquid
LiTB	lithium tetrakis(pentafluorophenyl)borate diethyl etherate
LSV	linear sweep voltammetry
MVN	modified Verwey-Niessen
NB	nitrobenzene
OHP	outer Helmholtz plane
O/R	oxidized form/ reduced form
ORR	oxygen reduction reaction
o or O/w or W	oil/water
PBS	phosphate buffer solution
PC	personal computer
PCET	proton-coupled electron transfer
PIGE	paraffin impregnated graphite electrode
PPW	polarized potential window
PT	proton transfer
Q	quencher
QRE	quasi-reference electrode
RC	redox competition

RDS	rate-determining step
RE	reference electrode
RGO	reduced graphene oxide
RTILs	room temperature ionic liquids
S	sensitizer
SAED	selected area electron diffraction
SCE	saturated calomel electrode
SECM	scanning electrochemical microscopy
SEM	scanning electron microscopy
SG/TC	substrate generation/tip collection
SHE	aqueous standard hydrogen electrode
SHG	second harmonic generation
SI	surface interrogation
SICM	scanning ion-conduction microscopy
S _N 1	unimolecular nucleophilic substitution
sp	solubility product
STM	scanning tunneling microscopy
SWV	square wave voltammetry
SX/EW	solvent extraction and electrowinning
TATB	tetraphenylarsonium-tetraphenylborate
TBATPB	tetrabutylammonium tetraphenylborate
TCD	thermal conductivity detector
TEA ⁺	tetraethylammonium cation
TEM	transmission electron microscopy
TFA	trifluoroacetic acid
TFT	trifluorotoluene
TG/SC	tip generation/substrate collection
TIC	transfer by interfacial complexation
TID	transfer by interfacial dissociation
TMA ⁺	tetramethylammonium cation
TOC	transfer followed by organic phase complexation
UME	ultramicroelectrode
UV/Vis	ultraviolet/visible
VN	Verwey-Niessen

List of Abbreviations

ZnTPP	5,10,15,20-tetraphenylporphyrinato zinc
ZnTPPC	zinc meso-tetra(4-carboxyphenyl)porphyrin

Table of Contents

Acknowledgments	i
Abstract	iii
Résumé	v
List of Symbols	vii
List of Abbreviations	xi
Table of Contents	xv
Chapter 1	1
Theoretical Aspects	1
1.1. The scope of the present thesis	1
1.2. Electrochemistry at the liquid/liquid interface	4
1.2.1. Introduction	4
1.2.2. A brief history of electrochemistry at the liquid/liquid interface	5
1.2.3. The structure of the electrode/electrolyte interface	9
1.2.4. The structure of the liquid/liquid interface	13
1.2.5. Thermodynamics of the liquid/liquid interface	18
1.2.6. Methods and techniques to study the ITIES	26
1.2.7. Charge transfer reactions at ITIES	35
1.3. Proton-coupled electron transfer reaction and S_N1 reaction at the ITIES	46
1.4. Scanning electrochemical microscopy	53
1.4.1. Introduction	53
1.4.2. Feedback mode	54
1.4.3. Generation/Collection (GC) mode	60
1.5. References	61
Chapter 2	71
Experimental and Instrumentation	71
2.1. Introduction	71
2.2. Chemicals	71
2.3. Electrochemical methods	72

2.3.1. Four-electrode system	72
2.3.2. Preparation of reference electrodes and organic supporting electrolytes	73
2.3.3. Three-electrode system.....	73
2.3.4. Scanning electrochemical microscopy	74
2.4. Shake-flask experiments	77
2.4.1. Oxygen reduction reaction	78
2.4.2. Gas chromatography analysis of shake flask reactions	84
2.4.3. ESI-MS analysis of shake flask reactions	84
2.5. Karl Fischer titration for water determination	85
2.6. References	85
Chapter 3	87
Oxygen and Hydrogen Peroxide Reduction by 1,2-diferrocenylethane at a Liquid/Liquid Interface	87
3.1. Introduction	87
3.2. Experimental section.....	88
3.2.1. Chemicals	88
3.2.2. Two-phase reactions controlled by a common ion distribution (shake flask reactions)	88
3.2.3. Electrochemical Measurements.....	90
3.3. Results and discussion.....	90
3.3.1. Redox properties of DFcE	90
3.3.2. Two-phase reactions controlled by a common ion distribution	92
3.3.3. Four electrode cell measurements	97
3.3.4. Mechanism	104
3.4. Conclusions	105
3.5. References	106
Chapter 4	109
Oxygen Reduction at Soft Interfaces Catalyzed by In Situ-Generated Reduced Graphene Oxide	109
4.1. Introduction	109
4.2. Experimental section.....	110
4.2.1. Chemicals	110
4.2.2. Preparation of reduced graphene oxide (RGO) at the liquid/liquid interface	111
4.2.3. Morphological characterization of RGO prepared at the liquid/liquid interface (<i>carried out by Véronique Amstutz</i>).....	111

4.2.4. Spectroscopic characterization of RGO prepared at the liquid/liquid interface (<i>carried out by Dr. A. Duncan, F. Matteini, and R. Gaal</i>)	112
4.2.5. Electrochemical characterization of RGO prepared at the liquid/liquid interface.	112
4.2.6. Potentiostatic polarization of the interface: biphasic electrochemical measurements using <i>in situ</i> generated RGO as an O ₂ reduction catalyst	113
4.2.7. Chemical polarization of the interface: biphasic shake-flask experiments using <i>in situ</i> generated RGO as an O ₂ reduction catalyst	113
4.2.8. Kinetics measurements using “shake-flasks”	113
4.3. Results and discussion.....	114
4.3.1. Four-electrode cell measurements.....	114
4.3.2. Morphological, spectroscopic and electrochemical characterization of RGO prepared at the liquid/liquid interface.....	116
4.3.3. Biphasic shake-flask reactions	125
4.3.4. Chemical kinetics	126
4.3.5. Hydrogen peroxide detection and yield.....	129
4.3.6. Mechanism	131
4.4. Conclusions	132
4.5. References	133
Chapter 5	135
Kinetics and Mechanism of Oxygen Reduction by Metallocenes in Single and Biphasic Liquid Phases	135
5.1. Introduction	135
5.2. Experimental.....	137
5.2.1. Chemicals	137
5.2.2. Homogeneous reactions measurements.....	137
5.2.3. Electrochemical measurements	137
5.2.4. Computations.....	138
5.3. Simulation (<i>carried out by T. Jane Stockmann</i>).....	138
5.4. Results and discussion.....	142
5.4.1. Chemical kinetics of homogeneous reactions	142
5.4.2. Mechanism elucidation by FEM simulations of electrochemical measurements (<i>carried out by T. Jane Stockmann</i>).....	148
5.5. Conclusions	163
5.6. References	164
Chapter 6	167

Kinetic Differentiation of Bulk/Interfacial Oxygen Reduction Mechanisms at/near Liquid/Liquid Interfaces using Scanning Electrochemical Microscopy..... 167

6.1. Introduction	167
6.2. Theory.....	168
6.2.1. Mechanism of oxygen reduction by DMFc.....	168
6.2.2. Simulations (<i>carried out by Pekka Peljo</i>)	170
6.3. Experimental section.....	172
6.3.1. Chemicals	172
6.3.2. Electrochemical measurements	172
6.4. Results and discussion.....	174
6.4.1. Characterization by UV-Vis spectroscopy and voltammetry.....	174
6.4.2. SECM feedback mode in biphasic system	177
6.4.3. SECM feedback mode in the homogeneous phase	181
6.5. Conclusions	183
6.6. References	183

Chapter 7 185

Lewis Acidity of Hydrated Alkali/Alkaline Earth Metal Cations in Biphasic Systems: Effect on Oxygen and Proton Reduction and S_N1 Reactions..... 185

7.1. Introduction	185
7.2. Experimental methods	186
7.2.1. Chemicals	186
7.2.2. Two-phase shake flask reactions.....	186
7.2.3. Electrospray ionization mass spectrometry (ESI-MS)	187
7.2.4. Water determination by Karl Fischer titration	187
7.2.5. Four-electrode liquid/liquid interface voltammetry	187
7.2.6. Computations.....	188
7.3. Simulations (<i>carried out by T. Jane Stockmann</i>).....	188
7.4. Results and Discussion	189
7.4.1. Two-phase shake flask reactions.....	189
7.4.2. ORR mechanism elucidation by FEM simulations of four-electrode electrochemical measurements	199
7.4.3. Effect of the charge density of the cations	210
7.4.4. Effect of the crown ether	211

7.5. Conclusions	212
7.6. References	213
Appendix.....	217
Photoinduced Electron Transfer Reaction at the Liquid/Liquid Interface.....	217
A.1 Introduction	217
A.2 Experimental section.....	218
A.2.1 Chemicals	218
A.2.2 Photoelectrochemical measurements.....	218
A.2.3 Two-phase shake flask reactions.....	219
A.3 Results and discussion.....	220
A.3.1 Photoelectrochemical measurements.....	220
A.3.2 Two-phase shake flask reactions.....	223
A.3.3 Mechanism	225
A.4 Conclusions	225
A.5 References	226
Chapter 8	229
Conclusions and Perspective	229
References	231
CURRICULUM VITAE	233

Chapter 1

Theoretical Aspects

1.1. The scope of the present thesis

The thesis work, conducted in the Laboratory of Physical and Analytical Electrochemistry (LEPA) at École Polytechnique Fédérale de Lausanne (EPFL), is aimed to investigate energy conversion related electrochemical reactions, namely oxygen reduction reaction (ORR), hydrogen evolution reaction (HER), and photoinduced electron transfer, in biphasic systems. Besides, S_N1 reactions in the biphasic system have been found to be affected significantly by hydrated lithium cations.

Chapter 1 gives a brief history of the electrochemistry at the ITIES, specifically the structure of the electrical double layer at the ITIES, thermodynamics of the ITIES, methods of state-of-the-art to study the ITIES, and charge transfer reactions. Then the SECM technique and, the progress in ORR, HER and S_N1 reaction in biphasic system, have been reviewed briefly.

Chapter 2 describes the experimental details, including instruments, electrochemical setups, and chemicals.

Chapter 3 investigates the oxygen and hydrogen peroxide reduction by a multi-ferrocenyl compound – 1,2-diferrocenylethane (DFcE) at the polarizable ITIES. The results show that the overall reaction is composed of transfer of both protons and electrons, where the first step consists of the protonation of DFcE to form the DFcE- H^+ in 1,2-dichloroethane (DCE) phase, either by proton transfer across the ITIES by external polarization or by chemical extraction by tetrakis(pentafluorophenyl)borate anion. The formation of DFcE- H^+ is followed up by the O_2 reduction to hydrogen peroxide and further reduction to water. Then the final products are detected by electrochemical methods as well as UV/visible spectroscopy. Results also show that mostly DFcE $^+$ is produced, although DFcE $^+$ can also reduce oxygen at longer time

scales. Interestingly, hydrogen peroxide reduction is actually faster than oxygen reduction.

Chapter 4 describes that a metal-free catalyst, reduced graphene oxide (RGO), can be generated *in situ* at the ITIES *via* partial reduction of aqueous hosted graphene oxide by decamethylferrocene (DMFc) or ferrocene (Fc) located in DCE and then participates in the catalysis of interfacial ORR with hydrogen peroxide as the main product. The RGO was characterized by using electron microscopy, spectroscopy (Raman, infrared, and electron energy loss), and electrochemical techniques. The kinetic enhancement effect by RGO in the biphasic ORR was investigated by on-line UV/visible monitoring, showing that this reaction is first order with respect to DMFc or Fc and much faster in the presence of GO in water. The yield of the produced hydrogen peroxide was investigated and confirmed by three methodologies, namely NaI titration, titanium-oxalate method, and Prussian-Blue sensor. Finally, a batch scheme for hydrogen peroxide production in industrial scale based on this biphasic system was proposed.

Chapter 5 investigates the mechanism of ORR at the ITIES by comparison between experimentally obtained cyclic voltammograms (CVs) and the simulated ones generated through COMSOL Multiphysics software, which employs the finite element method (FEM). The simulations incorporated a potential dependent proton transfer (*i.e.* ion transfer, IT) step from the water (w) to organic (o) phases along with two homogeneous reactions (C_1C_2) occurring in the organic phase – an IT- C_1C_2 mechanism. The reaction of DMFc with $H^+(o)$ to form protonated DMFc ($DMFc-H^+$) was considered the first step (reaction **1**), while reaction of $DMFc-H^+$ with oxygen to form a hydrogen peroxy radical species, HO_2^\cdot , and $DMFc^+$ was deemed the second step (reaction **2**). Subsequent reactions, between HO_2^\cdot and either DMFc or H^+ , were considered to be fast and irreversible so that **2** was a ‘proton-sink’, such that further reactions were not included; in this way, the simulation was greatly simplified. The rate of **1**, k_{cf} , and **2**, k_{chem} , were determined to be 5×10^2 and $1 \times 10^{10} \text{ L}\cdot\text{mol}^{-1}\cdot\text{s}^{-1}$, respectively, for DMFc as the electron donor. Similarly, the rates of biphasic ORR for 1,1'-dimethylferrocene (DFc) and Fc were both determined to be 1×10^2 and $5 \times 10^2 \text{ L}\cdot\text{mol}^{-1}\cdot\text{s}^{-1}$ for **1** and **2**, respectively. The reactive and diffusive layer thicknesses are also discussed.

Chapter 6 describes the application of scanning electrochemical microscopy (SECM) in the feedback mode to determine the kinetics of oxygen reduction in biphasic systems containing DMFc in DCE as electron donor and acids in water as a

proton source. Here, decamethylferrocenium (DMFc^+) is reduced at a microelectrode tip in DCE and the DMFc electrogenerated reacts with protons and oxygen to be re-oxidized in a (EC') scheme. SECM approach curves towards the liquid/liquid interface showed dramatic current increases at distances far from the interface at high Galvani potential differences where protons transfer rapidly to the organic phase, indicating that the oxygen reduction takes place mainly in the bulk DCE. However, at lower Galvani potential differences where the proton transfer is slow, oxygen reduction could also be observed at the interface. Finally, SECM feedback mode measurements with the tip approaching a conductive substrate were used to determine the kinetics of the homogeneous reaction, with an obtained apparent rate constant of $0.2\text{-}0.5 \text{ m}^3 \text{ mol}^{-1} \cdot \text{s}^{-1}$.

Chapter 7 describes a new effect arising from hydrophilic metallic cations on the ORR, HER, as well as $\text{S}_{\text{N}}1$ reaction in the biphasic system. For example, lithium cation is shown to have a significant role on catalyzing oxygen and proton reduction along with $\text{S}_{\text{N}}1$ reactions in biphasic systems. We propose that this catalytic effect is due to the surprising acidity of the hydrated cations; interactions between the cation and its surrounding solvation shell will make the constituent water molecules more acidic. The nature underlied this surprising acidity can be ascribed to the solvation differentiation between the small hydrophilic cations and the bulky lipophilic anions in the organic phase: cations are hydrated by water clusters dispersed in organic solution, while anions are solvated by organic solvent molecules. So the masking effect of anion on cation is diminished, as the strength of electric field of charge on ions is inversely proportional to the radius of the ions. So this strong electric field induced by the small cation will exert a strong force on hydrated water molecule (electric dipole moment). With the help of another water molecule *via* forming the hydrogen bond, finally the affected water molecule is dissociated to release a proton. This is supported by the trend of the ORR rate: it is faster with increasing charge densities of the metallic cations (*i.e.* $\text{Mg}^{2+} > \text{Li}^+ > \text{Na}^+ > \text{TMA}^+$). Then it goes to the pathway as same as the proton case in ORR or HER in the biphasic system. The mechanism of this reaction is explored through comparison of experimental CV curve features to simulated CVs generated through COMSOL Multiphysics software which employs the finite element method (FEM). The effect of counter-anions of the aqueous electrolytes on the rate of ORR will also be discussed. Finally, the effect of the crown ethers on the biphasic ORR is investigated.

The Appendix presents some preliminary results for a photoinduced electron transfer reaction at the ITIES with a hydrophilic porphyrin – zinc meso-tetra(4-

carboxyphenyl)porphyrin (ZnTPPC) as a reducible photosensitizer in aqueous phase and a lipophilic electron donor – DMFc, or Fc in DCE. Four-electrode CVs under conditions of with or without illumination from a monochromatic light source and with different pH in the aqueous phase were investigated. Results show that a quasi-square-wave shaped photocurrent response can be observed when DMFc is used as the lipophilic electron donor. However, the current will decay exponentially if Fc is used as the electron donor. Besides, this current can be enhanced significantly while decreasing the aqueous pH. A shake-flask experiment, aiming at clarifying the reaction mechanism, using TMA^+ as a shuttling common ion between the two adjacent phases, has been conducted. The results show that ZnTPPC is nonconsumable (regenerated) acting as an electron relay between DMFc in DCE and H^+/O_2 in aqueous. This heterogeneous H_2O_2 generation scheme with a highest yield (55.7%) achieved so far shows a promising potential for large-scale practical applications. In theory, H_2 should also be generated under anaerobic conditions, which has not been observed yet. The final goal is to regenerate the consumed DMFc in a two-electrode photoelectrochemical cell, employing such as a dark TiO_2 as a photoanode and a Pt plate as a cathode. Then a sustainable H_2O_2 or H_2 production system will be established.

Finally, the conclusions and perspective of the research will be addressed briefly.

1.2. Electrochemistry at the liquid/liquid interface

1.2.1. Introduction

Biomembranes play a critical role in sustaining the regular function of living cells. The exceptional importance of this membrane remains on the fact that it separates the cell into organelles between which the exchange of matter (*i.e.* neutral molecules or charges) is allowed to drive the metabolism of organisms or the synthesis of some important macromolecules such as proteins.¹ For example, photosynthesis, the most fundamental and greatest chemical reaction in nature, occurs at the double-membrane organelle – thylakoids. Its counterpart, namely respiration, in which oxygen reduction reaction (ORR) is involved, takes place at biomembranes as well. Due to the tremendous significance of this membrane in the real world, a simple model system with similar functions is of considerable interest for the understanding of many important biological processes.

The liquid/liquid (L/L) interface or the oil/water (O/W) interface or the interface between two immiscible electrolyte solutions (ITIES) has been studied extensively over the past few decades for this purpose.¹⁻⁵ The gist is that ITIES can be polarized as the conventional solid electrode/electrolyte interface and then used successfully as a model system to study charge (*i.e.* electron, ion or facilitated ion) transfer processes across the soft molecular interface which is of particular importance for a variety of fields such as in storage and conversion of energy,⁶⁻¹⁵ hydrometallurgy *e.g.* L/L electro-assisted extraction of metal cations¹⁶⁻¹⁸ and L/L redox extraction of nuclear^{19,20} and heavy metal²¹ ions, electroanalysis,²²⁻³¹ and life sciences.³²⁻³⁵

Below presented a brief history of the electrochemistry at the liquid/liquid interface dating back to the beginning of 20th century, up to now.

1.2.2. A brief history of electrochemistry at the liquid/liquid interface

The liquid/liquid interface that attracts electrochemists' interest is formed between two solvents with low (or ideally zero) mutual miscibility. Normally, one solvent is water, and another solvent is a polar organic solvent with a relatively high dielectric permittivity (ϵ) allowing the complete or at least partially dissociation of the dissolved electrolytes maintaining the solution conductivity. It should be stressed that for the formation of a physically stable liquid/liquid interface, there should be a distinct density difference between the two adjacent phases. Ideally, organic solvent should be heavier than water, taking into account the environmental concern. Until now, there are more than 20 organic solvents that have been used in the community of electrochemistry at the liquid/liquid interface, among which nitrobenzene (NB, $\epsilon = 34.8$ ³⁶, $\rho = 1.2 \text{ g/cm}^3$) and DCE ($\epsilon = 10.42$ ³⁷, $\rho = 1.25 \text{ g/cm}^3$) are the two most commonly used solvents.³⁸ Other solvents including dichloromethane,³⁹ *o*-nitrophenyloctyl ether,⁴⁰ and 1,2-dichlorobenzene⁴¹ have also been used quite often. Very recently trifluorotoluene (TFT) has also been employed as the organic solvent for investigation of ion transfer across the liquid/liquid interface.⁴² The water/TFT interface is superior to the water/NB or water/DCE interface with the former one featuring a lower toxicity of the organic solvent and a wider potential window. But the only drawback is that the dielectric permittivity (ϵ) of TFT is only 9.18 resulting in a stronger association of salts used as supporting electrolytes, decreasing the conductivity. Beyond the classical NB/water and DCE/water interfaces, room

temperature ionic liquids (RTILs) have been shown to have the potential to replace the conventional organic solutions.^{43,44} Whenever one or both solvents have ions, they will partition between the two phases and contribute to the buildup of the interfacial potential difference. Here, it should be mentioned that in fact the liquid/liquid extraction for the separation of molecular compounds has been used for a very long time, in which case no total charge transfer takes place. Under these conditions, the interfacial potential effect can be ignored. But the interfacial potential effect is significant for the practice of salt extraction, which goes into the scope of electrochemistry at liquid/liquid interface. For example, copper ions that are initially located at the weak aqueous acid side can be extracted and enriched in the strong aqueous acid side during the “solvent extraction and electrowinning” (SX/EW) process, which is controlled by the interfacial polarization by protons.⁴⁵

The first work for electrochemistry at liquid/liquid interface was dated back to 1902 when Nernst and Riesenfeld found that ion can transfer across the water/phenol interface.³⁸ They mainly focused on the evaluation of the ion transport numbers in the organic solvents. Later on Blank and Feig pointed out that to a rough approximation there is a similarity between the liquid/liquid interface and one half of a biomembrane.⁴⁶ Since then the liquid/liquid interface was employed as a simplified model to investigate the bio-electrical phenomena such as potentials and currents at biomembranes and spread into the field of electrophysiology.

However, this field progressed quite slowly until the end of 1960s, due to some inherent difficulties: 1) lack of the knowledge of the interfacial structure and the associated potential distribution; 2) the large iR drop in the organic solvent making collection of reliable data quite difficult. While this situation changed suddenly when Gavach in France realized that the liquid/liquid interface can be polarized by the external source as the metallic electrode/electrolyte interface under some conditions, spurred by the concept proposed by Blank and Feig mentioned above. Gavach's first work in this field was published in 1968,⁴⁷ indicating the start of modern electrochemistry at liquid/liquid interface. Gavach *et al.* pioneered in employing modern electrochemical techniques *e.g.* chronopotentiometry to study the ion transfer across the ITIES.⁴⁸ Then, it was Koryta *et al.* in Prague in what was then Czechoslovakia who coined the term ITIES in 1976.⁴⁹ To overcome the technological obstacle caused by highly resistive organic solvent, Samec *et al.* used a four-electrode potentiostat with iR drop compensation and precise control of the interfacial potential in the late 1970s.⁵⁰⁻⁵² In this experimental configuration (Figure 1-1), for voltammetric measurements, voltage is applied between two reference electrodes (RE_w and RE_o)

located on each side of the interfacial boundary with the help of glass capillary, and current flows between two counter electrodes with one in aqueous (CE_w) and another one in organic solutions (CE_o). It should be noted that the reference potential for the organic phase is realized by a secondary water (Ref. Water in Figure 1-1)/organic interface with the interfacial potential fixed by the shared common ion. For example, if the organic phase contains bis(triphenylphosphoranylidene)ammonium tetrakis(pentafluorophenyl)borate (BATB) as the supporting electrolyte, the Ref. water phase will contain bis(triphenylphosphoranylidene)ammonium chloride (BACl). The potential at the Ref. Water/organic interface will be given by the Nernst equation for BA⁺ partition between the two phases, reading as follows:

$$\Delta_o^w \phi = \Delta_o^w \phi_{BA^+}^\circ + \frac{RT}{F} \ln \left(\frac{a_{BA^+}^o}{a_{BA^+}^w} \right) \quad (1-1)$$

where $\Delta_o^w \phi$ is the Galvani potential difference at the Ref. water/organic interface, $\Delta_o^w \phi_{BA^+}^\circ$ is the standard transfer potential of BA⁺, $a_{BA^+}^i$ ($i = o, w$) is the activity of BA⁺ in each phase, R is the universal gas constant, T is the absolute temperature, and F is the Faraday constant. If the two phases contain equal concentrations of BA⁺, the potential difference at Ref. water/organic interface is equal to standard transfer potential of BA⁺ of -0.70 V.⁵³ A silver wire coated with a layer of silver chloride (Ag/AgCl) can be simply employed as the reference electrode in the Ref. water connecting with the external power source. This Ag/AgCl/BACl/BATB reference electrode was called an oil/water-type reference electrode coined by Senda *et al.*⁵⁴ This oil/water-type reference electrode was used because it is challenging to find a stable reference electrode directly immersed into the organic phase. However, it should be stressed that in this case the junction potential at the Ref. water/organic interface is not very stable in the long period, as BACl will diffuse into the oil phase that will create a diffusion potential due to the high lipophilicity of BA⁺. Hence, the mixed-potential difference of BA⁺/Cl⁻ at this interface is likely to prevail. But it is still stable in the time scale of a voltammetrical measurement as the diffusion process is quite sluggish. For the reference electrode in aqueous, one can simply employ a Ag/AgCl wire as the reference electrode if aqueous contains lithium chloride as the supporting electrolyte for example. Under these conditions, the liquid/liquid interface can be polarized by external power source as the metallic electrode/electrolyte

interface where electron transfer reaction occurred. With appropriate concentrations in supporting electrolytes in both phases (*e.g.* 10 mM), the potential window will be limited by Li^+ and Cl^- transfer at the positive and negative potentials, respectively.⁵³ Within this potential window, transfer of a series of trace ions that have standard transfer potentials between those of Li^+ and Cl^- can be studied. From equation 1-1, we know that applying potential at the interface by external source can induce a shift to the concentration ratio of the ions between the two phases. Thus, a net electric current will flow across the interfacial boundary and can be recorded by a galvanometer, forming the basis for voltammetry at liquid/liquid interface. In this electrochemical cell, oxidation of the solvent (*e.g.* water) or other accessible species (*e.g.* supporting electrolytes or impurities) occurs at the anodic counter electrode, while reduction occurs at the cathodic counter electrode, completing the electric circuit. If the products produced at the counter electrodes can be prevented from reaching the interface, these two half redox reactions can be ignored. A good strategy is to separate the counter electrodes from the interface by a glass frit, but normally it is not necessary due to the short time-scale of a typical experiment. Transfer of ions with the standard transfer potential beyond the limits of the potential window can be studied by complexing them with a ligand; this lowers the transfer energy, moving their transfer waves into the available potential window. Heterogeneous electron transfer can also be studied at this soft interface.³⁸ This shows that more diverse charge-transfer reactions can be studied at the liquid/liquid interface, compared to its counterpart – electrode/electrolyte interface. The illustration of the concepts of polarization and the corresponding polarized potential window (PPW) will be addressed below, starting from the case of conventional electrode/electrolyte interface. Then, it is adapted to the liquid/liquid interface with one liquid phase in place of the solid electrode. This methodology has set the standard in the field and most of the knowledge about charge transfer across the ITIES has been collected using this four-electrode configuration. The drawback for this experimental arrangement is that it requires relatively a large volume of each liquid phase. Besides, this specially designed four-electrode potentiostat (usually homemade in the early stage) is not as popular as its counterpart, namely three-electrode potentiostat, resulting in its limited use by electrochemists interested in this field. However, it should be noted that this four-electrode potentiostat has been commercialized by such as Autolab Ltd., making its impact spreading in life sciences.⁵⁵ Later on studies with a micro-ITIES formed at the orifice of a micropipette⁵⁶ or at a hole drilled in a solid plate holder²² has advanced this field further. The introduction of the concept of SECM in 1989⁵⁷ has also provided new

physical insights in this field,⁵⁸ as the combination between micro- or even nano-pipette supported ITIES and SECM has developed rapidly over the past few decades.⁵⁹ To employ the conventional three-electrode setup, Anson *et al.*^{60,61} and Scholz *et al.*,⁶² developed the thin-film and three-phase electrodes to study the kinetics and thermodynamics of charge transfer across the ITIES, respectively. Other novel techniques especially spectroelectrochemical ones such as second harmonic generation (SHG)⁶³⁻⁶⁶ that is sensitive to interface have been employed to study the ITIES.

In theoretical aspects, molecular dynamics simulations have provided some new physical insights.⁶⁷

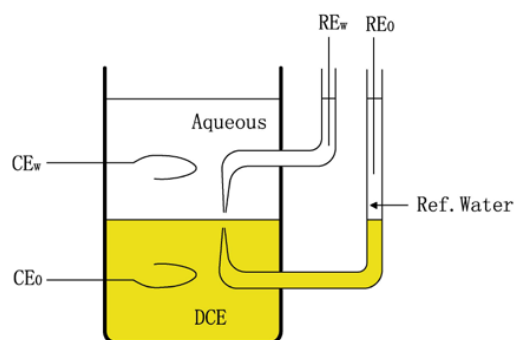


Figure 1-1. The four-electrode setup for liquid/liquid interface voltammetry. DCE: 1,2-dichloroethane.

However, prior to providing insights into the phenomena mentioned above, the nature and structure of the liquid/liquid interface needs to be discussed. But firstly, we need treat the conventional solid electrode/electrolyte interface, from which we can get some physical insights that can be adapted into the case of liquid/liquid interface.

1.2.3. The structure of the electrode/electrolyte interface

In theory, there are two classes of electrode/electrolyte interfaces, *i.e.* ideally polarizable electrode (IPE, Figure 1-2A) and ideally non-polarizable electrode (INPE, Figure 1-2B). An IPE is an electrode at which the potential across the electrode/electrolyte interface can be changed significantly without observable charge transfer, so only capacitive double-layer charging current can be observed. In this

sense, the IPE can be considered to be equivalent to a perfect capacitor (or condenser) without leakage. In reality, no electrode can behave as an IPE over the whole potential range available in a solution in which it is immersed. Some electrodes behave as the IPEs over limited potential range, which is determined by many factors like electrode materials, solvents, supporting electrolytes, and air (mainly O_2), etc. The limited potential range where the electrode behaves as an IPE is called the polarized potential window (PPW). For example, if platinum is used as the electrode material in aqueous acidic solution, the positive potential window will be limited by water oxidation ($2H_2O \rightarrow O_2 + 4H^+ + 4e^-$, $E^\circ = 1.23 \text{ V vs. SHE}^{68}$), provided that there is no other oxidizable species (*e.g.*, Br^- , $E^\circ = 1.087 \text{ V vs. SHE}^{68}$). On the other hand, the negative potential window is limited by proton reduction ($2H^+ + 2e^- \rightarrow H_2$, $E^\circ = 0 \text{ V vs. SHE}^{68}$). As platinum is a well-known catalyst for proton reduction with a small overpotential due to the Sabatier principle;^{69,70} hence the PPW is *ca.* 1.23 V for platinum under standard conditions. However, in reality the double layer region is much narrower owing to the strong adsorption of hydrogen and oxygen onto the platinum.⁷¹ It should be stressed that O_2 , a prevalent and redox-active molecule, often participates in an electrode process; however it is not needed to be removed from the solution for a platinum surface, as oxygen reduction will not occur at this negative potential window. If carbon is used instead, the positive potential limit is essentially the same as the platinum, but the negative potential limit can reach more negative values (*ca.* -0.76 V vs. SHE) in deaerated solution as proton reduction has a very high overvoltage on carbon. Under this condition, O_2 must be removed if measurements go more negative than 0 V vs. SHE . This is for the process in which (redox)species are in solution and it is also applicable for the surface-confined system *e.g.* a gold surface modified by a self-assembled monolayer of alkane thiol.⁷²

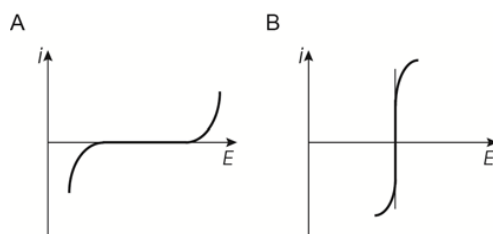


Figure 1-2. The i - E curves for an ideal (A) polarizable and (B) non-polarizable electrodes. The bold curves show the real electrodes that behave as ideal polarizable and non-polarizable electrodes only over limited potentials or currents.

An INPE is an electrode whose potential keeps constant even upon passage of charges. It is featured by a vertical line in an i - E curve (thin line in Figure 1-2B), again real electrodes can only behave as an IPNE over limited current range (bold curve in Figure 1-2B). An example is a saturated calomel electrode (SCE) or a silver/silver chloride electrode (Ag/AgCl/saturated KCl) that is usually employed as a reference electrode in electrochemical studies, under small current conditions.

A working electrode is the electrode on which the reaction of interest occurs. For the traditional electrochemistry, an electron transfer reaction between a redox species and the underlying working electrode is the reaction of interest. The consequence of the electron transfer that manifests as a current in a recorded i - E curve is the depolarization of the electrode/electrolyte interface. Hence, this redox species is also termed as a depolarizer. In brief, traditional electrochemists are interested in the ET reaction at an electrode/electrolyte interface, which behaves as an IPE over potential ranges as wide as possible. Therefore, intimate understanding of the structure and its corresponding potential distribution across the electrode/electrolyte boundary is essential for the practical applications in industry such as battery, semiconductor, corrosion, and electrosynthesis.

From the point of view of equivalent circuit, the IPE can be simply considered as a capacitor having a side-by-side double layer structure: one side hosts a positive excess charge, which is balanced by the equal amount of negative charge on another side (or vice versa), keeping the electroneutrality. For more detailed picture of the double layer, it evolves from Helmholtz to Gouy-Chapman to Stern and then to Grahame model.

In the primitive Helmholtz model, the double layer is treated as two rigid planes with electrode surface as one plane and ions solvated by solvent molecules as another plane. Specifically, at the solution side the solvated ions and solvent molecules arrange themselves along the electrode surface while keeping a separation from the electrode dictated by the size of the solvation sphere. The location of the center of the solvated ions is termed as the “outer Helmholtz plane” (OHP). Then, this arrangement creates a Galvani potential difference ($\phi_E - \phi_S$) at this double layer between the bulk

of the electrode (ϕ_E) and the bulk of the solution (ϕ_S), where ϕ is the inner potential of each phase. The potential varies linearly between the electrode surface and the OHP. Later on, a layer called as “inner Helmholtz plane” (IHP) was added into this model between the electrode surface and the OHP. In the IHP, ions strip off their solvating molecules and are adsorbed onto the electrode by chemical bond. But this simple model doesn't take into account the thermal fluctuation of the rigid OHP of solvated ions.

This thermal motion will disrupt the rigid structure of solvated ions in OHP and stimulates the development of Gouy-Chapman model. In this model, thermal motion will extend ions into the bulk of the solution to a greater distance from the electrode/electrolyte phase boundary. So the region between OHP and the bulk of the solution is defined as Gouy or diffuse layer. But neither the Helmholtz nor the Gouy-Chapman model can give an accurate picture of the electrical double layer.

Stern model combines all the merits from both Helmholtz and Gouy-Chapman models and has been well recognized. In Stern's model, ions will strip off their solvation sheath and can specifically adsorb on the electrode surface forming a so-called Stern or inner Helmholtz layer as suggested by Helmholtz while others form a Gouy or diffuse layer. Later on Grahame⁷³ developed an electrical double layer model based on Stern's work and shown in Figure 1-3 under conditions of cations specifically adsorbed on the electrode surface. This model constitutes three regions: IHP, OHP, and “diffuse layer”. In the IHP, solvent molecules as well as desolvated ions can adsorb on the electrode surface. While the solvated ions can approach the electrode surface only up to the OHP. Hence, the interaction between the electrode and the solvated ions mainly *via* the long-range electrostatic force and closest approaching solvated ions are called “non-specifically adsorbed ions”. Due to the thermal fluctuation, these non-specifically adsorbed ions will disperse beyond the OHP and extend into the bulk of the solution. The region bridged between OHP and the bulk of the solution is called “diffuse layer”. The charge neutrality principle results in a relation between the charge density on the electrode side and that on the solution side, reading as follows:

$\sigma_E = -\sigma_S = -(\sigma_i + \sigma_d)$, where σ_i is the charge density on the specific layer (“E” = electrode, “S” = solution, “i” = IHP, and “d” = diffuse layer), respectively.

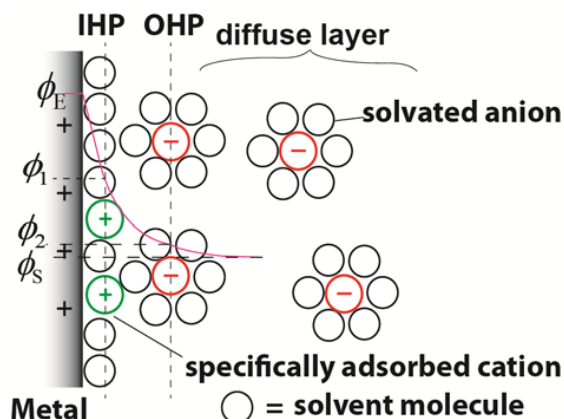


Figure 1-3. The Grahame model of the metal electrode/electrolyte double layer region under conditions where cations are specifically adsorbed. ϕ is called the inner potential for the bulk of each phase.

1.2.4. The structure of the liquid/liquid interface

Like the electrode/electrolyte interface, the liquid/liquid interface can also be either polarizable or nonpolarizable, depending on permeability to charged species distributed in either or both phases. If the interface is impermeable to charges (ions or electrons) it is called polarizable, otherwise it is called nonpolarizable or reversible.

The understanding of the interfacial structure is fundamental for theoretical treatment and practical applications of electrochemistry at liquid/liquid interfaces. For example, a clear picture of the liquid/liquid interface is needed for the correct interpretation of several interfacial processes such as charge transfer kinetics, potential distribution and adsorption of species. Therefore, many efforts have been made in order to uncover its structure by electrochemical, thermodynamic, spectroscopic and molecular dynamic simulation approaches. However, the ITIES's structure is still uncertain and just considered presumably as a defect-free soft molecular interface, which is in the nm scale for most electrochemists in the field. Up to date, four interfacial structure models have been proposed, namely Verwey-Niessen (VN), modified Verwey-Niessen (MVN),⁷⁴ Girault-Schiffrin (GS),⁷⁵ and a molecular dynamic model, in which MVN and GS models are mostly used in the classical electrochemistry.

1.2.4.1. Verwey-Niessen (VN) model

The first model to describe the electrical double layer at the ITIES was proposed by Verwey and Niessen (VN) in 1939.⁷⁶ In this VN model, two back-to-back diffuse layers form on both sides of the interface, each containing excess charges but with opposite signs. The potential distribution in the electrical double layer can be described by the Gouy-Chapman theory. When a potential difference is applied across the interface, space charge layers formed on both sides of the interface give rise to a capacity. This VN model gives a first approximation, but it deviates evidently from the experimental values. The experimental interfacial capacity is usually higher than that predicted by the VN model. This was alleviated by the introduction of a compact, ion-free inner layer bridged between the two diffuse layers, termed as the modified Verwey and Niessen (MVN) model, discussed further below.

1.2.4.2. Modified Verwey-Niessen (MVN) model

The modified Verwey-Niessen (MVN) model was developed by Gavach and co-workers in 1977,^{74,77} based on the Stern modification of the Gouy-Chapman theory, described in Figure 1-4. The introduced inner layer composed of oriented solvent molecules is analogous to the IHP in the classical electrode/electrolyte double layer, illustrated in Figure 1-3. In the MVN model, the Galvani potential difference $\Delta_o^w \phi$ across the ITIES is split into three parts:

$$\Delta_o^w \phi = \phi^w - \phi^o = \Delta_o^w \phi_{in} + \phi_2^w - \phi_2^o \quad (1-2)$$

where $\Delta_o^w \phi_{in} = \phi(X_2^w) - \phi(X_2^o)$, $\phi_2^w = \phi^w - \phi(X_2^w)$, and $\phi_2^o = \phi^o - \phi(X_2^o)$ are the potential differences across the inner layer, aqueous diffuse layer, and organic diffuse layer, respectively. The problem with this model is that there is still a debate on the existence of this inner layer. For example, the measured potential drop across the inner layer at the point of zero charge is small (0–40 mV),⁷⁷ while the capacity (*e.g.* NB/water interface) is rather high.⁷⁸ This questioned the existence of the ion-free inner layer, as a much lower capacity was expected based on the model for the electrolyte side at the electrode/electrolyte interface. So Samec *et al.*^{79,80} proposed that ions can penetrate into the inner layer and then this modified MVN model can describe the NB/water interface reasonably.

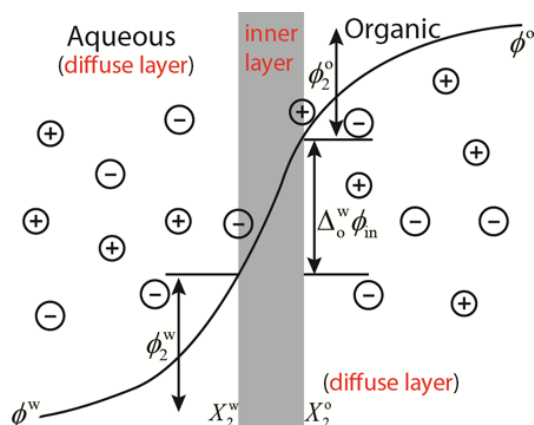


Figure 1-4. The MVN model and its corresponding potential distribution, adapted according to Gavach *et al.*⁷⁴

However, this MVN model is based on the surface tension and capacitance measurements that belong to the thermodynamics regime. A dynamic pictorial of the microscopic interface needs to be described.

1.2.4.3. Girault-Schiffrin (GS) model

Also based on the surface tension and capacitance measurements, Girault and Schiffrin proposed a mixed solvent layer model in 1983,⁷⁵ shown in Figure 1-5.⁸¹ They suggested that there was no compact inner layer composed of oriented solvent molecules and the associated potential drop across this layer. This is in agreement with the experimentally measured small potential drop across the inner layer.⁷⁷ So the potential distributes only in the two back-to-back diffuse layers. The thickness of this mixed solvent layer is no more than two or three molecular diameter. As similar as that proposed by Samec *et al.*,^{79,80} ions can penetrate into the interfacial region with the extent depending on their hydrophilicity or lipophilicity. For example, hydrophilic ions like potassium or chloride have smaller tendency to enter the interface evidenced by positive surface excess concentration of water.⁷⁵ It is depicted in Figure 1-5a with a KCl (w)/TBATPB (DCE) system, where TBATPB refers to tetrabutylammonium (TBA^+) tetraphenylborate (TPB^-). However, hydrophobic ions like TBA^+ will shed the hydration shell and are solvated predominately by the organic molecules when transferred into the organic phase from aqueous.⁸²⁻⁸⁴ So at the non-polarized interface

between two electrolytes featured by a shared common cation (e.g. TBACl (w)//TBATPB (DCE), Figure 1-5b), this cation will penetrate the interface freely to the extent that they can specifically adsorb at the interfacial region and form ion pairs with the counter anions from aqueous phase. This model was supported by theoretical calculations for the lattice-gas model of the liquid/liquid interface⁸⁵ and the experimental results from ellipsometry.⁸⁶

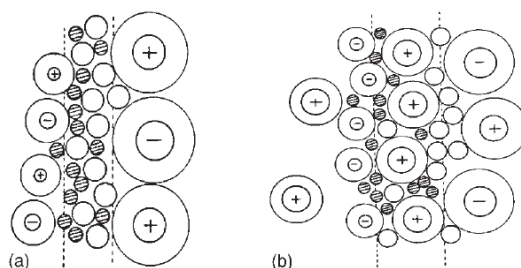


Figure 1-5. The mixed solvent layer model at the (a) polarized liquid/liquid interface and (b) non-polarized liquid/liquid interface that is reproduced from references.^{38,81}

It should be noted that this GS model is also based on the thermodynamics measurements and a model based on molecular dynamics is needed for more details.

1.2.4.4. Molecular dynamics simulations

Linse is the pioneer to study the bare water/benzene interface by Monte-Carlo simulations.⁸⁷ Then, Benjamin studied the DCE/water interface⁸⁸ and showed that the presence of a static electric field will broaden the interface and decrease the surface tension by increasing the magnitude of finger-like distortions.⁸⁹ These finger-like structures or capillary waves corroborate indirectly the concept of GS model mentioned above, but with more details. Until now, it has been well recognized that the DCE/water interface is a molecularly sharp but rough, with an average thickness of 1 nm. The interfacial structure is also affected by the polarity of the organic solvent, *e.g.* Walker and Richmond reported that CCl₄/water interface was thinner than the DCE/water interface.⁹⁰

For the aspect of electrolyte (w)/electrolyte (o) or electrolyte/solvent system, Benjamin pioneered in this field with a landmark paper published in 1993,⁹¹ showing that small hydrophilic anions can transfer into the organic phase by creating water

fingers (by ion-dipole interactions) protruding towards the organic phase. It means that the ion transfer is an activated rather than a simple diffusive process. This also applies to the hydrophilic cation case.⁹² They also studied the transfer of hydrophobic ions like tetramethylammonium (TMA^+) at the NB/water interface.⁹³ The conclusion obtained from these two comparative studies is: (1) small inorganic ions will keep their first hydration shell when transferred into the organic phase; (2) transfer of hydrophobic ions involves only a small change in the (re)solvation free energy and the transferred hydrophobic ions will shed their hydration shells when going into the organic phase. This will provide physical insights that can be used in biological science and industry. Figure 1-6 illustrates a snapshot of the DCE/water interface, showing the local surface roughness. This roughness may assist the transfer of solute across the interface.⁶⁷

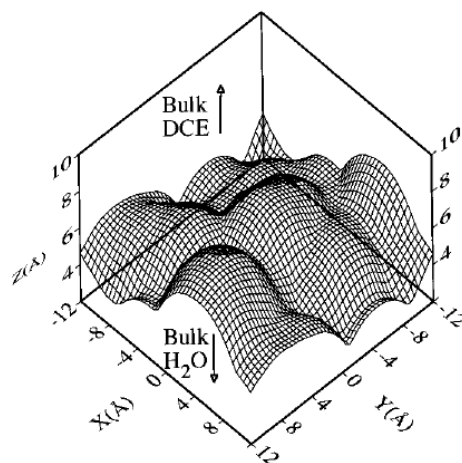


Figure 1-6. A snapshot of the DCE/water interface reproduced from reference.⁶⁷

In summary, the liquid/liquid interface is molecularly sharp but with finger-like roughness caused by thermal fluctuations and capillary waves. From the viewpoint of classical electrochemistry, namely studies on electron or ion transfer process, these molecular soft interfaces present some advantages: they are defect-free and easier to be prepared compared to its counterpart – the solid electrode surface. Another merit is that the experimental results obtained on these soft molecular interfaces are highly reproducible.

1.2.5. Thermodynamics of the liquid/liquid interface

1.2.5.1. Galvani potential difference

According to the definition suggested by the IUPAC, electrochemical potential $\tilde{\mu}$ is the partial molar Gibbs energy of the substance in a specified phase at the specified electric potential. In phase α for a charged species i , the electrochemical potential $\tilde{\mu}_i^\alpha$ is expressed as:

$$\tilde{\mu}_i^\alpha = \mu_i^\alpha + z_i F \phi^\alpha \quad (1-3)$$

where z_i is the charge number of i including the sign, F has been defined, and ϕ^α is the inner (or Galvani) potential in phase α . The term μ_i^α is the chemical contribution and called the chemical potential,

$$\mu_i^\alpha = \mu_i^{\circ,\alpha} + RT \ln a_i^\alpha \quad (1-4)$$

in which $\mu_i^{\circ,\alpha}$ is the standard chemical potential of i in phase α , R and T have been defined, and a_i^α is the activity of i in phase α , respectively.

Combining equations 1-3 and 1-4, we obtain

$$\tilde{\mu}_i^\alpha = \mu_i^{\circ,\alpha} + RT \ln a_i^\alpha + z_i F \phi^\alpha \quad (1-5)$$

Hence, the first two terms of the right-hand side of equation 1-5 standard for the chemical contribution, while the last term is the electrostatic contribution.

The inner potential ϕ^α is composed of a surface potential, χ^α , and an outer potential, ψ^α .⁹⁴

$$\phi^\alpha = \chi^\alpha + \psi^\alpha \quad (1-6)$$

Upon contact between two phases α and β , a Galvani potential difference rises:

$$\phi^\alpha - \phi^\beta = (\chi^\alpha - \chi^\beta) + (\psi^\alpha - \psi^\beta) \quad (1-7)$$

equivalently

$$\Delta_\beta^\alpha \phi = \Delta_\beta^\alpha \chi + \Delta_\beta^\alpha \psi \quad (1-8)$$

The Galvani potential difference $\Delta_\beta^\alpha \phi$ is of primary importance to electrochemical processes at the phase boundary between α and β and will be encountered frequently in the present work. Next, an equivalent Nernst equation for ion transfer between aqueous and organic phases will be derived, based on the equality of electrochemical potential of the ion between the adjacent phases at equilibrium and the concept of $\Delta_\beta^\alpha \phi$.

1.2.5.2. Equivalent Nernst equation for ion transfer

Under conditions of constant temperature T and pressure P_{air} , the equilibrium of ion transfer between aqueous and organic phases (o and w) only holds if the electrochemical potential of a given ion, i , is equal in the two phases, reading as:

$$\mu_i^{\circ, \text{w}} + RT \ln a_i^{\text{w}} + z_i F \phi^{\text{w}} = \mu_i^{\circ, \text{o}} + RT \ln a_i^{\text{o}} + z_i F \phi^{\text{o}} \quad (1-9)$$

Rearranging equation 1-9, a formal Nernst equation for ion transfer can be obtained:

$$\Delta_\text{o}^{\text{w}} \phi = \phi^{\text{w}} - \phi^{\text{o}} = \Delta_\text{o}^{\text{w}} \phi_i^\circ + \frac{RT}{z_i F} \ln \left(\frac{a_i^{\text{o}}}{a_i^{\text{w}}} \right) \quad (1-10)$$

where $\Delta_\text{o}^{\text{w}} \phi_i^\circ$ is the standard transfer potentials of i , expressed in a voltage scale, and equals to

$$\Delta_o^w \phi_i^\circ = \frac{\Delta G_{tr,i}^{\circ,w \rightarrow o}}{z_i F} \quad (1-11)$$

in which $\Delta G_{tr,i}^{\circ,w \rightarrow o}$ is the standard Gibbs energy of transfer from aqueous to organic phase.

At the half-wave potential and if the ion i transfer is reversible, *i.e.*⁶⁸

$$\sqrt{D_i^w c_i^w} = \sqrt{D_i^o c_i^o} \quad (1-12)$$

equation 1-10 can be written further as

$$\begin{aligned} \Delta_o^w \phi_{1/2} &= \Delta_o^w \phi_i^\circ + \frac{RT}{z_i F} \ln \left(\frac{\gamma_i^o c_i^o}{\gamma_i^w c_i^w} \right) = \Delta_o^w \phi_i^\circ + \frac{RT}{z_i F} \ln \left(\frac{\gamma_i^o}{\gamma_i^w} \right) - \frac{RT}{2z_i F} \ln \left(\frac{D_i^o}{D_i^w} \right) \\ &= \Delta_o^w \phi_i^{\circ'} - \frac{RT}{2z_i F} \ln \left(\frac{D_i^o}{D_i^w} \right) \end{aligned} \quad (1-13)$$

where $\Delta_o^w \phi_i^{\circ'}$ is the formal ion transfer potential, γ_i^α and D_i^α are the activity coefficient and diffusion coefficient of the ion i in phase α , respectively. The ratio $\frac{D_i^w}{D_i^o}$ can be estimated by the Walden's rule $\eta^w D_i^w = \eta^o D_i^o$, with η the viscosity of the respective solvent.

From equation 1-10, the partition coefficient, P , of the ion i in a biphasic system can be obtained:

$$P_i = \frac{a_i^o}{a_i^w} = \exp \left[\frac{z_i F}{RT} (\Delta_o^w \phi - \Delta_o^w \phi_i^\circ) \right] \quad (1-14)$$

and usually the lipophilicity of the ion i is expressed as the standard partition coefficient in the logarithmic scale when the interface is not polarized ($\Delta_o^w \phi = 0$), namely

$$\ln P_i^\circ = \frac{-z_i F}{RT} \Delta_o^w \phi_i^\circ \quad (1-15)$$

$$\text{or } \log P_i^\circ = \frac{-z_i F}{2.303RT} \Delta_o^w \phi_i^\circ \quad (1-16)$$

Hence, lipophilicity of the ion i can be estimated by cyclic voltammetry (CV) or square wave voltammetry (SWV) at the macro-ITIES (cm^2 or mm^2), by noting that $\Delta_o^w \phi_{1/2}$ is equal to the mid-peak potential in CV or peak potential in SWV. The mid-peak potential in CV is the average of the equivalent anodic ($\Delta_o^w \phi_{\text{pa}}$) and cathodic ($\Delta_o^w \phi_{\text{pc}}$) peak potentials, respectively, by analogy with that in the redox reactions at the solid electrode/electrolyte interfaces. Besides, current signal representing transfer of the positive ion from aqueous to organic phase or negative ion to the reverse direction can be defined as the anodic wave in CV. The cathodic wave can be defined similarly. While at micro-ITIES, $\Delta_o^w \phi_{1/2}$ is equal to the potential value at the half height of the steady-state current with respect to the base line.

This indicates that voltammetry at the ITIES can be used for estimation of the lipophilicity of ionic or ionizable drugs in pharmaceutical sciences. This concept was further developed by Girault and co-workers to construct an ionic partition diagram defined as the domains of predominance of all available species in both phases as a function of the interfacial potential difference and aqueous pH.³² This is an important supplement to the conventional water-octanol partition coefficient⁹⁵ that is used for evaluation of the pharmacological activity of drugs.

Equation 1-10 also implies that cations will transfer from the aqueous to the organic phase or anions to the reverse direction when a Galvani potential applied by an external source is more positive than the standard transfer potential of the transferred ions.

1.2.5.3. Nonpolarizable ITIES

An ITIES can be also classified into polarizable and nonpolarizable depending on the permeability of the interface towards the ions or electrolytes present.

A nonpolarizable ITIES can be simply represented by the partition of a single binary electrolyte RX, which is assumed to dissociate completely in both phases into R^+ and X^- , depicted by the equation below:



and the biphasic system can be described as below:



At equilibrium, the electrochemical potentials of both cation and anion are equal between the two phases:

$$\mu_{R^+}^{\circ,w} + RT \ln a_{R^+}^w + F\phi^w = \mu_{R^+}^{\circ,o} + RT \ln a_{R^+}^o + F\phi^o \quad (1-19)$$

$$\mu_{X^-}^{\circ,w} + RT \ln a_{X^-}^w - F\phi^w = \mu_{X^-}^{\circ,o} + RT \ln a_{X^-}^o - F\phi^o \quad (1-20)$$

Rearranging and combining equations 1-19 and 1-20, the Galvani potential difference (also known as the distribution potential) $\Delta_o^w\phi$ at the ITIES will establish⁹⁶

$$\Delta_o^w\phi = \frac{\Delta_o^w\phi_{R^+}^{\circ} + \Delta_o^w\phi_{X^-}^{\circ}}{2} + \frac{RT}{2F} \ln \left(\frac{a_{R^+}^o a_{X^-}^w}{a_{R^+}^w a_{X^-}^o} \right) \quad (1-21)$$

Taking into account the charge neutrality must be met in each phase:

$$c_{R^+}^o = c_{X^-}^o \text{ and } c_{R^+}^w = c_{X^-}^w, \text{ with } a = \gamma c \quad (1-22)$$

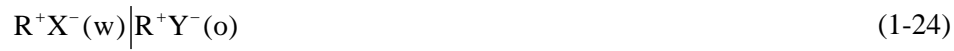
We obtain the equation 1-23 shown below:

$$\Delta_o^w\phi = \frac{\Delta_o^w\phi_{R^+}^{\circ} + \Delta_o^w\phi_{X^-}^{\circ}}{2} + \frac{RT}{2F} \ln \left(\frac{\gamma_{R^+}^w \gamma_{X^-}^o}{\gamma_{R^+}^o \gamma_{X^-}^w} \right) \quad (1-23)$$

where $\Delta_o^w \phi_{R^+}^\circ$ and $\Delta_o^w \phi_{X^-}^\circ$ are the standard transfer potentials of R^+ and X^- , respectively, γ , R , T , and F have their usual meanings. Equation 1-23 implies that $\Delta_o^w \phi$ is independent of the electrolyte concentration and the volume ratio between the two adjacent solutions. It is the reason that this system is nonpolarizable. Under conditions of dilute electrolytes, the second term of equation 1-23 can be neglected.

1.2.5.4. ITIES with a common ion

For a biphasic system featured by a common ion described below:



Under certain conditions ($\Delta_o^w \phi_{X^-}^\circ \ll \Delta_o^w \phi_{R^+}^\circ \ll \Delta_o^w \phi_{Y^-}^\circ$), the equilibrium potential difference is determined by the distribution of the common ion R^+ in each phase, by virtue of the Nernst equation 1-10, we have

$$\Delta_o^w \phi = \phi^w - \phi^o = \Delta_o^w \phi_{R^+}^\circ + \frac{RT}{F} \ln \left(\frac{a_{R^+}^o}{a_{R^+}^w} \right) \quad (1-25)$$

It implies that the interface is nonpolarizable as any attempt to perturb the potential (by external source) from the distribution potential imposed by the common ion will be opposed by readjusting the activity ratio of the common ion between the two adjacent phases, returning the system into equilibrium. But we can say that the interface is polarized chemically by the common ion, as a well-defined potential difference has been established.

1.2.5.5. General expression of distribution potential

It should be noted that $\Delta_o^w \phi$ is dependent on all ionic species distributed in the two phases and the equilibrium value of $\Delta_o^w \phi$ can be calculated based on the initial concentrations of electrolytes, the values of $\Delta_o^w \phi_i^\circ$ for all ionic species, and the volumes of the two phases.

The mass balance conditions for each ion i hold:

$$n_{i,\text{total}} = n_i^{\circ} + n_i^{\text{w}} \quad (1-26)$$

i.e.

$$V^{\circ} c_i^{0,\circ} + V^{\text{w}} c_i^{0,\text{w}} = V^{\circ} c_i^{\circ} + V^{\text{w}} c_i^{\text{w}} \quad (1-27)$$

where $c_i^{0,\circ}$ and $c_i^{0,\text{w}}$ are the initial concentrations of the ion i in organic and aqueous phases, and c_i° and c_i^{w} are the equilibrium concentrations, respectively; V° and V^{w} are the volumes of the two phases and it is assumed that $V^{\circ} = V^{\text{w}}$ (1-28).

To calculate Δ_{ϕ}^{w} , the Nernst equation 1-10 for each ion i needs to be considered:

$$\Delta_{\phi}^{\text{w}} = \Delta_{\phi}^{\text{w}} \phi_i^{\circ'} + \frac{RT}{z_i F} \ln \left(\frac{c_i^{\circ}}{c_i^{\text{w}}} \right) \quad (1-29)$$

where the activity coefficient terms have been merged together with the standard ion transfer potential to derive the formal ion transfer potential:

$$\Delta_{\phi}^{\text{w}} \phi_i^{\circ'} = \Delta_{\phi}^{\text{w}} \phi_i^{\circ} + \frac{RT}{z_i F} \ln \left(\frac{\gamma_i^{\circ}}{\gamma_i^{\text{w}}} \right) \quad (1-30)$$

The charge neutrality must also be met in each phase:

$$\sum_{i=1}^m z_i c_i^{\text{w}} = \sum_{i=1}^m z_i c_i^{\circ} = 0 \quad (1-31)$$

Combining equations 1-27, 1-28, 1-29, and 1-31 yields

$$\sum_{i=1}^m \frac{z_i (c_i^{0,\circ} + c_i^{0,\text{w}})}{1 + \exp \left[\frac{z_i F}{RT} (\Delta_{\phi}^{\text{w}} \phi - \Delta_{\phi}^{\text{w}} \phi_i^{\circ'}) \right]} = 0 \quad (1-32)$$

when m kinds of ions are distributed at equilibrium between the liquid/liquid interface.

Equation 1-32 was derived firstly by Hung,⁹⁷ allowing the evaluation of $\Delta_o^w \phi$, provided that all the values of initial concentrations as well as the $\Delta_o^w \phi_i^{\circ}$ for all ions are known. Then, the equilibrium concentrations for all ions can be calculated based on equations 1-27 and 1-29. It should be stressed that all the equations derived above don't take into account the ion-pair formation for simplicity.

If equation 1-32 is solved for a system containing only one binary electrolyte RX, the equation 1-23 is obtained again.

1.2.5.6. Ideally polarizable ITIES

From the viewpoint of electrochemists at ITIES, they are more interested in an ideally polarizable ITIES with a potential window as wide as possible. Then more kinds of charge transfer reactions can be investigated, as similar as the electrode/electrolyte interface. A polarizable ITIES can be simply represented by a system with two different electrolytes RX and SY in aqueous (w) and organic (o) phases, respectively. R^+ and X^- are very hydrophilic like LiCl and S^+ and Y^- are very hydrophobic like tetrabutylammonium tetraphenylborate (TBATPB). It is illustrated as below:



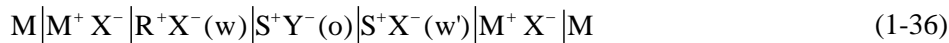
The standard Gibbs transfer energies of R^+ and X^- are very positive from w to o, while they are very negative for S^+ and Y^- , expressed as

$$\begin{aligned} \Delta G_{tr,R^+}^{\circ,w \rightarrow o} &\gg 0 \text{ and } \Delta G_{tr,X^-}^{\circ,w \rightarrow o} > 0 \\ \Delta G_{tr,S^+}^{\circ,w \rightarrow o} &\ll 0 \text{ and } \Delta G_{tr,Y^-}^{\circ,w \rightarrow o} \ll 0 \end{aligned} \quad (1-34)$$

or in Galvani potential scale

$$\begin{aligned} \Delta_o^w \phi_{R^+}^{\circ} &\gg 0 \text{ and } \Delta_o^w \phi_{X^-}^{\circ} > 0 \\ \Delta_o^w \phi_{S^+}^{\circ} &\ll 0 \text{ and } \Delta_o^w \phi_{Y^-}^{\circ} > 0 \end{aligned} \quad (1-35)$$

The Galvani potential difference $\Delta_o^w\phi$ at the ITIES is controlled by the excess electrical charge at the double layer, which can be supplied by an external power source. This interface can be studied by a Galvanic cell connected with an external source



where M is a metal (*e.g.* silver). The cell potential is defined as the terminal potential at the right hand with respect to that at the left hand:

$$E = \Delta_o^w\phi + \Delta E_{\text{ref}} \quad (1-37)$$

in which ΔE_{ref} is dependent on the composition of the two reference electrodes $M|M^+X^-|R^+X^-(w)$ and $M|M^+X^-|S^+X^-(w')$. The potential difference at the $o|w'$ boundary is constant and dictated by the partition of the common ion S^+ . It is called as the reference interface, as mentioned before in section 1.2.2. So, $M|M^+X^-|R^+X^-(w)$, $M|M^+X^-|S^+X^-(w')$, and $o|w'$ are the nonpolarizable interfaces. It implies that $R^+X^-(w)|S^+Y^-(o)$ is the only polarizable interface at which charge transfer (of the depolarizer in suitable concentration) processes can be studied.

In the past, TBATPB was the most frequently used supporting electrolyte in organic solvent, which usually determines the potential window, if aqueous solution contains such as LiCl. While much efforts were made to find more hydrophobic salts to widen the potential window as big as possible, for example bis[triphenylphosphoranylidene]ammonium tetrakis [4-chlorophenyl]borate (BATPBCl) or BATB has been employed as the hydrophobic salt successfully to make the potential window mostly limited by the aqueous electrolytes.⁵³

1.2.6. Methods and techniques to study the ITIES

In section 1.2.2, a brief history for the evolution of the methods employed for studying the ITIES has been addressed. However, more details will be given in this

part for better understanding and exploiting the properties of different methods for practical applications.

1.2.6.1. Four-electrode system

Most experimental results, especially the thermodynamic and kinetic data of charge transfer processes, at a large ITIES (mm^2 or cm^2 scale), were obtained at the polarizable interface in the four-electrode setup, with the electrical charge supplied by the external source, *i.e.* by electrochemical polarization. The setup has been shown in Figure 1-1, in which a non-planar interface is formed due to the surface tension effect. Although this non-ideality causes non-uniformity of electric field and difficulty in calculations related to the interfacial area, it is not a major problem. Besides, the interface is tuned to be located closer to the organic Luggin capillary in order to minimize the iR drop in the resistive organic solvent. If a precise control for the position and flatness of the interface is needed, a setup shown in Figure 1-7 can be employed. Alternatively, one can modify the inner part (where the organic phase is located) to be hydrophobic by *e.g.* dimethyldichlorosilane⁹⁸ or by inserting a piece of plastic tubing.⁹⁹ An ITIES with a spherical geometry can be enabled by a dropping electrolyte electrode.¹⁰⁰ This four-electrode setup has expanded its impact to the studies of charge transfer across lipid bilayer membranes separating two aqueous phases.⁵⁵

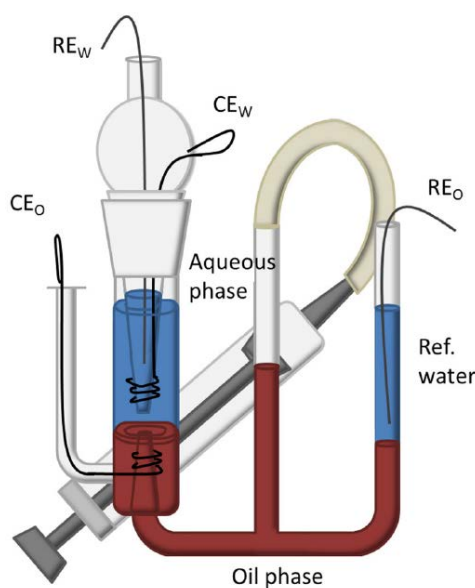


Figure 1-7. The four-electrode setup used for voltammetric measurements, in which a syringe is connected to the middle tube to adjust the position and flatness of the interface, reproduced from reference.¹⁰¹

A block diagram of the four-electrode potentiostat is shown in Figure 1-8. More details on the working principle of this potentiostat have been discussed in literature.⁵⁰⁻⁵² While, the limitations for this four-electrode setup are: 1) both phases need supporting electrolytes resulting in a relatively narrow potential window; 2) the number of available organic solvents is small; 3) both phases and the dissolved electrolytes are in large quantity that is related to the issues of cost and environmental concern.

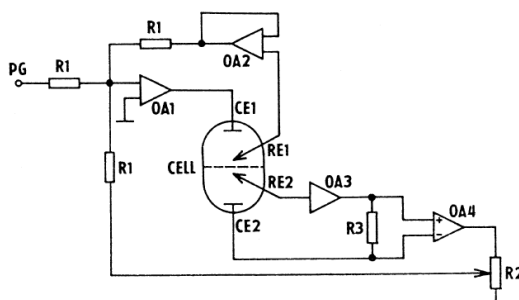


Figure 1-8. Block diagram of a four-electrode potentiostat used for ITIES electrochemical polarization with the positive feedback for the iR drop compensation, reproduced from reference.¹⁰²

1.2.6.2. Micro- or nano-ITIES system

As in conventional electrochemistry which has been revolutionized by the solid micro- and nano-electrodes,^{103,104} the emergence of micro- and nano-ITIES has also significantly changed the electrochemistry at liquid/liquid interfaces.⁵⁹ In 1986, Girault and co-workers supported the ITIES on a glass micropipette to study the ion transfer,⁵⁶ indicating the start of the micro-ITIES electrochemistry. This novel concept was inspired by the patch-clamp technique used for recording the ionic currents across the biomembranes in electrophysiology.¹⁰⁵ The merits of this methodology are the minimization of capacitive current and iR drop, as well as a dramatic improvement of mass transfer rate. So a two-electrode setup, shown in Figure 1-9, can be employed to simplify the complicated electronics in the classical four-electrode potentiostat, thanks

to a current scale of nA or pA normally encountered in micro- or nano-ITIES, respectively. The geometry of the pipette in micro-scale causes an asymmetrical diffusion field – hemispherical for ingress and linear for egress of the transported species. Hence, the voltammogram of ion transfer shows a peak for ion egress and a steady-state wave for ion ingress the pipette, respectively.

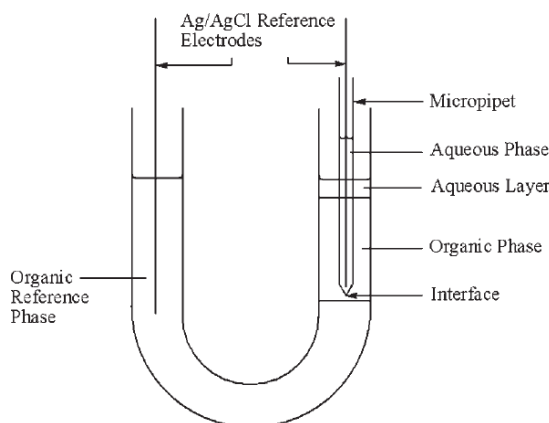


Figure 1-9. A two-electrode setup with the ITIES supported at a glass micropipette, reproduced from reference.³⁸

Later on, the concept of miniaturization was adapted to an ITIES supported in a microhole drilled in a polymer film¹⁰⁶ and then extended to micro-ITIES arrays on silicon film.²² This geometry causes a symmetrical diffusion field characterized with a steady-state voltammogram as that obtained on a solid microdisk electrode. But a nano-ITIES can only be achieved at a glass/quartz pipette until now.⁵⁹ An interesting feature should be mentioned that with the decrease of the pipette size from μm to nm , a transition in voltammogram from an asymmetrical to a pseudo-steady state can be observed, as shown in Figure 1-10. In fact, when the size of the opening at the pipette tip goes to few nm, the pipette shape can be considered as a hyperbola, and then the diffusion fields inside and outside the pipette are spherical in nature, and finally the steady state current I_{ss} can be expressed as¹⁰⁷

$$I_{ss} = \pi n F D c r \theta \quad (1-38)$$

where r is the tip radius, θ is the shank angle, and all others have their usual meanings.

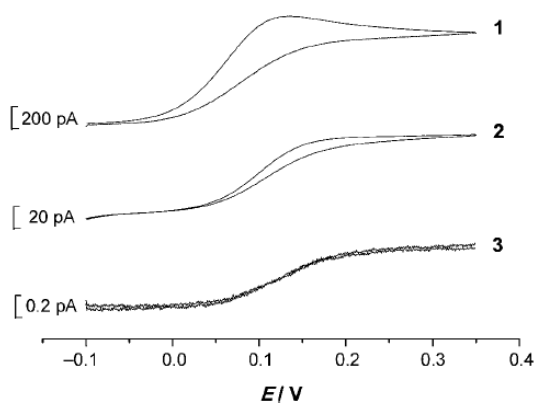


Figure 1-10. Cyclic voltammograms (50 mVs^{-1}) of tetraethylammonium cation (TEA^+) transfer across the w/DCE interface supported at glass pipettes with variable sizes from $4 \mu\text{m}$ (curve 1), to 100 nm (curve 2), and to 1.2 nm (curve 3), respectively. Reproduced from reference.¹⁰⁷

This micro- or nano-ITIES is very useful for measuring kinetics of very fast ion transfer¹⁰⁷ and Gibbs transfer energy of extreme hydrophilic or lipophilic ions.⁵³

1.2.6.3. Scanning electrochemical microscopy

The hyphenation between micro- or nano-pipette and SECM has already demonstrated its significance and great in the investigation of simple or facilitated ion transfer and high-resolution electrochemical imaging.^{108,109} In fact, the gist of the concept of scanning ion-conduction microscopy (SICM) is the employment of a micropipette as the probe.¹¹⁰ SICM appeared almost the same time as SECM, both in 1989.^{57,110}

A metallic microelectrode can also be employed as the probe in SECM but for studying the heterogeneous bimolecular electron transfer kinetics across the ITIES, pioneered by Bard and co-workers.^{58,111} The polarization of the ITIES in these two works^{58,111} is controlled by the distribution of a common ion between the two adjacent phases in different concentration ratios and a potential dependence of the electron transfer rate in the Butler-Volmer formalism has been observed.¹¹¹ In fact, the driving force for this heterogeneous electron transfer is composed of two components: 1)

difference in standard redox potentials between the aqueous and organic redox species referred to an identical reference scale *e.g.* the aqueous SHE; 2) interfacial Galvani potential difference determined by the common ion distribution. With a steady increase in the driving force for the heterogeneous electron transfer reactions to an extent that, a Marcus inverted region can be observed.^{112,113} In another work of Bard and co-workers,¹¹² they tuned the driving force for the heterogeneous electron transfer reaction by varying the aqueous redox species but keeping the organic redox species. While Shao's group¹¹³ realized the tuning of driving force for the heterogeneous electron transfer at the ITIES by changing the interfacial Galvani potential difference from an external power source. The merits of Shao's methodology are that they can be controlled more precisely and easily. The experimental setup is shown in Figure 1-11.

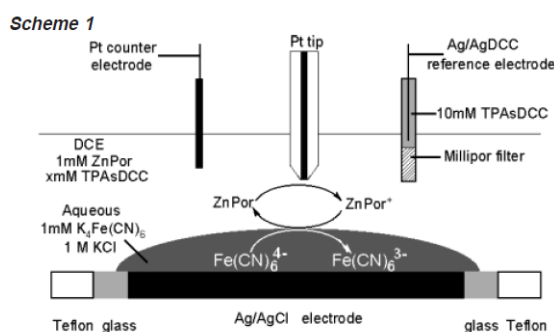


Figure 1-11. The experimental setup used for studying the heterogeneous electron transfer processes across the ITIES, reproduced from reference.¹¹³

One issue that should be mentioned is that cyclic voltammograms (CVs) of ion or electron transfer at the ITIES with the four-electrode system are similar, which makes difficulty in differentiation between electron and ion transfers occurred at the ITIES. This can be circumvented by the application of SECM to the ITIES, since SECM can address independently the electron or ion transfer at the liquid/liquid interface.^{58,112,114}

1.2.6.4. Three-electrode system

In 1998, Shi and Anson reported a simple methodology to study the electron transfer across the ITIES by covering a thin organic solvent layer onto an edge plane pyrolytic graphite (EPPG) electrode which was then immersed in an aqueous

solution.^{60,61} The redox couples are located into both phases. This concept is a variant of the electrochemical rectification at a monolayer modified electrode, *i.e.* a vectorial electron transfer can be realized *via* a redox mediator confined in the monolayer.¹¹⁵ This strategy can be used in a three-electrode system that has attracted extensive interests into this field.³ There are a lot of advantages in this methodology: minute organic solvent (μL), supporting electrolyte, and redox species are needed; small iR drop; wider potential window composed of two polarizable interfaces, *i.e.* the organic/electrode interface and the ITIES, in series, and easier data treatment to extract the kinetic information without complicated digital simulation and curve fitting. The environmental concern is also minimized because the organic layer modified electrode is immersed into the aqueous solution, avoiding the evaporation of the organic solvent. If there is no redox species present in the aqueous phase, ion transfer across the ITIES can be investigated *via* the electron transfer and ion transfer coupling occurring at the electrode surface and the ITIES respectively.^{60,61} The experimental setup (Figure 1-12), operating mechanism, and theoretical background on this methodology are discussed briefly below:

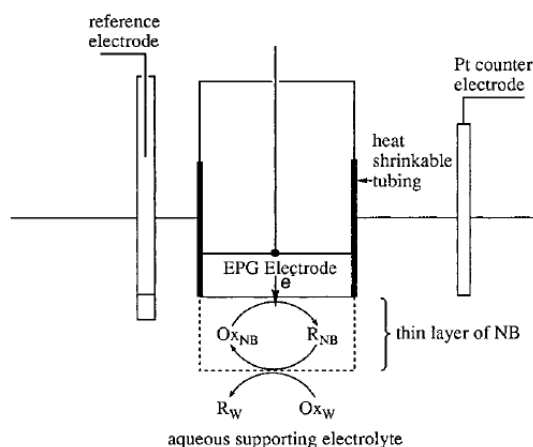


Figure 1-12. Schematic depiction of the thin-layer arrangement in a three-electrode system for the investigation of electron transfer at the NB/w interface, reproduced from reference.⁶¹

The electrochemical cell is composed of a reference, a counter, and a NB layer (10–100 μm) modified EPPG electrodes, all of which are immersed into an aqueous solution (Figure 1-12). Then the ITIES is formed between the NB layer and the

aqueous solution. Assuming initially a hydrophobic redox species Ox_{NB} and another hydrophilic redox species Ox_w are present in the NB layer and aqueous phase, respectively. Due to this thin organic layer, Ox_w cannot make electronic communication on the EPPG electrode surface directly. But if R_{NB} that, produced on EPPG electrode by Ox_{NB} electroreduction, can be oxidized by Ox_w at the ITIES, a vectorial electron transfer from EPPG to Ox_w occurs.



So Ox_{NB} is recycled, and a cathodic plateau (or catalytic) current will be observed if the potential scan rate is sufficiently small. No return peak is observed when the potential scan is reversed, due to the consumption of R_{NB} by reaction with Ox_w heterogeneously. Under suitable conditions, Shi and Anson developed a simple method to get the rate constant for this heterogeneous electron transfer at the ITIES.^{61,116,117}

$$\frac{1}{i_{obs}} = \frac{1}{i_D} + \frac{1}{i_{et}} \quad (1-41)$$

$$i_D = nFAc_{Ox_{NB}} D_{Ox_{NB}} / \delta \quad (1-42)$$

$$i_{et} = nFAk_{et} c_{Ox_{NB}} c_{Ox_w} \quad (1-43)$$

Where i_{obs} is the observed plateau current, i_{D} the diffusion-limited current of Ox_{NB} in the NB thin layer, i_{et} the kinetic current of the heterogeneous biphasic electron transfer reaction, A the EPPG electrode surface area, $c_{\text{Ox}_{\text{NB}}}$ and $D_{\text{Ox}_{\text{NB}}}$ are the concentration and diffusion coefficient of Ox_{NB} in the NB thin layer, respectively, δ the NB layer thickness, k_{et} the bimolecular electron transfer rate constant, $c_{\text{Ox}_{\text{w}}}$ the concentration of Ox_{w} in aqueous phase, and all other terms have been defined previously. One should mention that based on the comments from Barker and Unwin,¹¹⁸ Shi and Anson have optimized the experimental conditions to make this methodology more reliable.¹¹⁷

In Anson's method, the electrode surface is covered by the organic thin layer completely. While Compton and co-workers demonstrated a new concept to study the liquid/liquid interface electrochemically, namely numerous organic redox microdroplets were deposited onto a solid electrode such as a graphite electrode and then immersed in an aqueous electrolyte.¹¹⁹ Under these conditions, the electrode surface is not covered completely and a three-phase junction between the solid electrode, aqueous, and organic droplet is formed.¹²⁰ In the absence of any redox couple in aqueous phase, the overall electrochemical reaction at the three-phase junction is an electron-transfer induced ion-transfer process. For example, upon oxidation of the redox droplet on the electrode surface, anions will be inserted into the organic phase from the aqueous phase to keep the charge neutrality in the organic phase. In 2000, Scholz *et al.* showed that it was very useful to employ this experimental arrangement to estimate the Gibbs energy of ion transfer across the ITIES.⁶² The difference between Compton's method and that of Scholz lies in that only a single macro-hemispheric organic droplet rather than numerous microdroplets is formed on a paraffin impregnated graphite electrode (PIGE). A series of ions and organic solvents, including those cannot be accessed by the classical four-electrode setup, have been studied successfully *via* this PIGE three-phase junction methodology.^{1,121}

Additionally, different approaches have been developed for measuring the kinetics of ion transfer across the ITIES based on thin-film modified electrodes,^{60,122,123} in combination with Osteryoung square wave voltammetry (SWV)¹²² and Fourier transformed large amplitude square-wave voltammetry (FT-SWV)¹²³ in a

conventional three-electrode configuration. Efforts have also been made to find a method for inspecting electrochemically the kinetics and thermodynamics of ion transfer reaction simultaneously in a single experiment with an identical experimental arrangement. The latter has been enabled recently by the successful hyphenation between the three-phase EPPG electrode with SWV¹²⁴ and FT-SWV.¹²⁵

In 2001, Shao *et al.*¹²⁶ and Girault *et al.*³³ extended Shi and Anson's method by supporting a small aqueous/organic droplet on a solid electrode (Pt or Ag/AgX). X can be a small hydrophilic anion or a big hydrophobic anion, depending on the supported droplet is aqueous or organic, respectively. Very recently, Zhou *et al.* modified Shao and Girault's method to measure a series of ions with extreme hydrophilicity.¹²⁷ In fact, it is similar as the Shi and Anson's and Scholz's methods, both of which featured by a two polarizable interface. One should mention a nice methodology of a thin aqueous layer deposited by layer-by-layer method on a solid electrode developed by Cheng *et al.* can be used to form a thin aqueous layer/organic interface.^{128,129} In brief, the methodology of thin-film and three-phase electrodes has made electrochemistry at the ITIES more popular since most electrochemical labs are equipped with a three-electrode potentiostat.

Other techniques, including spectroelectrochemical ones such as SHG⁶⁴ and molecular dynamics simulations⁶⁷ have pushed this field forward.

1.2.7. Charge transfer reactions at ITIES

Compared with the solid/liquid interface, not only the electron transfer (ET) between two redox species located respectively in each phase, but also the transfer of electrochemically inactive charged species (*i.e.* ion transfer, IT; and facilitated ion transfer, FIT) across the interface can be studied at the ITIES. The latter represents the versatility of ITIES studies in terms of the reaction targets involved at the ITIES. In the following part we will see briefly all the processes that take place at an ITIES.

1.2.7.1. Ion transfer

When an ion *i* has a relatively low standard transfer potential that is located inside the PPW of the experimental system, polarization of the ITIES can drive the *i* transfer across the interface. This process can be described in equation 1-44:



The potential dependence for the i transfer across the ITIES at equilibrium obeys a Nernst equation taking exactly the same form as the equation 1-10, defined before.

The ion transfer (IT) at the ITIES was reported firstly by Gavach in 1974,⁴⁸ on the TBA⁺ transfer at the polarized NB/w interface. An IT can be recorded electrochemically when a CV for example, is performed at the ITIES in a four-electrode setup as shown in Figure 1-13 for the aqueous solution containing tetramethylammonium cation – TMA⁺. The potential window is defined by the transfer of H⁺ (*i.e.* at positive potentials) and HSO₄⁻/SO₄²⁻ (*i.e.* at negative potentials) from aqueous to organic phase at the positive and negative limits respectively and the transfer of TMA⁺ can be seen as a typical electrochemical wave in a process controlled by mass transport of semi-infinite linear diffusion.

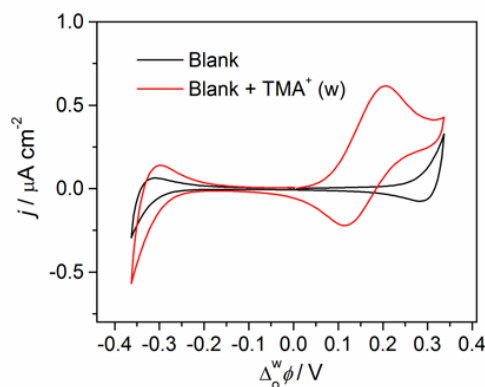
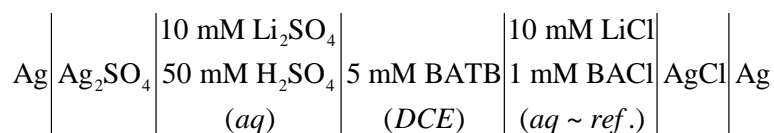


Figure 1-13. Illustration of the employed electrochemical cell composition (top panel, BA⁺ = bis(triphenylphosphoranylidene)ammonium, TB⁻ = tetrakis(pentafluorophenyl)borate) and polarization of the water/1,2-dichloroethane interface (black full line) and cyclic voltammogram recorded after adding TMA₂SO₄ into the aqueous phase (red full line, bottom panel) . Experimental conditions: scan rate 50 mV/s.

It is important to notice that IT occurs without the help from deliberately added ion carrier in any phase, which makes the investigation of IT easier. Compared to the redox reaction occurred at the solid/liquid interface, only the solvation state rather than the valence state of the transferred ion changes during the IT process. The overall theoretical basis of the IT was laid by Marcus in 2000 and the IT mechanism is divided into four successive steps depicted in Figure 1-14: 1) formation of a protrusion from the adjacent phase that penetrates into the phase where the ion is initially located, 2) interaction between the ion and the protrusion, 3) transfer of the attached ion across the interface and 4) detachment of the ion.¹³⁰

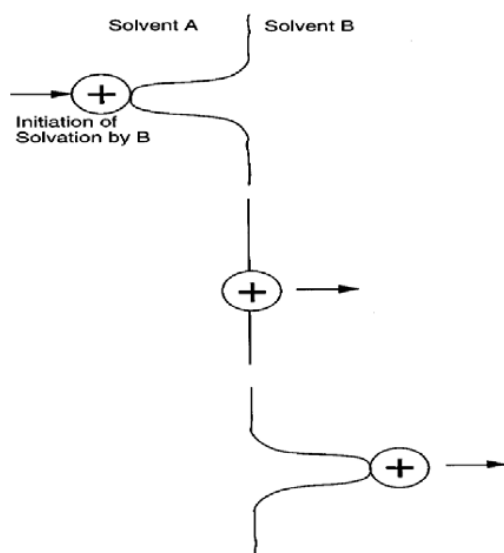


Figure 1-14. Schematic illustration of the ion transfer theory proposed by Marcus, adapted from reference.¹³⁰

Although a lot of experimental and theoretical works have been dedicated to this issue, the accurate mechanism is still a matter of debate and needs to be elucidated further. But it has been well recognized that the IT process is fast (standard rate constant k° of *ca.* $0.5\text{--}1\text{ cm s}^{-1}$)¹³¹ and reversible as it is always observed as a diffusion-limited process in voltammetric measurements. It indicates that the peak potentials are not dependent on the scan rate and theoretically have a peak separation

of $59/z_i$ mV at 298 K. This reversible IT peak current also obeys the Randles-Sevcik equation⁶⁸

$$i_p = 0.4463 z_i A F c_i^0 \sqrt{\frac{z_i F}{RT}} \sqrt{v D_i} \quad (1-45)$$

where v is the scan rate, and all other terms have been defined.

It should be mentioned that the potential scale in Figure 1-13 is the Galvani potential difference across the w/DCE interface. To convert the experimental potential difference into the Galvani potential difference, an extrathermodynamic assumption, for example the “TATB” assumption, which states that the standard transfer potentials of tetraphenylarsonium (TPAs⁺) and tetraphenylborate (TPB[−]) are identical for any pair of solvent, must be used. So, the standard transfer potential of TPAs⁺ or TPB[−] is equal to the half value of their common salt TPAsTPB that can be estimated from such as the partition coefficient measurements. The standard transfer potentials of TPAs⁺ and TPB[−] across the w/DCE interface are −365 and 365 mV, respectively. While, from an experimental viewpoint, it is more convenient to use TMA⁺ or tetraethylammonium (TEA⁺) as an internal reference ion, with a standard transfer potential at the w/DCE interface of 0.160 V¹³² or 0.019 V,¹³² respectively, to calibrate the potential window.

1.2.7.2. Facilitated ion transfer

When an ion has a higher standard potential of transfer located near the limit or outside of the PPW, its transfer cannot be studied by simply polarizing the ITIES. However, if a charged/neutral ion carrier or ionophore that can form a complex with the target ion is added in the appropriate phase, the transfer barrier can be lowered and consequently moving the transfer wave inside the PPW. In other words, the ion carrier facilitates the targeted ion transfer. Accordingly, the term of facilitated ion transfer (FIT) was coined. The pioneering work in FIT at the ITIES was made by Koryta in 1979,¹³³ showing that the transfer of potassium ion can be facilitated by either a synthetic ionophore – di-benzo-18-crown-6 (DB18C6) or a natural antibiotic ionophore – valinomycin. In fact, this concept was inspired by the ion pump/channel existing in nature – an integral protein embedded at a biomembrane forming a hydrophilic pore facilitating ion transfer inside and outside of the cell,⁹⁴ and by the discovery of crown ethers made by Petersen at du Pont in 1967.¹³⁴⁻¹³⁷ The advent of

the crown ethers indicates the start of the field of synthetic host-guest chemistry. So we can coin the FIT at the ITIES as the host-guest chemistry at the ITIES, by analogy. Then, some other ionophores, including ETH series and calixarenes, have also been employed to facilitate cation transfer.¹³⁸ Facilitated anion such as sulfate¹³⁹ or nitrate²⁹ transfer across the ITIES has also been reported. The process for a facilitated cation transfer can be depicted in equation 1-46:



where M is the transferred ionic species, L is the neutral carrier, n is the stoichiometric number between M and L, z has been defined before.

If all the species, namely the ion, the neutral carrier, and the complex can partition between the two adjacent phases, the thermodynamic equation for FIT at the ITIES can be expressed in Nernst type either for the ion or the complex as in equation 1-47 in the case of a 1:1 reaction (*i.e.* $n = 1$ in equation 1-46) between a cation and a carrier:³

$$\Delta_o^w \phi = \Delta_o^w \phi_{M^+}^o + \frac{RT}{F} \ln \left(\frac{a_{M^+}^o}{a_{M^+}^w} \right) = \Delta_o^w \phi_{ML^+}^o + \frac{RT}{F} \ln \left(\frac{a_{ML^+}^o}{a_{ML^+}^w} \right) = \Delta_o^w \phi_{M^+}^{o'} + \frac{RT}{F} \ln \left(\frac{c_{M^+}^o}{c_{M^+}^w} \right) \quad (1-47)$$

From which we can get

$$\Delta_o^w \phi = \Delta_o^w \phi_{M^+}^{o'} + \frac{RT}{F} \ln \left(\frac{c_{ML^+}^o}{K_{ML} c_L^o c_{M^+}^w} \right) \quad (1-48)$$

where $K_{ML} \approx \frac{c_{ML^+}^o}{c_{M^+}^o c_L^o}$ is the equilibrium constant for the 1:1 complexation reaction

between M^+ (transferred from aqueous) and L in the organic phase.

Under conditions of $c_{M^+}^w \gg c_L^o$ and hence $\sqrt{D_{ML^+}^o} c_{ML^+}^o = \sqrt{D_L^o} c_L^o$ (cf. equation 1-12),⁶⁸ finally we can get the half-wave potential (or the mid-peak potential in CV) for the facilitated M^+ transfer as¹⁴⁰

$$\Delta_o^w \phi_{1/2} = \Delta_o^w \phi_{M^+}^{\circ'} + \frac{RT}{2F} \ln \left(\sqrt{\frac{D_L^o}{D_{ML^+}^o}} \right) - \frac{RT}{F} \ln (K_{ML^+} c_{M^+}^w) \quad (1-49)$$

Equation 1-49 indicates that increasing K_{ML} or $c_{M^+}^w$ will shift the half-wave potential to more negative values for cations and it is *vice versa* for anions.

In the case of assisted proton transfer such as by a free-base porphyrin, which is the first step in the proton-coupled electron transfer (PCET) for oxygen reduction reaction or hydrogen evolution at the ITIES, equation 1-49 will be transformed as:¹⁴⁰

$$\Delta_o^w \phi_{LH^+}^{1/2} = \Delta_o^w \phi_{H^+}^{\circ'} + \frac{RT}{2F} \ln \left(\frac{D_L^o}{D_{LH^+}^o} \right) - \frac{2.303RT}{F} pK_a^o + \frac{2.303RT}{F} pH^w \quad (1-50)$$

where $\Delta_o^w \phi_{H^+}^{\circ'}$ is the formal transfer potential for H^+ that is 0.55 V.¹⁴¹ D_L^o and $D_{LH^+}^o$ represent the diffusion coefficients of L and LH^+ in the organic phase, respectively, and are assumed to be equal for simplicity. pH^w is the aqueous pH. Equation 1-50 is of significant importance that can be used to determine the charge number of the ion transferred across the ITIES and pK_a^o , the acidity constant of LH^+ in the organic phase.

The mechanism of the FIT was classified by Girault's group in 1991 and divided into four different cases shown in Figure 1-15: i) transfer by interfacial complexation (TIC), ii) transfer by interfacial dissociation (TID), iii) transfer followed by organic phase complexation (TOC), and iv) aqueous complexation followed by the transfer of the complex (ACT).¹⁴² It should be noted that TID is the reverse reaction of TIC.

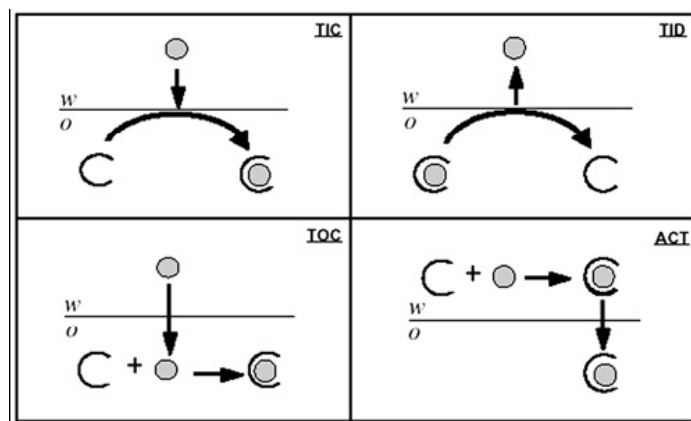


Figure 1-15. Mechanisms of the facilitated ion transfer at a liquid/liquid interface, adapted from reference.¹⁴²

It should be noted that the simple ion transfer described before is just a relative phenomenon. It has been demonstrated by Mirkin and co-workers that in fact transfer of hydrophilic alkali metal cations is facilitated by the counter anions of the supporting electrolytes in the organic phase by ion-pair formation at the interface.¹⁴³ Specifically speaking, ion transfer occurs *via* a shuttling mechanism in which the counter anion forms an ion pair with the target cation in the mixed solvent layer of the liquid/liquid interface firstly and then releases it to the bulk of the organic phase. Besides, the water molecules present even in trace amounts in the organic phase can facilitate the alkali metal transfer significantly.⁸² However, it is not the case for the more hydrophobic ions such as TMA^+ . So it seems that TMA^+ transfer is a true ion transfer.

FIT can be used for the design of amperometric or potentiometric ion selective electrodes and the IT study of extremely hydrophobic/hydrophilic ions. This is useful in the environment-related studies. It is also of significant importance for the study of energy-related reactions, namely PCET at the ITIES (*vide infra*).

1.2.7.3. Electron transfer

When each phase of a liquid/liquid interface has a redox couple, a bimolecular electron transfer (ET) can occur under conditions where the driving force is large enough to trigger this reaction. This process can be expressed by equation 1-51 and shown schematically in Figure 1-16:



where O_1 is the oxidized form of a redox couple in aqueous phase and R_1 its reduced form, O_2 is the oxidized form of a redox couple in organic phase and R_2 its reduced form. The number of electrons involved in the interfacial redox reaction is assumed to be 1.

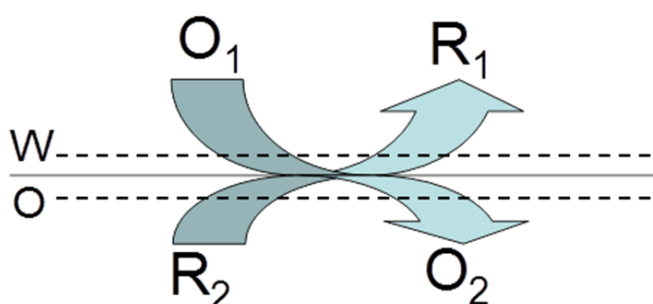


Figure 1-16. Schematic plot of electron transfer across the immiscible liquid/liquid interface, in which the dashed line represents the location where a bulk electron transfer reaction occurs.

It should be mentioned that ET at the ITIES might be one of the most difficult reactions to investigate, since it is difficult to match the potentials between the respective redox couples in each phase (*i.e.* to drive the reaction spontaneously) and to maintain the respective redox couples confined in each phase to observe a truly interfacial electron transfer as shown in Figure 1-16. The first report of heterogeneous ET at the ITIES was made by Guainazzi *et al.* in 1975, showing that a copper layer can be deposited at the interface by direct current electrolysis with CuSO_4 in aqueous and $[\text{Bu}_4\text{N}][\text{V}(\text{CO})_6]$ in DCE or CH_2Cl_2 , respectively.¹⁴⁴ Later on, Samec *et al.*¹⁴⁵ and Schiffrin *et al.*¹⁴⁶ studied this phenomenon systematically by using the four-electrode setup. Experimental efforts have also been made by Bard's group^{58,112} and Shao's group^{113,147} who combined SECM with non-polarizable or polarizable ITIES to study the driving force-dependent kinetics of heterogeneous ET, respectively. In 2003, Osakai and co-workers proposed a so-called ion transfer mechanism for explaining the results of the bimolecular ET reaction, in which the oxidation of lipophilic ferrocene by aqueous ferricyanide proceeds firstly by the partitioning of ferrocene to water phase followed by a homogeneous aqueous ET reaction between ferrocene and

ferricyanide, resulting in that the produced ferricenium cation transfers back to the organic phase which is responsible for the current flow across the ITIES.¹⁴⁸ The “Osakai mechanism” is caused by the fact that the lipophilicity of ferrocene is just medium and the hydrophilicity of ferricyanide seems to be higher than the lipophilicity of ferrocene. Otherwise, an inverse “Osakai mechanism” may be observed in which the homogeneous ET reaction should occur at the organic side of the ITIES. The “Osakai mechanism” is also dependent on the relative concentration ratio between the two redox species located in respective phase. Specifically, the ET reaction becomes more heterogeneous if aqueous redox species are in excess, as the mean free path of redox species (partitioned from organic) in water is reduced. Hence, the truly heterogeneous ET at the ITIES only occurs under conditions where both redox couples are confined in each phase strictly during ET at the ITIES. For a heterogeneous ET at the ITIES, at equilibrium equality of the electrochemical potentials of redox species in the two phases reads:

$$\tilde{\mu}_{O_1}^w + \tilde{\mu}_{R_2}^o = \tilde{\mu}_{R_1}^w + \tilde{\mu}_{O_2}^o \quad (1-52)$$

Then the Nernst equation for a heterogeneous single electron transfer reaction at the ITIES can be expressed in equation (1-53):

$$\Delta_o^w \phi = \Delta_o^w \phi_{ET}^{\circ} + \frac{RT}{F} \ln \left(\frac{a_{R_1}^w a_{O_2}^o}{a_{O_1}^w a_{R_2}^o} \right) \quad (1-53)$$

with $\Delta_o^w \phi_{ET}^{\circ}$ the standard redox potential for the interfacial electron transfer.

$$\Delta_o^w \phi_{ET}^{\circ} = (\tilde{\mu}_{R_1}^{\circ,w} + \tilde{\mu}_{O_2}^{\circ,o} - \tilde{\mu}_{O_1}^{\circ,w} - \tilde{\mu}_{R_2}^{\circ,o}) / F \quad (1-54)$$

This value is simply the difference of the standard redox potential between these two redox couples, both expressed on the same aqueous SHE scale, being expressed in equation (1-55):

$$\Delta_o^w \phi_{ET}^{\circ} = [E_{O_2/R_2}^{\circ}]_{SHE}^o - [E_{O_1/R_1}^{\circ}]_{SHE}^w \quad (1-55)$$

Actually, it is experimentally difficult to measure the standard redox potential of organic redox couples versus the aqueous SHE, and one strategy to circumvent this difficulty is to measure the standard redox potential of organic redox couples on the ferrocene (Fc) or decamethylferrocene (DMFc, even better in practice) scale that can be referred to the aqueous SHE by calculating from thermodynamic cycles. For instance it has been determined that in DCE (o = DCE):⁵

$$\left[E_{\text{Fc}^+/\text{Fc}}^{\circ} \right]_{\text{SHE}}^{\text{DCE}} = \left[E_{\text{Fc}^+/\text{Fc}}^{\circ} \right]_{\text{SHE}}^{\text{w}} + \left(\Delta G_{\text{tr}, \text{Fc}^+}^{\circ, \text{w} \rightarrow \text{DCE}} - \Delta G_{\text{tr}, \text{Fc}}^{\circ, \text{w} \rightarrow \text{DCE}} \right) / F = 0.64 \text{ V} \quad (1-56)$$

in which $\left[E_{\text{Fc}^+/\text{Fc}}^{\circ} \right]_{\text{SHE}}^{\text{w}}$ is 0.380 V,⁵ and $\Delta G_{\text{tr}, \text{Fc}^+}^{\circ, \text{w} \rightarrow \text{DCE}}$ and $\Delta G_{\text{tr}, \text{Fc}}^{\circ, \text{w} \rightarrow \text{DCE}}$ are 0.5 and $-24.5 \text{ kJ} \cdot \text{mol}^{-1}$,³ respectively. Finally, equation 1-55 can be more conveniently to be expressed as:

$$\Delta_o^{\text{w}} \phi_{\text{ET}}^{\circ} = \left[E_{\text{O}_2/\text{R}_2}^{\circ} \right]_{\text{Fc}}^{\text{DCE}} - \left[E_{\text{O}_1/\text{R}_1}^{\circ} \right]_{\text{SHE}}^{\text{w}} + 0.64 \text{ V} \quad (1-57)$$

If the standard redox potential in aqueous phase is known, for example the two-electron reduction of oxygen to hydrogen peroxide that is the focus of this thesis, it is then possible to calculate its value in DCE with respect to the aqueous SHE if the standard Gibbs transfer energies of all the participated species at the w/DCE interface are known. The calculation process for this reaction 1-58 is shown in equation 1-59:



$$\left[E_{\text{O}_2/\text{H}_2\text{O}_2}^{\circ} \right]_{\text{SHE}}^{\text{DCE}} = \left[E_{\text{O}_2/\text{H}_2\text{O}_2}^{\circ} \right]_{\text{SHE}}^{\text{w}} + \left(2\Delta G_{\text{tr}, \text{H}^+}^{\circ, \text{w} \rightarrow \text{DCE}} + \Delta G_{\text{tr}, \text{O}_2}^{\circ, \text{w} \rightarrow \text{DCE}} - \Delta G_{\text{tr}, \text{H}_2\text{O}_2}^{\circ, \text{w} \rightarrow \text{DCE}} \right) / 2F \quad (1-59)$$

where $\left[E_{\text{O}_2/\text{H}_2\text{O}_2}^{\circ} \right]_{\text{SHE}}^{\text{DCE}}$ and $\left[E_{\text{O}_2/\text{H}_2\text{O}_2}^{\circ} \right]_{\text{SHE}}^{\text{w}}$ are the standard redox potentials for oxygen reduction to hydrogen peroxide in DCE and water, respectively; $\Delta G_{\text{tr}, \text{H}_2\text{O}_2}^{\circ, \text{w} \rightarrow \text{DCE}}$, $\Delta G_{\text{tr}, \text{O}_2}^{\circ, \text{w} \rightarrow \text{DCE}}$, and $\Delta G_{\text{tr}, \text{H}^+}^{\circ, \text{w} \rightarrow \text{DCE}}$ are the standard Gibbs transfer energies of H_2O_2 , O_2 , and H^+ from water to DCE, respectively. Figure 1-17 illustrates the potential scales in the aqueous and DCE phases for some redox reactions that are related with energy aspects.¹⁴⁹

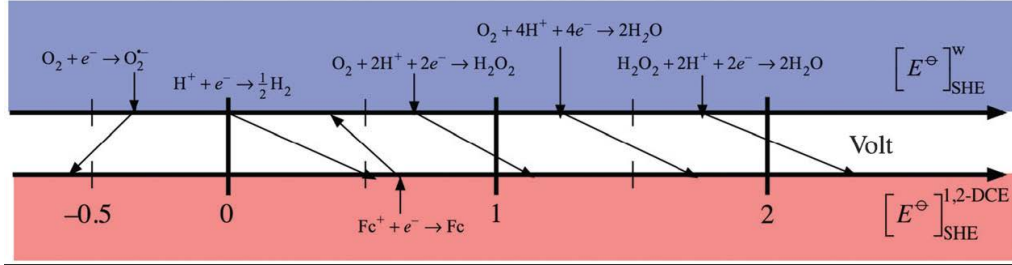


Figure 1-17. The potential scale for oxygen reduction in water (top scale) and in DCE (bottom scale) versus the aqueous standard hydrogen electrode (SHE), reproduced from reference.¹⁵⁰

For the kinetic aspect, a second-order rate constant of the forward (k_f) and backward (k_b) reactions of equation 1-51 are given by the Butler-Volmer equations:

$$I_{ET} = FA(k_f c_{O_1}^w c_{R_2}^o - k_b c_{R_1}^w c_{O_2}^o) \quad (1-60)$$

$$k_f = k^\circ \exp \left[\frac{(1-\alpha)F}{RT} (\Delta_o^w \phi - \Delta_o^w \phi_{ET}^\circ) \right] \quad (1-61)$$

$$k_b = k^\circ \exp \left[\frac{-\alpha F}{RT} (\Delta_o^w \phi - \Delta_o^w \phi_{ET}^\circ) \right] \quad (1-62)$$

where k_f and k_b are dependent on the interfacial potential difference $\Delta_o^w \phi$, k° is the standard rate constant at $\Delta_o^w \phi = \Delta_o^w \phi_{ET}^\circ$, and α is the electron transfer coefficient. Using k° and α as the adjusting parameters, we can extract the standard rate constants for the system under study, by performing curve-fitting between theoretical and experimental voltammograms.

The theoretical aspects of the ET reactions at the ITIES were proposed by Marcus between 1990 and 1991.¹⁵¹⁻¹⁵⁴ Since then, different ET reactions have been studied at the liquid/liquid interface, for instance, the oxygen reduction reaction (ORR) that has

attracted a lot of attention due to the increased interest on new alternatives of generation and storage of energy.

Due to the similarity between the ITIES and a semi-biomembrane as implicated by Blank and Feig,⁴⁶ the ITIES is also very useful for studying the photoinduced electron transfer process, *i.e.* artificial photosynthesis. The pioneering work was made by Girault and co-workers in 1988, showing that photocurrent was passed across the interface with $\text{Ru}(\text{bpy})_3^{2+}$ as the aqueous photosensitizer.¹⁵⁵ The merit of this biphasic system is that products of the photoinduced electron transfer are separated by the interface, minimizing the recombination reaction that is evident in bulk solutions. Later on, a series of papers of photoinduced electron transfer reactions employing porphyrins as sensitizers have been published.³ A general analytical model for the dynamic photocurrent responses at the ITIES has been established to facilitate better understanding of this important physicochemical process.¹⁵⁶ It has also been shown that photocurrent can be enhanced by a gold film present at the ITIES due to the surface plasmon resonance effect.¹⁵⁷ One should also mention that photo- H_2 generation at the ITIES was possible in the presence of a lipophilic photosensitizer and a lipophilic electron donor in contact with an acidic aqueous solution.¹⁴ The photocurrents are sometimes related to the product ions generated in one bulk phase upon irradiation of an ITIES.^{158,159} Very recently, a photo-ionic cell in a biphasic system based on the pioneering works of Rabinowitch *et al.*^{160,161} was simulated and a concept of a complete photoredox battery was proposed,¹⁶² demonstrating the promising potential of this battery.

1.3. Proton-coupled electron transfer reaction and $\text{S}_{\text{N}}1$ reaction at the ITIES

Proton-coupled electron transfer (PCET) reactions play a crucial role both in biological processes such as photosynthesis and respiration and energy conversion in artificial photosynthesis or fuel cells.¹⁶³ Generally, PCET can be classified into two categories: either as stepwise electron and proton transfer (ET-PT or PT-ET) or as concerted proton and electron transfer (CPET).¹⁶³ So it has two separate steps in the former case while involves only a single step in the latter case. There is an advantage in the coupling of electron and proton transfer that high-energy intermediates can be avoided. In aqueous solution, many redox reactions often involve transfer of both protons and electrons, for example the interconversion between oxygen and

water/hydrogen peroxide in acidic medium and hydrogen evolution reaction, shown below:



The $2\text{e}^-/2\text{H}^+$ route for ORR to hydrogen peroxide has been defined in equation 1-58. It is very useful to analyze such as equation 1-64 by a square scheme as shown in Figure 1-18. From Figure 1-18, we know that there are many pathways heading to the final product. The thermodynamics of a PCET reaction is the sum of those for all the individual steps. So with the knowledge of redox potentials and acidity constants for each ET and PT steps, respectively, it is feasible to analyze the PCET process.

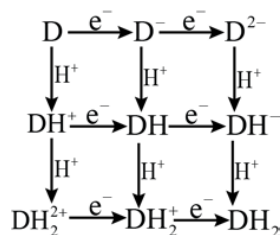


Figure 1-18. Square scheme for H_2 formation on a metallic surface D.

Figure 1-19 illustrates the overall mechanism involved in equation 1-63 on weakly adsorbing electrodes such as silver.

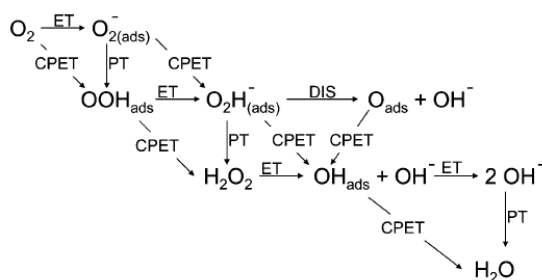
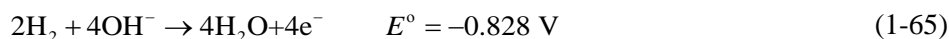


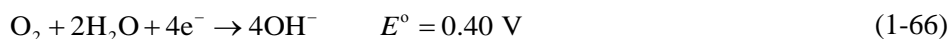
Figure 1-19. ORR mechanism in acidic media on weakly adsorbing electrodes, reproduced from reference.¹⁶⁴

Both the ORR and HER processes are important in the fuel cell technology. Fuel cell is an electrochemical energy converter that turns chemical energy of fuel (ideally H₂) directly into electricity. The fuel cell effect was observed firstly by a Basel scientist, Christian Schonbein, in 1838 and later demonstrated by a Welsh scientist, William Robert Grove in 1839.¹⁶⁵ The physical chemist, Friedrich Wilhelm Ostwald, laid the foundation of theoretical understanding of how fuel cells operate and pointed out the difference between combustion engines and fuel cells. In one of his publications, he wrote that for combustion engines, they are limited by Carnot efficiency and are concerned with the environmental issues; whereas fuel cells generate electricity directly and are more efficient, silent, as well as environmental-friendly.

The fuel cell is usually made up of an anode, an electrolyte (immobilized or mobile), and a cathode. According to the employed electrolyte, fuel cell is generally divided into two types: acidic and alkaline. The fuel includes H₂, formic acid, methanol, ethanol, and so on. For a H₂ fuel cell, the oxidant is O₂. For a H₂-O₂ alkaline fuel cell, the electrode reactions can be formulated as following:



Anodic



Cathodic



In theory, the energy conversion efficiency ($\Delta G^\circ / \Delta H^\circ$) can reach 83%. Even though the importance of fuel cells has been known very early, the practical realization will take a long time.

The major challenge arises from the electrode materials.¹⁶⁶ Without appropriate electrode materials as the good catalysts for both anodic and cathodic reactions, the actual cell potential in equation 1-67 will be much smaller than the thermodynamic

value due to the activation overpotentials. Although Pt and Pd are the best catalysts showing excellent catalytic performance towards the HER (Sabatier's principle)¹⁶⁷ and ORR, their large-scale use is limited by the low earth abundance and accordingly the high price. A good strategy to reduce the cost is to load Pt or Pd nanoparticles on a large surface-area carbon support while without the degradation of cell performance. Besides, many efforts have been made to search or explore for the alternative catalysts especially comprised of earth-abundant materials. For example, MoS₂¹⁶⁸ and Mo₂C¹⁶⁹ have been identified as suitable candidates as a HER catalyst. The high activity lies in that MoS₂ and Mo₂C resemble the active center of the hydrogenase. For the ORR catalysts, a biomimetic strategy is to synthesize molecular catalysts such as metalloporphyrins that function similarly as the biomembrane-bound multi-metalloenzyme, cytochrome *c* oxidase, in nature. Many groups and in particular Collman and co-workers^{170,171} and Fukuzumi and co-workers^{172,173} have contributed significantly to this field, with the famous cofacial dicobalt porphyrins as a good 4e⁻/4H⁺ ORR molecular catalyst that has been synthesized for example.¹⁷²

Until now, there are three approaches to study the performance of the catalysts involved in these energy-related PCET reactions. The first method is heterogeneous in nature – adsorbing the catalysts onto an inactive carbon electrode surface and then performing the non-destructive electrochemical such as CV measurements.¹⁷⁴ The second one is homogeneous in nature – dissolving the water-insoluble catalyst in nonaqueous media with the use of an organic acid as the proton source and a lipophilic reductant as the electron donor.¹⁷² The third method investigates these PCET reactions at the ITIES which have been studied systematically by Girault and co-workers.¹⁵⁰ The third method combines the merits from the former two methods, namely direct use of aqueous rather than organic acid as the proton source, highly reproducible results, and easier product identification. The gist for all these three methods is to investigate the onset potential and current density in the current-potential profile that can characterize the catalyst performance. Theoretical simulations have been proved to be powerful in this field.

It is worth noting that the most common electron donors employed are group VIII metallocenes. Metallocenes are a group of organometallic compounds containing two cyclopentadienyl rings (Cp₂, C₅H₅⁻) coordinated to a transition metal (M²⁺) at the center of a sandwich-type structure. They can be formulated as Cp₂M. The advent of this field was spurred by the discovery of ferrocene in 1950s.¹⁷⁵ Ferrocene and its derivatives have been shown to have a good electrochemical property reflecting by its superb reversibility and stability according to the 18-electron rule proposed by Irving

Langmuir in 1921.¹⁷⁶ With regard to the energetic aspect, it has been demonstrated that reduction or photo-reduction of protons to hydrogen is possible with ferrocene derivatives like decamethylferrocene¹⁴¹ or osmocene,¹⁷⁷ respectively.

Regardless of the ORR or HER, without a catalyst present, the first step is believed to be protonation of the metallocenes forming an intermediate species. But the protonation pathway or the primary attack site by the electrophile (here H^+) on the metallocenes remains an issue of debate. They can go *via* either an *exo* (Cp ring) or an *endo* (metal center) pathway.¹⁷⁸

While this thesis is aimed at studying the PCET reactions at the ITIES, a brief history in this field will be presented below.

The pioneering work was carried out by Schiffrin's group in 1995, in which they employed ferrocene (Fc) and its derivatives as the electron donors located in the organic phase for studying the biphasic intermolecular electron transfer at the ITIES.¹⁷⁹ They observed an irreversible current wave at the positive potential range when only oxygen is available as the oxidant in both aqueous and organic phases and DMFc is the lipophilic electron donor. They ascribed this phenomenon to the sequential ORR with water (H_2O) as the final product. However, no further efforts were made to elucidate the mechanism of this reaction. In 2000, Kihara and co-workers studied ORR at the water/1,2-dichloroethane interface (w/DCE) in the presence of tetrachlorohydroquinone located in DCE at different aqueous pH values, and showed that water (H_2O) or hydrogen peroxide (H_2O_2) were the final products depending on the potential difference applied at the w/DCE.¹⁸⁰ These two works were the earliest studies of a PCET reaction at the ITIES as the reduction of oxygen in DCE requires the coupling of electron donors in DCE and proton sources present in the aqueous phase. Kihara's work is also an excellent example of electrocatalytic reactions occurring at the ITIES, since the kinetics and the final products are dependent on the applied interfacial potential. To facilitate the use of conventional voltammetry (three-electrode setup) to study this kind of reactions, Anson and co-workers proposed the use of graphite electrodes (GE) that have been modified with a thin layer of organic phase that is immiscible with water.^{60,61} The introduction of the thin layer containing a molecular catalyst – cobalt 5,10,15,20-tetraphenylporphyrin can improve greatly the rate of the ORR and the fraction of H_2O produced.¹⁸¹ The overall electrochemical system couples the electron transfer at the graphite electrode/organic solution (GE/o) interface with the ion transfer at the organic solution/aqueous solution (o/w) interface by virtue of the same current and proceeds simultaneously. It has also been shown that ORR at the ITIES can be facilitated by

functionalizing the interface with adsorbed catalysts. Samec and co-workers have demonstrated that platinum nanoparticles can be synthesized *in situ* and adsorbed at the ITIES acting as catalysts for the interfacial reduction of oxygen.¹⁸²

In fact, the ORR at the ITIES mentioned above, is a bio-inspired system mimicking biomembranes that provide both a physical separation of the reactants and products, and an electrochemical driving force resulting from the membrane electrical potential difference. Hence, this biphasic reaction is very important in the viewpoint of energy context and until now ORR at naked and modified ITIES, hydrogen evolution, and carbon dioxide (CO₂) reduction have been studied at this soft molecular interface.¹⁵⁰ Over the years, Girault and co-workers have investigated ORR enabled by direct electron donors such as decamethylferrocene (DMFc),^{183,184} and catalyzed by different porphyrins¹⁸⁵⁻¹⁹⁰ and dodecylaniline.¹⁴⁹ In the case of direct oxygen reduction by stronger electron donors, such as DMFc arising from the higher electron donating property of the ten methyl groups on the Cp ring, the first step of oxygen reduction is the protonation of DMFc. DFT calculations have shown that the next step is the binding of O₂ to [DMFc-H]⁺, followed by the release of the hydroperoxyl radical and the formation of DMFc⁺. While for the case of catalyzed (catalyst adsorbed at the ITIES or dissolved in appropriate phase) oxygen reduction by weak electron donors (*e.g.* ferrocene), the PCET, namely a big forward voltammetric signal without backward signal at positive potentials, only occurs when all the four reactants are present, *i.e.*, O₂, aqueous H⁺, catalyst, and electron donor in the organic phase. It has been shown that the product of all these reactions is H₂O₂ *via* a two-electron reduction pathway, although the yield is rather low due to its decomposition or further reduction to water. Besides, homogeneous two-electron oxygen reduction was investigated directly by DMFc in the presence of an organic acid and has been shown that the proton reduction competes with oxygen reduction under aerobic conditions.¹⁹¹ From the point of view of kinetics, the oxygen reduction is much faster than the evolution of H₂, being demonstrated by the more positive redox potential for oxygen reduction with respect to that of proton reduction. Recently, Olaya *et al.* observed the direct four-electron reduction of oxygen at ITIES by tetrathiafulvalene to produce water.¹⁹² Peljo *et al.* investigated the mechanism of ORR by the so-called “Pacman” type porphyrins at the ITIES¹⁹³ and the same authors proved a novel concept of fuel cell based on ORR at a solidified ITIES.⁴¹ Samec *et al.* also investigated the inhibiting behavior of organic acid anions¹⁹⁴ and water¹⁹⁵ on the homogeneous ORR catalyzed by a metal-free porphyrin. More recently, Opallo’s group showed that H₂O₂ could be generated from ORR at the liquid/liquid interface under conditions unfavorable for

proton transfer and detected *in situ* by SECM with the help of an enzyme – horseradish peroxidase.¹⁹⁶ In brief, polarization of the ITIES has been performed by using four- and three-electrode configurations, as well as *via* a common ion distribution (see Figure 1-20) showing that the catalytic reactions are dependent on the soft interface polarization.

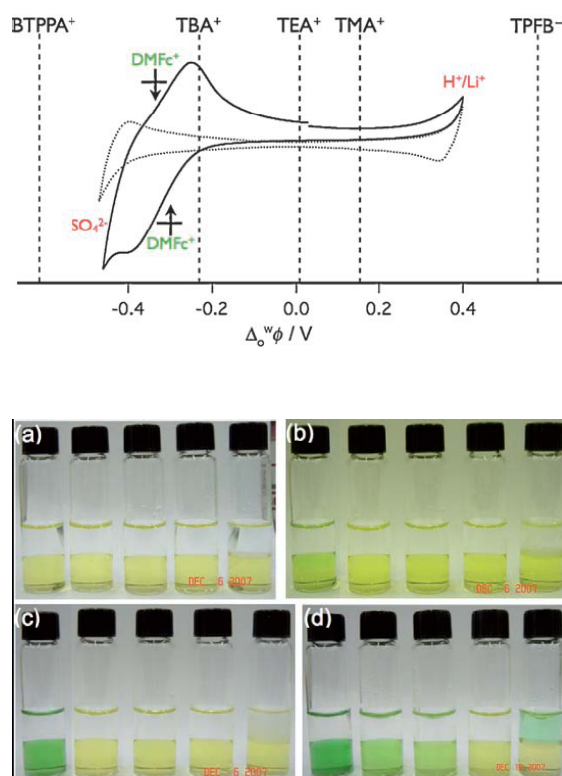


Figure 1-20. Top panel: Polarization of the w/DCE interface by various common ions. The dotted and solid curves represent the potential window and transfer of DMFc^+ by polarization of the interface by external bias, respectively. Bottom panel: Biphasic reaction controlled by different common ions: TPFB^- , TMA^+ , TEA^+ , TBA^+ , and BTPPA^+ from left to right (5 mM in both phases) after 0 min (a), 62 min (b), 17.5 h (c), and 102 h (d). Reproduced from reference.¹⁸³

Regarding the biphasic HER, it was reported firstly in 2009 by Hatay *et al.*¹⁴¹ Then HER at the ITIES catalyzed by MoS_2 was reported by the same authors in 2011.¹⁹⁷ Some other catalysts including carbon supported MoS_2 ,¹⁹⁸ MoB and Mo_2C ,¹⁶⁹ and $\text{Mo}_2\text{C}/\text{CNT}$ composite¹⁹⁹ floated at the ITIES used for catalyzing HER have also been investigated recently. The common feature in these studies is that DMFc with a

formal redox potential of 0.07 V (vs. aqueous SHE) is used as the reductant. As the driving force is not high enough, thermodynamically the heterogeneous HER between aqueous protons and lipophilic DMFc cannot occur. However, after transporting protons from aqueous to organic solvents such as DCE by the chemical or electrochemical way, it is possible to reduce the protons by DMFc in DCE. It is caused by the fact that very positive Gibbs transfer energy of proton from aqueous to DCE raises the formal redox potential of H^+/H_2 couple to 0.55 V by thermodynamic cycle calculation.¹⁴¹ Then, the product of H_2 can be detected by gas chromatography.

S_N1 reaction is a substitution reaction in organic chemistry in which the reaction mechanism was proposed firstly by Ingold *et al.* in 1940.²⁰⁰ Carbocation is an intermediate that is central to the S_N1 mechanism.²⁰¹ In 2012, Peljo *et al.* demonstrated a proton-transfer catalyzed S_N1 reaction on ferrocene methanol and the phase transfer catalysis was explained by the distribution potential difference across the biphasic boundary.¹⁰¹ The merit in this strategy lies in that the carbocation formation can be controlled precisely by adjusting the proton flux across the ITIES either by a potentiostat or a suitable salt distribution. This will definitely be beneficial for the organic chemistry community.

In this thesis, more details in terms of mechanism on the PCET reactions such as oxygen/proton reduction as well as S_N1 reaction will be addressed. One issue that has been missing in previous works,¹⁵⁰ is the kinetics of ORR at the ITIES, which is vital for screening potential electrocatalysts or electron donors. The approach for studying the kinetics of ORR at the ITIES is based on CV or SECM; the latter one is a very useful tool for precise determination of the kinetic constants for both homogeneous and heterogeneous reactions, and a great progress has been made in this field during the past decades. Hence a brief introduction to SECM will be presented below and some basic concepts and also some commonly used operation modes will be covered.

1.4. Scanning electrochemical microscopy

1.4.1. Introduction

The term of scanning electrochemical microscopy (SECM) was coined on the basis of two different concepts, namely, scanning tunneling microscopy (STM) and ultramicroelectrode (UME) emerged in the 1980s.^{57,202-204} Since then, SECM studies have been reported in more than 1000 original papers.²⁰² The similarity between SECM and STM lies in their common use of a probe that is scanned over or moving

towards a substrate surface. However, there are fundamental differences in the operation principle and application fields between these two techniques. STM employs the flow of a tunneling current originated from quantum mechanical effect between an atomic-scale tip and a conductive substrate located in a very close proximity (*i.e.* sub nm or less) to determine the topography of the surface.²⁰⁵ In the case of SECM a redox process occurred between the tip and the substrate is employed for determining both the topography and the surface reactivity of the specimen. The latter is made possible because the recorded faradaic current at the probe depends on the kinetics of the process that is taking place at the different interfaces (*i.e.* tip/solution and solution/substrate) and the mass transport of redox species from and toward the tip and the substrate. Furthermore, the UME used in SECM is usually bigger than the one used in STM. The dimension of conventional UMEs used in SECM ranges from few nanometers to *ca.* 30 μm . Moreover, UMEs are characterized by a hemispherical diffusion field (see Figure 1-21) that allows a more efficient mass transport than the one achieved at macroscopic electrodes and reaching a steady-state condition in a very short period of time (*e.g.* in the order of ms). Additionally, very low capacitive currents and low ohmic drop are observed with UMEs (see Figure 1-22). It should be noted that the tip of SECM usually possesses a disk-shaped active electrode area surrounded by an insulating sheath, but different geometries have been used as well. However, most of the analytical, quasi-analytical and numerical treatments of SECM studies have been performed for disk-shaped electrodes. In terms of operation modes, the most widely used one is the feedback mode, however the tip generation/substrate collection (TG/SC) mode, and the substrate generation/tip collection (SG/TC) mode are also popular modes in SECM studies. Other operation modes, such as the penetration mode,²⁰⁶ surface interrogation (SI)²⁰⁷ and the redox competition (RC)²⁰⁸ modes will not be addressed here.

1.4.2. Feedback mode

In the feedback mode, the tip is located in the bulk of a solution containing a redox mediator, R. When the tip is biased at a sufficient positive potential, for instance, R is oxidized to O according to equation 1-68 and then a current is recorded as a result of the electron transfer between the species R and the electrode.



Once R starts to be depleted in the vicinity of the tip surface, the diffusion layer is modified to drive more R species from the bulk to the electrode surface. Due to the special hemispherical diffusion at microelectrodes, a steady-state (independent of the time) diffusion-limited current $i_{T,\infty}$ is established rapidly according to the equation 1-69:²⁰⁹

$$i_{T,\infty} = gnFDc^*r \quad (1-69)$$

where g is a geometry factor that is a function of the ratio between the radius of the insulating sheath plus the active electrode and that of the active electrode (also called RG), n is the number of electrons transferred, c^* is the bulk concentration of the redox species, r is the radius of the UME, and F and D have been defined previously. When a disk-shaped UME is embedded in an infinitely large insulator, g is calculated to be 4.²⁰⁹ In practice, when RG is equal to or larger than 10, the g of UME can be approximately considered as 4. When the RG is smaller than that, a different g value has to be used in order to take into account the contribution of the species that are behind the plane of the electrode.

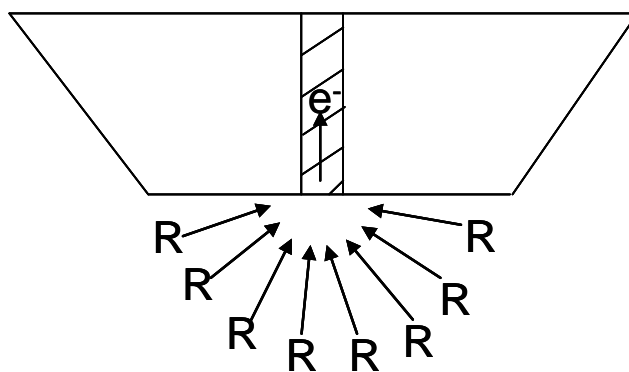


Figure 1-21. Hemispherical diffusion field at the UME, R stands for the reduced form of a redox couple.

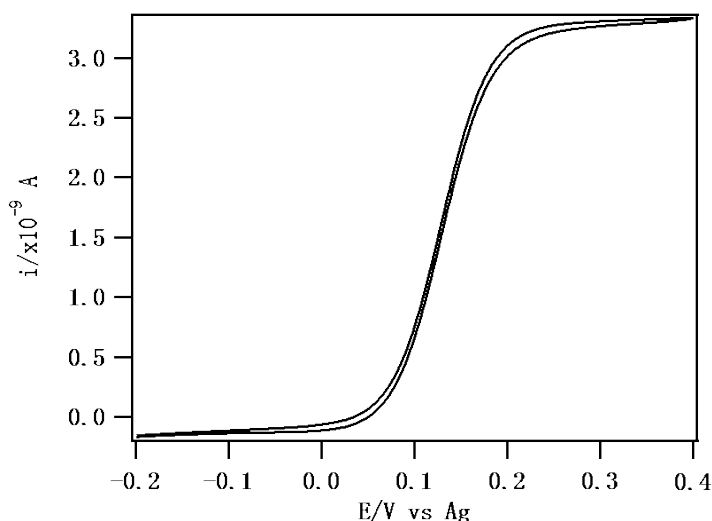


Figure 1-22. Characterization of a Pt UME (diameter = 10 μm , RG = 5.5) in 2 mM ferrocenemethanol + 0.1 M KCl, quasi-reference electrode is a Ag wire, counter electrode Pt wire. Scan rate is 20 $\text{mV}\cdot\text{s}^{-1}$.

When the tip potential of a microelectrode is fixed at a value (*e.g.* 0.3 V in Figure 1-22) to produce a steady-state current and at the meantime the tip is approaching from the bulk of the solution towards the substrate, monitoring of the tip current as a function of the scanned distance can be used to plot a so-called approach curve (Figure 1-23).²⁰² In such kind of experiments two different behaviors are found depending on the ability of the substrate to regenerate the redox mediator R that can be oxidized at the microelectrode, for instance. In the case in which the substrate is not able to regenerate R, the current as a function of the distance will decrease as the substrate surface hinders the diffusion of R towards the tip (red trace in Figure 1-23 and illustrated in Figure 1-24a). This behavior is called a negative feedback. In the opposite case, where the substrate is able to regenerate R, the tip current will increase as the tip is approaching the substrate, due to the recycling of the redox mediator and the increased flux of R in the gap between the electrode and the substrate (blue trace in Figure 1-23 and Figure 1-24b). This behavior is called a positive feedback. It should be noted that positive feedback can be observed even without any external bias at the active substrate. In this case, the substrate behaves like a bipolar electrode: reduction of O to R occurs on the substrate in the region just below the tip (perturbation region) while oxidation of R to O proceeds at either side on the substrate far away from the perturbation region. In brief, it is the potential difference generated

along the substrate upon the perturbation by the tip that accounts for the phenomenon of the positive feedback.

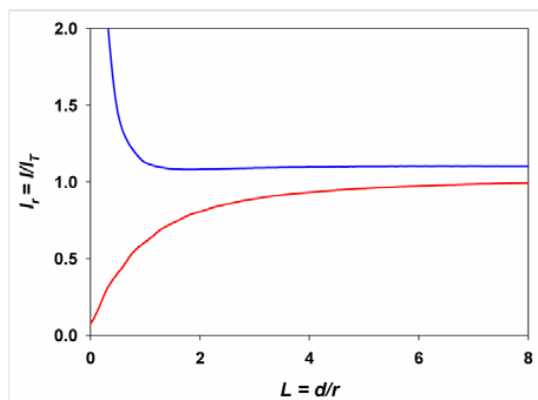


Figure 1-23. Approach curves obtained for negative (red trace) and positive (blue trace) feedback. L is the normalized distance defined by the ratio of the tip-substrate separation d to the radius of the electrode r . I_r is the normalized current defined by the ratio of the tip current I recorded at any position of z axis to the current in the bulk of the solution I_T . The currents were recorded in aqueous solution of 2 mM FcMeOH and 0.1 M KCl employing a Pt microelectrode (diameter: 10 μm , $\text{RG} = 5.5$) as the working electrode, with a silver wire as the quasi-reference electrode and a Pt wire as the counter electrode.

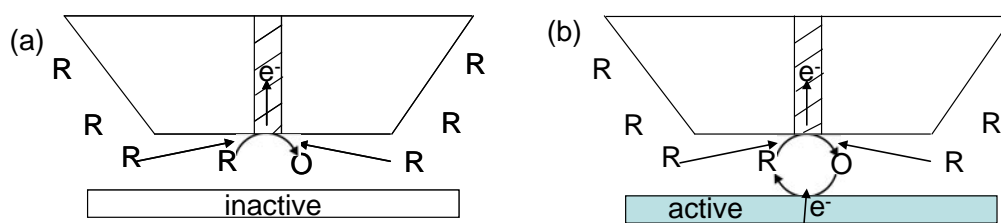


Figure 1-24. (a) Negative feedback by the hindered diffusion when the tip approaches the inactive substrate, and (b) positive feedback by the regeneration of R via a heterogeneous reaction at an active substrate.

These two kinds of tip current perturbation effect in the feedback mode represent two extreme cases: hindered diffusion and diffusion-controlled recycling of the mediator. Thanks to this fact, the surface reactivity of almost any interface can be classified into categories between active (*e.g.* positive feedback) and non-active (*e.g.*

negative feedback) interface by performing an approach curve. Moreover, a quantitative analysis is also possible, since the accessible substrate kinetic range is limited by these two extreme cases (see curves 1 and 2 in Figure 1-25) as shown in Figure 1-25 where a set of approach curves over a substrate with intermediate reaction rates are presented (see curves 3 to 6 in Figure 1-25). Therefore, extraction of kinetic information might be obtained by fitting the experimental approach curves to theoretical or simulated ones such as the approximate current equations from 1-70 to 1-75.²¹⁰

$$I_T(L, \Lambda, RG) = I_T^{\text{active}}\left(L + \frac{1}{\Lambda}, RG\right) + \frac{I_T^{\text{inactive}}(L, RG) - 1}{\left(1 + 2.47RG^{0.31}L\Lambda\right)\left(1 + L^{0.006RG+0.113}\Lambda^{-0.0236RG+0.91}\right)} \quad (1-70)$$

Where the normalized currents for active (I_T^{active}) and inactive (I_T^{inactive}) substrates are equal to

$$I_T^{\text{active}}\left(L + \frac{1}{\Lambda}, RG\right) = \alpha(RG) + \frac{\pi}{4\beta(RG)\text{ArcTan}\left(L + \frac{1}{\Lambda}\right)} + \left(1 - \alpha(RG) - \frac{1}{2\beta(RG)}\right) \frac{2}{\pi} \text{ArcTan}\left(L + \frac{1}{\Lambda}\right) \quad (1-71)$$

$$I_T^{\text{inactive}}(L, RG) = \frac{\frac{2.08}{RG^{0.358}}\left(L - \frac{0.145}{RG}\right) + 1.585}{\frac{2.08}{RG^{0.358}}(L + 0.0023RG) + 1.57 + \frac{\ln RG}{L} + \frac{2}{\pi RG} \ln\left(1 + \frac{\pi RG}{2L}\right)} \quad (1-72)$$

and with

$$\alpha(RG) = \ln 2 + \ln 2 \left(1 - \frac{2}{\pi} \text{ArcCos}\left(\frac{1}{RG}\right)\right) - \ln 2 \left(1 - \left(\frac{2}{\pi} \text{ArcCos}\left(\frac{1}{RG}\right)\right)^2\right) \quad (1-73)$$

$$\beta(RG) = 1 + 0.639 \left(1 - \frac{2}{\pi} \text{ArcCos} \left(\frac{1}{RG} \right) \right) - 0.186 \left(1 - \left(\frac{2}{\pi} \text{ArcCos} \left(\frac{1}{RG} \right) \right)^2 \right) \quad (1-74)$$

$$\Lambda = \frac{kr}{D} \quad (1-75)$$

By knowing L , r , D , and RG , k can be extracted.

In addition, the range of kinetics studied can be tuned by changing the size of the UME, for instance a shorter time constant (*i.e.* equal to r^2/D) for the electrochemical response at the tip will be achieved with smaller UME.²⁰² Smaller UMEs are also beneficial for the higher lateral resolution when performing SECM imaging.

It is also important to notice that the closer the tip is placed from the substrate the higher the current contrast will be between two areas of different reactivity. In fact, the working distance between the tip and the substrate (d) should be lower than two times the radius of the UME in order to see evident current changes caused by different surface kinetics.

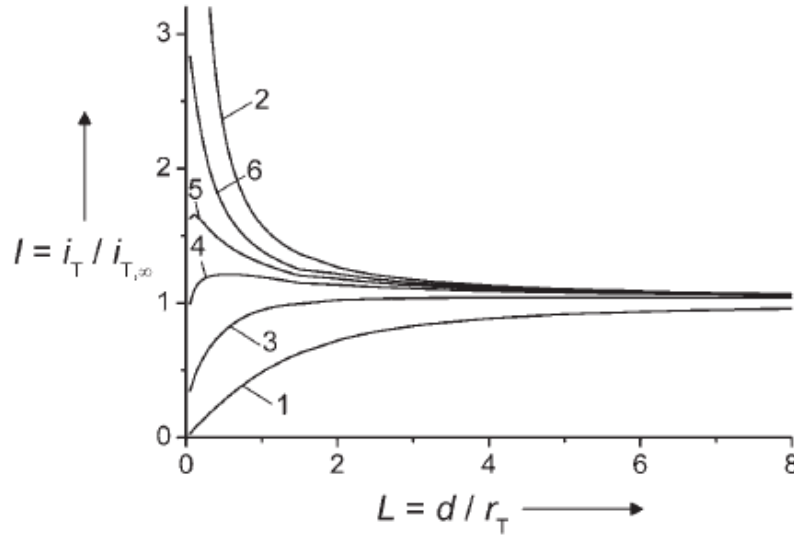


Figure 1-25. Calculated approach curves of a UME ($RG = 10$) for hindered diffusion (curve 1), diffusion-controlled recycling of the mediator (curve 2), and finitely kinetic recycling with the values increased from curve 3 to 6, reproduced from reference.²⁰⁴

1.4.3. Generation/Collection (GC) mode

The GC mode is divided into substrate generation/tip collection (SG/TC) and tip generation/substrate collection (TG/SC) modes, where the second one is more sensitive, since it has a much smaller background signal. This is caused by the fact that when using a macro-sized substrate for SECM experiments, a truly steady-state response is difficult to be obtained at the substrate.²¹¹ In the SG/TC mode, species generated at the substrate can diffuse through the tip/substrate gap and be collected by the tip with an appropriate biased potential provided that the tip is brought close to the substrate (see Figure 1-26a). Under SG/TC conditions, a potentiometric UME can also be used as the tip with some advantages with respect to the amperometric one. On the one hand, it minimizes the disturbance of the diffusion layer produced by the substrate when the tip is scanned in the z direction approaching the substrate (see Figure 1-26b). On the other hand, it can be used to probe the concentration profile of the species produced near the substrate. In the TG/SC mode (see Figure 1-26c), the tip is held at a potential where an electrode reaction occurs and at the same time the substrate is perturbed at another potential where the species produced at the tip can be detected. Therefore, simultaneous measurements of substrate i_S and tip i_T currents are performed. If the substrate area is large enough, the separation between the tip and the substrate is less than 2 times the radius of the UME and the generated species are stable at least during the course of the experiment, the collection efficiency (defined as i_S/i_T) might reach 100 %. Naturally, intermediate cases are common in which the collection efficiency profile as a function of d can be used to extract kinetic information of such kinds of heterogeneous reactions. Similar to the feedback mode, it has been demonstrated that TG/SC mode is an effective tool for energy-related studies, such as screening of ORR catalysts.^{212,213}

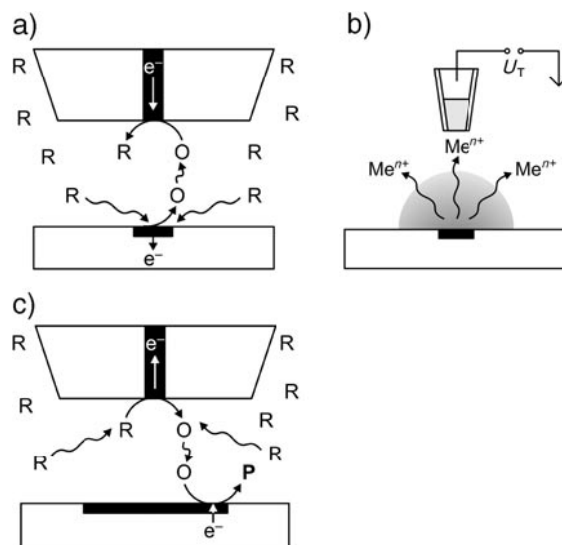


Figure 1-26. Schematic representation of SECM operated in a) SG/TC mode with an amperometric UME, b) SG/TC mode with a passive potentiometric microelectrode, and c) TG/SC mode with an amperometric UME, reproduced from reference.²⁰⁴

The performance of the GC mode used in imaging is poorer than that made by the feedback mode. However, a much higher sensitivity is provided by the GC mode because the signal resulting from the flux of species coming from the substrate is essentially immune to a background signal.²⁰²

1.5. References

- (1) Scholz, F. *Annu. Rep. Prog. Chem., Sect. C: Phys. Chem.* **2006**, *102*, 43.
- (2) Girault, H. H.; Schiffrin, D. J. In *Electroanalytical Chemistry. A series of advances*; Bard, A. J., Ed.; Marcel Dekker: New York, 1989; Vol. 15, p 1.
- (3) Girault, H. H. In *Electroanalytical Chemistry, Vol 23*; Bard, A. J., Zoski, C. G., Eds. 2010; Vol. 23, p 1.
- (4) Reymond, F.; Fermín, D.; Lee, H. J.; Girault, H. H. *Electrochim. Acta* **2000**, *45*, 2647.
- (5) *Liquid Interfaces in Chemical, Biological and Pharmaceutical Applications*; Volkov, A., G., Ed.; Marcel Dekker New York, 2001; Vol. 95.
- (6) Fermín, D. J.; Ding, Z.; Duong, H. D.; Brevet, P. F.; Girault, H. H. *J. Phys. Chem. B* **1998**, *102*, 10334.
- (7) Fermín, D. J.; Duong, H. D.; Ding, Z.; Brevet, P. F.; Girault, H. H. *Phys. Chem. Chem. Phys.* **1999**, *1*, 1461.

- (8) Fermín, D. J.; Duong, H. D.; Ding, Z.; Brevet, P.-F.; Girault, H. H. *J. Am. Chem. Soc.* **1999**, *121*, 10203.
- (9) Lahtinen, R.; Fermín, D. J.; Kontturi, K.; Girault, H. H. *J. Electroanal. Chem.* **2000**, *483*, 81.
- (10) Jensen, H.; Kakkassery, J. J.; Nagatani, H.; Fermín, D. J.; Girault, H. H. *J. Am. Chem. Soc.* **2000**, *122*, 10943.
- (11) Jensen, H.; Fermin, D. J.; Girault, H. H. *Phys. Chem. Chem. Phys.* **2001**, *3*, 2503.
- (12) Eugster, N.; Fermín, D. J.; Girault, H. H. *J. Phys. Chem. B* **2002**, *106*, 3428.
- (13) Eugster, N.; Fermín, D. J.; Girault, H. H. *J. Am. Chem. Soc.* **2003**, *125*, 4862.
- (14) Nagatani, H.; Dejima, S.; Hotta, H.; Ozeki, T.; Osakai, T. *Anal. Sci.* **2004**, *20*, 1575.
- (15) Cooper, J. K.; Benjamin, I. *J. Phys. Chem. B* **2014**.
- (16) Yamada, M.; Perera, J. M.; Grieser, F.; Stevens, G. W. *Anal. Sci.* **1998**, *14*, 225.
- (17) Stockmann, T. J.; Montgomery, A.-M.; Ding, Z. *Anal. Chem.* **2012**, *84*, 6143.
- (18) Hoogerstraete, T. V.; Onghena, B.; Binnemans, K. *J. Phys. Chem. Lett.* **2013**, *4*, 1659.
- (19) Clark, J. F.; Clark, D. L.; Whitener, G. D.; Schroeder, N. C.; Strauss, S. H. *Environ. Sci. Technol.* **1996**, *30*, 3124.
- (20) Chambliss, C. K.; Odom, M. A.; Morales, C. M. L.; Martin, C. R.; Strauss, S. H. *Anal. Chem.* **1998**, *70*, 757.
- (21) Gash, A. E.; Spain, A. L.; Dysleski, L. M.; Flaschenriem, C. J.; Kalaveshi, A.; Dorhout, P. K.; Strauss, S. H. *Environ. Sci. Technol.* **1998**, *32*, 1007.
- (22) Strutwolf, J.; Scanlon, M. D.; Arrigan, D. W. M. *Analyst* **2009**, *134*, 148.
- (23) O'Sullivan, S.; Arrigan, D. W. M. *Anal. Chem.* **2012**, *85*, 1389.
- (24) O'Sullivan, S.; Alvarez de Eulate, E.; Yuen, Y. H.; Helmerhorst, E.; Arrigan, D. W. M. *Analyst* **2013**, *138*, 6192.
- (25) Arrigan, D. W. M. *Annu. Rep. Prog. Chem., Sect. C: Phys. Chem.* **2013**, *109*, 167.
- (26) Mareček, V.; Samec, Z. *Anal. Chim. Acta* **1983**, *151*, 265.
- (27) Sawada, S.; Osakai, T.; Senda, M. *Anal. Sci.* **1995**, *11*, 733.
- (28) Osakai, T.; Yuguchi, Y.; Gohara, E.; Katano, H. *Langmuir* **2010**, *26*, 11530.
- (29) Qian, Q.; Wilson, G. S.; Bowman-James, K.; Girault, H. H. *Anal. Chem.* **2000**, *73*, 497.
- (30) Zhang, J.; Harris, A. R.; Cattrall, R. W.; Bond, A. M. *Anal. Chem.* **2010**, *82*, 1624.
- (31) Ishimatsu, R.; Izadyar, A.; Kabagambe, B.; Kim, Y.; Kim, J.; Amemiya, S. *J. Am. Chem. Soc.* **2011**, *133*, 16300.
- (32) Reymond, F.; Steyaert, G.; Carrupt, P.-A.; Testa, B.; Girault, H. *J. Am. Chem. Soc.* **1996**, *118*, 11951.

- (33) Gobry, V.; Ulmeanu, S.; Reymond, F.; Bouchard, G.; Carrupt, P.-A.; Testa, B.; Girault, H. H. *J. Am. Chem. Soc.* **2001**, *123*, 10684.
- (34) Laforge, F. O.; Carpino, J.; Rotenberg, S. A.; Mirkin, M. V. *Proc. Natl. Acad. Sci. U. S. A.* **2007**, *104*, 11895.
- (35) Scheu, R.; Chen, Y.; de Aguiar, H. B.; Rankin, B. M.; Ben-Amotz, D.; Roke, S. *J. Am. Chem. Soc.* **2014**, *136*, 2040.
- (36) Vanysek, P. *Anal. Chem.* **1990**, *62*, 827A.
- (37) *CRC handbook of chemistry and physics, 85th ed.*; Lide, D. R., Ed.; CRC Press: Boca Raton, 2005.
- (38) Shao, Y. In *Handbook of Electrochemistry*; Zoski, C. G., Ed.; Elsevier: Amsterdam, 2007, p 785.
- (39) Samec, Z.; Homolka, D.; Mareček, V.; Kavan, L. *J. Electroanal. Chem.* **1983**, *145*, 213.
- (40) Valent, O.; Koryta, J.; Panoch, M. *J. Electroanal. Chem.* **1987**, *226*, 21.
- (41) Peljo, P.; Rauhala, T.; Murtomäki, L.; Kallio, T.; Kontturi, K. *Int. J. Hydrogen Energy* **2011**, *36*, 10033.
- (42) Olaya, A. J.; Ge, P.; Girault, H. H. *Electrochem. Commun.* **2012**, *19*, 101.
- (43) Nishi, N.; Imakura, S.; Kakiuchi, T. *Anal. Chem.* **2006**, *78*, 2726.
- (44) Kakiuchi, T. *Anal. Chem.* **2007**, *79*, 6442.
- (45) Bartos, P. J. *Resour. Policy* **2002**, *28*, 85.
- (46) Blank, M.; Feig, S. *Science* **1963**, *141*, 1173.
- (47) Gavach, C.; Mlodnicka, T.; Guastalla, J. *Acad. Sci. Paris, Ser. C.* **1968**, 266, 1196.
- (48) Gavach, C.; Henry, F. *J. Electroanal. Chem.* **1974**, *54*, 361.
- (49) Koryta, J.; Vanýsek, P.; Březina, M. *J. Electroanal. Chem.* **1976**, *67*, 263.
- (50) Samec, Z.; Mareček, V.; Koryta, J.; Khalil, M. W. *J. Electroanal. Chem. Interfacial Electrochem.* **1977**, *83*, 393.
- (51) Samec, Z.; Marecek, V.; Weber, J.; Homolka, D. *J. Electroanal. Chem.* **1979**, *99*, 385.
- (52) Samec, Z.; Mareček, V.; Weber, J. *J. Electroanal. Chem.* **1979**, *100*, 841.
- (53) Olaya, A. J.; Méndez, M. A.; Cortes-Salazar, F.; Girault, H. H. *J. Electroanal. Chem.* **2010**, *644*, 60.
- (54) Senda, M.; Kakiuchi, T.; Osaka, T. *Electrochim. Acta* **1991**, *36*, 253.
- (55) Kalinowski, S.; Figaszewski, Z. *Meas. Sci. Technol.* **1995**, *6*, 1050.
- (56) Taylor, G.; Girault, H. H. *J. Electroanal. Chem.* **1986**, *208*, 179.
- (57) Bard, A. J.; Fan, F. R. F.; Kwak, J.; Lev, O. *Anal. Chem.* **1989**, *61*, 132.
- (58) Wei, C.; Bard, A. J.; Mirkin, M. V. *J. Phys. Chem.* **1995**, *99*, 16033.
- (59) Liu, S.; Li, Q.; Shao, Y. *Chem. Soc. Rev.* **2011**, *40*, 2236.
- (60) Shi, C.; Anson, F. C. *Anal. Chem.* **1998**, *70*, 3114.
- (61) Shi, C.; Anson, F. C. *J. Phys. Chem. B* **1998**, *102*, 9850.

- (62) Scholz, F.; Komorsky-Lovrić, Š.; Lovrić, M. *Electrochem. Commun.* **2000**, *2*, 112.
- (63) Kott, K. L.; Higgins, D. A.; McMahon, R. J.; Corn, R. M. *J. Am. Chem. Soc.* **1993**, *115*, 5342.
- (64) Eisenthal, K. B. *Chem. Rev.* **1996**, *96*, 1343.
- (65) Conboy, J. C.; Richmond, G. L. *J. Phys. Chem. B* **1997**, *101*, 983.
- (66) Miranda, P. B.; Shen, Y. R. *J. Phys. Chem. B* **1999**, *103*, 3292.
- (67) Benjamin, I. *Chem. Rev.* **1996**, *96*, 1449.
- (68) Bard, A. J.; Faulkner, L. R. *Electrochemical Methods*; 2nd ed.; John Wiley & Sons: New York, 2001.
- (69) Laursen, A. B.; Varela, A. S.; Dionigi, F.; Fanchiu, H.; Miller, C.; Trinhammer, O. L.; Rossmeisl, J.; Dahl, S. *J. Chem. Educ.* **2012**, *89*, 1595.
- (70) Marin, D.; Medicuti, F.; Teijeiro, C. *J. Chem. Educ.* **1994**, *71*, A277.
- (71) Ross, P. N. *J. Electrochem. Soc.* **1979**, *126*, 67.
- (72) Smalley, J. F.; Feldberg, S. W.; Chidsey, C. E. D.; Linford, M. R.; Newton, M. D.; Liu, Y.-P. *J. Phys. Chem.* **1995**, *99*, 13141.
- (73) Grahame, D. C. *Chem. Rev.* **1947**, *41*, 441.
- (74) Gavach, C.; Seta, P.; D'Epenoux, B. *J. Electroanal. Chem.* **1977**, *83*, 225.
- (75) Girault, H. H.; Schiffrin, D. J. *J. Electroanal. Chem.* **1983**, *150*, 43.
- (76) Verwey, E. J. W.; Niessen, K. F. *Philos. Mag. Ser. 7* **1939**, *28*, 435.
- (77) Gros, M.; Gromb, S.; Gavach, C. *J. Electroanal. Chem.* **1978**, *89*, 29.
- (78) Homolka, D.; Hájková, P.; Mareček, V.; Samec, Z. *J. Electroanal. Chem.* **1983**, *159*, 233.
- (79) Samec, Z.; Mareček, V.; Homolka, D. *J. Electroanal. Chem.* **1981**, *126*, 121.
- (80) Samec, Z.; Mareček, V.; Homolka, D. *J. Electroanal. Chem.* **1985**, *187*, 31.
- (81) Girault, H. H. *Electrochim. Acta* **1987**, *32*, 383.
- (82) Sun, P.; Laforge, F. O.; Mirkin, M. V. *J. Am. Chem. Soc.* **2007**, *129*, 12410.
- (83) Rose, D.; Benjamin, I. *J. Phys. Chem. B* **2009**, *113*, 9296.
- (84) Murakami, W.; Eda, K.; Yamamoto, M.; Osakai, T. *J. Electroanal. Chem.* **2013**, *704*, 38.
- (85) Schmickler, W. *J. Electroanal. Chem.* **1997**, *426*, 5.
- (86) Webster, R. D.; Beaglehole, D. *Phys. Chem. Chem. Phys.* **2000**, *2*, 5660.
- (87) Linse, P. *J. Chem. Phys.* **1987**, *86*, 4177.
- (88) Benjamin, I. *J. Chem. Phys.* **1992**, *97*, 1432.
- (89) Schweighofer, K. J.; Benjamin, I. *J. Electroanal. Chem.* **1995**, *391*, 1.
- (90) Walker, D. S.; Richmond, G. L. *J. Am. Chem. Soc.* **2007**, *129*, 9446.
- (91) Benjamin, I. *Science* **1993**, *261*, 1558.
- (92) Schweighofer, K. J.; Benjamin, I. *J. Phys. Chem.* **1995**, *99*, 9974.
- (93) Schweighofer, K.; Benjamin, I. *J. Phys. Chem. A* **1999**, *103*, 10274.
- (94) Atkins, P. W. *Physical Chemistry*, 4th ed.; Oxford University Press: Oxford, 1990.
- (95) Smith, R. N.; Hansch, C.; Ames, M. M. *J. Pharm. Sci.* **1975**, *64*, 599.

- (96) Karpfen, F. M.; Randles, J. E. B. *Trans. Faraday Soc.* **1953**, *49*, 823.
- (97) Quoc Hung, L. *J. Electroanal. Chem.* **1980**, *115*, 159.
- (98) Osakai, T.; Kakutani, T.; Senda, M. *Bull. Chem. Soc. Jpn.* **1984**, *57*, 370.
- (99) Melroy, O. R.; Bronner, W. E.; Buck, R. P. *J. Electrochem. Soc.* **1983**, *130*, 373.
- (100) Vanýsek, P.; Buck, R. P. *J. Electrochem. Soc.* **1984**, *131*, 1792.
- (101) Peljo, P.; Qiao, L.; Murtomäki, L.; Johans, C.; Girault, H. H.; Kontturi, K. *ChemPhysChem* **2013**, *14*, 311.
- (102) Samec, Z. *Pure Appl. Chem.* **2004**, *76*, 2147.
- (103) Takahashi, Y.; Shevchuk, A. I.; Novak, P.; Zhang, Y.; Ebejer, N.; Macpherson, J. V.; Unwin, P. R.; Pollard, A. J.; Roy, D.; Clifford, C. A.; Shiku, H.; Matsue, T.; Klenerman, D.; Korchev, Y. E. *Angew. Chem., Int. Ed.* **2011**, *50*, 9638.
- (104) Wightman, R. M. *Science* **1988**, *240*, 415.
- (105) Hamill, O. P.; Marty, A.; Neher, E.; Sakmann, B.; Sigworth, F. J. *Pflugers Arch.* **1981**, *391*, 85.
- (106) Campbell, J. A.; Girault, H. H. *J. Electroanal. Chem.* **1989**, *266*, 465.
- (107) Li, Q.; Xie, S.; Liang, Z.; Meng, X.; Liu, S.; Girault, H. H.; Shao, Y. *Angew. Chem., Int. Ed.* **2009**, *48*, 8010.
- (108) Shao, Y.; Mirkin, M. V. *J. Electroanal. Chem.* **1997**, *439*, 137.
- (109) Shao, Y.; Mirkin, M. V. *J. Phys. Chem. B* **1998**, *102*, 9915.
- (110) Hansma, P.; Drake, B.; Marti, O.; Gould, S.; Prater, C. *Science* **1989**, *243*, 641.
- (111) Tsionsky, M.; Bard, A. J.; Mirkin, M. V. *J. Phys. Chem.* **1996**, *100*, 17881.
- (112) Ding, Z.; Quinn, B. M.; Bard, A. J. *J. Phys. Chem. B* **2001**, *105*, 6367.
- (113) Sun, P.; Li, F.; Chen, Y.; Zhang, M.; Zhang, Z.; Gao, Z.; Shao, Y. *J. Am. Chem. Soc.* **2003**, *125*, 9600.
- (114) Tsionsky, M.; Bard, A. J.; Mirkin, M. V. *J. Am. Chem. Soc.* **1997**, *119*, 10785.
- (115) Alleman, K. S.; Weber, K.; Creager, S. E. *J. Phys. Chem.* **1996**, *100*, 17050.
- (116) Shi, C.; Anson, F. C. *J. Phys. Chem. B* **1999**, *103*, 6283.
- (117) Shi, C.; Anson, F. C. *J. Phys. Chem. B* **2001**, *105*, 1047.
- (118) Barker, A. L.; Unwin, P. R. *J. Phys. Chem. B* **2000**, *104*, 2330.
- (119) Marken, F.; Webster, R. D.; Bull, S. D.; Davies, S. G. *J. Electroanal. Chem.* **1997**, *437*, 209.
- (120) Banks, C. E.; Davies, T. J.; Evans, R. G.; Hignett, G.; Wain, A. J.; Lawrence, N. S.; Wadhawan, J. D.; Marken, F.; Compton, R. G. *Phys. Chem. Chem. Phys.* **2003**, *5*, 4053.
- (121) Scholz, F.; Gulaboski, R. *ChemPhysChem* **2005**, *6*, 16.
- (122) Quentel, F.; Mirčeski, V.; L'Her, M. *Anal. Chem.* **2005**, *77*, 1940.
- (123) Deng, H.; Huang, X.; Wang, L.; Tang, A. *Electrochem. Commun.* **2009**, *11*, 1333.
- (124) Quentel, F.; Mirčeski, V.; L'Her, M.; Mladenov, M.; Scholz, F.; Elleouet, C. *J. Phys. Chem. B* **2005**, *109*, 13228.

- (125)Deng, H.; Huang, X.; Wang, L. *Langmuir* **2010**, *26*, 19209.
- (126)Ulmeanu, S.; Lee, H. J.; Fermin, D. J.; Girault, H. H.; Shao, Y. *Electrochem. Commun.* **2001**, *3*, 219.
- (127)Zhou, M.; Gan, S.; Zhong, L.; Su, B.; Niu, L. *Anal. Chem.* **2010**, *82*, 7857.
- (128)Cheng, Y.; Corn, R. M. *J. Phys. Chem. B* **1999**, *103*, 8726.
- (129)Cheng, Y.; Murtomäki, L.; Corn, R. M. *J. Electroanal. Chem.* **2000**, *483*, 88.
- (130)Marcus, R. A. *J. Chem. Phys.* **2000**, *113*, 1618.
- (131)Samec, Z. *Electrochim. Acta* **2012**, *84*, 21.
- (132)Wandlowski, T.; Mareček, V.; Samec, Z. *Electrochim. Acta* **1990**, *35*, 1173.
- (133)Koryta, J. *Electrochim. Acta* **1979**, *24*, 293.
- (134)Pedersen, C. J. *J. Am. Chem. Soc.* **1967**, *89*, 2495.
- (135)Pedersen, C. J. *J. Am. Chem. Soc.* **1967**, *89*, 7017.
- (136)Pedersen, C. J. *Angew. Chem., Int. Ed.* **1988**, *27*, 1021.
- (137)Läuger, P. *Science* **1972**, *178*, 24.
- (138)Liu, B.; Mirkin, M. V. *Anal. Chem.* **2001**, *73*, 670 A.
- (139)Shioya, T.; Nishizawa, S.; Teramae, N. *J. Am. Chem. Soc.* **1998**, *120*, 11534.
- (140)Homolka, D.; Hung, L. Q.; Hofmanová, A.; Khalil, M. W.; Koryta, J.; Mareček, V.; Samec, Z.; Sen, S. K.; Vanýsek, P.; Weber, J.; Březina, M.; Janda, M.; Stibor, I. *Anal. Chem.* **1980**, *52*, 1606.
- (141)Hatay, I.; Su, B.; Li, F.; Partovi-Nia, R.; Vrabel, H.; Hu, X.; Ersoz, M.; Girault, H. H. *Angew. Chem., Int. Ed.* **2009**, *48*, 5139.
- (142)Shao, Y.; Osborne, M. D.; Girault, H. H. *J. Electroanal. Chem.* **1991**, *318*, 101.
- (143)Laforge, F. O.; Sun, P.; Mirkin, M. V. *J. Am. Chem. Soc.* **2006**, *128*, 15019.
- (144)Guainazzi, M.; Silvestri, G.; Serravalle, G. *J. Chem. Soc., Chem. Commun.* **1975**, 200.
- (145)Samec, Z.; Mareček, V.; Weber, J. *J. Electroanal. Chem.* **1979**, *96*, 245.
- (146)Geblewicz, G.; Schiffrin, D. J. *J. Electroanal. Chem.* **1988**, *244*, 27.
- (147)Zhang, Z.; Yuan, Y.; Sun, P.; Su, B.; Guo, J.; Shao, Y.; Girault, H. H. *J. Phys. Chem. B* **2002**, *106*, 6713.
- (148)Hotta, H.; Ichikawa, S.; Sugihara, T.; Osakai, T. *J. Phys. Chem. B* **2003**, *107*, 9717.
- (149)Su, B.; Hatay, I.; Li, F.; Partovi-Nia, R.; Méndez, M. A.; Samec, Z.; Ersoz, M.; Girault, H. H. *J. Electroanal. Chem.* **2010**, *639*, 102.
- (150)Méndez, M. A.; Partovi-Nia, R.; Hatay, I.; Su, B.; Ge, P.; Olaya, A.; Younan, N.; Hojeij, M.; Girault, H. H. *Phys. Chem. Chem. Phys.* **2010**, *12*, 15163.
- (151)Marcus, R. A. *J. Phys. Chem.* **1990**, *94*, 1050.
- (152)Marcus, R. A. *J. Phys. Chem.* **1990**, *94*, 4152.
- (153)Marcus, R. A. *J. Phys. Chem.* **1990**, *94*, 7742.
- (154)Marcus, R. A. *J. Phys. Chem.* **1991**, *95*, 2010.
- (155)Thomson, F. L.; Yellowlees, L. J.; Girault, H. H. *J. Chem. Soc., Chem. Commun.* **1988**, 1547.

- (156)Samec, Z.; Eugster, N.; Fermín, D. J.; Girault, H. H. *J. Electroanal. Chem.* **2005**, *577*, 323.
- (157)Schaming, D.; Hojeij, M.; Younan, N.; Nagatani, H.; Lee, H. J.; Girault, H. H. *Phys. Chem. Chem. Phys.* **2011**, *13*, 17704.
- (158)Kotov, N. A.; Kuzmin, M. G. *J. Electroanal. Chem.* **1990**, *285*, 223.
- (159)Samec, Z.; Brown, A. R.; Yellowlees, L. J.; Girault, H. H. *J. Electroanal. Chem.* **1990**, *288*, 245.
- (160)Mathai, K. G.; Rabinowitch, E. *J. Phys. Chem.* **1962**, *66*, 663.
- (161)Srinivasan, V.; Rabinowitch, E. *J. Chem. Phys.* **1970**, *52*, 1165.
- (162)Méndez, M. A.; Peljo, P.; Scanlon, M. D.; Vrubel, H.; Girault, H. H. *J. Phys. Chem. C* **2014**, *118*, 16872.
- (163)Costentin, C. *Chem. Rev.* **2008**, *108*, 2145.
- (164)Koper, M. T. M. *Chem. Sci.* **2013**, *4*, 2710.
- (165)Grove, W. R. *Philos. Mag. Ser. 3* **1839**, *14*, 127.
- (166)Steele, B. C. H.; Heinzl, A. *Nature* **2001**, *414*, 345.
- (167)Nørskov, J. K.; Bligaard, T.; Logadottir, A.; Kitchin, J. R.; Chen, J. G.; Pandalov, S.; Stimming, U. *J. Electrochem. Soc.* **2005**, *152*, J23.
- (168)Jaramillo, T. F.; Jørgensen, K. P.; Bonde, J.; Nielsen, J. H.; Horch, S.; Chorkendorff, I. *Science* **2007**, *317*, 100.
- (169)Scanlon, M. D.; Bian, X.; Vrubel, H.; Amstutz, V.; Schenk, K.; Hu, X.; Liu, B.; Girault, H. H. *Phys. Chem. Chem. Phys.* **2013**, *15*, 2847.
- (170)Collman, J. P.; Fu, L.; Herrmann, P. C.; Zhang, X. *Science* **1997**, *275*, 949.
- (171)Collman, J. P.; Wagenknecht, P. S.; Hutchison, J. E. *Angew. Chem., Int. Ed.* **1994**, *33*, 1537.
- (172)Fukuzumi, S.; Okamoto, K.; Gros, C. P.; Guillard, R. *J. Am. Chem. Soc.* **2004**, *126*, 10441.
- (173)Fukuzumi, S.; Yamada, Y.; Karlin, K. D. *Electrochim. Acta* **2012**, *82*, 493.
- (174)Chang, C. J.; Loh, Z. H.; Shi, C.; Anson, F. C.; Nocera, D. G. *J. Am. Chem. Soc.* **2004**, *126*, 10013.
- (175)Kealy, T. J.; Pauson, P. L. *Nature* **1951**, *168*, 1039.
- (176)Langmuir, I. *Science* **1921**, *54*, 59.
- (177)Kunkely, H.; Vogler, A. *Angew. Chem., Int. Ed.* **2009**, *48*, 1685.
- (178)Mueller-Westerhoff, U. T.; Haas, T. J.; Swiegers, G. F.; Leipert, T. K. *J. Organomet. Chem.* **1994**, *472*, 229.
- (179)Cunnane, V. J.; Geblewicz, G.; Schiffrin, D. J. *Electrochim. Acta* **1995**, *40*, 3005.
- (180)Ohde, H.; Maeda, K.; Yoshida, Y.; Kihara, S. *J. Electroanal. Chem.* **2000**, *483*, 108.
- (181)Chung, T. D.; Anson, F. C. *J. Electroanal. Chem.* **2001**, *508*, 115.
- (182)Trojánek, A.; Langmaier, J.; Samec, Z. *Electrochem. Commun.* **2006**, *8*, 475.

- (183)Su, B.; Nia, R. P.; Li, F.; Hojeij, M.; Prudent, M.; Corminboeuf, C.; Samec, Z.; Girault, H. H. *Angew. Chem., Int. Ed.* **2008**, *47*, 4675.
- (184)Li, F.; Su, B.; Salazar, F. C.; Nia, R. P.; Girault, H. H. *Electrochem. Commun.* **2009**, *11*, 473.
- (185)Trojánek, A.; Langmaier, J.; Su, B.; Girault, H. H.; Samec, Z. *Electrochem. Commun.* **2009**, *11*, 1940.
- (186)Partovi-Nia, R.; Su, B.; Li, F.; Gros, C. P.; Barbe, J. M.; Samec, Z.; Girault, H. H. *Chem.-Eur. J.* **2009**, *15*, 2335.
- (187)Hatay, I.; Su, B.; Li, F.; Méndez, M. A.; Khoury, T.; Gros, C. P.; Barbe, J. M.; Ersoz, M.; Samec, Z.; Girault, H. H. *J. Am. Chem. Soc.* **2009**, *131*, 13453.
- (188)Su, B.; Hatay, I.; Trojánek, A.; Samec, Z.; Khoury, T.; Gros, C. P.; Barbe, J. M.; Daina, A.; Carrupt, P. A.; Girault, H. H. *J. Am. Chem. Soc.* **2010**, *132*, 2655.
- (189)Hatay, I.; Su, B.; Méndez, M. A.; Corminboeuf, C.; Khoury, T.; Gros, C. P.; Bourdillon, M.; Meyer, M.; Barbe, J. M.; Ersoz, M.; Záliš, S.; Samec, Z.; Girault, H. H. *J. Am. Chem. Soc.* **2010**, *132*, 13733.
- (190)Partovi-Nia, R.; Su, B.; Méndez, M. A.; Habermeyer, B.; Gros, C. P.; Barbe, J. M.; Samec, Z.; Girault, H. H. *ChemPhysChem* **2010**, *11*, 2979.
- (191)Su, B.; Hatay, I.; Ge, P. Y.; Mendez, M.; Corminboeuf, C.; Samec, Z.; Ersoz, M.; Girault, H. H. *Chem. Commun.* **2010**, *46*, 2918.
- (192)Olaya, A. J.; Ge, P.; Gonthier, J. F.; Pechy, P.; Corminboeuf, C.; Girault, H. H. *J. Am. Chem. Soc.* **2011**, *133*, 12115.
- (193)Peljo, P.; Murtomäki, L.; Kallio, T.; Xu, H. J.; Meyer, M.; Gros, C. P.; Barbe, J. M.; Girault, H. H.; Laasonen, K.; Kontturi, K. *J. Am. Chem. Soc.* **2012**, *134*, 5974.
- (194)Trojánek, A.; Langmaier, J.; Ebera, J.; Záli, S.; Barbe, J. M.; Girault, H. H.; Samec, Z. *Chem. Commun.* **2011**, *47*, 5446.
- (195)Trojánek, A.; Langmaier, J.; Záliš, S.; Samec, Z. *Chem. Commun.* **2012**, *48*, 4094.
- (196)Jedraszko, J.; Nogala, W.; Adamiak, W.; Rozniecka, E.; Lubarska-Radziejewska, I.; Girault, H. H.; Opallo, M. *J. Phys. Chem. C* **2013**, *117*, 20681.
- (197)Hatay, I.; Ge, P. Y.; Vruble, H.; Hu, X.; Girault, H. H. *Energy Environ. Sci.* **2011**, *4*, 4246.
- (198)Ge, P.; Scanlon, M. D.; Peljo, P.; Bian, X.; Vubrel, H.; O'Neill, A.; Coleman, J. N.; Cantoni, M.; Hu, X.; Kontturi, K.; Liu, B.; Girault, H. H. *Chem. Commun.* **2012**, *48*, 6484.
- (199)Bian, X.; Scanlon, M. D.; Wang, S.; Liao, L.; Tang, Y.; Liu, B.; Girault, H. H. *Chem. Sci.* **2013**, *4*, 3432.
- (200)Bateman, L. C.; Church, M. G.; Hughes, E. D.; Ingold, C. K.; Taher, N. A. *J. Chem. Soc.* **1940**, 979.
- (201)Peters, K. S. *Chem. Rev.* **2007**, *107*, 859.
- (202)*Scanning Electrochemical Microscopy*; Bard, A. J.; Mirkin, M. V., Eds.; Marcel Dekker: New York, 2001.
- (203)Sun, P.; Laforge, F. O.; Mirkin, M. V. *Phys. Chem. Chem. Phys.* **2007**, *9*, 802.

- (204)Wittstock, G.; Burchardt, M.; Pust, S. E.; Shen, Y.; Zhao, C. *Angew. Chem., Int. Ed.* **2007**, *46*, 1584.
- (205)Pethica, J. B. *Phys. Rev. Lett.* **1986**, *57*, 3235.
- (206)Cannes, C.; Kanoufi, F.; Bard, A. J. *Langmuir* **2002**, *18*, 8134.
- (207)Rodríguez-López, J.; Alpuche-Avilés, M. A.; Bard, A. J. *J. Am. Chem. Soc.* **2008**, *130*, 16985.
- (208)Eckhard, K.; Chen, X.; Turcu, F.; Schuhmann, W. *Phys. Chem. Chem. Phys.* **2006**, *8*, 5359.
- (209)Saito, Y. *Rev. Polarography* **1968**, *15*, 177.
- (210)Cornut, R.; Lefrou, C. *J. Electroanal. Chem.* **2008**, *621*, 178.
- (211)Bertoncello, P. *Energy Environ. Sci.* **2010**, *3*, 1620.
- (212)Fernández, J. L.; Bard, A. J. *Anal. Chem.* **2003**, *75*, 2967.
- (213)Fernández, J. L.; Walsh, D. A.; Bard, A. J. *J. Am. Chem. Soc.* **2005**, *127*, 357.

Chapter 2

Experimental and Instrumentation

2.1. Introduction

In this chapter, chemicals, some frequently-used experimental techniques and the corresponding protocols will be presented. The experimental techniques are mainly classified into two categories: electrochemical methods and so-called shake-flask experiments. Electrochemical methods include the four-electrode system (potentiostat and electrochemical cells), traditional three-electrode system, scanning electrochemical microscopy and its probe – microelectrode fabrication, etc. In shake-flask experiments, details will be given for (real-time) analysis of reactants and products with the techniques including UV/Vis spectroscopy, mass spectrometry, Karl Fischer titration for water content determination, H₂ detection by gas chromatography, and so on. Photoinduced electron transfer reaction will be addressed in the Appendix of this thesis, but the only additional experimental element is a light source, compared to the dark reactions. So it will not be discussed here. For other characterization techniques on the solid catalysts, these will be detailed in the corresponding chapters.

2.2. Chemicals

All chemicals are analytical grade and used as received without further purification. Graphene oxide (GO) was ordered from Graphene Supermarket (Graphene Laboratories, Inc.). Potassium hexacyanoferrate(III) (K₃Fe(CN)₆, 99%) was purchased from Merck. Potassium hexacyanoferrate(II) trihydrate (K₄Fe(CN)₆•3H₂O, 99%) was purchased from AppliChem. 1H-indole was bought from Fluorochem. 1,2-diferrocenylethane (DFcE) and molybdenum carbide (Mo₂C, ~325 mesh, ≥99.5%) were purchased from Aldrich. Hydrochloric acid (HCl), potassium chloride (KCl, 99%), lithium hydroxide monohydrate (LiOH•H₂O), sodium hydroxide (NaOH), sodium sulfate (Na₂SO₄), magnesium sulfate heptahydrate (MgSO₄•7H₂O),

tetraethylammonium chloride (TEACl, 98%), hydrogen peroxide (3% solution), anhydrous lithium chloride (LiCl), bis(triphenylphosphoranylidene) ammonium chloride (BACl), lithium sulfate (Li₂SO₄), 1,2-dichloroethane (DCE), sodium iodide (NaI), and tetramethylammonium sulfate (TMA₂SO₄) were obtained from Fluka. Lithium tetrakis(pentafluorophenyl)borate diethyl etherate (LiTB) was purchased from Boulder Scientific and sulfuric acid (H₂SO₄, 95-97%), ferrocene (Fc, 98%), 1,1'-dimethylferrocene (DMFc), ferrocene methanol (FcCH₂OH, 97%), dibenzo-18-crown-6 (DB18C6, 98%), N, N-dimethylformamide (DMF) and tetrahexylammonium tetrafluoroborate were purchased from Sigma-Aldrich. Decamethylferrocene (DMFc, 99%) and Potassium bis(oxalato)-oxotitanate(IV) dihydrate (K₂TiO(C₂O₄)₂·2H₂O) were provided by Alfa Aesar. ZnTPPC was sourced from Frontier Scientific and 0.1 mM ZnTPPC + 10 mM NaCl aqueous solution (pH *ca.* 7) was prepared by addition of 100 µL of 1M NaOH onto ZnTPPC powder (0.8 mg) and then addition of 100 µL of 1M HCl and finally diluted to 10 mL by water. The pH of the ZnTPPC solution was also adjusted to *ca.* 5.45 by dropwise addition of 1M HCl for shake-flask reactions. The aqueous solutions were prepared with ultrapure water (18.2 MΩcm) from a Millipore-Q system. 0.1 M phosphate buffer solution was used for solutions of pH 7.

Biscobalt2,2'-bis[5-(2,8,13,17-tetraethyl-3,7,12,18-tetramethylporphyrinyl)] diphenylether (Co₂(DPOx)) was synthesized as described earlier.¹

2.3. Electrochemical methods

2.3.1. Four-electrode system

From the experimental viewpoint, the development of the four-electrode potentiostat and the associated electrochemical cells in the late 1970s²⁻⁴ is a landmark event, indicating the start of modern electrochemistry at the ITIES. Since then, the ITIES can be polarized by the external power source and the most experimental data regarding the electrical double layer as well as the heterogeneous charge transfer reactions have been collected by this setup.^{5,6} The block diagram of the four-electrode potentiostat has been shown in Figure 1-8 in Chapter 1. The employed glass cells are shown in Figure 1-1 and Figure 1-7 in Chapter 1. The general expression for a polarizable ITIES in a four-electrode electrochemical cell has been described in equation 1-36 in Chapter 1.

2.3.2. Preparation of reference electrodes and organic supporting electrolytes

The reference electrodes, Ag/AgCl, Ag/Ag₂SO₄, and Ag/AgTB, were prepared by electrolysis of a clean Ag wire as an anode and a Pt wire as a cathode, in 10 mM NaCl plus 100 mM HCl or 5 mM Li₂SO₄ plus 50 mM H₂SO₄ or 10 mM LiTB solution, respectively, at a voltage output bigger than 1.5 V. The passage of current oxidizes the Ag forming a layer of insoluble silver salt – AgCl, Ag₂SO₄, or AgTB, respectively, accompanying the electrolytic hydrogen evolution at the Pt wire.

The organic supporting electrolyte BATB, with the molecular structure shown in Figure 2-1, was obtained by metathesis of an equivalent molar ratio of bis(triphenylphosphoranylidene)ammonium chloride (BACl) and lithium tetrakis(pentafluorophenyl)borate diethyl etherate (LiTB) in 2:1 volume ratio of methanol/water mixture. The resulting white precipitate was washed thoroughly with pure water and then recrystallized in acetone. The obtained white crystals were washed again by copious amount of water and dried under vacuum and transferred into a glass bottle waiting for use.

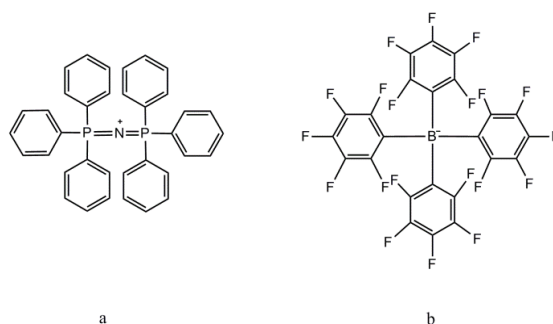


Figure 2-1. Molecular structures of organic ions (a) BA⁺ and (b) TB⁻.

2.3.3. Three-electrode system

The three-electrode cell is the most-commonly used system in electrochemical measurements when the test solution is relatively resistive and the current relatively large. Normally, a solid and inert electrode (such as Pt or glassy carbon) is used as a

working electrode, with a Pt wire as a counter electrode, and a reference electrode with chemical compositions depending on the specific experimental requirements. In this arrangement, potential of the working electrode is controlled with respect to the reference electrode, while the current passes the loop between the working and the counter electrodes. The electrochemistry in organic solutions was conducted in DCE with BATB as the supporting electrolyte, unless specified elsewhere. Fc or DMFc was employed as an internal reference to calibrate the potential scale in organic solutions, even though a silver wire was normally used as a quasi-reference electrode.

2.3.4. Scanning electrochemical microscopy

2.3.4.1. Instrument

Here, a brief description of the main components of a scanning electrochemical microscopy (SECM) instrument will be presented. A SECM device is shown in Figure 2-2, which is composed of six main elements: disk-shaped amperometric microelectrode (Pt or carbon fiber) as the probe, substrate as the sample, potentiostat or bipotentiostat for potential control, counter and reference electrodes in an electrochemical cell mounted on an adjustable tilting platform, 3-axes piezo positioner for positioning the probe, and a personal computer (PC) for control of the whole system.

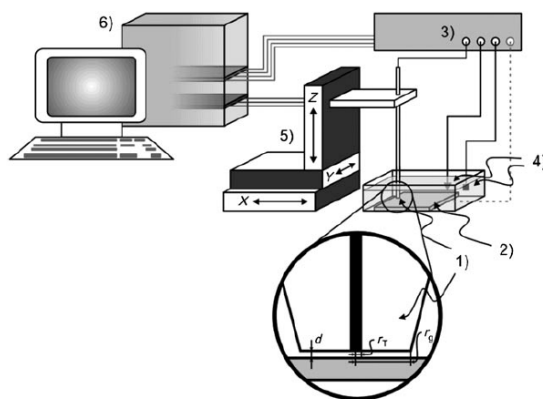


Figure 2-2. Block diagram of the SECM apparatus. (1) disk-shaped amperometric microelectrode, (2) sample or substrate, (3) potentiostat or bipotentiostat, (4) counter and reference electrodes in an electrochemical cell, (5) piezo positioner, and (6) personal computer. Reproduced from reference.⁷

When a SECM device is at work, the (bi)potentiostat is used to control the tip (and also frequently the substrate) potential, while the piezo positioner moves the tip either scanning or approaching with respect to the substrate. The signal is caused by a redox reaction both on the tip and substrate. Until now, there have been some commercial SECM instruments available on the market, such as CHI-900 electrochemical workstation (CH Instruments, Austin, USA), EIProScan system (Heka), and SECM370 (Uniscan instruments, BioLogic company), and so on. The SECM apparatus currently used in this thesis is either a commercial CHI-900 electrochemical workstation or a custom-built SECM setup controlled by SECMx software⁸ and interfaced with an IVIUM Compactstat (IVIUM Technologies, The Netherlands).

As the probe tip is a critical element to perform any SECM experiment, its fabrication and characterization will be described below.

2.3.4.2. Fabrication and characterization of amperometric microelectrodes

Fabrication of a Pt and carbon fiber UMEs was performed by sealing a 10- 20- or 25 μm -diameter Pt wire or a 10 μm -diameter carbon fiber (Goodfellow, Oxford, UK) at one end of a glass capillary (*i.e.* inner diameter 1 mm, outer diameter 1.5 mm, Bio-logic) by a butane/propane/oxygen flame (C206 Super, CAMPINGAZ). Afterwards, the glass capillary with a sealed Pt wire or carbon fiber is subject to a vacuum system for *ca.* 30 min. Then, the capillary is slowly sealed onto the Pt wire or the carbon fiber by placing it inside a resistor heater coil (Model 720, David Kopf Instruments, USA). Special attention has to be paid in order to place the capillary in the center of the coil to avoid capillary deformations leading to non-straight UMEs. After a capillary section equal to *ca.* 1 cm-length is properly sealed; the electrical connection is made by melting a given amount of tin powder between the Pt wire or carbon fiber and a larger tin/copper lead wire. Lastly, the tin/copper lead wire is fixed to the glass capillary by a two-component epoxy resin (Araldit, Reckitt & Colman AG), letting a free tin/copper wire section outside the glass capillary for electrical connection purposes.⁹

Alternatively, a commercial glassy carbon microelectrode (13.7 μm diameter, Princeton Applied Research) was also used as the working electrode in SECM or voltammetric measurements.

As discussed in Section 1.4.2 in Chapter 1, the microelectrode's RG and surface smoothness play an important role in performing an approach curve in the feedback mode in SECM and in conventional voltammetrical measurements. To this end the microelectrode tip was sharpened using a metallographic abrasive paper (# 1200) to make the RG smaller than 5.5. Then the surface of the electrode was mechanically polished successively with polishing wheels made of alumina with different particle sizes (*i.e.* 6, 1, 0.5, 0.1, 0.05 μm). It is important to monitor the polishing progress under optical microscope from time to time in order to check the smoothness and flatness of the electrode. Finally, the microelectrode is washed with isopropanol in order to remove any residues from the polishing process. Figure 2-3 shows a final carbon microelectrode in side and top views with a RG of 5.5. As it can be seen from Figure 2-3b that, the electrode surface with an inlaid active disk looks very flat and smooth. After checking the physical properties of the prepared microelectrode, the electrochemical properties must be tested to confirm the capabilities of the carbon fiber microelectrode in electrochemical studies.

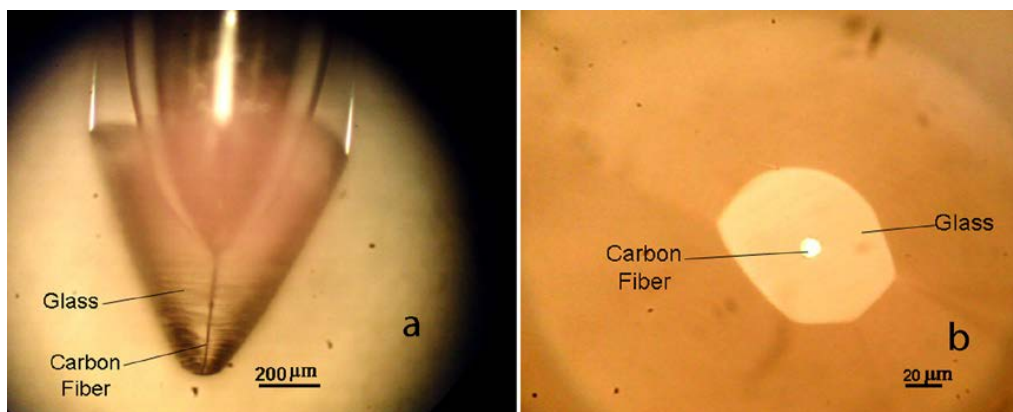


Figure 2-3. Side (a) and top (b) views of a carbon fiber microelectrode. Notes: In the top view the electrode tip has been sharpened to have a RG value of 5.5.

Cyclic voltammetry was conducted for the characterization of the new carbon microelectrode. A steady-state voltammogram where the reverse scan is almost retraced to the forward scan was obtained as shown in Figure 2-4. A solution of 2 mM ferrocenemethanol in 0.1 M KCl was used for recording this voltammogram. An electrochemical behavior characterized by a low capacitive current and an ideal

steady-state current proves the successful fabrication of a carbon fiber microelectrode. Besides, it can be seen that the slope (-56 mV) for the relationship between the applied electrode potential E and $\log((I_{\infty}-I)/I)$ shown in the inset of Figure 2-4 is very close to the ideal value -59 mV , indicating the redox reactions occurred at the microelectrode surface is fast and reversible and uncompensated solution iR drop is minimal.

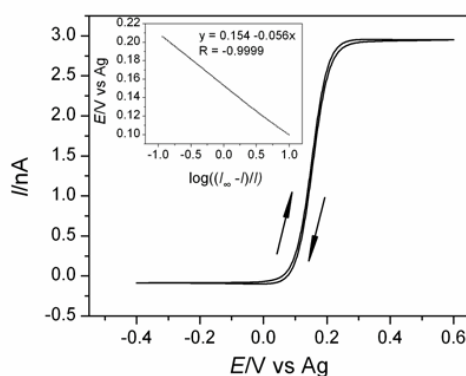


Figure 2-4. Cyclic voltammogram of FcMeOH at a carbon fiber microelectrode (diameter = $10\text{ }\mu\text{m}$, RG = 5.5) in 2 mM ferrocenemethanol + 0.1 M KCl, with a Ag wire as the quasi-reference electrode, and a Pt wire as the counter electrode. Scan rate is $20\text{ mV}\cdot\text{s}^{-1}$. The inset shows the dependence of the applied electrode potential from 0.1 to 0.206 V on the logarithm of $(I_{\infty}-I)/I$ for the forward scan, where I_{∞} represents the diffusion-limited current at 0.4 V , I is the current at the given potential.

2.4. Shake-flask experiments

Shake-flask experiments were conducted as complementary means to electrochemical methods to get more insights in the viewpoint of reaction mechanisms. Single- or two-phase shake-flask experiments were carried out under aerobic or anaerobic conditions to investigate the oxygen reduction reaction (ORR) or hydrogen evolution reaction (HER), respectively. Generally, reactant mixtures in single or biphasic liquid phase was added in a glass vial and then stirred by a magnetic stirrer vigorously. The specific chemical compositions of the reactant mixtures depend on the experimental requirements and will be detailed in the following chapters. Photo-activated reactions were conducted under illumination with the light wavelength depending on the photochemistry of the involved photosensitizer molecules. After

reaction, the products were detected by UV/Vis spectroscopy, microelectrode voltammetry, mass spectrometry, and gas chromatography, and so on. In this thesis, mainly four reactions – ORR, HER, S_N1 reactions, and photoinduced electron transfer reaction, were investigated. Here, the experimental techniques used for studying the former three shake-flask reactions will be described.

2.4.1. Oxygen reduction reaction

For a biphasic reaction under aerobic conditions, after reaction aqueous and organic phases were separated and the organic phase was subject to UV/Vis spectroscopy or microelectrode voltammetry measurements directly. Measurements of organic phase were used to study the amount of lipophilic electron donor consumed in the reaction. Then, this value was used in calculating the yield of the products. As discussed in Section 1.3 in Chapter 1, there are mainly two pathways in the ORR in acidic medium: $2e^-/2H^+$ route to hydrogen peroxide (H₂O₂) or $4e^-/4H^+$ route to water (H₂O). To study the yield and selectivity of the generated H₂O₂, three methods for H₂O₂ detection will be detailed. They are NaI titration, titanium oxalate titration, and Prussian Blue sensor methods.

2.4.1.1. Hydrogen peroxide detection

2.4.1.1.1. NaI titration method

In the NaI titration method, the aqueous phase was firstly treated with excess NaI (equivalent to 0.1 M) for 0.5 h. H₂O₂ will react with I⁻ according to the equation 2-1 to produce I₃⁻, which has a characteristic absorbance peak at 352 nm.^{10,11}



It can be seen that one mole of I₃⁻ is produced for each mole of H₂O₂. So the amount of H₂O₂ produced after ORR can be obtained indirectly. UV/Vis spectra were obtained with an Ocean Optics CHEM2000 spectrophotometer with a quartz cuvette (path length: 1 cm).

A calibration curve for H₂O₂ detection was constructed from UV/Vis measurements of a series of standard H₂O₂ solutions in different concentrations. It was shown in

Figure 2-5 and Figure 2-6. It can be seen from panel “a” of Figure 2-5 that the absorbance reaches saturation for H_2O_2 concentration higher than 100 μM . This is caused by the fact that Lambert-Beer’s law (detailed in Section 2.4.1.2) is a strict limiting law that is valid only for a dilute analyte solution, as the molar absorptivity of the analyte might change at higher concentrations due to the more evident interaction between the analyte particles. Change in the sample’s refractive index at analyte’s higher concentration might also account for the deviation from Lambert-Beer’s law. However, it is more likely due to the longer cell pathlength (1 cm) that the light penetrates during the measurements. So, it can be expected that the linearity range of the relationship between absorbance versus concentration will be wider if a shorter cell pathlength (*e.g.* 0.1 cm) was employed. Anyway, the measurements for the samples are always valid in the linear range with the help of a calibration curve such as that in Figure 2-6. From Figure 2-6 we got an extinction coefficient of 29994 $\text{M}^{-1}\text{cm}^{-1}$ for I_3^- at 352 nm in the concentration range of 3.4 μM to 55.1 μM , which is in reasonable agreement with a value of 27600 $\text{M}^{-1}\text{cm}^{-1}$ reported by Rahn *et al.*¹² With this data, the amount of the produced H_2O_2 can be estimated easily.

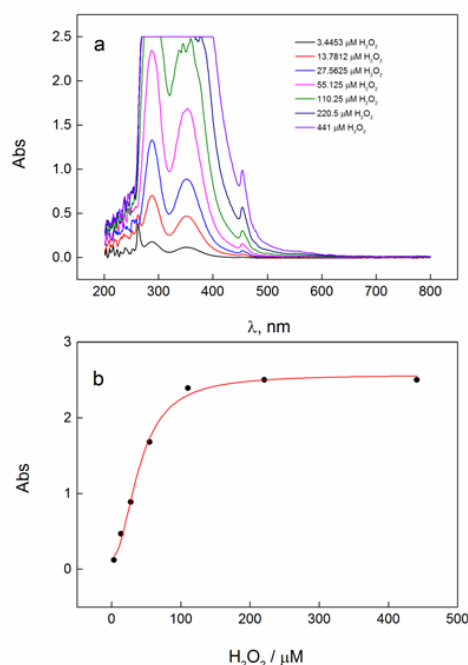


Figure 2-5. (a) The UV/Vis absorption spectra of the standard H_2O_2 solution at different concentrations (see details in the legend) after treatment with excess NaI (0.1 M) for 0.5 h, with a cell pathlength of 1 cm; and (b) the corresponding relationship between absorption at 352 nm from (a) and H_2O_2 concentration.

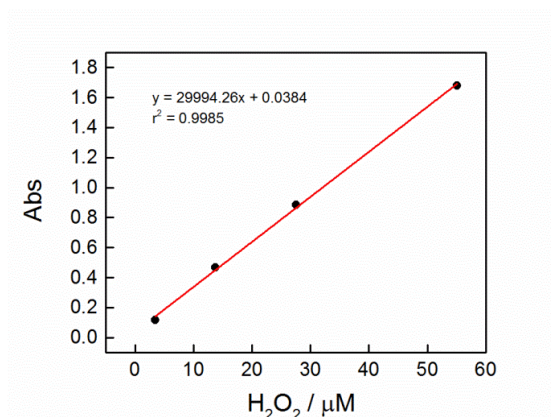


Figure 2-6. The linear calibration curve for H_2O_2 detection built from the data in **Figure 2-5** (b), in which the linear concentration range of H_2O_2 is located between 3.4 μM to 55.1 μM .

2.4.1.1.2. Titanium oxalate titration method

In the titanium oxalate titration method developed by Sellers in 1980,¹³ two reagents, *i.e.* 1:3 (v/v) H_2SO_4 and 50 g/L $\text{K}_2\text{TiO}(\text{C}_2\text{O}_4)_2 \cdot 2\text{H}_2\text{O}$, were prepared for use. 1 mL of the separated aqueous phase from the biphasic reaction flask was put into a small glass vial. 0.1 mL of 1:3 (v/v) H_2SO_4 and 0.2 mL of 50 g/L $\text{K}_2\text{TiO}(\text{C}_2\text{O}_4)_2 \cdot 2\text{H}_2\text{O}$ were sequentially added into the sample, and the solution was diluted with 1.2 mL of deionized water. TiO_2^{2+} forms a yellow complex with H_2O_2 and the amount of hydrogen peroxide could be assayed by measuring the absorption of the solution in 1 cm path-length quartz cuvette at 400 nm using a molar absorptivity of $935 \text{ M}^{-1}\text{cm}^{-1}$ reported by Sellers.¹³

2.4.1.1.3. Prussian Blue sensor for hydrogen peroxide

Prussian Blue sensor for hydrogen peroxide^{14,15} consisting of an integrated three-electrode system with a working (“W”, Prussian Blue), a reference (“R”, Ag/AgCl),

and a counter electrode (“C”, carbon paste) on a plastic plate with silver paste as electrical contact is shown in Figure 2-7.

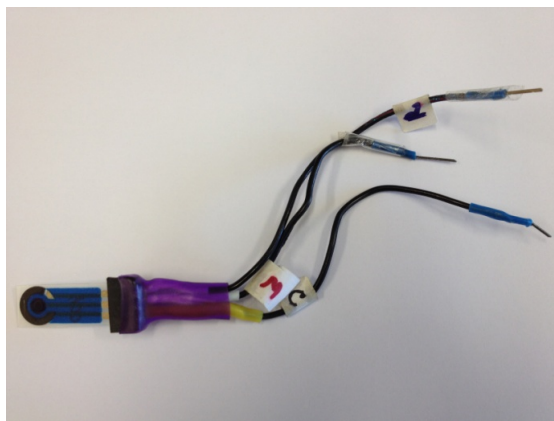


Figure 2-7. The Prussian Blue sensor composed of a Ag/AgCl reference, a carbon paste counter, and a Prussian Blue working electrode.

Prussian Blue has “soluble” and “insoluble” forms and the “soluble” form has the molecular formula – $\text{KFe}^{\text{III}}[\text{Fe}^{\text{II}}(\text{CN})_6]$ while the “insoluble” one has the molecular formula of $\text{Fe}^{\text{III}}[\text{Fe}^{\text{III}}\text{Fe}^{\text{II}}(\text{CN})_6]_3$. The operation principle of the Prussian Blue sensor lies in its superior catalytic activity towards H_2O_2 reduction over the interferent – O_2 reduction.¹⁴

In this thesis, a standard addition method to eliminate the “medium effect” was employed to analyze quantitatively the produced H_2O_2 during the ORR at the ITIES. Specifically, 1) 5500 μL pH 6 phosphate buffer was put into a glass vial and the baseline current was recorded by chronoamperometry at applied potential of 0 V *vs.* Ag/AgCl; 2) 500 μL of sample from aqueous phase after shake-flask experiment was added into the vial and the signal was recorded; 3) 10 μL of 44.1 mM standard H_2O_2 solution (fresh solution) was added 3 times sequentially while recording the current; 4) 500 μL of aqueous phase after shake-flask experiment was added again into the vial to confirm the results. Now the current *vs.* H_2O_2 concentration curve can be plotted, and H_2O_2 concentration ($[\text{H}_2\text{O}_2]$) in the original sample can be calculated from the intercept at the x axis ($x_{\text{intercept}}$) with the relation shown below:

$$\frac{500 \times [\text{H}_2\text{O}_2]}{6000} = x_{\text{intercept}} \quad (2-2)$$

2.4.1.2. Chemical kinetics

One aspect of ORR at the ITIES that needs to be investigated is its chemical kinetics which is of particular importance for being able to evaluate how fast this reaction is (approaching equilibrium) or how good a catalyst works on the reaction. Another reason is that the study of kinetics can shed light on the mechanisms of reactions, from which more efficient and novel reaction pathways may be devised. In this thesis, in total three methods will be employed to study the kinetics of this reaction, namely, *in situ* UV/Vis monitoring, SECM in feedback mode, and CV simulations through COMSOL software employing finite element method (FEM). While SECM in feedback mode has been introduced briefly in Section 1.4 in Chapter 1 and in Section 2.3.4 in this Chapter and CV simulations by the FEM will be detailed in Chapters 5 and 7, only the methodology of *in situ* UV/Vis monitoring will be illustrated herein.

The *in situ* UV/Vis monitoring setup is shown in Figure 2-8, which includes a light source, a cuvette in a holder, a spectrometer, and a PC. The light source sends light *via* an optical fiber through the sample in the cuvette. The outgoing light from the sample is then sent *via* another optical fiber into the spectrophotometer interfaced with a PC for data handling.



Figure 2-8. The shake-flask experiments monitored by *in situ* UV/Vis spectroscopy, which includes a light source, a cuvette in a holder, a spectrometer, and a PC. Reproduced from the “Installation and Operation Manual of USB2000 Fiber Optic Spectrometer”, Ocean Optics Inc.

Normally, for chemical kinetics measurements, the evolution of the concentrations of either reactants or products in function of time will be monitored. According to the Lambert-Beer's law ($A = \epsilon bc$, in which A is absorbance, ϵ is the molar absorptivity or extinction coefficient of the analyte, b is the path length of the cuvette, and c is the concentration of the analyte), the concentration of the analyte is proportional to its absorbance in some appropriate concentration range. Hence, monitoring the absorbance at a fixed wavelength that is associated with either the reactant or product at different times is the general way in chemical kinetics measurements by *in situ* UV/Vis spectroscopy. However, the requirement for this approach is that the products must have different absorption bands compared to the reactants. In this thesis, Fc or DMFc was employed as the lipophilic electron donor. The oxidation product of Fc or DMFc, namely, Fc^+ or DMFc^+ , has different absorption band (620 or 779 nm, respectively) with respect to its reactant (439 or 425 nm, respectively). Extinction coefficients of these species are critical for kinetics measurements. The employed extinction coefficient of DMFc^+ is $632 \text{ M}^{-1}\text{cm}^{-1}$ at 779 nm as estimated by Hatay *et al.*,¹⁶ and the measured value for Fc^+ was $70.4 \text{ M}^{-1}\text{cm}^{-1}$ at 620 nm, shown in Figure 2-9. However, it should be stressed that the employed extinction coefficient of Fc^+ at 620 nm is $350 \text{ M}^{-1}\text{cm}^{-1}$ in Chapter 4, which is different from the value estimated here.

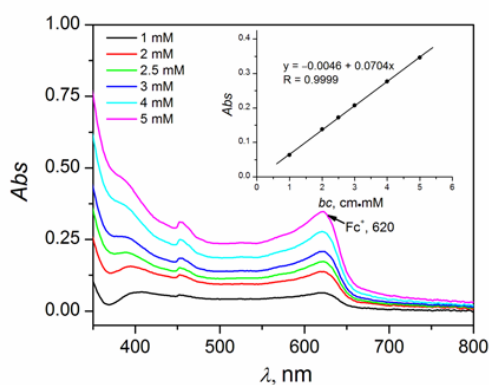


Figure 2-9. The absorbance of Fc^+ made by biphasic oxidation at different concentrations. Inset shows the calibration curve established by plotting the absorbance of Fc^+ at 620 nm in function of Fc^+ concentration at a given path length (1 cm).

2.4.2. Gas chromatography analysis of shake flask reactions

The shake-flask experiments for hydrogen evolution were performed in a nitrogen filled glove-box for 16 h in septum sealed glass vials. The reaction mixtures in the vials were prepared in the glove-box. Magnetic stirring (900 rpm) was used to emulsify the two phases for the course of each experiment. Post-shake flask reaction, 1 mL samples of the headspace gas were obtained using a lock-in syringe with a push-pull valve (SGE Analytical Sciences) in the glovebox and subsequently analyzed by gas chromatography (GC) in terms of retention time using a Perkin-Elmer GC instrument (Clarus 400, equipped with 5 Å molecular sieves and an 80/100 mesh) with a thermal conductivity detector (TCD) and argon as a carrier gas.

2.4.3. ESI-MS analysis of shake flask reactions

As mentioned in Section 1.1 in Chapter 1, hydrophilic metallic cations can catalyze biphasic S_N1 reactions. To study these reactions, a dedicated two-channel microchip was used as an emitter in electrospray ionization mass spectrometry (ESI-MS) to analyze the products of the two-phase reactions, shown in Figure 2-10. Samples taken from the DCE phase were infused *via* channel A at a flow rate of 60 $\mu\text{L/h}$. A sheath flow of ESI buffer (50% water, 49% methanol, and 1% acetic acid) was infused *via* channel B at a flow rate of 60 $\mu\text{L/h}$ to stabilize the ESI performance. High voltage (+3.7 kV) was applied to the electrode to induce ESI. A linear ion trap mass spectrometer (Thermo LTQ Velos) was used to characterize the emitted ions under positive scanning mode.

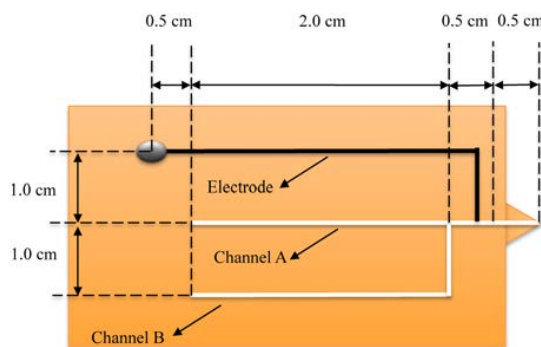


Figure 2-10. Illustration of the two-channel microchip emitter for ESI-MS. The channel A and B each have a cross-section size of $50\ \mu\text{m} \times 100\ \mu\text{m}$. The electrode was made in carbon paste with a cross-section size of $30\ \mu\text{m} \times 100\ \mu\text{m}$.

2.5. Karl Fischer titration for water determination

Karl Fischer titration^{17,18} is used to determine trace amounts of water in a sample, which was invented by Karl Fischer in 1935.¹⁷ The quantity of water in DCE was determined using a Radiometer TitrLab system consisting of a VIT90 Video Titrator, ABU91 Autoburette, and a SAM90 Sample Station. The Karl Fischer solvent was CombiMethanol, and the titrant was CombiTitrant 5, both purchased from Merck. A standard dead-stop end-point titration method was used, where the solvent and its container were titrated dry prior to sample addition to an end-point polarization voltage of a double-platinum electrode to which a constant current was applied. Sample volumes of 1 mL, 2 mL, and 5 mL were titrated and the determined quantities of water were found to increase in a linear fashion with the sample volume. It should be noted that this experiment was conducted by Tuomas Vainikka in the Department of Chemistry, Aalto University, Finland.

2.6. References

- (1) Olaya, A. J.; Schaming, D.; Brevet, P. F.; Nagatani, H.; Zimmermann, T.; Vanicek, J.; Xu, H. J.; Gros, C. P.; Barbe, J. M.; Girault, H. H. *J. Am. Chem. Soc.* **2012**, *134*, 498.
- (2) Samec, Z.; Mareček, V.; Koryta, J.; Khalil, M. W. *J. Electroanal. Chem. Interfacial Electrochem.* **1977**, *83*, 393.
- (3) Samec, Z.; Marecek, V.; Weber, J.; Homolka, D. *J. Electroanal. Chem.* **1979**, *99*, 385.
- (4) Samec, Z.; Mareček, V.; Weber, J. *J. Electroanal. Chem.* **1979**, *100*, 841.
- (5) Samec, Z. *Chem. Rev.* **1988**, *88*, 617.
- (6) Samec, Z. *Pure Appl. Chem.* **2004**, *76*, 2147.
- (7) Wittstock, G.; Burchardt, M.; Pust, S. E.; Shen, Y.; Zhao, C. *Angew. Chem., Int. Ed.* **2007**, *46*, 1584.
- (8) Kirchner, C. N.; Hallmeier, K. H.; Szargan, R.; Raschke, T.; Radehaus, C.; Wittstock, G. *Electroanalysis* **2007**, *19*, 1023.
- (9) Gao, F.; Yang, Y.; Liu, J.; Shao, H. *Ionics* **2010**, *16*, 45.
- (10) Su, B.; Nia, R. P.; Li, F.; Hojeij, M.; Prudent, M.; Corminboeuf, C.; Samec, Z.; Girault, H. H. *Angew. Chem., Int. Ed.* **2008**, *47*, 4675.

- (11) Su, B.; Hatay, I.; Ge, P. Y.; Mendez, M.; Corminboeuf, C.; Samec, Z.; Ersoz, M.; Girault, H. H. *Chem. Commun.* **2010**, 46, 2918.
- (12) Rahn, R. O.; Stefan, M. I.; Bolton, J. R.; Goren, E.; Shaw, P.-S.; Lykke, K. R. *Photochem. Photobiol.* **2003**, 78, 146.
- (13) Sellers, R. M. *Analyst* **1980**, 105, 950.
- (14) Karyakin, A. A. *Electroanalysis* **2001**, 13, 813.
- (15) Komkova, M. A.; Karyakina, E. E.; Marken, F.; Karyakin, A. A. *Anal. Chem.* **2013**, 85, 2574.
- (16) Hatay, I.; Ge, P. Y.; Vrubel, H.; Hu, X.; Girault, H. H. *Energy Environ. Sci.* **2011**, 4, 4246.
- (17) Fischer, K. *Angew. Chem., Int. Ed.* **1935**, 48, 394.
- (18) Xiao, C.; Weremfo, A.; Wan, C.; Zhao, C. *Electroanalysis* **2014**, 26, 596.

Chapter 3

Oxygen and Hydrogen Peroxide Reduction by 1,2-diferrocenylethane at a Liquid/Liquid Interface

Based on J. Electroanal. Chem. 2012, 681, 16.

3.1. Introduction

The charge transfer processes across the interface between two immiscible electrolyte solutions (ITIES) are of fundamental importance for a variety of applications such as in storage and conversion of energy, solvent extraction, electroanalysis, and life sciences.¹ Within the context of green energy, vital processes such as photosynthesis and respiration (*i.e.* oxygen reduction) taking place at the lipid bilayers of biomembranes can be studied at the ITIES. Oxygen reduction reaction (ORR) at the water/1,2-dichloroethane interface (W/DCE) has been studied for *ca.* 20 years and has been briefly reviewed in Section 1.3 in Chapter 1. This reaction could be considered as a proton-coupled electron transfer (PCET) reaction at the ITIES as the reduction of oxygen in DCE requires a suitable electron donor (D) in the oil phase and a proton source in the aqueous phase. However, it is very difficult to differentiate experimentally between the concerted and the stepwise pathways in a PCET reaction, as discussed in Section 1.3 in Chapter 1.² In this biphasic system the reaction rate is controlled by the proton concentration in the oil phase, which is determined by the Galvani potential difference across the interface that is conveniently controlled by modern electrochemical techniques.

ORR by metallocenes at liquid/liquid interface has been proposed to proceed in two steps: Galvani potential dependent proton transfer from the aqueous to the oil phase followed by a homogenous oxygen reduction in the oil phase. In the case of decamethylferrocene (DMFc) a formation of the protonated complex – DMFcH⁺ with the proton binding to the iron is the first step.³ Density functional theory (DFT) calculations suggest that instead of the coordination of a triplet molecular oxygen to the iron atom (spin-forbidden)⁴ or insertion into Fe–H bond, the reaction with oxygen proceeds through a delocalized triplet transition state, leading to the formation of DMFc⁺ and a hydrogen peroxy radical.³ Also, a mechanism where molecular oxygen is coordinated between two protonated ferrocenes has been proposed.⁵ This mechanism has some similarities with the oxygen reduction by cofacial metal

porphyrins,^{6,7} mimicking the oxygen reduction occurring in the bimetallic iron/copper center of cytochrome *c* oxidase.⁸ Because of this it was decided to study oxygen reduction by 1,2-diferrocenylethane, a multi-ferrocenyl compound, at the polarized water/DCE interface in this Chapter. This compound has been successfully used as an electron donor for electron transfer studies at the liquid/liquid interface,^{9,10} and previous NMR results indicate that protonation of both ferrocenyl groups should take place in boron trifluoride monohydrate solution.¹¹ Thus, ORR to hydrogen peroxide could take place with molecular oxygen sandwiched between the protonated centers. The experimental results show in fact, that two DFcE molecules are needed for two-electron oxygen reduction, and thus cast doubt on whether diprotonated DFcE is indeed formed in DCE. Hydrogen peroxide reduction is less well understood, as this reaction is mentioned only to explain the observed four-electron oxygen reduction.^{4,12} A mechanism suggested by Fomin indicates that the protonated ferrocene can react with H₂O₂ forming water, Fc⁺ and OH[•] radical, which further reacts with Fc and a proton to produce water.⁵ From this point of view, DFcE seems ideal for hydrogen peroxide reduction, as hydrogen peroxide can react with one protonated ferrocenyl group and then the generated OH[•] radical can easily oxidize the other ferrocenyl group. The experimental results obtained in this Chapter show that hydrogen peroxide reduction is faster than oxygen reduction, corroborating the proposed mechanism.

3.2. Experimental section

3.2.1. Chemicals

All chemicals used throughout this Chapter have been summarized in Section 2.2 in Chapter 2.

3.2.2. Two-phase reactions controlled by a common ion distribution (shake flask reactions)

Two-phase shake flask reactions for oxygen reduction were performed in a small flask under stirring. For these experiments, equal volumes (2 mL) of DCE and aqueous solutions containing the reactants (composition of both phases shown in Scheme 3-1) were mixed together and stirred vigorously.

5 mM BATB	5 mM LiTB
5 mM DFcE	50 mM H ₂ SO ₄
(DCE)	(aq)

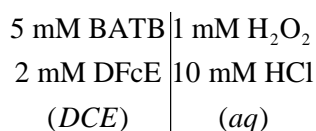
Scheme 3-1. Schematic representation of the initial compositions of the aqueous phase and the organic phase for studying oxygen reduction in a biphasic reaction.

After reaction, aqueous and organic phases were separated and the UV-Vis spectrum of the DCE phase was measured directly with an Ocean Optics CHEM2000

spectrophotometer with a quartz cuvette (path length: 10 mm). The aqueous phase was treated with the NaI¹³ and titanium oxalate¹⁴ methods which have been described in Section 2.4.1.1 in Chapter 2 to analyze the produced hydrogen peroxide.

To study the amount of DFcE consumed in the reaction, the ratio of different DFcE species was determined by measuring cyclic voltammograms (CVs) at a scan rate of 20 mV·s⁻¹ with a Pt (25 µm diameter), a carbon fiber (10 µm diameter) and a glassy carbon (10 µm diameter, Princeton Applied Research) ultramicroelectrodes (UMEs) with a CHI900 electrochemical workstation (CH Instruments, Austin, USA). Fabrication of the Pt and carbon fiber UMEs has been detailed in Section 2.3.4.2 in Chapter 2, according to the methodology developed by Gao *et al.*¹⁵ For comparison, CVs of a freshly prepared DCE solution of 5 mM DFcE under anaerobic conditions were also recorded. For achieving the anaerobic conditions the solution was degassed by bubbling pure N₂ through it for 30 min and then keeping a N₂ atmosphere over the solution during the voltammetric measurements. For recording the CVs, a three-electrode system with a Pt wire as the counter electrode and a Ag/AgTB wire as the reference electrode was employed. The potential scale was calibrated with the addition of decamethylferrocene (0.04 V vs. SHE in DCE¹⁶) at the end of the voltammetry experiments.

Hydrogen peroxide decomposition was investigated by having H₂O₂ solution in contact with DFcE in the DCE phase (Scheme 3-2), without a partition of a common ion. The reaction was monitored with UV/Vis spectroscopy and UME voltammetry.



Scheme 3-2. Schematic representation of the initial composition of the aqueous phase and the organic phase for studying hydrogen peroxide decomposition in a biphasic reaction.

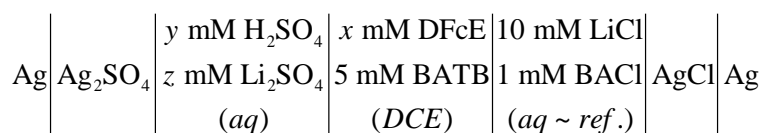
Hydrogen peroxide reduction was studied in a glove box with a nitrogen atmosphere, using the cell described in Scheme 3-3. For this, equal volumes of deoxygenated solutions were mixed together and stirred vigorously for 30 min, and the reaction products were analyzed as described above, with UV/Vis spectroscopy and UME voltammetry with a glassy carbon electrode.

	1 mM H ₂ O ₂
5 mM BATB	5 mM LiTB
2.6 mM DFcE	10 mM HCl
(DCE)	(aq)

Scheme 3-3. Schematic representation of the initial composition of the aqueous phase and the organic phase for studying hydrogen peroxide reduction in a biphasic reaction.

3.2.3. Electrochemical Measurements

All the electrochemical measurements were performed at ambient temperature (20±2 °C) under aerobic conditions in a Faraday cage. CVs at the W/DCE interface were obtained using an Autolab four-electrode potentiostat (PGSTAT 30, Ecochemie, the Netherlands). Two glass cells designed for liquid-liquid interface experiments with the interfacial area of 0.159 cm² (shown in Figure 1-7 in Chapter 1) or 1.53 cm² (shown in Figure 1-1 in Chapter 1) were used in the experiments. Two reference electrodes (Ag/Ag₂SO₄ or Ag quasi-reference electrode (AgQRE), and Ag/AgCl) were placed in Luggin capillaries to reduce the *iR* drop, and used for controlling the potential difference across the interface, while tungsten or platinum counter electrodes in both phases provided the current. The organic reference phase had a common cation with the supporting electrolyte of the organic phase, as described in Scheme 3-4. The potential was converted to the Galvani potential scale ($\Delta_o^w \phi$), based on CV measurement of the reversible half-wave potential $\Delta_o^w \phi_{TMA^+}^{1/2}$ of the TMA⁺ ion transfer (0.16 V in DCE¹⁷).



Scheme 3-4. Schematic depiction of the electrochemical cell composition used in the four-electrode configuration.

3.3. Results and discussion

3.3.1. Redox properties of DFcE

The redox properties of DFcE in DCE were studied by cyclic voltammetry as shown in Figure 3-1. From this figure, it can be seen that DFcE has two oxidation waves corresponding to DFcE⁺/DFcE and DFcE²⁺/DFcE⁺ in DCE with the half-wave potentials $E_{1/2}$ at 0.565 V and 0.770 V vs. SHE (*i.e.* $E_{1/2}$ separation 205 mV), respectively. It has been reported previously for DFcE in dichloromethane a $E_{1/2}$ separation of 180 mV, when TB[−] was used as a counter anion.¹⁸ The fact that two consecutive oxidation waves (*i.e.* one electron transfer for each wave) are observed

for DFcE in cyclic voltammetry instead of a single two-electron transfer process, indicates that strong intramolecular electronic communication between the two ferrocenyl groups in the same reactant molecule occurred.¹⁹ When one of the two ferrocenyl groups is oxidized, the electron-withdrawing monocation DFcE⁺ is formed, which leads to the oxidation of the second ferrocenyl group to the dication, DFcE²⁺, at a more positive potential. Accordingly, the strong electrostatic interaction between the positively charged ferrocenyl groups (*via* stepwise oxidation) results in significant wave separation as shown in Figure 3-1.²⁰ The latter is further explained by the effect that the employed solvent and supporting electrolyte have on the separation of the two oxidation waves. Generally, more strongly coordinating anions like ClO₄⁻, BF₄⁻ and PF₆⁻ are able to stabilize the formed monocations by ion-pairing, offsetting the electron-withdrawing effect of DFcE⁺ toward the other ferrocenyl group and decreasing the difference between the observed half-wave potentials of the two oxidation waves. Contrarily, the use of weakly coordinating anions like TB⁻ increases the separation of the observed half-wave potentials. The solvent has a similar effect: highly polar solvents like dimethyl sulfoxide and solvents with significant donor character (for example tetrahydrofuran, donor number = 20) are also able to stabilize the formed monocations, making the second oxidation easier to take place.²¹ For example, in a polar solvent like dimethylformamide, DFcE has only one oxidation wave when ClO₄⁻ is used as a counter anion.²²

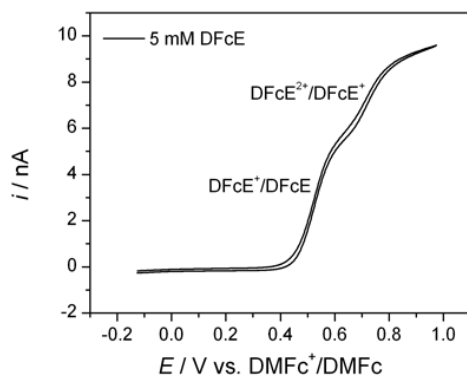


Figure 3-1. Cyclic voltammogram (20 mV·s⁻¹) of freshly prepared 5 mM DFcE solution under N₂ atmosphere on a carbon fiber UME (diameter = 10 μm). The potential scale was referred to the DMFc⁺/DMFc couple.

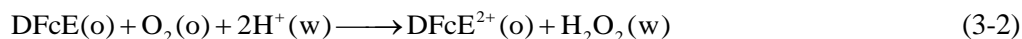
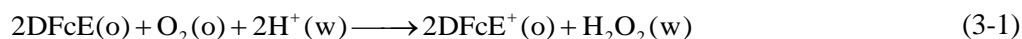
Voltammetry measurements show that the formal potential of DFcE species (0.565 and 0.770 V *vs.* SHE) is not low enough for proton reduction to occur in the oil phase (standard redox potential of 0.55 V *vs.* SHE in DCE²³), but oxygen reduction in the presence of protons (standard redox potential of 1.17 V *vs.* SHE for hydrogen peroxide and 1.75 V *vs.* SHE for water in DCE²⁴) by DFcE and DFcE⁺ is thermodynamically feasible. However, the reduction of oxygen to the superoxide is

highly unfavorable (standard redox potential of -0.81 V vs. SHE in DCE²⁵). This point will be detailed in section 3.3.2.1. The limiting currents measured on a $10\text{ }\mu\text{m}$ carbon fiber UME were used to evaluate the diffusion coefficients of the neutral and DFcE^+ species as 5.8 and $3.7 \times 10^{-6}\text{ cm}^2\text{ s}^{-1}$, respectively.

3.3.2. Two-phase reactions controlled by a common ion distribution

3.3.2.1. Oxygen reduction

Oxygen reduction by DFcE is described by equations 3-1 or 3-2. Ferrocene derivatives also catalyze decomposition and also further reduce hydrogen peroxide, as described by equations 3-3 and 3-4.



The reduction of O_2 by DFcE was investigated by shake-flask experiments, where the Galvani potential difference across the interface is controlled by a common ion distribution. When TB^- was used as a common ion, the Galvani potential difference is fixed at a potential greater than 0.59 V, so that protons are extracted to oil phase. A fresh solution of DFcE in DCE has a brown color and displays an absorption band in the UV/Vis spectrum at $\lambda_{\text{max}} = 436$ nm (dotted curve in Figure 3-2). After the two-phase shake flask reaction (*i.e.* reaction time = 10 min), the DCE phase turned dark green, and a broad absorption band at $\lambda_{\text{max}} = 619$ nm (dash-dotted curve in Figure 3-2) corresponding to DFcE^+ was observed. The presence of H_2O_2 in the aqueous solution after the shake-flask reaction was confirmed with the NaI and titanium oxalate (data not shown) methods, as represented by the appearance of the I_3^- characteristic absorption band at $\lambda_{\text{max}} = 352$ nm (solid curve in Figure 3-2). On the contrary, no signal was observed in the UV/Vis spectrum for the aqueous phase before the biphasic reaction (dashed curve in Figure 3-2).

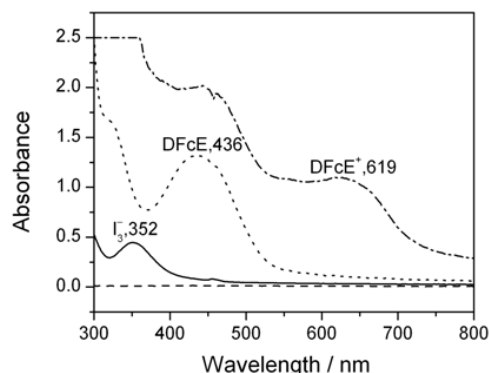


Figure 3-2. UV/Vis spectra of the aqueous phase before (control, dashed line) and after (target, solid line) 10 min of aerobic two-phase reaction under stirring conditions: both of the aqueous solutions (control and target) were treated with 0.1 M NaI prior to UV/Vis measurements. The dotted and dash-dotted traces correspond to the UV/Vis spectra of DFcE solutions in DCE before and after 10 min of aerobic two-phase reaction under stirring conditions (diluted by half), respectively. For the two-phase reaction: the aqueous phase contained 50 mM H₂SO₄ + 5 mM LiTB (2 mL); the DCE phase contained 5 mM DFcE + 5 mM BATB (2 mL).

Formation of the DFcE⁺ cation was also confirmed by the cyclic voltammograms of a carbon fiber (diameter = 10 μm) and a Pt (diameter = 25 μm) UMEs in the isolated DCE phase after shake-flask reaction, as illustrated in Figure 3-3. After 10 min of shake-flask reaction, three steady-state current waves, namely DFcE²⁺ ↔ DFcE⁺, DFcE⁺ ↔ DFcE, and H⁺ → ½H₂ were observed at the DMFc⁺/DMFc potential scale. The percentage of DFcE oxidized to DFcE⁺ could be calculated from the first oxidation wave of DFcE to be about 20%, so *ca.* 1 mM DFcE⁺ was generated during the reaction. The sum of the magnitudes of cathodic and anodic current for DFcE⁺ ↔ DFcE is close to that of freshly prepared DFcE in DCE (data not shown) showing almost no DFcE²⁺ was produced in the time scale of this experiment. Also, the half-wave potential $E_{1/2}$ for H⁺ reduction at a carbon UME is about 577 mV more negative than that at a Pt UME, as observed in Figure 3-3. This makes carbon UMEs more suitable for studying the products of this reaction. The selectivity for the production of hydrogen peroxide over water was less than 6%, calculated based on the amount of produced hydrogen peroxide and the amount of consumed DFcE.

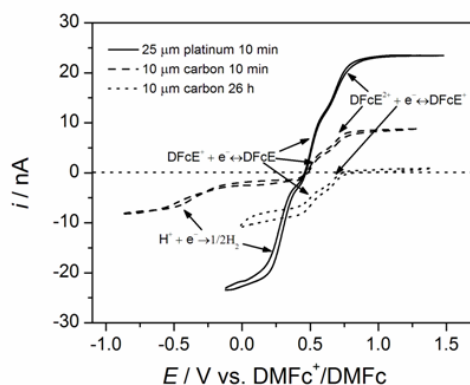
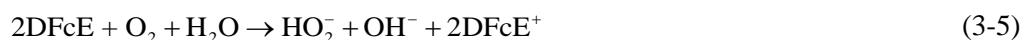


Figure 3-3. Cyclic voltammograms at a Pt (diameter = 25 μm , solid line) and a carbon fiber UME (diameter = 10 μm) located in DCE solution containing 5 mM DFCE and 5 mM BATB after 10 min (dashed line) of the two-phase shake flask reaction under aerobic conditions, in which the potential scale was referred to the $\text{DMFc}^+/\text{DMFc}$ couple. For comparison, cyclic voltammogram of $\text{DFcE}^{2+}/\text{DFcE}^+$ solution obtained by 26 h shake flask experiment (dotted line) under aerobic conditions on a carbon fiber UME (diameter = 10 μm) is included. Scan rate is $20 \text{ mV}\cdot\text{s}^{-1}$. The horizontal line depicts the position of zero current.

A shake flask experiment with $\text{LiTB}:\text{DFcE}$ (5 mM DFCE) molar ratio of 4 was performed for 48 hours, and the conversion of DFCE was monitored by voltammetry with a carbon fiber UME during reaction. About half of the DFCE had been oxidized to DFcE^+ after 1 hour, but further oxidation to DFcE^{2+} took much longer time. After 18 hours about half of the DFCE was converted to DFcE^{2+} , and the reaction was not complete until after 26 hours of reaction (see Figure 3-3). Results show that the kinetics of oxygen reduction by DFCE is very slow, and the produced DFcE^+ is also able to reduce oxygen, although at even slower rate, as expected from the higher redox potential. Ferrocene derivatives have been shown to catalyze the decomposition of hydrogen peroxide, and they may also be able to further reduce hydrogen peroxide.¹² Thus, with such a long time scale the reactions with hydrogen peroxide are not negligible, and the exact efficiency of hydrogen peroxide production cannot be evaluated from shake flask experiments. The CV of the organic phase after 26 hours of reaction shown in Figure 3-3 demonstrates that the complete oxidation of DFCE to DFcE^{2+} is possible. The diffusion coefficient of DFcE^{2+} calculated from the first steady-state cathodic process observed with this solution (dotted line in Figure 3-3) is equal to $3.8 \times 10^{-6} \text{ cm}^2\text{s}^{-1}$, almost the same as that of DFcE^+ .

A control shake-flask experiment without aqueous acid (Scheme 3-1, without aqueous H_2SO_4) under aerobic conditions was also conducted (reaction time 10 min, data not shown). The color of DCE phase turned slightly green after the two-phase shake flask reaction, while the characteristic absorption peaks both for DFcE^+ in DCE phase and that for I_3^- in aqueous are not evident, indicating that the reaction is even slower in the absence of aqueous additional acid. The CV recorded with a glassy carbon UME (10 μm diameter) showed that *ca.* 9.7% of DFCE was oxidized, while

this value was about 20% with 50 mM H_2SO_4 in the aqueous phase. The pH in aqueous phase increased from initial value of 7.72 (5 mM LiTB) to 9.68 during the experiment. The reaction can be described as the oxygen reduction in alkaline conditions (equation 3-5). From the experimental point of view, it is not easy to distinguish between the reaction going through the superoxide and the one producing HO_2^- by a single direct reaction, but thermodynamically superoxide step is highly unfavourable, and thus less likely than the HO_2^- pathway. The protons present in the aqueous phase are extracted into the oil phase by TB^- and more water will dissociate to protons and OH^- to keep the system in equilibrium. As the concentration of protons at aqueous $\text{pH} > 7$ is very small, this extraction is slow. Protons react with oxygen and DFCe in the oil phase, and hence more protons are extracted to keep the distribution of ions between both phases at equilibrium. The concentration of OH^- increases in the aqueous phase, increasing the pH.



It should be noted that under aqueous acidified conditions, reaction in equation 3-5 will be the same as described in equation 3-1. Besides, this explanation was what we thought while the paper was being published, but in fact the lithium acidity in the organic phase is responsible for this reaction that will be discussed in Chapter 7.

3.3.2.2. Hydrogen peroxide decomposition and reduction

The effect of hydrogen peroxide decomposition on the observed selectivity for two-electron oxygen reduction was studied by mixing equal volumes of DCE solution containing DFCe and aqueous hydrogen peroxide solution in a vial (Scheme 3-2). The amount of hydrogen peroxide determined with TiOx method decreased by 5% after 10 minutes and 76% after 60 minutes (in separate experiments). The aqueous phase turned slightly bluish after 60 min experiment, indicating that DFCe partitions into the aqueous phase and reduces hydrogen peroxide to form DFcE^+ . No oxidation of DFCe in the DCE phase was observed, but the amount of DFCe in DCE decreased significantly, 4% after 10 minutes and 30% after 60 minutes, confirming that DFCe partitions into the aqueous phase where it reduces hydrogen peroxide. However, partition coefficient ($\log P^\circ$) of DFCe between DCE and water was determined to be 37.96 (see section 3.3.3), so the equilibrium concentration of DFCe in water is negligible. So, the evident loss of DFCe in DCE phase after the reaction can only be explained as the dynamic partition of DFCe driven by the reaction occurred in the aqueous phase. Thus, 30% of DFCe lost from the DCE phase (0.6 mM) after 60 min of reaction is oxidized to DFcE^+ by stoichiometric amount of 0.3 mM of hydrogen peroxide. This accounts for 40% of the loss of H_2O_2 , and the rest is lost by decomposition. Hydrogen peroxide is also slightly partitioning into the DCE phase, but further reduction is now impossible as no protons are available in the DCE phase.

Hydrogen peroxide reduction was investigated in the absence of oxygen, in a glove box. 2 mL of DCE solution was mixed with 2 mL of hydrogen peroxide solution and

stirred vigorously for 30 minutes (Scheme 3-3). The oil phase was analyzed with UME voltammetry and UV/Vis spectroscopy before and after the reaction, and the hydrogen peroxide was analyzed with TiOx and NaI –methods. Now 45% of DFcE (1.2 mM) was oxidized to DFcE⁺, and DFcE⁺ peak was clearly observed in UME voltammetry and UV/Vis spectra of the DCE phase (Figure 3-4 and Figure 3-5). 96% of hydrogen peroxide was consumed (93% when analyzed with TiOx method) during the reaction. As the stoichiometric amount of reduced hydrogen peroxide would be 0.6 mM or 60% (eq. 3-4), part of the hydrogen peroxide was decomposed during the reaction (eq. 3-3). Now this reaction can take place in both phases, as protons and DFcE (even though negligible in aqueous phase) are both available everywhere in the system. However, the reaction is thermodynamically more favorable in the oil phase (standard redox potential of 2.31 V vs. SHE in DCE and 1.76 V vs. SHE in water²⁵), and proceeds much faster than observed in the absence of LiTB (60% of H₂O₂ reduced after 30 minutes vs. 30% of H₂O₂ reduced after 60 minutes in the absence of LiTB). Again, lithium acidity in the DCE phase may be a minor contributor to these results. In comparison, 60 min aerobic shake flask reaction with 2 mM DFcE + 5 mM BATB and 5 mM LiTB + 10 mM HCl had only a 33% conversion of DFcE to DFcE⁺, indicating that hydrogen peroxide reduction by DFcE is faster than oxygen reduction. This explains why so small amounts of hydrogen peroxide are detected in the shake flask experiments, as oxygen is firstly reduced to hydrogen peroxide, followed by faster hydrogen peroxide reduction step.

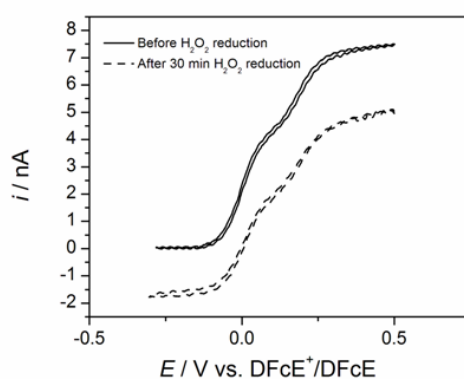


Figure 3-4. Cyclic voltammograms (with 10 μ m diameter glassy carbon UME) of 2.6 mM DFcE + 5 mM BATB in DCE before (solid line) and after (dashed line) 30 min biphasic hydrogen peroxide reduction inside a glove box. The potential scale was calibrated with respect to the DFcE⁺/DFcE couple.

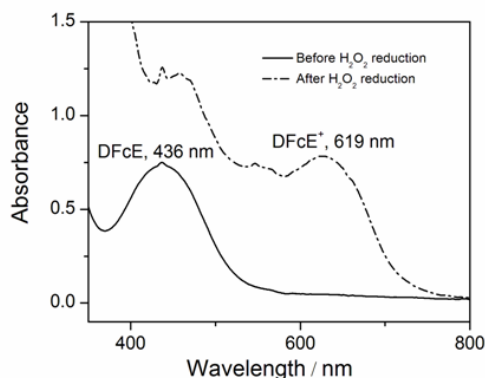


Figure 3-5. UV/Vis spectra of 2.6 mM DFcE + 5 mM BATB in DCE before (solid line) and after (dash-dotted line) 30 min biphasic hydrogen peroxide reduction inside a glove box.

Ferrocene and its derivatives have been used as electron donors for oxygen reduction in the absence¹² or presence of catalysts,²⁶⁻²⁸ but these results show that certain care has to be taken when determining the selectivity of oxygen reduction to water, as the electron donor itself can reduce hydrogen peroxide, thus increasing the observed apparent selectivity of the catalyst towards four-electron reduction of molecular oxygen. This ability to reduce hydrogen peroxide is expected to be even stronger in the case of stronger reductants like decamethylferrocene, so control experiments both for hydrogen peroxide reduction and decomposition should always be performed.

3.3.3. Four electrode cell measurements

The CVs obtained with the four-electrode electrochemical cell described in Scheme 3-4 are shown in Figure 3-6.

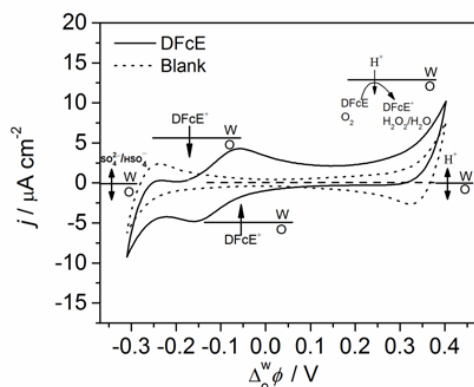


Figure 3-6. Cyclic voltammograms obtained with the electrochemical cell shown in **Scheme 3-4** in the absence of DFcE (dotted line, aerobic, $x = 0$, $y = 50$, $z = 10$) and in the presence of DFcE (solid line, aerobic, $x = 5$, $y = 50$, $z = 10$) in the DCE phase; scan rate: $50 \text{ mV} \cdot \text{s}^{-1}$.

When $\text{H}_2\text{SO}_4/\text{Li}_2\text{SO}_4$ and BATB were used as the hydrophilic and hydrophobic electrolytes in aqueous and DCE phases respectively, a polarized potential window (PPW) from about -0.30 to 0.40 V in the Galvani potential scale at aqueous $\text{pH} = 1$ can be obtained, as displayed by the cyclic voltammogram shown in Figure 3-6 (dotted line). The potential window is limited by the transfer of H^+ and $\text{HSO}_4^-/\text{SO}_4^{2-}$ from water to DCE at positive and negative potentials (*i.e.* water vs. DCE), respectively.

Under aerobic conditions, the current increased remarkably on the positive limit of the potential window upon addition of 5 mM DFCE, and no clear return peak was observed for the transferred protons (solid line in Fig. 3-6), indicating that they were consumed in a homogeneous reaction according to eq. 3-1 or 3-2. The apparent heterogeneity in eq. 3-1 or 3-2 is caused by the fact that oxygen reduction in DCE occurs only at Galvani potentials where proton transfer is feasible. From a mechanistic point of view, it has been proposed that the first step in the oxygen reduction at the ITIES is the protonation of the electron donor.²⁹ This is observed as an apparently facilitated proton transfer from aqueous to oil phase by the electron donor acting as a ligand (L), being displayed as a negative shift of the onset potential of proton transfer (solid line in Figure 3-6). The Nernst equation for this facilitated proton transfer process can be described as shown in eq. 3-6:³⁰

$$\Delta_o^w \phi_{\text{LH}^+}^{1/2} = \Delta_o^w \phi_{\text{H}^+}^{\circ'} + \frac{RT}{2F} \ln \left(\frac{D_{\text{L}}}{D_{\text{LH}^+}} \right) - \frac{2.303RT}{F} \text{p}K_a + \frac{2.303RT}{F} \text{pH}^w \quad (3-6)$$

where $\Delta_o^w \phi_{\text{LH}^+}^{1/2}$ and $\Delta_o^w \phi_{\text{H}^+}^{\circ'}$ are the formal transfer potentials of LH^+ and H^+ (0.55 V at the W/DCE interface), respectively. LH^+ stands for the protonated complex, D represents the diffusion coefficient of species in the oil phase, K_a is the equilibrium constant of the protonation reaction of L and pH^w is the aqueous pH. However, this explanation was made at the time of the paper published.

But in fact it was shown later (Chapters 5 and 6) that the proton affinity of ferrocene derivatives was rather low, the apparently facilitated proton transfer observed here was more likely a consequence of the following chemical reaction triggered by the interfacial proton transfer. So eq. 3-6 should be replaced by the Nernst equation for a simple ion transfer. Alternatively, the current feature at the positive potential limit (solid line in Fig. 3-6) can also be explained as the proton assisted electron transfer from DFCE in DCE phase to oxygen in aqueous phase. But, this would be a trimolecular reaction scheme that be deemed more unlikely.

Anyway, the ITIES essentially functions as a proton pump. The next step is the reduction of oxygen by the formed protonated complex homogeneously to produce hydrogen peroxide or water. This whole process has been sketched at the positive potential range for the solid line of Figure 3-6. It has been demonstrated that proton can bind at the iron core of ferrocene derivatives during oxygen reduction.³¹ The mechanism for the formation of the protonated complex can be described by “transfer followed by organic phase complexation (TOC)”.³²

The transfer of DFcE^+ generated in the oxygen reduction is observed in the range of -0.2 to -0.05 V with the half-wave potential at -0.12 V, and the onset potential of the proton transfer took place at lower potentials with respect to the blank. A small current resulting from proton transfer from the oil phase after reversal of the scan direction at around 0.4 V shows that oxygen reduction is not fast enough to consume all the transferred protons in the time scale of the experiment. Similar results have been reported previously by Su *et al.* when DMFc was used as electron donor for the oxygen reduction at the ITIES.³³ The forward current enhancement by DFcE is less than that by DMFc, indicating most likely slower kinetics due to the difference in electrochemical driving force (0.04 V for DMFc *vs.* 0.57 V for DFcE *vs.* SHE). In effect, DFcE acts as a lipophilic base to complex H^+ at the oil side of the ITIES during the forward potential scan, while the polarized ITIES acts as a pump to drive H^+ transfer from aqueous to organic phase.

Figure 3-7 illustrates the pH dependence of the present system, in which the onset potential for the H^+ transfer shifts positively with the increasing aqueous pH. It can be noticed that the PPW decreases as the aqueous pH decreases, thereby confirming that the potential window is limited by the transfer of H^+ and $\text{HSO}_4^-/\text{SO}_4^{2-}$.

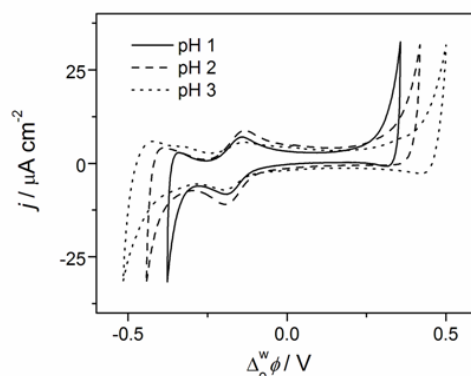


Figure 3-7. Cyclic voltammogram showing the pH dependence of assisted proton transfer by DFcE under aerobic conditions. The electrochemical cell employed was shown in **Scheme 3-4** ($x = 5$, $y = 50$, 5 , 0.5 corresponding to pH 1, 2, 3 of aqueous phase, respectively, $z = 0$). Scan rate = $50 \text{ mV} \cdot \text{s}^{-1}$.

The scan rate dependence of the electrochemical signal observed by CV was also investigated (see Figure 3-8), showing that the current magnitude for both DFcE^+ transfer and the H^+ transfer increases with the increase in the scan rate. Specifically, it is proportional to the square root of the scan rate (see inset in Figure 3-8). This scan rate dependence indicates the overall process is limited by the linear diffusion of DFcE^+ or H^+ transfer to the interface. Besides, the CVs in Figure 3-8 show a so-called “Osakai mechanism”,³⁴ represented by a positive current offset between 0.1 and 0.3 V that increases with increasing scan rate. The latter indicates that DFcE partitions between the two phases and reacts with aqueous protons and oxygen, forming DFcE^+

that is transferred back to oil phase at potentials higher than the observed half-wave potential for DFcE^+ transfer and thus producing a positive current offset in the CVs. A similar behavior has been observed for DMFc system.²⁵ It should be noted that an overlap between the current due to the DFcE^+ transfer from aqueous to DCE phase and the onset current at the positive potential limit might also account. But until now it is difficult to differentiate experimentally between these two mechanisms. Moreover, the increasing currents resulting from the transfer of protons from oil to aqueous phase with the scan rate during the reverse scan at 0.3-0.4 V indicate that the kinetics of ORR in DCE is not fast.

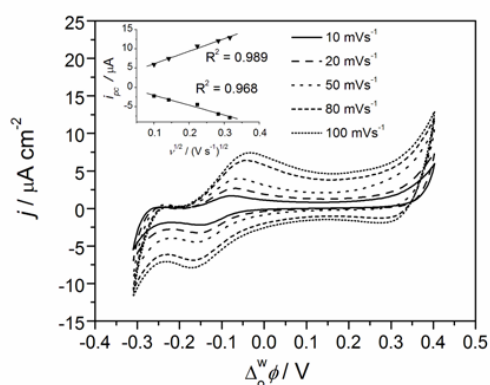


Figure 3-8. Cyclic voltammograms obtained with the electrochemical cell shown in **Scheme 3-4** in the presence of DFcE (aerobic, $x = 5$, $y = 50$, $z = 10$) at various scan rates: 10, 20, 50, 80, 100 $\text{mV} \cdot \text{s}^{-1}$ from inner to outer. The inset shows the dependence of the cathodic peak current (square) and the assisted proton transfer current at 0.4 V (triangle) on the square root of the scan rate.

The uncompensated resistance broadens the observed peak of DFcE^+ -transfer, but if the peak potentials are plotted as a function of the scan rate and extrapolated to zero scan rate, the peak separation approaches 68 mV (Figure 3-9), confirming that the observed species is indeed DFcE^+ . Potential was scanned to even more positive potentials to see if any additional peaks from the formation of DFcE^{2+} or DFcE-H^+ could be observed, but the only effects were the increase of the proton back transfer peak and the peak of DFcE^+ -transfer, confirming that formation of DFcE^{2+} is slow. This is probably due to the low proton affinity of the DFcE-H^+ : second protonation of the molecule is not likely to take place due to the repulsion of the positive charge of DFcE-H^+ , but instead the proton will favor association with free DFcE or TB^- .

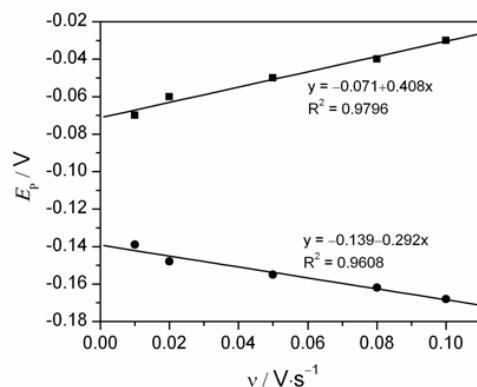


Figure 3-9. The relationship between peak potentials displayed in **Figure 3-8** and the scan rate, in which the linear regression equations are included.

The 0.1 mM DFcE²⁺ DCE solution prepared by 26 h biphasic reaction was studied in a four-electrode cell. The comparison of CVs of DFcE and DFcE²⁺ solutions are shown in Figure 3-10.

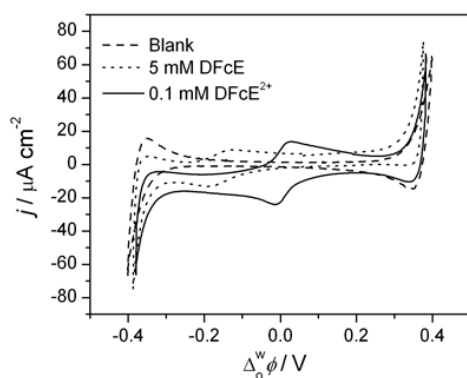


Figure 3-10. Comparison of iR compensated voltammograms of 5 mM DFcE (dotted line) and 0.1 mM DFcE²⁺ (solid line) solutions in the electrochemical cell described in **Scheme 3-4** (aerobic, $y = 50$, $z = 0$). For comparison, blank CV recorded with iR compensation in the electrochemical cell described in **Scheme 3-4** (dashed line, aerobic, $x = 0$, $y = 50$, $z = 0$) is also included. Scan rate = $50 \text{ mV} \cdot \text{s}^{-1}$.

Figure 3-10 shows the peaks for reversible transfer of DFcE⁺ (formed after ORR, where the initial species in DCE is DFcE) and DFcE²⁺ across the W/DCE interface at -0.16 V and 0.00 V , respectively. DFcE⁺ was formed according to equation 3-1, as described earlier. The peak separation of the transfer peak of DFcE²⁺ was about 30 mV, confirming that the transferred species had a charge equal to 2. The peak current

of DFcE^{2+} transfer depended on the square root of the scan rate. The standard Gibbs free energy of transfer for both ionic species was estimated with eq. 3-7.

$$\Delta G_{\text{tr}}^{\circ, \text{w} \rightarrow \text{o}} = z_i F \Delta_o^{\text{w}} \phi^{\circ} \approx z_i F \Delta_o^{\text{w}} \phi^{\circ} \quad (3-7)$$

The transfer energy of the ionic species can also be calculated for example with the theoretical model of Born (eq. 3-8) or Abraham-Liszi, or with a semi-empirical model by Osakai *et al.*³⁵

$$\Delta G_{\text{tr, ion}}^{\circ, \text{w} \rightarrow \text{o}} = \frac{N_A z^2 e^2}{8\pi\epsilon_0 r} \left(\frac{1}{\epsilon_o} - \frac{1}{\epsilon_w} \right) \quad (3-8)$$

where N_A is Avogadro's constant, e is the elementary charge, z is the charge number of the ion with the sign, ϵ_0 is the permittivity of vacuum, and ϵ_w and ϵ_o are the relative permittivity of aqueous and oil phase, respectively taken as 78.54³⁵ and 10.42.³⁶ The radius of 1,2-diferrocenylethane was estimated to be close to 10 Å (Crystallographic radius of ferrocene is reported as 3.65 Å³⁷ and the length of the ethane chain is three times C-C bond length of 1.54 Å³⁸). Eq. 3-8 is divided into two terms, shown in Eq. 3-9, in which $\Delta G_{\text{tr, neutral}}^{\circ, \text{w} \rightarrow \text{o}}$ is the charge-independent term and $\Delta G_{\text{tr}}^{\circ, \text{w} \rightarrow \text{o}}$ (charge dependent) is the charge-dependent term.³⁹ $\Delta G_{\text{tr, neutral}}^{\circ, \text{w} \rightarrow \text{o}}$ can be evaluated employing the semi-empirical Uhlig formula,⁴⁰ shown in Eq. 3-10, in which $\sigma_{\text{o/w}}$ is the interfacial tension between DCE and water taken as 28.6 mN m⁻¹.⁴¹ Eq. 3-10 was used to calculate the standard Gibbs transfer energy of the neutral species – DFCE, and the standard partition coefficient of DFCE ($\log P^{\circ}$) between DCE and water was calculated with eq. 3-11.⁴²

$$\Delta G_{\text{tr, ion}}^{\circ, \text{w} \rightarrow \text{o}} = \Delta G_{\text{tr, neutral}}^{\circ, \text{w} \rightarrow \text{o}} + \Delta G_{\text{tr}}^{\circ, \text{w} \rightarrow \text{o}} \text{ (charge dependent)} \quad (3-9)$$

$$\Delta G_{\text{tr, neutral}}^{\circ, \text{w} \rightarrow \text{o}} = -4\pi N_A r^2 \sigma_{\text{o/w}} \quad (3-10)$$

$$\log P^{\circ} = -\frac{\Delta G_{\text{tr, neutral}}^{\circ, \text{w} \rightarrow \text{o}}}{2.3RT} \quad (3-11)$$

The difference of the transfer energies of DFcE^{2+} and DFcE^{+} was calculated to be 17.3 kJ/mol (using eq. 3-8), while the measured value was 16.6 kJ/mol (using eq. 3-7). The values are in reasonable agreement with each other, but it has to be taken into account that eq. 3-8 is very sensitive to the molecular radius, and the accurate estimation of that is uncertain. $\log P^{\circ}$ for DFCE was determined as 37.96 employing eqs. 3-10 and 3-11.

As shown above, the ORR at the ITIES by DFCE is rather slow. However, when a catalyst like $\text{Co}_2(\text{DPOx})$ is added to the system, the oxygen reduction reaction is much

faster, as indicated by the absence of proton transfer from oil to aqueous phase during the reverse scan (Figure 3-11).

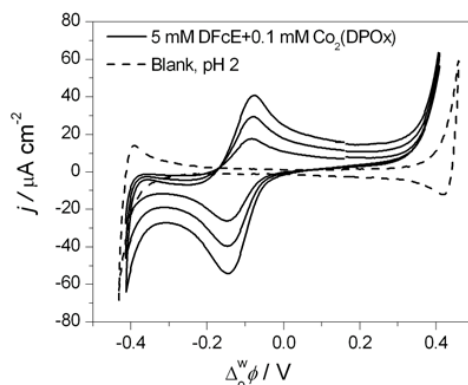


Figure 3-11. The iR compensated cyclic voltammograms (solid lines) at the W/DCE interface between 5 mM DFCE + 0.1 mM $\text{Co}_2(\text{DPOx})$ + 5 mM BATB in DCE and 5 mM H_2SO_4 in aqueous phase using the four-electrode cell (all other conditions are shown in **Scheme 3-4**, aerobic, $z = 0$), with the scan rates of 10, 25 and 50 $\text{mV}\cdot\text{s}^{-1}$ from inner to outer. For comparison, blank CV (scan rate = 50 $\text{mV}\cdot\text{s}^{-1}$) with iR compensation recorded in the electrochemical cell described in **Scheme 3-4** (dashed line, aerobic, $x = 0$, $y = 5$, $z = 0$) is also included.

Moreover, only the transfer of DFCE^+ is observed, and that depends linearly on the square root of the scan rate, confirming that the oxidation of DFCE^+ is slow even in the presence of a catalyst. Now a typical scan rate independent PCET peak is observed at the positive limit of the potential window. Also, the positive offset of current at 0.1-0.3 V indicates to the presence of “Osakai mechanism”, as in the case without the catalyst shown in Figure 3-8. The mechanism of oxygen reduction by cofacial porphyrins is discussed in detail in refs..^{6,26} Briefly, the cofacial porphyrin coordinates the molecular oxygen between the metal centers, activating the O–O bond. This is followed by protonation of the complex accompanied with electron transfer steps, resulting in oxygen reduction to water or hydrogen peroxide. Now DFCE acts only as a source of electrons. The catalyst has two roles in the system: it facilitates the proton transfer and activates the molecular oxygen.⁴³ More details on the mechanism of oxygen reduction catalyzed by cofacial porphyrins at liquid/liquid interfaces have been discussed by Peljo *et al.*⁴⁴ and this is not the focus in this chapter.

The measured standard transfer potentials/energies, formal redox potentials and diffusion coefficients of all the species are tabulated in Table 3-1.

Table 3-1. Diffusion coefficients (D), formal oxidation potential of vs. SHE in DCE ($E^{\circ'}$), the formal transfer potentials ($\Delta_\phi^{\text{w}} \phi^{\circ'}$) and standard Gibbs free energies of transfer from water to DCE ($\Delta G_{\text{tr}}^{\circ, \text{w} \rightarrow \text{o}}$) for all observed species of DFCE.

	$D \times 10^6 (\text{cm}^2 \text{s}^{-1})$	$E^{\circ'} (\text{V})$ vs. SHE	$\Delta_o^w \phi^{\circ'} (\text{V})$	$\Delta G_{\text{tr}}^{\circ, w \rightarrow o} (\text{kJ mol}^{-1})$
DFcE	5.8	0.565	–	–
DFcE ⁺	3.7	0.77	–0.162	–15.6
DFcE ²⁺	3.8	–	0.005	0.96

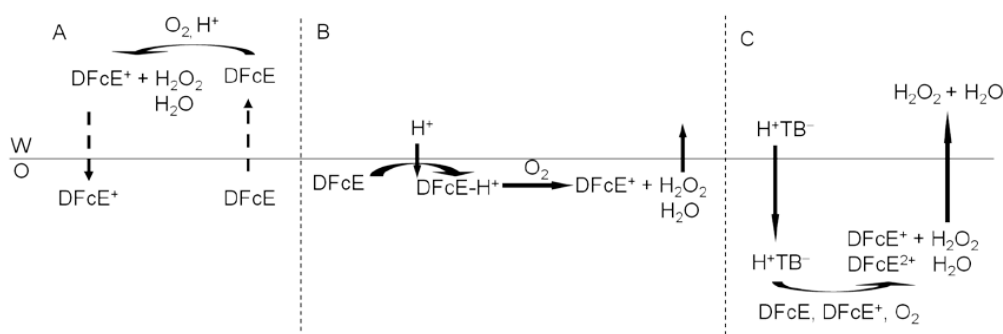
3.3.4. Mechanism

The measurements indicate that oxygen reduction by DFcE does not proceed through oxygen molecule sandwiched inside the two protonated iron centers of DFcE, as hypothesized by Fomin,⁵ as no DFcE²⁺ is observed in four-electrode cell measurements. Thus it is more likely that the reaction proceeds as proposed by Girault *et al.* for decamethylferrocene through a delocalized triplet transition state, leading to the formation of DFcE⁺ and a hydrogen peroxy radical.³ Hydrogen peroxy radical will then react fast with DFcE and H⁺ to form H₂O₂. Alternatively, the reaction could still proceed through molecular oxygen located between two DFcE–H⁺ molecules, but this would require a trimolecular reaction deeming it more unlikely. Another interesting question is, whether the electron is donated by the protonated iron or the non-protonated one. In this case, probably the protonation will take place outside of the molecule due to the steric hindrance of the other ferrocenyl group, and thus the non-protonated iron would be too far to have an effect on the reaction.

Hydrogen peroxide reduction by ferrocene derivatives has been briefly mentioned previously in the literature to explain observed four-electron reduction of molecular oxygen but it has been less well studied.^{4,12} A mechanism for ferrocene oxidation by hydrogen peroxide suggested by Fomin indicates that the protonated ferrocene can react with H₂O₂ to form water, Fc⁺ and OH[•] radical, which further reacts with Fc and a proton to produce water.⁵ From this point of view, DFcE seems ideal for hydrogen peroxide reduction, as hydrogen peroxide can react with the protonated ferrocenyl group and the generated OH[•] radical can then easily oxidize the other ferrocenyl group. The experimental results show that hydrogen peroxide reduction is faster than oxygen reduction, corroborating the proposed mechanism.

Taking into account all the previous results, it can be proposed that O₂ reduction by DFcE can take place near the W/DCE interface or in the bulk DCE phase (see Scheme 3-5B). The first step consists of the protonation of DFcE to form the DFcE–H⁺ in DCE phase, as observed with other metallocenes. Then, the formed DFcE–H⁺ is attacked by dissolved O₂ in DCE side at the W/DCE interface or in the DCE bulk to produce H₂O₂ or water and DFcE⁺. Hydrogen peroxide reduction is assumed to proceed in a similar manner, but the reaction is assumed to take place close to the interface due to the small solubility of H₂O₂ in DCE.

DFcE can also partition into the aqueous phase and react with aqueous oxygen (see Scheme 3-5A) or hydrogen peroxide (not shown), as shown by H_2O_2 decomposition experiments. In that case no protons were present in DCE, so the observed DFcE^+ in aqueous phase was the reaction product of H_2O_2 reduction by partitioned DFcE. In biphasic shake-flask experiments, the protons are extracted to the oil phase by TB^- . This fast extraction is followed by slower oxygen reduction initially by DFcE and later by DFcE^+ in the bulk DCE phase (see Scheme 3-5C). From voltammetry and shake-flask results, it can be concluded that the reaction is controlled by the Galvani potential difference applied at the ITIES, which mainly functions as the driving force for the proton pump at the soft molecular interface.



Scheme 3-5. Proposed mechanism of O_2 reduction by DFcE at the W/O interface. W = aqueous phase, O = DCE phase. Hydrogen peroxide can replace oxygen in the scheme, producing water. (A): DFcE partitions to aqueous phase and reacts with protons and oxygen or hydrogen peroxide (not shown) to produce H_2O_2 or H_2O (“Osakai mechanism”); (B): Galvani potential dependent proton transfer into DCE phase followed by oxygen or hydrogen peroxide (not shown) reduction to H_2O_2 or H_2O partitioning back to aqueous phase; (C): Biphasic shake-flask reaction where TB^- extracts protons to DCE phase, followed by oxygen and hydrogen peroxide (not shown) reduction in the bulk of DCE phase.

3.4. Conclusions

In summary, we have shown that O_2 and H_2O_2 reduction by DFcE occurs at a polarized water/DCE interface. The first step consists of the protonation of DFcE to form the DFcE-H^+ in DCE phase, either by proton transfer observed in the four-electrode cell experiments or by the homogeneous protonation of DFcE in the presence of protons extracted in the oil phase by TB^- . The formed DFcE-H^+ is then attacked by dissolved O_2 in DCE side at the W/DCE interface or in the DCE bulk to produce H_2O_2 and DFcE^+ . Hydrogen peroxide is reduced by the protonated DFcE in a similar manner. The products, H_2O_2 or H_2O , generated in DCE phase are extracted into the aqueous phase. This separation of products from reactants is one advantage of the biphasic system used herein. The reaction can be triggered by driving protons to the oil phase with the Galvani potential difference across the interface, which can be easily tuned by the chemical way (common ion distribution) or by the external potential polarization. However, lithium acidity detailed in Chapter 7 should also be

taken into account to explain the results described in this chapter. The results show that DFCe can be used as an electron donor for oxygen and hydrogen peroxide reduction, although the reaction without a catalyst is rather slow. This is mainly due to a very low electrochemical driving force, and in the future this type of linked ferrocene compounds could prove to be very interesting electron donors for oxygen reduction and hydrogen evolution, if the redox potential of the compound could be reduced for example by methylation. Besides, it has been demonstrated that the rate of oxygen reduction by DFCe can be significantly improved by the use of suitable catalysts such as a cofacial biscobalt bisporphyrin.

3.5. References

- (1) Girault, H. H.; Schiffrin, D. J. In *Electroanalytical Chemistry. A series of advances*; Bard, A. J., Ed.; Marcel Dekker: New York, 1989; Vol. 15, p 1.
- (2) Costentin, C. *Chem. Rev.* **2008**, *108*, 2145.
- (3) Su, B.; Hatay, I.; Ge, P. Y.; Mendez, M.; Corminboeuf, C.; Samec, Z.; Ersoz, M.; Girault, H. H. *Chem. Commun.* **2010**, *46*, 2918.
- (4) Bitterwolf, T. E.; Ling, A. C. *J. Organomet. Chem.* **1972**, *40*, C29.
- (5) Fomin, V. M. *Russ. J. Gen. Chem.* **2007**, *77*, 954.
- (6) Chang, C. J.; Loh, Z. H.; Shi, C.; Anson, F. C.; Nocera, D. G. *J. Am. Chem. Soc.* **2004**, *126*, 10013.
- (7) Collman, J. P.; Denisevich, P.; Konai, Y.; Marrocco, M.; Koval, C.; Anson, F. C. *J. Am. Chem. Soc.* **1980**, *102*, 6027.
- (8) Siegbahn, P. E. M.; Blomberg, M. R. A. *Chem. Rev.* **2010**, *110*, 7040.
- (9) Eugster, N.; Fermín, D. J.; Girault, H. H. *J. Phys. Chem. B* **2002**, *106*, 3428.
- (10) Fermín, D. J.; Duong, H. D.; Ding, Z.; Brevet, P. F.; Girault, H. H. *Phys. Chem. Chem. Phys.* **1999**, *1*, 1461.
- (11) Bitterwolf, T. E.; Ling, A. C. *J. Organomet. Chem.* **1973**, *57*, C15.
- (12) Lubach, J.; Drenth, W. *Rec. Trau. Chim. Pays-Bas* **1973**, *92*, 586.
- (13) Su, B.; Nia, R. P.; Li, F.; Hojeij, M.; Prudent, M.; Corminboeuf, C.; Samec, Z.; Girault, H. H. *Angew. Chem., Int. Ed.* **2008**, *47*, 4675.
- (14) Sellers, R. M. *Analyst* **1980**, *105*, 950.
- (15) Gao, F.; Yang, Y.; Liu, J.; Shao, H. *Ionics* **2010**, *16*, 45.
- (16) Nieminen, J. J.; Hatay, I.; Ge, P.; Méndez, M. A.; Murtomäki, L.; Girault, H. H. *Chem. Commun.* **2011**, *47*, 5548.
- (17) Wandlowski, T.; Mareček, V.; Samec, Z. *Electrochim. Acta* **1990**, *35*, 1173.
- (18) Camire, N.; Mueller-Westerhoff, U. T.; Geiger, W. E. *J. Organomet. Chem.* **2001**, *637-639*, 823.
- (19) Xu, J.; Frcic, A.; Clyburne, J. A. C.; Gossage, R. A.; Yu, H. Z. *J. Phys. Chem. B* **2004**, *108*, 5742.
- (20) Xiang, D.; Merbouh, N.; Shao, H.; Yu, H. Z. *Electrochim. Acta* **2011**, *56*, 5788.
- (21) Geiger, W. E.; Barrière, F. *Acc. Chem. Res.* **2010**, *43*, 1030.
- (22) Nowicka, A. M.; Stojek, Z.; Ciszowska, M. *Anal. Lett.* **2004**, *37*, 979.
- (23) Hatay, I.; Su, B.; Li, F.; Partovi-Nia, R.; Vrubel, H.; Hu, X.; Ersoz, M.; Girault, H. H. *Angew. Chem., Int. Ed.* **2009**, *48*, 5139.
- (24) Hatay, I.; Su, B.; Li, F.; Méndez, M. A.; Khoury, T.; Gros, C. P.; Barbe, J. M.; Ersoz, M.; Samec, Z.; Girault, H. H. *J. Am. Chem. Soc.* **2009**, *131*, 13453.

- (25) Su, B.; Hatay, I.; Li, F.; Partovi-Nia, R.; Méndez, M. A.; Samec, Z.; Ersoz, M.; Girault, H. H. *J. Electroanal. Chem.* **2010**, *639*, 102.
- (26) Fukuzumi, S.; Okamoto, K.; Gros, C. P.; Guillard, R. *J. Am. Chem. Soc.* **2004**, *126*, 10441.
- (27) Fukuzumi, S.; Kotani, H.; Lucas, H. R.; Doi, K.; Suenobu, T.; Peterson, R. L.; Karlin, K. D. *J. Am. Chem. Soc.* **2010**, *132*, 6874.
- (28) Halime, Z.; Kotani, H.; Li, Y.; Fukuzumi, S.; Karlin, K. D. *Proc. Natl. Acad. Sci. U. S. A.* **2011**, *108*, 13990.
- (29) Hatay, I.; Su, B.; Li, F.; Partovi-Nia, R.; Vrubel, H.; Hu, X.; Ersoz, M.; Girault, H. H. *Angew. Chem., Int. Ed.* **2009**, *48*, 5139.
- (30) Homolka, D.; Hung, L. Q.; Hofmanova, A.; Khalil, M. W.; Koryta, J.; Marecek, V.; Samec, Z.; Sen, S. K.; Vanysek, P. *Anal. Chem.* **1980**, *52*, 1606.
- (31) Su, B.; Hatay, I.; Ge, P. Y.; Mendez, M.; Corminboeuf, C.; Samec, Z.; Ersoz, M.; Girault, H. H. *Chem. Commun.* **2010**, *46*, 2918.
- (32) Shao, Y.; Osborne, M. D.; Girault, H. H. *J. Electroanal. Chem.* **1991**, *318*, 101.
- (33) Su, B.; Partovi-Nia, R.; Li, F.; Hojeij, M.; Prudent, M.; Corminboeuf, C.; Samec, Z.; Girault, H. H. *Angew. Chem., Int. Ed.* **2008**, *47*, 4675.
- (34) Hotta, H.; Ichikawa, S.; Sugihara, T.; Osakai, T. *J. Phys. Chem. B* **2003**, *107*, 9717.
- (35) Osakai, T.; Ebina, K. In *Liquid Interfaces in Chemical, Biological and Pharmaceutical Applications*; Volkov, A., G., Ed.; Marcel Dekker: New York, 2001; Vol. 95, p 27.
- (36) *CRC handbook of chemistry and physics, 85th ed.*; Lide, D. R., Ed.; CRC Press: Boca Raton, 2005.
- (37) Tsierkezos, N. G.; Ritter, U. *J. Appl. Electrochem.* **2010**, *40*, 409.
- (38) Clayden, J.; Greeves, N.; Warren, S.; Wothers, P. *Organic Chemistry, 1st ed.*; Oxford University Press: Oxford, 2000.
- (39) Osakai, T.; Ebina, K. *J. Phys. Chem. B* **1998**, *102*, 5691.
- (40) Uhlig, H. H. *J. Phys. Chem.* **1937**, *41*, 1215.
- (41) Trojánek, A.; Mareček, V.; Jänchenová, H.; Samec, Z. *Electrochem. Commun.* **2007**, *9*, 2185.
- (42) Kontturi, K.; Murtomäki, L. *J. Pharm. Sci.* **1992**, *81*, 970.
- (43) Peljo, P.; Rauhala, T.; Murtomäki, L.; Kallio, T.; Kontturi, K. *Int. J. Hydrogen Energy* **2011**, *36*, 10033.
- (44) Peljo, P.; Murtomäki, L.; Kallio, T.; Xu, H. J.; Meyer, M.; Gros, C. P.; Barbe, J. M.; Girault, H. H.; Laasonen, K.; Kontturi, K. *J. Am. Chem. Soc.* **2012**, *134*, 5974.

Chapter 4

Oxygen Reduction at Soft Interfaces Catalyzed by In Situ-Generated Reduced Graphene Oxide

Based on ChemElectroChem 2014, 1, 59, in collaboration with Shokoufeh Rastgar.

4.1. Introduction

Modern electrochemistry at the liquid/liquid interface or the interface between two immiscible electrolyte solutions (ITIES) has developed over the past 30 years, where charge (electron and ion) transfer reactions have found applications in areas such as phase transfer catalysis, solvent extraction processes, chemical sensing, solar energy conversion systems, drug release and delivery, and in mimicking the function of biological membranes.¹ Liquid/liquid interfaces provide a unique platform at which to study O₂ reduction reactions (ORR) where aqueous protons react with organic solubilized electron donors in the absence or presence of adsorbed catalysts, usually through a proton-coupled electron transfer (PCET) reaction.² The catalysts studied include cobalt,³⁻⁵ free base porphyrins,⁶ and *in situ* deposited platinum particles.⁷ The ORR proceeds either by a 4e⁻/4H⁺ pathway to produce water or a 2e⁻/2H⁺ route to yield hydrogen peroxide (H₂O₂), considered a green oxidant.

H₂O₂ is widely used in many industrial areas, particularly in the chemical industry or for environmental protection, and is currently produced on an industrial scale by the biphasic anthrahydroquinone oxidation (AO) process (representing *ca.* 95% of the world's H₂O₂ production).⁸⁻¹¹ Generally, anthrahydroquinone is oxidized by O₂ to produce H₂O₂ and anthraquinone and, subsequently, the formed anthraquinone is reduced back to the anthrahydroquinone using H₂ in the presence of a metal (*e.g.* palladium¹¹) catalyst. Both reactions occur in the organic phase and H₂O₂ is recovered by extraction to the aqueous phase.⁸⁻¹¹ The advantage of the AO process is the very high yield of H₂O₂ generated per cycle. Conversely, side reactions generating organic by-products need to be dealt with by regenerating the solution and using separation techniques to eliminate such impurities. Conceptually following the AO process, the reduction of O₂ was investigated at quinone modified carbon surfaces. O₂ reduction to H₂O₂ was mediated by surface-bound quinone groups *via* superoxide anion intermediates¹² and such modified electrodes have shown great catalytic activity towards the 2e⁻/2H⁺ ORR. Recently, Fukuzumi *et al.* reviewed the current state-of-the-art for the homogeneous and heterogeneous electrocatalytic production of H₂O₂ using a variety of metal complexes including cobalt porphyrins, biscobalt porphyrin-corrole complexes, cytochrome *c* oxidase models and Cu complexes as ORR catalysts.¹³ An important development is the production of H₂O₂ by the electrocatalytic 2e⁻ reduction of O₂

electrically powered by an integrated photovoltaic solar cell. Stored H_2O_2 can then be used as a sustainable solar fuel to generate power using H_2O_2 fuel cells.¹³ Thus, implementing new efficient and inexpensive catalysts for the biphasic production of H_2O_2 is of high relevance and might lay the foundations for new industrial processes.

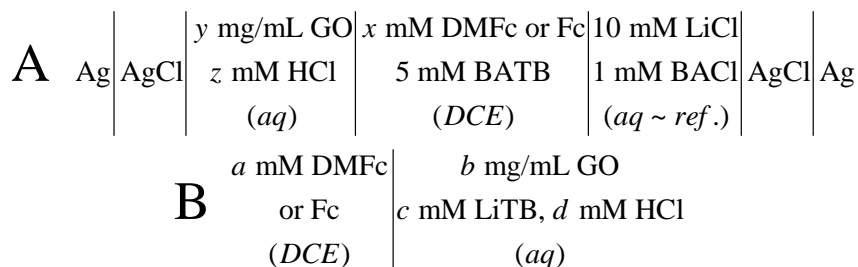
Graphene, a carbon-based nanomaterial, is a one-atom-thick planar sheet of sp^2 bonded carbon atoms densely arranged into a 2D honeycomb crystal lattice.^{14,15} Thanks to a high specific surface area (theoretically $2630 \text{ m}^2/\text{g}$ for single-layer graphene),¹⁶ large amounts of edge-planes/defects,¹⁷ a high electron transfer rate ($15'000 \text{ cm}^2/\text{V/s}$), strong mechanical strength and both excellent thermal and electrical conductivities,¹⁸ graphene sheets are also of interest in electrochemistry. Graphene oxide (GO), a precursor for graphene synthesis, consists of a hexagonal ring-based carbon network having both (largely) sp^2 -hybridized carbon atoms and (partly) sp^3 -hybridized carbons. These carbon atoms bear oxygen functional groups in the form of hydroxyl and epoxy moieties on the basal plane, with smaller amounts of carboxyl, carbonyl, phenol, lactone and quinone at the sheet edges. These can be viewed as oxidized regions disrupting the extended sp^2 conjugated network of the original honeycomb-lattice structured graphene sheet.¹⁹ Reduced graphene oxide (RGO), the more conductive product of the partial reduction of GO, has also been studied in recent years as a catalyst for the ORR in both alkaline and acidic media and has been considered for potential applications in microbial fuel cells.²⁰⁻²² Recently, it was shown that GO and ferrocene composites may be prepared and employed for photo-induced charge transfer processes.²³

With the aim of developing an alternative biphasic system for H_2O_2 production, in this chapter, the catalytic properties of RGO towards O_2 reduction at the ITIES were investigated. RGO was generated *in situ* at the water/1,2-dichloroethane (DCE) interface by partial reduction of water-dispersed GO *via* DMFc or Fc solubilized in the DCE phase. DMFc or Fc have dual roles, acting as electron donors for the reduction of GO adsorbed at the interface and, subsequently, as reductants for O_2 molecules adsorbed on the RGO sheets. RGO produced in this manner was characterized by electron microscopy, spectroscopy (infra-red (IR), electron energy loss (EELS) and Raman), in addition to electrochemical methods.

4.2. Experimental section

4.2.1. Chemicals

All chemicals used throughout this Chapter have been summarized in Section 2.2 in Chapter 2. The preparation of the organic acid HTB was carried out using the biphasic system illustrated in Scheme 4-1B ($a = 0$, $b = 0$, $c = 10$ and $d = 100$). Each phase had a volume of 2 mL. The aqueous solubilized TB^- acts as a phase transfer catalyst to extract protons to the organic phase as HTB.^{2,24} The system was stirred for 1 h at 900 rpm. After formation of HTB, both phases were separated, the organic phase evaporated and the dried HTB re-dissolved in DCE.



Scheme 4-1. (A) Potentiostatic and (B) chemical polarisation of the interface: schematic representation of the compositions of the electrochemical cells used for ion transfer voltammetry and the shake-flask experiments. All experiments, unless noted otherwise, were performed under aerobic conditions.

4.2.2. Preparation of reduced graphene oxide (RGO) at the liquid/liquid interface

The preparation of RGO sheets was carried out using the biphasic system illustrated in Scheme 4-1B ($a = 5$, $b = 0.2$, $c = 10$ and $d = 100$). The reaction was allowed to proceed for 48 h under stirring conditions. It is worth noting that, after this reaction time, the initially brown solution of GO in the water phase was converted to a black solution that partially distributed into the DCE phase. This was in contrast to GO sheets that sediment in their entirety at the interface in the absence of reducing agents. Subsequently, the two phases were isolated from each other and separately centrifuged. This was necessary as RGO can partially dissolve in both phases, as mentioned. Therefore, after centrifugation, the RGO samples were collected, thoroughly washed with DCE and acetone to remove any residual Fc^+ or DMFc^+ from the biphasic reaction, and finally, dried in an oven overnight at 80 °C.

4.2.3. Morphological characterization of RGO prepared at the liquid/liquid interface (*carried out by Véronique Amstutz*)

The morphologies of the flake like structures of RGO and GO sheets were obtained using scanning electron microscopy (SEM) and transmission electron microscopy (TEM). SEM images were obtained using a Phillips (FEI) XLF-30 FEG Schottky field-emission SEM operated at beam voltages between 1 and 30 keV. TEM images were obtained with a high resolution TEM (FEI) with Schottky field emission gun (FEG) operated at 200 kV acceleration voltage and which has ultra-twin objective lens with spherical aberration coefficient (Cs) of 0.7 mm and a maximum resolution of 1.7 Å at 300 kV. The samples were dispersed in DMF, dropped on a Cu grid and left to dry under an IR lamp for 2 min.

4.2.4. Spectroscopic characterization of RGO prepared at the liquid/liquid interface (*carried out by Dr. A. Duncan, F. Matteini, and R. Gaal*)

Infra-red (IR) spectra were recorded on a MIR (600–4000 cm^{-1}) Perkin-Elmer FTIR spectrometer. Raman spectra were obtained using a Labram HR 800 spectrometer with the laser operating at 532 nm. Electron energy loss spectroscopy (EELS) measurements were performed in TEM mode with a JEOL 2200FS model operated at 200 kV. Inelastic scattering by the TEM specimen results in energy losses of the electron beam that are measured in the electron energy-loss (EEL) spectrum. An EEL spectrum allows the identification and quantification of low atomic number elements, such as carbon or oxygen. Specimen thickness, relative to the inelastic scattering mean-free path, is also easily determined from an EEL spectrum.

4.2.5. Electrochemical characterization of RGO prepared at the liquid/liquid interface.

Electrochemical characterization was performed on a PGSTAT 30 (Eco-Chemie, NL) potentiostat using a conventional three-electrode system with a glassy carbon working electrode (GCE, 3 mm diameter), an Ag/AgCl (saturated KCl) reference electrode and a Pt wire counter electrode. Prior to each experiment, the GCE was carefully polished sequentially with 1, 0.5, and 0.1 μm -sized alumina slurry on a polishing cloth, rinsed thoroughly and then sonicated in ultrapure water for 5 min and, finally, dried in air. Subsequently, the GCEs were modified by either GO or RGO. A 1 mg sample of the GO (or RGO) was dispersed in 1 mL of DMF and homogenized in an ultrasonic bath for 30 min. Then, 2 μL of the suspension was placed on the GCE surface using a micropipette and the solvent allowed to evaporate at 55 $^{\circ}\text{C}$ in an oven to obtain the GO/GCE (or RGO/GCE).

Scanning Electrochemical Microscopy (SECM) measurements in feedback mode were performed as a contactless method to probe the conductivity of the immobilized GO and RGO films. The corresponding approach curves were recorded using a commercially available SECM instrument (CHI-900, CH Instruments, USA), operated in a classical three-electrode setup. The electrochemical cell comprised of an Ag/AgCl reference electrode, a Pt wire counter electrode, and a Pt ultramicroelectrode (UME; 10 or 20 μm diameter) working electrode.

Fabrication of the Pt UMEs has been detailed in Section 2.3.4.2 in Chapter 2, according to the methodology described in the literature.^{25,26} After mechanical polishing of the glass encapsulated UMEs, the ratio of the overall probe radius to that of the platinum disk, *i.e.* RG, was equal to 10, as determined with a Laborlux D optical microscope (Leitz, Germany).

For SECM experiments, GO or RGO homogenous films were prepared on the surface of a glass slide by drop-coating GO or RGO dispersed in DMF. To this end, the solution of GO (or RGO) dispersed in DMF was initially centrifuged to concentrate the solution prior to drop-coating. After drying overnight, these samples were used for measuring SECM approach curves with the probe potential poised at 0.4 V *vs.* Ag/AgCl and using an approach rate of 0.1 $\mu\text{m/s}$ in the presence of 2 mM FcMeOH and 0.1 M KCl as the test solution.

4.2.6. Potentiostatic polarization of the interface: biphasic electrochemical measurements using *in situ* generated RGO as an O₂ reduction catalyst

Ion transfer voltammetry measurements at the water/DCE interface were performed in a four-electrode cell (see Figure 1-1 in Chapter 1) with two reference electrodes and two platinum counter electrodes, one of each positioned in either phase, to polarize the interface and supply the current, respectively. A four-electrode potentiostat (PGSTAT 30, Eco-Chemie, NL) was used. The external potential was applied by means of two silver/silver chloride (Ag/AgCl) reference electrodes, connected to the aqueous and DCE phases, respectively, by means of a Luggin capillary. The area of the liquid/liquid interface was 1.53 cm². The electrochemical cell composition is schematically illustrated in Scheme 4-1A. The Galvani potential difference ($\Delta_o^w\phi$) was estimated by taking the formal ion transfer potential of tetraethylammonium cation (TEA⁺) as 0.019 V.²⁷

4.2.7. Chemical polarization of the interface: biphasic shake-flask experiments using *in situ* generated RGO as an O₂ reduction catalyst

Shake-flask experiments were performed by polarizing the interface *via* distribution of a common ion (TB[−]) between both phases. Biphasic reactions for O₂ reduction were performed in a small glass vial with stirring, under aerobic conditions and with equal volumes (2 mL) of water and DCE solution present. The precise compositions of the latter are outlined in Scheme 4-1B. After reaction, the two phases were allowed to settle and fully separate. The aqueous and organic solutions were isolated and analyzed individually. The organic phase was analyzed by UV/Vis spectroscopy in order to confirm the formation of Fc⁺ or DMFc⁺ (λ_{max} = 620 and 779 nm, respectively). The aqueous phase was analyzed by the NaI titration method (see Section 2.4.1.1.1 in Chapter 2) to detect the expected biphasic shake-flask reaction product H₂O₂. The concentration of H₂O₂ produced was calculated based on a calibration curve prepared by correlating the observed UV/Vis absorption spectra with standard H₂O₂ concentrations (by dilution from 3% H₂O₂), see Section 2.4.1.1.1 in Chapter 2. UV/Vis spectra were obtained on an Ocean Optics CHEM 2000 spectrophotometer with a quartz cuvette with a path length of 1 cm, volume of 4 mL, and equipped with a Teflon cap to prevent evaporation of the organic phase during analysis. All experiments carried out under aerobic conditions were performed with air-saturated solutions at an ambient temperature (23 ± 2 °C) unless specified elsewhere. Experiments performed under anaerobic conditions took place in a glovebox purged by nitrogen, again at an ambient temperature.

4.2.8. Kinetics measurements using “shake-flasks”

The composition of the shake flasks used for kinetic studies were identical to that described in Scheme 4-1B. The kinetics of the biphasic ORR were analyzed by monitoring the variation of the intensity of the UV/Vis absorbance peak of the reaction product, either Fc⁺ or DMFc⁺, and hence the *in situ* variation of [Fc⁺] or [DMFc⁺], with time. The UV/Vis spectra were once

more measured on an Ocean Optics CHEM2000 spectrophotometer, as above, except 1 mL of each phase was added to the quartz cuvette. UV/Vis scans were taken at regular intervals, typically every 30 s, for a period of time and during scan intervals the solution in the cuvette was constantly agitated using a magnetic stirrer (900 rpm). Specific experimental setup has been described in Section 2.4.1.2 in Chapter 2. Quantitative determination of $[\text{Fc}^+]$ and $[\text{DMFc}^+]$ in DCE by UV/Vis spectroscopy was possible as the molar extinction coefficients (ϵ) of Fc^+ and DMFc^+ in 1,2-DCE were determined previously as $0.350 \text{ mM}^{-1} \cdot \text{cm}^{-1}$ and $0.632 \text{ mM}^{-1} \cdot \text{cm}^{-1}$, respectively.^{28,29}

4.3. Results and discussion

4.3.1. Four-electrode cell measurements

Cyclic voltammograms (CVs) were obtained at the water/DCE interface under aerobic conditions (Figure 4-1), unless stated otherwise, using the four-electrode electrochemical cell outlined in Scheme 4-1A. The baseline CV response of the background electrolytes, *i.e.* protons (H^+) and chloride (Cl^-) ions in the acidic aqueous phase (w) and bis(triphenylphosphoranylidene) ammonium tetrakis(pentafluorophenyl) borate (BATB) in DCE (o), exhibits a potential window limited by the transfer of H^+ and Cl^- from w to o and *vice versa* at the positive and negative potential limits, respectively. On introduction of 1 mM DMFc to o, a current wave at positive potentials, indicating the protonation of DMFc in o, is observed and associated with the production of H_2O_2 in agreement with previous reports.^{3,30,31} The mechanism for the formation of H_2O_2 *via* ORR will be detailed in Chapters 5 and 6. The subsequent addition of 0.2 mg/mL of GO to w leads to a drastic increase of the current, as well as a decrease of the onset potential of the current wave. The current may be further enhanced by dispersing higher concentrations of GO in w (Figure 4-2A). These results demonstrate the catalytic role of interfacial GO for O_2 reduction *via* DMFc in this biphasic system. Control experiments confirmed that these trends were only observed under aerobic conditions (Figure 4-2B). Moreover, a shift of the onset potential of the current wave by *ca.* 60 mV/pH unit corroborated the role of the proton in this voltammetric signal (Figure 4-2C).

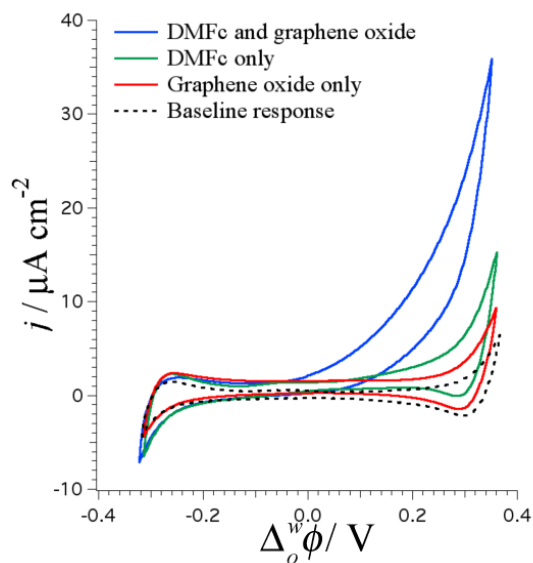


Figure 4-1. Cyclic voltammograms obtained under aerobic conditions, using the electrochemical cell outlined in **Scheme 4-1A**, in the absence of both DMFc and GO ($x = 0$, $y = 0$, $z = 100$, dashed line), with only GO ($x = 0$, $y = 0.2$, $z = 100$, red line), with only DMFc ($x = 1$, $y = 0$, $z = 100$, green line) and with both DMFc and GO ($x = 1$, $y = 0.2$, $z = 100$, blue line) present. Scan rate used: 50 mV/s.

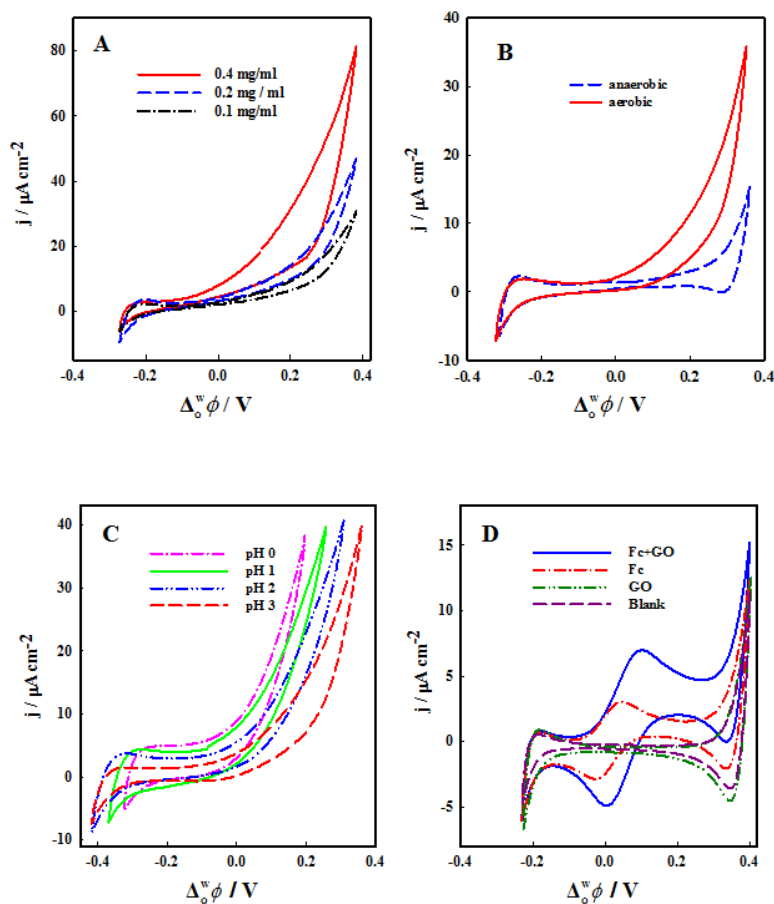
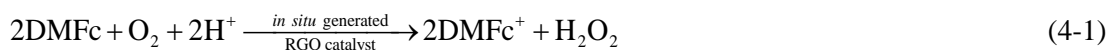


Figure 4-2. Control O₂ reduction experiments at a potentiostatically polarized liquid/liquid interface. CVs were obtained using the electrochemical cell outlined in **Scheme 4-1A**, (A) with DMFc and various concentrations of GO under aerobic conditions ($x = 1$, $y = 0.1, 0.2$ or 0.4 , $z = 100$) and (B) with DMFc and GO ($x = 1$, $y = 0.2$, $z = 100$) either under aerobic or anaerobic conditions, as indicated. (C) The influence of pH. CVs obtained under aerobic conditions ($x = 1$, $y = 0.2$) at various pH values (from right to left: $z = 1, 10, 100$ and 1000). (D) The influence of electron donor. CVs obtained in absence of both Fc and GO (dashed line, purple, $x = 0$, $y = 0$, $z = 100$), with only Fc (dash-dot line, red, $x = 1$, $y = 0$, $z = 100$), with only GO (dash-dot-dot line, green, $x = 0$, $y = 0.2$, $z = 100$) and with both Fc and GO (solid line, blue, $x = 1$, $y = 0.2$, $z = 100$) present under aerobic conditions. Scan rates used were 50 mV/s for (A), (B) and (C) but 20 mV/s for (D); the second scans were compared for each experiment.

These observations unambiguously show that GO, O₂, H⁺ and DMFc must be present simultaneously for the ORR catalytic process to proceed. It should be noted that the catalytic behavior of RGO for O₂ reduction at solid electrodes has been reported previously.^{20-22,32} So it can be proposed reasonably that the *in situ* formed RGO *via* reduction of GO heterogeneously by the lipophilic DMFc plays the crucial catalytic role in the following biphasic ORR, as outlined in equation 4-1.



The catalytic effect of RGO can be explained by the enhanced conductivity (relative to GO) that facilitates electron injection by DMFc to the catalytically active ORR sites at the RGO surface. To verify this point, RGO prepared at the liquid/liquid interface has been characterized by different techniques that will be discussed in Section 4.3.2.

Besides, the current wave at positive potentials varies linearly with the square root of scan rate (data not shown), indicating that this process is limited by the diffusion of DMFc to the interface as all other species are in excess.

On replacing DMFc (standard redox potential in DCE *vs.* the aqueous standard hydrogen electrode (SHE), $[E_{\text{DMFc}^+/\text{DMFc}}^\circ]_{\text{SHE}}^\circ$, of 0.04 V)³³ with a weaker reductant such as ferrocene, (Fc), $[E_{\text{Fc}^+/\text{Fc}}^\circ]_{\text{SHE}}^\circ$ of 0.64 V,² the current wave associated with the ORR process at the positive potential range is not so evident as that in the DMFc case due to the large difference of the redox potentials between DMFc and Fc. Nonetheless, an enhanced production of ferrocenium ions (Fc⁺) in the presence of GO was clearly observed by ion transfer voltammetry (Figure 4-2D) indicating that oxygen reduction by Fc catalyzed by the *in situ* formed RGO still took place at the positive edge of the potential window.

4.3.2. Morphological, spectroscopic and electrochemical characterization of RGO prepared at the liquid/liquid interface

4.3.2.1. Morphological characterization

The morphologies and microstructures of the precursor material, GO, and the material prepared at the liquid/liquid interface, RGO, were investigated by SEM and TEM (or HR-

TEM), respectively. The SEM image of GO shows the close association of GO sheets inside the GO structure (Figure 4-3A). The SEM image of the RGO film, on the other hand, shows a rougher or “wrinkled” surface morphology with apparent cracks visible (Figure 4-4A). Additionally, the layered RGO sheets were tightly packed with the edges of each individual layer distinguishable from the crumpled areas (Figure 4-4A). TEM images also illustrate the flake-like shapes of RGO nanosheets and their resemblance to a crumpled silk veil with rippled waves (Figure 4-4B), a feature intrinsic to graphene nanosheets, as shown previously.³⁴ The selected area electron diffraction (SAED) pattern, obtained using HR-TEM, of the RGO sheets exhibited well-defined diffraction spots, thereby confirming the crystalline structure of the RGO nanosheets (Figure 4-4C and inset). The TEM images of GO sheets were also recorded, as displayed in the Figure 4-3B and C.

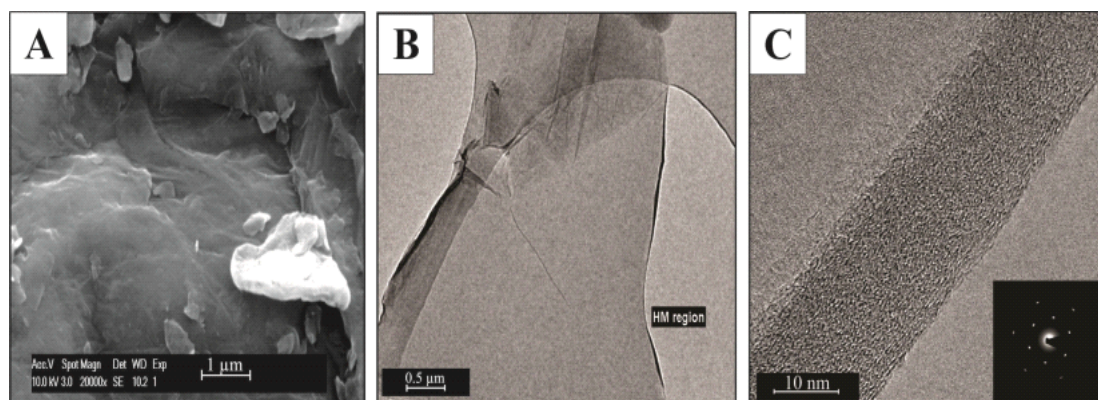


Figure 4-3. (A) SEM, (B) TEM (C) and HR-TEM images of graphene oxide (GO). The inset in panel C is the selected area electron diffraction pattern (SAED).

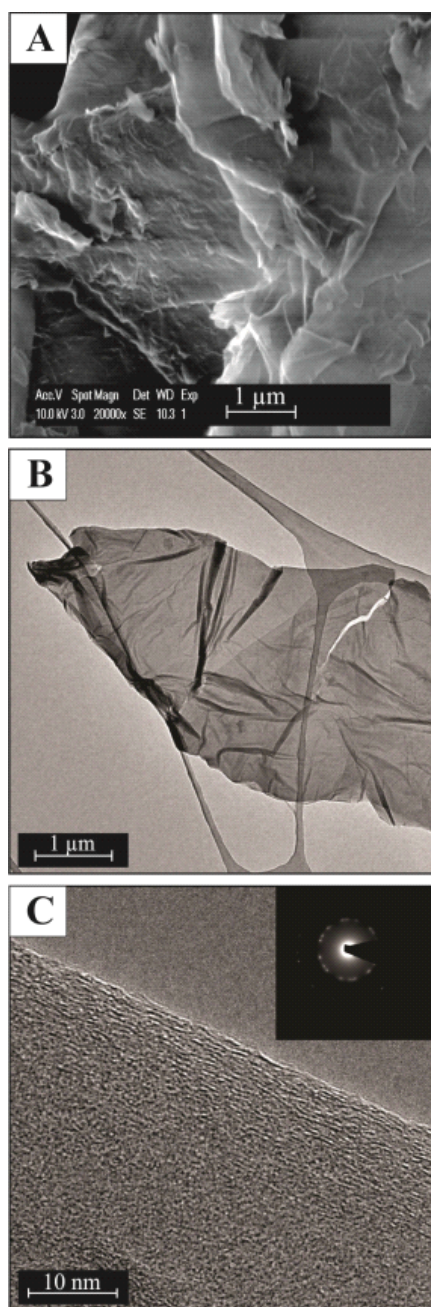


Figure 4-4. (A) SEM, (B) TEM (C) and HR-TEM images of reduced graphene oxide (RGO) sheets prepared at the liquid/liquid interface. The inset in panel C is the selected area electron diffraction pattern (SAED).

4.3.2.2. Spectroscopic Characterization

FT-IR, UV/Vis, electron energy loss and Raman spectroscopy were employed for further chemical characterization of GO and RGO. FT-IR spectra of GO were obtained before and after the reduction process (Figure 4-5A). The characteristic absorption peaks of GO at 3085, 1735, 1626, 1385, and 1044 cm^{-1} are attributable to an O–H stretching mode, C=O stretching vibrations from the carbonyl and carboxylic groups, skeletal vibrations from non-oxidized graphene domains, C–OH stretching vibrations in the carbonyl, and C–O stretching vibrations in the epoxy or alkoxy, respectively. For RGO an IR transmission peak at 1646 cm^{-1} is due to skeletal vibrations from graphene domains; the peaks at 1315 and 1160 cm^{-1} may correspond to O–H bending from the hydroxyl/phenol groups and C–O stretching. Indeed, there is also a small shoulder at 1730 cm^{-1} belonging to the C=O stretching vibrations of the remaining quinone-like carbonyl moieties on the RGO sheets (Figure 4-5A).^{32,35-40} These observations are interpreted as the removal of oxygenated functionalities due to the interfacial reduction of GO to RGO, however, with the retention of some carbonyl groups on the RGO. Herein, the degree of loss of oxygenated groups is less extensive when compared to previously reported RGO preparation methodologies.^{32,35-40}

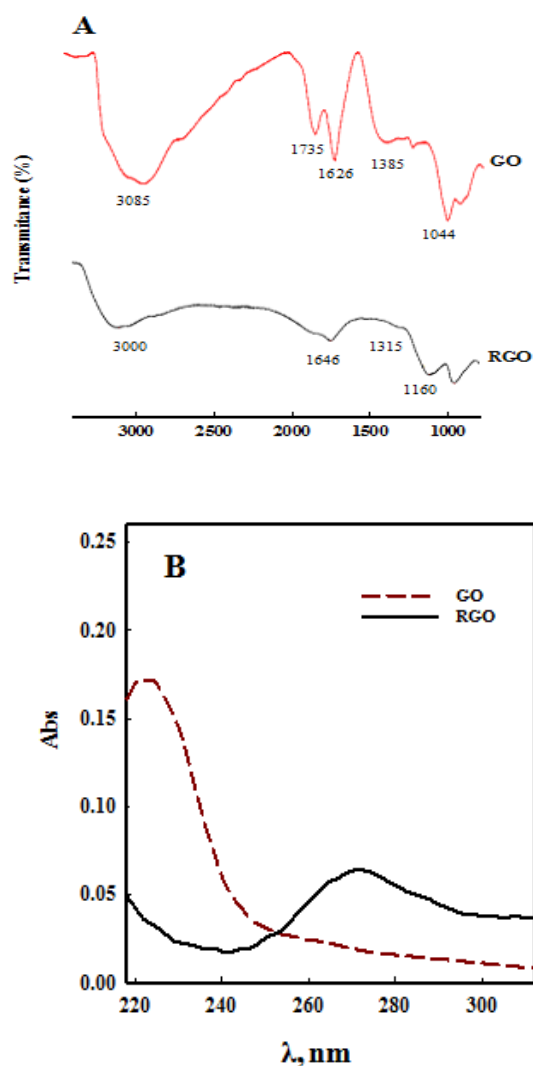


Figure 4-5. (A) FT-IR and (B) UV/Vis spectra of GO pre- and post-reduction to RGO, as indicated, at the liquid/liquid interface.

The C/O ratio for GO and RGO can be compared quantitatively by using electron energy loss spectroscopy (EELS). The data confirmed the slight decrease of oxygen content in the interfacially-prepared RGO relative to GO (Table 4-1). Indeed, these oxygen-containing groups, such as quinone-like functionalities, on the surface of carbon materials may facilitate the catalytic behavior of this material towards the oxygen reduction, as discussed in the Mechanism part (Section 4.3.6).

Table 4-1. Data obtained from electron energy loss spectroscopy (EELS) analysis of GO and interfacially prepared RGO, where t is the RGO thickness divided by the inelastic scattering mean.

Sample	$t / \lambda^{[a]}$	Atomic C / %	Atomic O / %
GO	0.16 ± 0.05	82 ± 1	18 ± 1
RGO	0.42 ± 0.1	87 ± 3	13 ± 3

^aSample thickness divided by the inelastic scattering mean free path.

Moreover, the UV/Vis absorption spectra of GO exhibited one absorption peak with the maximum centered at 220 nm (Figure 4-5B), characteristic of a π - π^* transition for aromatic C-C bonds.⁴¹⁻⁴³ After reaction of GO at the interface, the absorption peak for RGO was red shifted to 268 nm (Figure 4-5B), suggesting the reduction of GO and the restoration of the aromatic structure.⁴⁴

Changes in the electronic conjugation state taking place after the reduction of GO to RGO^{14,45} were also reflected in their Raman spectra (Figure 4-6). The Raman spectra of GO and RGO displayed two characteristic G (at 1589 cm^{-1}) and D (at 1348 cm^{-1}) bands corresponding to first-order scattering of the E_{2g} mode of sp^2 -hybridized carbon atoms and the symmetry A_{1g} mode arising from the presence of attached oxygenated groups.

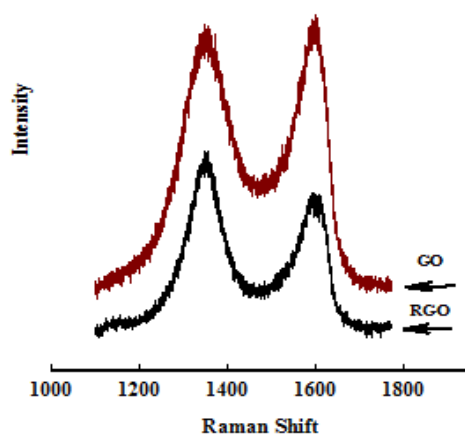


Figure 4-6. Raman spectra of GO pre- and post-reduction to RGO, as indicated, at the liquid/liquid interface.

The D/G intensity ratio increased from 0.91 to 1.60 after reduction. This significant change suggested a decrease in the average size of the sp^2 domains upon reduction of GO. The latter decrease probably has its origins in the creation of new graphitic domains that are smaller in size but present in greater quantities compared to those pre-reduction, as reported previously.^{35,40,46}

4.3.2.3. Electrochemical Characterization.

One of the unique properties of graphene is its high electrical conductivity.⁴⁷ By comparison, GO is an insulator primarily due to disruption of the sp^2 -conjugated network of the original honeycomb-lattice structured graphene sheet. RGO, produced following various procedures, usually exhibits a semiconducting behavior with good electrical conductivity. This improvement in conductivity relative to GO simply reflects the extent of the reduction that has taken place and, in turn, the consequent restoration of the electronic conjugation state of the material.

SECM in feedback mode has been introduced as a ‘contactless’ method to quantitatively probe the conductivity of ultra-thin films. With SECM, one may approach the vicinity of the film of interest with an UME and, by applying an appropriate potential, achieve mass transport limited oxidation (or reduction) of an introduced redox mediator. Since the substrate potential is defined by the ratio of the concentrations of the reduced to oxidized species (*i.e.* by the Nernst equation), locally changing the concentration of the redox species modifies the local substrate potential. Thus, this creates both cathodic and anodic zones on the same substrate. The observation of “positive feedback” or “negative feedback” as the UME approaches the substrate surface depends on a plethora of variables and, specifically with GO and RGO in mind, key amongst these is the lateral charge transport or conductivity of the film.^{48,49} Indeed, SECM has recently been applied as a tool to study the conductivity of GO samples,⁴⁹ thereby confirming the feasibility of extracting the electrical conductivity of such samples in a relatively simple manner.

Normalized current-distance approach curves were acquired by monitoring the current at the biased UME approaching GO or RGO films deposited on an inert glass substrate, *i.e.* for the mass transport-controlled oxidation of 2 mM FcMeOH in 0.1 M KCl (Figure 4-7). A clear current increase was observed as the UME approached the RGO surface (dashed blue line, Figure 4-7), while for the GO film the recorded current decreased gradually (solid red line, Figure 4-7). By fitting these experimental SECM approach curves to numerical simulations using previously reported models,^{48,50} the conductivities of the GO and RGO films were determined as $4.2 \cdot 10^{-5}$ and 0.03 S/m, respectively. RGO produced biphasically shows lower conductivity compared to the conductivities of RGO semiconductor samples reported previously.^{37,51} The likelihood is that GO is only partially reduced by DMFc at the liquid/liquid interface, thus limiting the conductivity of the resultant RGO.

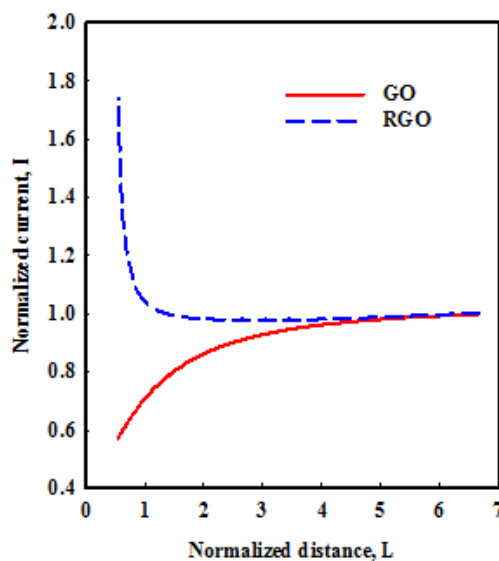


Figure 4-7. Scanning electrochemical microscopy (SECM) approach curves of GO (solid line, red) and RGO (dashed line, blue) films deposited on an insulating glass substrate for the oxidation of a redox mediator, 2 mM FeMeOH, in 0.1 M KCl. A Pt UME was used to approach the substrate. Probe potential = 0.4 V (vs. Ag/AgCl) and approach rate = 0.1 $\mu\text{m/s}$.

The electrochemical properties of the prepared RGO were also investigated *via* cyclic voltammetry (CV) by modification of a glassy carbon electrode (GCE) with GO or RGO sheets. The CVs obtained in a nitrogen-purged solution of 0.1 M PBS (pH = 7.0) for a bare GCE and a RGO/GCE are shown in Figure 4-8A. As expected, the CV response of a bare GCE was featureless, while the RGO/GCE exhibited a redox response at 0.023 V (vs. Ag/AgCl). These signals corresponded to the residual quinone-type functional groups on the RGO surface after GO reduction, as reported previously.³² CV studies at the GO/GCE and RGO/GCE were made in the presence of a redox probe (Figure 4-8B). Compared to GO/GCE, the RGO/GC showed better electrocatalytic activity with a much higher peak current, and also a smaller peak potential separation.

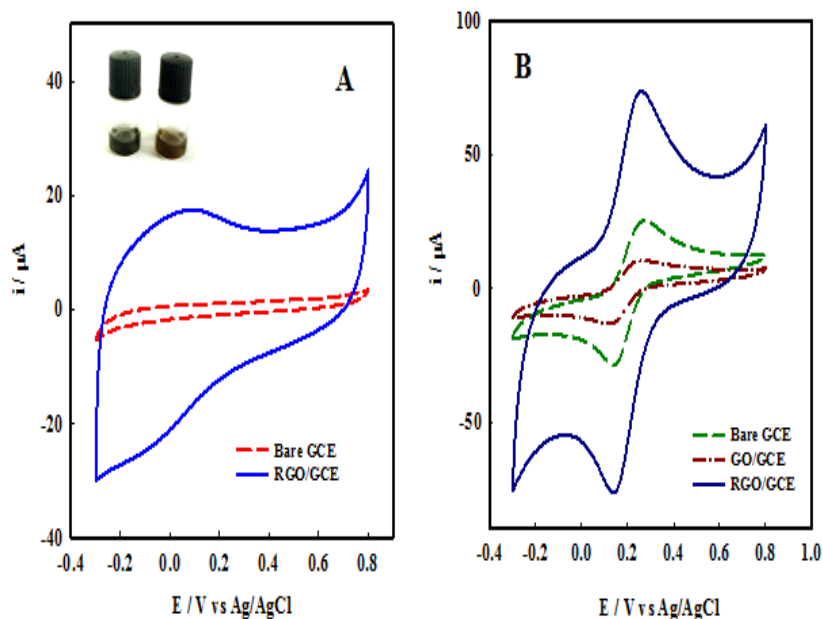


Figure 4-8. (A) CVs of a bare GCE and a RGO/GCE in the 0.1 M phosphate buffer solution (pH = 7.0). Inset: Images of GO (left) and RGO (right) dispersed in DMF solvent with at a concentration of 0.1 mg/mL. (B) CVs of a bare GCE, a GO/GCE and a RGO/GCE in a solution of 1 mM $\text{K}_3\text{Fe}(\text{CN})_6/\text{K}_4\text{Fe}(\text{CN})_6$ containing 0.1 M KCl as background electrolyte.

CVs of the ORR at a bare GCE and a RGO/GCE in DCE were obtained both in the presence and absence of HTB and either under aerobic or anaerobic conditions (Figure 4-9). The bare GCE showed no clear O_2 reduction signal in the absence of HTB, whereas two cathodic peaks at -0.67 V and -0.98 V were recorded in its presence (Figure 4-9). As reported previously, both peaks may be attributed to a $2\text{e}^-/2\text{H}^+$ reduction of O_2 to hydrogen peroxide in the presence of H^+ . The first electron transfer is mediated electrochemically by surface-active quinone-like groups, with superoxide anion as the intermediate, while the second is a direct one electron reduction process at the electrode.^{12,52}

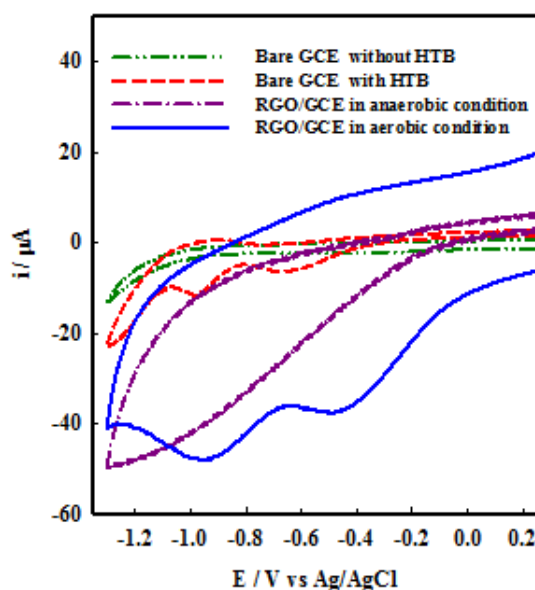


Figure 4-9. Electrochemical monitoring of the ORR in DCE: control experiments. CVs were obtained in a DCE solution containing 100 mM tetrahexylammonium tetrafluoroborate as the supporting electrolyte (a) with the organic acid, 10 mM HTB, under aerobic conditions at a bare GCE (dashed line, red) and a RGO/GCE (solid line, blue), (b) without HTB under aerobic conditions at a bare GCE (dash-dot-dot line, green) and (c) with HTB under anaerobic conditions at a RGO/GCE (dash-dot line, purple). The scan rate used was 100 mV/s.

An analogous behavior was observed on performing the same experiment with a RGO/GCE. However, the latter produced a clear and substantial (by a factor of 6) increase of the cathodic currents and the positive shift of peak potentials (Figure 4-9). The first reduction peak at -0.49 V was redox mediated by quinone-like groups at the RGO surface and consistent with previous reports.^{20-22,32} The increased current for the second electron transfer on the surface of RGO at -0.91 V emphasized that the interaction of RGO nanosheets with O_2 is considerably stronger than that of the bare GCE surface. This enhanced O_2 -substrate interaction may be due to the influence of structural edge-like defects created on the RGO surface during the preparatory biphasic reduction process. Finally, the RGO/GCE exhibits no obvious cathodic peaks under anaerobic conditions, thereby confirming the catalytic activity of the biphasically synthesized RGO towards the ORR (Figure 4-9).

4.3.3. Biphasic shake-flask reactions

The catalytic reduction of O_2 by RGO sheets was also investigated by shake-flask experiments where the polarization of the water/DCE interface was controlled chemically by distribution of a highly hydrophobic anion (TB^-), as described in Scheme 4-1B. Under such conditions, the water/DCE interface is polarized positively,²⁷ and TB^- acts as a pump to drive H^+ from w to o to form the organic acid HTB. Evidence of the enhancement in the rate of the oxidation of the electron donors by the *in situ* generated RGO is clearly seen by comparing the UV/Vis spectra of products in o (either decamethylferrocenium ($DMFc^+$) or Fc^+ ions pre-

and post-shake-flask, with and without GO present) and noting the increased production of the biphasic reaction ($\lambda_{\text{max}} = 779$ and 620 nm, respectively) in the presence of GO (Figure 4-10). The data obtained in the absence of GO is in perfect agreement with that previously reported.³¹

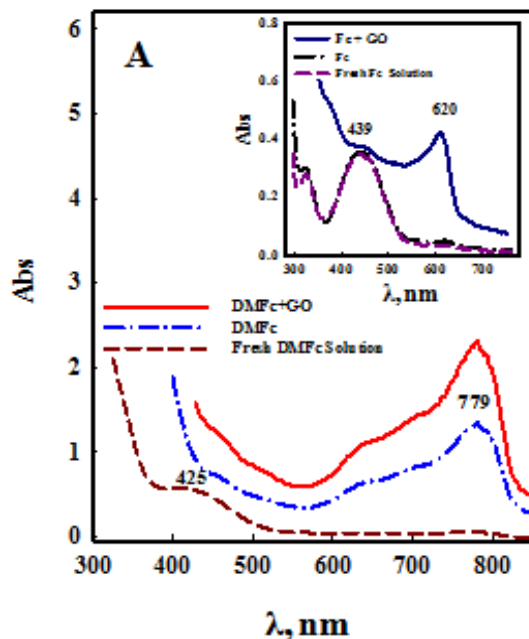


Figure 4-10. Biphasic “shake-flask” experiments performed using the cell outlined in **Scheme 4-1B**. UV/Vis absorption spectra of the DCE phase comparing shake-flask experiments after 10 min of biphasic reaction containing DMFc only (dash-dotted line, blue, $a = 2.5$, $b = 0$, $c = 10$, $d = 100$) and both DMFc and GO (solid line, red, $a = 2.5$, $b = 0.2$, $c = 10$, $d = 100$) with that of a fresh (*i.e.* unreacted) solution of 2.5 mM DMFc in DCE (dashed line, brown). Inset: Analogous UV/Vis spectra of the DCE phase except using Fc as the electron donor and extending the biphasic reaction time to 30 min, *i.e.* comparison of Fc only (dash-dotted line, black, $a = 2.5$, $b = 0$, $c = 10$, $d = 100$) and both DMFc and GO (solid line, blue, $a = 2.5$, $b = 0.2$, $c = 10$, $d = 100$) with a fresh (*i.e.* unreacted) solution of 2.5 mM Fc in DCE (dashed line, purple).

4.3.4. Chemical kinetics

Quantitative real-time monitoring of DMFc^+ or Fc^+ was possible by following changes in their particular UV/Vis spectra with time at 779 and 620 nm, respectively (Figure 4-11). The resultant kinetically limited time profiles of the formation of DMFc^+ or Fc^+ in the absence and presence of GO show that the oxidation of the electron donors proceeds much faster in the presence of GO in water.

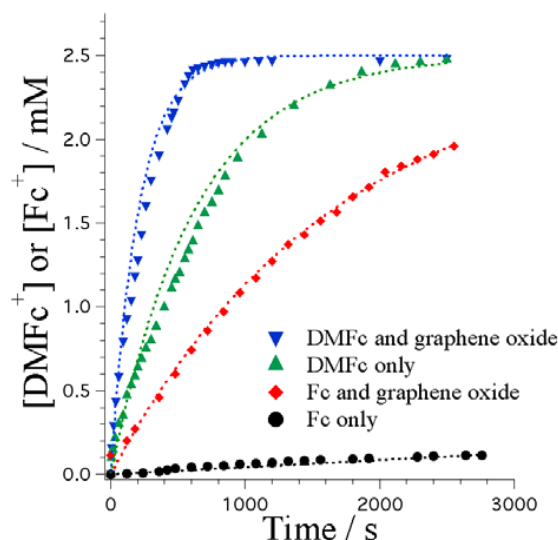


Figure 4-11. Kinetics of the biphasic oxidation of the electron donors in the absence and presence of graphene oxide (GO). Monitoring the formation of DMFc^+ and Fc^+ via chemically controlled polarization, see **Scheme 4-1B**, in the absence or presence of GO ($a = 2.5$, $b = 0$ or 0.2 , $c = 10$, $d = 100$), as followed by recording changes in the UV/Vis absorbance at $\lambda_{\text{max}} = 779$ and 620 nm, respectively, under aerobic conditions.

The rate of the ORR was found to be first order with respect to $[\text{DMFc}]$ or $[\text{Fc}]^{24}$ in the presence of GO by plotting the natural logarithm of the reaction rate ($\ln(v)$; estimated by the derivative of a polynomial fit of the measured data) vs. the natural logarithm of $[\text{DMFc}]$ or $[\text{Fc}]$ as shown in Figure 4-12A. In the absence of GO, the rate of the ORR was once more found to be first order with respect to $[\text{DMFc}]$. However, the reaction proceeded very slowly with Fc in the absence of GO, to the extent that fitting of the data was ambiguous. Thus, the rate of ORR was assumed to be first order with respect to $[\text{Fc}]$ in the absence of GO for comparative reasons.

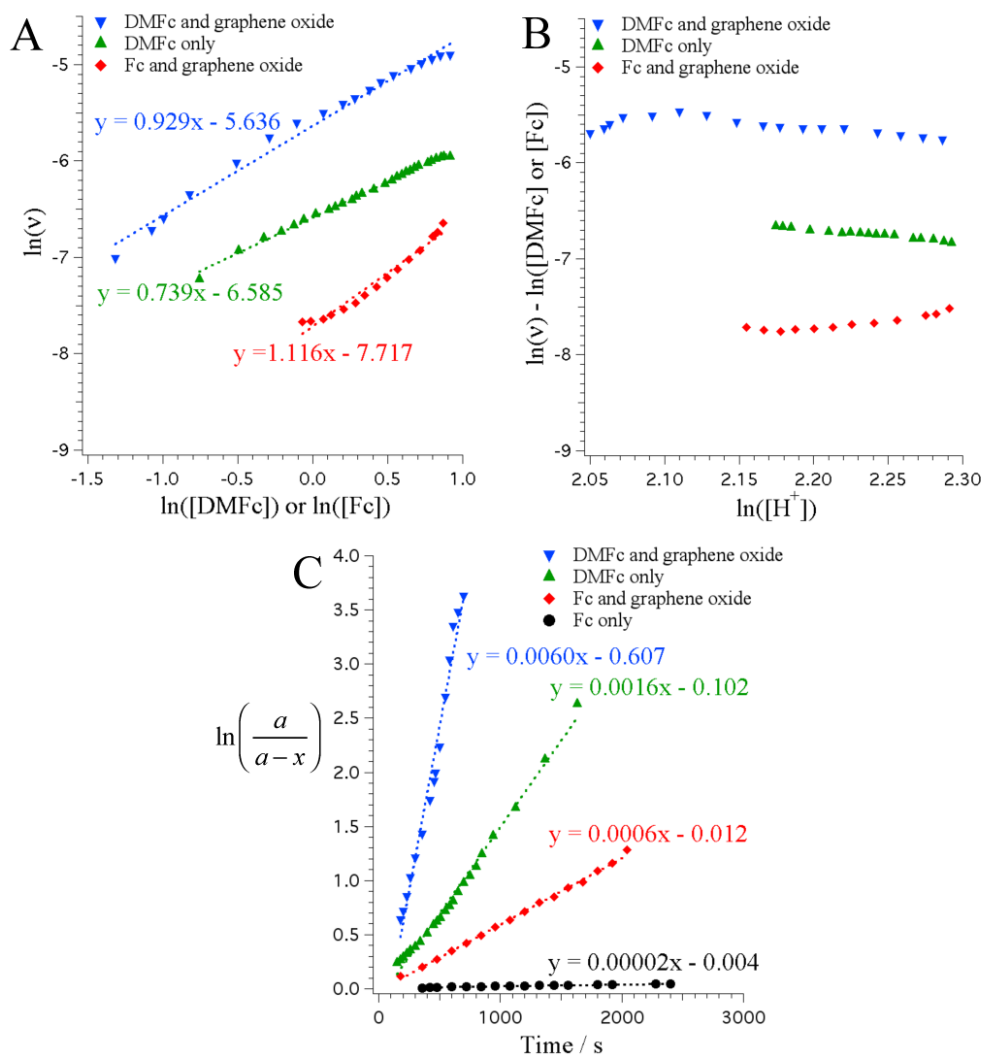


Figure 4-12. Determination of the rate orders and rates of reaction (k) for the biphasic cell outlined in **Scheme 4-1B** for DMFc with and without GO or Fc with GO ($a = 2.5$, $b = 0$ or 0.2 , $c = 10$, $d = 100$). (A) Rate order determination with respect to [DMFc] or [Fc], (B) rate order determination with respect to $[H^+]$ and (C) plot of the integrated rate law, see Equation 4-3, for a first order reaction.

Subsequently, the reaction rate was found to be independent of proton concentration, when $[H^+] > 1$ mM, in the presence of GO with either DMFc or Fc present in the organic phase, and in the absence of GO with DMFc, by plotting $\ln(v) - \ln([DMFc])$ or $\ln([Fc])$ vs. $\ln([H^+])$ (Figure 4-12B).

Therefore, the rate of reaction for the biphasic ORR in the absence and presence of GO with either DMFc or Fc present in the organic phase may be expressed as

$$v = \frac{d[DMFc^+]}{dt} \text{ or } \frac{d[Fc^+]}{dt} = k[DMFc] \text{ or } k[Fc] \quad (4-2)$$

where k is the apparent rate constant of the reaction. The integrated rate law was expressed as⁵³

$$kt = \ln \frac{a}{a-x} \quad (4-3)$$

where a is the initial concentration of DMFc or Fc in DCE and x is the concentration of DMFc⁺ or Fc⁺. Plots of the right-hand side of equation 4-3 as a function of time gave straight lines with a slope of k (Figure 4-12C). These calculated apparent rate constants for the ORR with and without GO either in the presence of DMFc or Fc as an electron donor were tabulated in Table 4-2 and used to determine the theoretical [DMFc⁺] or [Fc⁺] in DCE as a function of time. The theoretical curves, dotted lines in Figure 4-11, match the experimental data precisely, thereby confirming the validity of the assumed rate equation. It can be seen from Table 4-2 that increases in the rate of *ca.* 3.75 and 30 times were observed for DMFc and Fc, respectively, with GO. The large difference in the rate increase by GO for Fc and DMFc can come from the more evident mass transfer limitations when DMFc was employed as the electron donor.

Table 4-2. Apparent rate constants (k/s^{-1}) for the biphasic reaction and the corresponding catalyst-enhancement factor ($k/k_{\text{no cat}}$).

Electron donor/catalyst	k/s^{-1}	$k/k_{\text{no cat}}$
DMFc only	0.0016	1
DMFc and GO	0.0060	3.75
Fc only	0.00002	1
Fc and GO	0.0006	30

It has to be stressed that when GO is present, the increase in rate can be attributed to the oxidation of the electron donor when electrons are consumed to convert GO to RGO at the interface as well as to the subsequent RGO-catalyzed ORR reaction. The precise contribution of each process to the apparent rate was not deconvoluted during this study.

4.3.5. Hydrogen peroxide detection and yield

Finally, quantitative increases in concentration of the other biphasic reaction product, H₂O₂ in w, post shake-flask reaction for both electron donors in the presence and absence of GO were confirmed by NaI titration, where H₂O₂ oxidizes I⁻ to I³⁻, shown in Figure 4-13, Table 4-3. This is a crucial finding with regard to the use of Fc as a reductant as the increased

quantity of H_2O_2 found in the presence of GO clearly shows that Fc not only reduces GO but is also categorically involved in the ORR step. Under biphasic aerobic conditions, DMFc is fully converted to DMFc^+ after 1 h, both in the presence and absence of GO. As a result, the quantities of H_2O_2 produced after 1 h in the presence or absence of GO for DMFc were identical within experimental error ($\pm 5\%$ H_2O_2 yield), see Table 4-3. Fc, on the other hand, is substantially converted to Fc^+ after 1 h in the presence of GO (88.4%) but significantly less so in its absence (6.96 %). The more rapid conversion of Fc in the presence of GO suggests a considerable portion of the electrons donated by Fc are consumed to reduce GO to RGO. The remaining electrons are subsequently used in the RGO catalysed reduction of O_2 with Fc, and the catalysis effect is reflected in the larger concentration of H_2O_2 detected with Fc in the presence of GO after 1 h. The relatively low yields of H_2O_2 (calculated as discussed in Table 4-3) were expected and are primarily a consequence of a portion of the available electrons being consumed to produce RGO *in situ*. It should be noted that the partial decomposition or further reduction of H_2O_2 by the action of transition metal compounds such as DMFc and Fc prior to detection using the NaI method may also lower the yield.⁸ Thus, an inference may be made that despite a portion of the electrons being consumed during the reaction to generate RGO *in situ*, the remaining electrons are utilized more efficiently during the RGO catalyzed ORR (the mechanism of which is discussed below), thereby generating higher concentrations of H_2O_2 on shorter time scales in the presence of either electron donor.

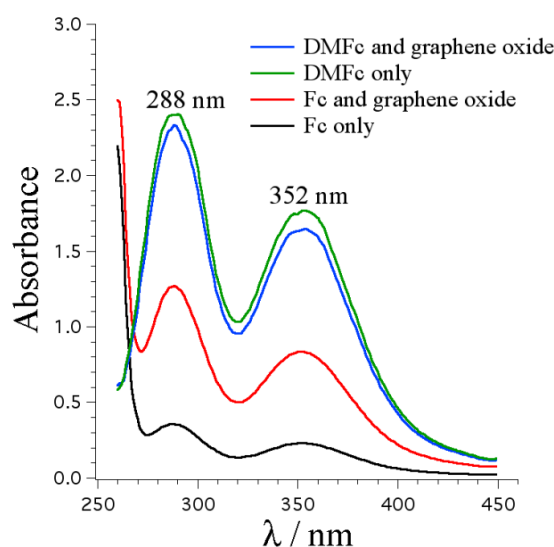


Figure 4-13. Monitoring the formation of H_2O_2 . UV/Vis absorption spectra of the aqueous phase after shake-flask reactions upon treatment with excess NaI for cells containing DMFc (the aqueous phase was diluted 10-fold prior to analysis) or Fc (aqueous phase undiluted), under aerobic conditions, either with or without GO ($a = 2.5$, $b = 0$ or 0.2 , $c = 10$, $d = 100$, see **Scheme 4-1B**). The reaction time for all experiments was 1 h.

Table 4-3. Detected H_2O_2 after shake-flask reaction for cells containing DMFc or Fc, under aerobic conditions, either with or without GO ($a = 2.5$, $b = 0$ or 0.2 , $c = 10$, $d = 100$, see **Scheme 4-1B**). H_2O_2 was detected by NaI titration (see **Figure 4-13**). Reaction time for all experiments was 1 h.

Electron donor/catalyst	Detected H_2O_2 / mM	Conversion ^[a] / %	H_2O_2 per oxidized donor yield ^[b,c] / %
DMFc only	0.576	100	46.08
DMFc and GO	0.535	100	42.80
Fc only	0.0064	6.96	7.36
Fc and GO	0.026	88.4	2.35

^aThe conversion represents the ratio of the concentration of produced DMFc⁺ (or Fc⁺) detected by UV/Vis spectroscopy (after 1 h of shake-flask reaction) to the initial concentration of DMFc (or Fc) present in the cell.

^bThe yield of H_2O_2 represents the ratio of the detected concentration of H_2O_2 (from NaI titration) to the theoretical H_2O_2 concentration, which is calculated stoichiometrically from the concentration of DMFc⁺ (or Fc⁺) after 1 h of reaction. ^cThe results were verified by using two alternative methods to determine H_2O_2 concentrations in the aqueous phase, namely a Prussian Blue (PB) sensor⁵⁴ and a titanium-oxalate methodology⁵⁵ (data not shown). A very good agreement was found among all strategies employed.

4.3.6. Mechanism

The results herein clearly show that RGO prepared *in situ* at the liquid/liquid interface is a catalyst towards the ORR. A key feature is that O_2 reduction stops at the peroxide stage, enabling its use as a catalyst for the synthesis of H_2O_2 . This catalytic activity can be attributed to surface-bound oxygen-containing groups remaining at defect sites on the RGO sheets after reduction, as revealed by spectroscopic and electrochemical experiments. It is expected that the reduction of O_2 proceeds *via* a $2\text{e}^-/2\text{H}^+$ mechanism to yield H_2O_2 , in which the quinone-type groups at the surface of the RGO sheets (RGO-Q) are initially chemically reduced to semiquinone radicals (RGO-Q[•]) by an electron donor, such as DMFc or Fc in our case. Advantageously, DMFc and Fc are capable of injecting their electrons anywhere on the RGO backbone, thereby greatly increasing the cross-section of reaction between the electron donor and catalytic substrate. The rate-determining step (RDS) is expected to be the reaction between the chemically generated semiquinone radicals, adsorbed protons, and O_2 , resulting in the formation of a protonated intermediate superoxo species (RGO-Q-HO₂[•]). Proton adsorption is critical to increase the reduction rate by accelerating the protonation of O_2 . Further reduction by DMFc or Fc, and simultaneous reaction with an additional adsorbed proton, enables the release of H_2O_2 and the regeneration of the quinone-type groups at the surface of RGO (see equations 4-4 to 4-6). This mechanism of quinone-mediated reduction of

molecular O_2 to H_2O_2 is consistent with previous reports for O_2 reduction at quinone-modified electrode surfaces.^{7,56,57}



in which the electrons (e^-) are injected by DMFc or Fc.

4.4. Conclusions

In summary, a new approach for a two-phase reduction of O_2 has been developed by partially reducing GO at the ITIES. The resulting RGO is an efficient catalyst for the ORR because of quinone-type catalysis *via* the formation of a superoxo intermediate. The catalytic activity of RGO has been verified in this work by using two different reducing species, namely DMFc and Fc, of different electron-donating ability. The biphasic features of the employed strategy favor the collection of H_2O_2 by immediate extraction to the water phase and, thus, preventing further side reactions with organic solubilized Fc-derivatives or degradation in the DCE phase. In general, RGO could be considered for a biphasic H_2O_2 batch-production scheme where, upon completion of the cycle described above, the oxidized donor, *i.e.* $DMFc^+$ or Fc^+ , is recycled electrochemically in the same biphasic system after extraction of the solid RGO phase (see Figure 4-14). A two-step process is envisioned, in which the oxidized lipophilic electron donor is reduced at a cathode and the O_2 and protons are produced at the anode after replacement of the H_2O_2 solution with a fresh aqueous solution. In such a biphasic electrolysis system, the reduction of the oxidized donor is accompanied by a transfer of aqueous protons from the aqueous to the organic phase to regenerate the organic acid, HTB.

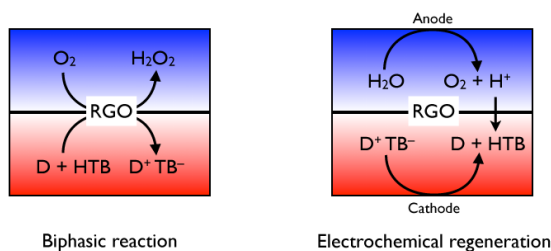


Figure 4-14. Possible batch production of H_2O_2 based on a RGO liquid/liquid interface system, in which D is an electron-donating species, such as DMFc or Fc.

4.5. References

- (1) Shao, Y. In *Handbook of Electrochemistry*; Zoski, C. G., Ed.; Elsevier: Amsterdam, 2007, p 785.
- (2) Méndez, M. A.; Partovi-Nia, R.; Hatay, I.; Su, B.; Ge, P.; Olaya, A.; Younan, N.; Hojeij, M.; Girault, H. H. *Phys. Chem. Chem. Phys.* **2010**, *12*, 15163.
- (3) Fukuzumi, S.; Okamoto, K.; Gros, C. P.; Guillard, R. J. *Am. Chem. Soc.* **2004**, *126*, 10441.
- (4) Trojánek, A.; Mareček, V.; Jänchenová, H.; Samec, Z. *Electrochem. Commun.* **2007**, *9*, 2185.
- (5) Peljo, P.; Murtomäki, L.; Kallio, T.; Xu, H. J.; Meyer, M.; Gros, C. P.; Barbe, J. M.; Girault, H. H.; Laasonen, K.; Kontturi, K. *J. Am. Chem. Soc.* **2012**, *134*, 5974.
- (6) Hatay, I.; Su, B.; Méndez, M. A.; Corminboeuf, C.; Khoury, T.; Gros, C. P.; Bourdillon, M.; Meyer, M.; Barbe, J. M.; Ersoz, M.; Zálíš, S.; Samec, Z.; Girault, H. H. *J. Am. Chem. Soc.* **2010**, *132*, 13733.
- (7) Trojánek, A.; Langmaier, J.; Samec, Z. *Electrochem. Commun.* **2006**, *8*, 475.
- (8) Campos-Martin, J. M.; Blanco-Brieva, G.; Fierro, J. L. G. *Angew. Chem., Int. Ed.* **2006**, *45*, 6962.
- (9) Chen, Q. *Chem. Eng. Process. Process Intensif.* **2008**, *47*, 787.
- (10) Lu, S.; Wang, L.; Wang, Y.; Mi, Z. *Chem. Eng. Technol.* **2011**, *34*, 823.
- (11) Nishimi, T.; Kamachi, T.; Kato, K.; Kato, T.; Yoshizawa, K. *Eur. J. Org. Chem.* **2011**, *2011*, 4113.
- (12) Wass, J. R. T. J.; Ahlberg, E.; Panas, I.; Schiffrin, D. J. *Phys. Chem. Chem. Phys.* **2006**, *8*, 4189.
- (13) Fukuzumi, S.; Yamada, Y.; Karlin, K. D. *Electrochim. Acta* **2012**, *82*, 493.
- (14) Geim, A. K.; Novoselov, K. S. *Nat. Mater.* **2007**, *6*, 183.
- (15) Geim, A. K. *Science* **2009**, *324*, 1530.
- (16) Stoller, M. D.; Park, S.; Zhu, Y.; An, J.; Ruoff, R. S. *Nano Lett.* **2008**, *8*, 3498.
- (17) McAllister, M. J.; Li, J.-L.; Adamson, D. H.; Schniepp, H. C.; Abdala, A. A.; Liu, J.; Herrera-Alonso, M.; Milius, D. L.; Car, R.; Prud'homme, R. K.; Aksay, I. A. *Chem. Mater.* **2007**, *19*, 4396.
- (18) Allen, M. J.; Tung, V. C.; Kaner, R. B. *Chem. Rev.* **2009**, *110*, 132.
- (19) Chen, D.; Feng, H.; Li, J. *Chem. Rev.* **2012**, *112*, 6027.
- (20) Tang, L.; Wang, Y.; Li, Y.; Feng, H.; Lu, J.; Li, J. *Adv. Funct. Mater.* **2009**, *19*, 2782.
- (21) Shao, Y.; Wang, J.; Engelhard, M.; Wang, C.; Lin, Y. *J. Mater. Chem.* **2010**, *20*, 743.
- (22) Wu, J.; Wang, Y.; Zhang, D.; Hou, B. *J. Power Sources* **2011**, *196*, 1141.
- (23) Kalita, G.; Sharma, S.; Wakita, K.; Umeno, M.; Hayashi, Y.; Tanemura, M. *Phys. Chem. Chem. Phys.* **2013**, *15*, 1271.
- (24) Ge, P.; Scanlon, M. D.; Peljo, P.; Bian, X.; Vubrel, H.; O'Neill, A.; Coleman, J. N.; Cantoni, M.; Hu, X.; Kontturi, K.; Liu, B.; Girault, H. H. *Chem. Commun.* **2012**, *48*, 6484.
- (25) Deng, H.; Peljo, P.; Cortés-Salazar, F.; Ge, P.; Kontturi, K.; Girault, H. H. *J. Electroanal. Chem.* **2012**, *681*, 16.
- (26) Gao, F.; Yang, Y.; Liu, J.; Shao, H. *Ionics* **2010**, *16*, 45.
- (27) Wandlowski, T.; Mareček, V.; Samec, Z. *Electrochim. Acta* **1990**, *35*, 1173.
- (28) Trojánek, A.; Langmaier, J.; Ebera, J.; Záli, S.; Barbe, J. M.; Girault, H. H.; Samec, Z. *Chem. Commun.* **2011**, *47*, 5446.
- (29) Hatay, I.; Ge, P. Y.; Vrubel, H.; Hu, X.; Girault, H. H. *Energy Environ. Sci.* **2011**, *4*, 4246.
- (30) Su, B.; Nia, R. P.; Li, F.; Hojeij, M.; Prudent, M.; Corminboeuf, C.; Samec, Z.; Girault, H. H. *Angew. Chem., Int. Ed.* **2008**, *47*, 4675.

- (31) Partovi-Nia, R.; Su, B.; Li, F.; Gros, C. P.; Barbe, J. M.; Samec, Z.; Girault, H. H. *Chem.-Eur. J.* **2009**, *15*, 2335.
- (32) Zhou, Y.; Zhang, G.; Chen, J.; Yuan, G. e.; Xu, L.; Liu, L.; Yang, F. *Electrochem. Commun.* **2012**, *22*, 69.
- (33) Nieminen, J. J.; Hatay, I.; Ge, P.; Méndez, M. A.; Murtomäki, L.; Girault, H. H. *Chem. Commun.* **2011**, *47*, 5548.
- (34) Meyer, J. C.; Geim, A. K.; Katsnelson, M. I.; Novoselov, K. S.; Booth, T. J.; Roth, S. *Nature* **2007**, *446*, 60.
- (35) Dreyer, D. R.; Murali, S.; Zhu, Y.; Ruoff, R. S.; Bielawski, C. W. *J. Mater. Chem.* **2011**, *21*, 3443.
- (36) Guo, H.-L.; Wang, X.-F.; Qian, Q.-Y.; Wang, F.-B.; Xia, X.-H. *ACS Nano* **2009**, *3*, 2653.
- (37) Park, S.; Ruoff, R. S. *Nat. Nanotechnol.* **2009**, *4*, 217.
- (38) Yang, G.; Zhang, G.; Sheng, P.; Sun, F.; Xu, W.; Zhang, D. *J. Mater. Chem.* **2012**, *22*, 4391.
- (39) Yin, Z.; Sun, S.; Salim, T.; Wu, S.; Huang, X.; He, Q.; Lam, Y. M.; Zhang, H. *ACS Nano* **2010**, *4*, 5263.
- (40) Zhang, J.; Yang, H.; Shen, G.; Cheng, P.; Zhang, J.; Guo, S. *Chem. Commun.* **2010**, *46*, 1112.
- (41) Moon, I. K.; Lee, J.; Ruoff, R. S.; Lee, H. *Nat. Commun.* **2010**, *1*.
- (42) Paredes, J. I.; Villar-Rodil, S.; Martínez-Alonso, A.; Tascón, J. M. D. *Langmuir* **2008**, *24*, 10560.
- (43) Pham, V. H.; Pham, H. D.; Dang, T. T.; Hur, S. H.; Kim, E. J.; Kong, B. S.; Kim, S.; Chung, J. S. *J. Mater. Chem.* **2012**, *22*, 10530.
- (44) Li, D.; Mueller, M. B.; Gilje, S.; Kaner, R. B.; Wallace, G. G. *Nat. Nanotechnol.* **2008**, *3*, 101.
- (45) Tuinstra, F.; Koenig, J. L. *J. Chem. Phys.* **1970**, *53*, 1126.
- (46) Ramesha, G. K.; Sampath, S. *J. Phys. Chem. C* **2009**, *113*, 7985.
- (47) Zhang, L. L.; Zhao, X.; Stoller, M. D.; Zhu, Y.; Ji, H.; Murali, S.; Wu, Y.; Perales, S.; Clevenger, B.; Ruoff, R. S. *Nano Lett.* **2012**, *12*, 1806.
- (48) Whitworth, A. L.; Mandler, D.; Unwin, P. R. *Phys. Chem. Chem. Phys.* **2005**, *7*, 356.
- (49) Azevedo, J.; Bourdillon, C.; Derycke, V.; Campidelli, S.; Lefrou, C.; Cornut, R. *Anal. Chem.* **2012**, *85*, 1812.
- (50) Zhang, J.; Barker, A. L.; Mandler, D.; Unwin, P. R. *J. Am. Chem. Soc.* **2003**, *125*, 9312.
- (51) Stankovich, S.; Dikin, D. A.; Piner, R. D.; Kohlhaas, K. A.; Kleinhammes, A.; Jia, Y.; Wu, Y.; Nguyen, S. T.; Ruoff, R. S. *Carbon* **2007**, *45*, 1558.
- (52) Tammeveski, K.; Kontturi, K.; Nichols, R. J.; Potter, R. J.; Schiffrin, D. J. *J. Electroanal. Chem.* **2001**, *515*, 101.
- (53) Atkins, P. W. *Physical Chemistry, 4th ed.*; Oxford University Press: Oxford, 1990.
- (54) Karyakin, A. A. *Electroanalysis* **2001**, *13*, 813.
- (55) Sellers, R. M. *Analyst* **1980**, *105*, 950.
- (56) Xu, J.; Huang, W.; McCreery, R. L. *J. Electroanal. Chem.* **1996**, *410*, 235.
- (57) Yang, H. H.; McCreery, R. L. *J. Electrochem. Soc.* **2000**, *147*, 3420.

Chapter 5

Kinetics and Mechanism of Oxygen Reduction by Metallocenes in Single and Biphasic Liquid Phases

Based on J. Electroanal. Chem. 2014, 729, 43.

5.1. Introduction

The oxygen reduction reaction (ORR) has been investigated extensively over the past 30 years owing in part to its biological significance^{1,2} as well as possible applications in fuel cell technologies.³⁻¹¹ In biological systems, oxygen is an electron acceptor in the electron transport chain; this is a key step in cellular respiration that occurs as a trans-membrane process ultimately generating adenosine triphosphate (ATP), the so-called ‘energy currency’ of the cell, and is housed predominately in the mitochondria.^{1,2}

The interface between two immiscible electrolytic solutions (ITIES) provides a useful biomimetic utility for the investigation of trans-membrane processes, like ORR.¹²⁻¹⁷ The liquid/liquid interface behaves as the junction for charge separation such that the two phases are typically composed of water (w) and an organic solvent, such as 1,2-dichloroethane (DCE);¹²⁻¹⁵ indeed, this is similar to the behavior exhibited at biological membranes. The potential across the ITIES, called the Galvani potential difference, can be controlled in two ways. First, ions of intermediate solubility can be dissolved in one phase so that their partitioning across the interface generates a potential difference.^{18,19} More commonly, the potential can be controlled externally through the use of a potentiostat and electrodes immersed in either phase.¹²⁻¹⁵ In this second case, electrochemical measurements can be acquired and are analogous to those obtained through conventional solid-solution, or solid-electrolyte, interfaces. For liquid/liquid electrochemistry, the potentials in the water, ϕ_w , and organic, ϕ_o , phases can be used to control the Galvani potential difference, $\Delta_o^w\phi = \phi_w - \phi_o$, which then becomes the driving force for ion transfer (IT).^{12,13}

Biphasic ORR is a key chemical process that has been studied extensively^{6,16,20-25} over the past decade by groups such as Kihara *et al.*,²⁶ Samec *et al.*,²⁴ Opallo *et al.*,²⁵ as well as our group,^{20,22,23,27} as discussed in Section 1.3 in Chapter 1. These studies have typically used an organometallic catalyst, for example porphyrins, along with an electron donor, such as ferrocene (Fc) or decamethylferrocene (DMFc).^{23,24} As demonstrated recently using biscobalt co-facial porphyrins,²³ oxygen, through a proposed mechanism studied using density

functional theory (DFT), is first bound to the metal center, while acid in the aqueous phase and a Fc derivative in the organic phase provided the protons and electrons, respectively. ORR can also take place without the addition of a catalyst, *i.e.* that DMFc and other Fc derivatives can perform ORR, albeit at reduced rates of reaction;^{21,24} the mechanism of this reaction was again investigated using DFT calculations where it differed somewhat from the porphyrin catalyzed pathway. Therein, the first step was proton binding to the iron center to form DMFc-H⁺.²¹ This would subsequently react with dissolved oxygen to form a hydrogen peroxy radical species that, through further steps, generates the reduction products H₂O₂ or water.²¹

The ORR is of considerable importance at both solid-electrolyte²⁸⁻³⁰ and liquid/liquid^{6,20-26} interfaces owing to its role in fuel cell and energy conversion applications. The liquid/liquid interface, between water and an organic solvent, affords several advantages over conventional solid-electrolyte studies in that aqueous acids, such as HCl or H₂SO₄, can be employed while organic acids can be avoided – such as would be necessary for a homogenous organic solvent approach. Additionally, many hydrophobic organometallic catalysts are available, whilst there are very few water-soluble versions that would be required for a single-phase aqueous system. In this way, the two phases provide a convenient method for separating reagents and using existing compounds, while the liquid/liquid interface behaves as a junction for charge separation and is a facile biomimetic.^{12,13} With this in mind, biphasic electrochemistry at a large ITIES (centimeter scale) was used to investigate the ORR.

Understanding the thermodynamics/kinetics as well as the mechanism of ORR at biphasic system is advantageous as it allows for a modicum of prediction towards possible successful avenues of future research by highlighting significant structural, physicochemical, or reaction conditions. Generally, there are two ways to reach this aim: either homogeneous using an organic acid or heterogeneous using an aqueous inorganic acid but with the Galvani potential controlled externally, as mentioned above. In this way, firstly ORR in the bulk DCE phase in the presence of an organic acid was studied by *in-situ* absorption spectroscopy, mainly including three aspects: 1) acid in constant concentration but with various concentrations of DMFc; 2) DMFc in constant concentration but with various concentrations of acid; 3) effect of counter-anions and water on the ORR kinetics. The results showed that ORR in the DCE phase is not a simple elementary reaction but composed of multiple steps, so other ways to improve the understanding of these reactions are needed. Computational analysis in the form of DFT²¹ and finite element analysis, or method (FEM),³¹⁻³⁴ has been used, in tandem with experimental data, to confirm or elucidate proposed reaction pathways. Herein, COMSOL Multiphysics software employing FEM was utilized, with comparison to experimental curve features found in the cyclic voltammetric (CV) experimental data, to further understand ORRs facilitated by DMFc, 1,1'-dimethylferrocene (DMFc), and Fc at the w/DCE interface. In this case, it is proposed that DMFc, dissolved in the organic phase, reacts with protons pumped across the interface through three reaction steps to reduce dissolved oxygen (O₂) to hydrogen peroxide (H₂O₂).

5.2. Experimental

5.2.1. Chemicals

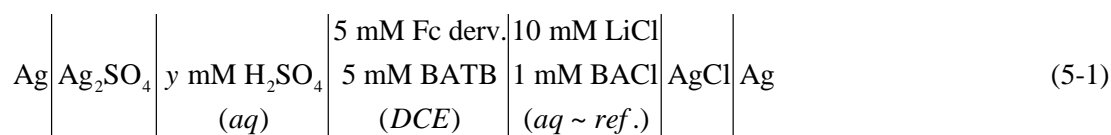
The common chemicals used throughout this Chapter have been summarized in Section 2.2 in Chapter 2. HTB (10 mM) in DCE was prepared by shaking 10 mM LiTB and 50 mM H₂SO₄ in water phase with equal volume of pure DCE for 1 h. Then the DCE phase was separated from the aqueous phase and the concentration of HTB was assumed to be 10 mM.²¹ As DCE phase is saturated with water, water concentration is 127 mM.³⁵ This 10 mM HTB in DCE was used as stock solutions for preparing the target concentrations of HTB. DMFc solutions were prepared gravimetrically using commercial DCE (without saturation by water) before experiments. Pt-disk microelectrodes were prepared as has been previously described in Section 2.3.4.2 in Chapter 2.^{22,34}

5.2.2. Homogeneous reactions measurements

In-situ UV/Vis spectra were obtained on an Ocean Optics CHEM 2000 spectrophotometer with a 1 cm path-length quartz cuvette (4 mL in volume), stirred magnetically at a constant rate of 600 rpm (see Section 2.4.1.2 in Chapter 2 for details). During reaction, the cuvette was equipped with a Teflon cap to prevent evaporation of the organic phase. Generation of DMFc⁺ was measured at 779 nm. As the UV/Vis signal is not very stable, the absorbance at 900 nm (where there is no absorption by any species) was measured as a background, and subtracted from the signal at 779 nm. 1.5 mL of DMFc solution was added to the cuvette, and the residual amount of DMFc⁺ (existed in the commercial product) in the solution was evaluated from the UV/Vis signal. Then 1.5 mL of HTB solution was added to the cuvette, and evolution of the production of DMFc⁺ was measured with time. The molar extinction coefficients (ϵ) of DMFc⁺ at 779 nm in 1,2-DCE used for calculating the concentration of produced DMFc⁺ is 0.632 mM⁻¹·cm⁻¹.³⁶ Specific initial concentrations of the reactant mixtures (DMFc and HTB) are described in Section 5.4.1 of this chapter.

5.2.3. Electrochemical measurements

Electrochemical measurements were performed under aerobic conditions, unless otherwise stated, inside a Faraday cage using an Autolab PGSTAT100 (Ecochemie, the Netherlands) four electrode potentiostat. The working and counter electrode leads were attached to platinum wires fixed in either phase and used to monitor the current, while two reference electrodes immersed in either phase, made proximal to the ITIES through the use of Luggin capillaries incorporated in the cell design, were used to control the interfacial potential (where it is effectively described relative to the aqueous phase). BATB was the organic phase supporting electrolyte and sulfuric acid was the source of protons as well as the supporting electrolyte in the aqueous phase in the following electrochemical cell:



Where the concentration of H_2SO_4 (y) was changed from 0.5 mM to 5, 50, and 500 mM, while 'Fc deriv.' was either DMFc, DFC, or Fc as indicated.

5.2.4. Computations

All computations were carried out using COMSOL Multiphysics 3.5a on a Macintosh computer with four 2.66 GHz Intel Xeon processors, 9.8 GB of RAM, and the Ubuntu operating system; each simulation required approximately 25 to 30 minutes to complete.

5.3. Simulation (*carried out by T. Jane Stockmann*)

COMSOL Multiphysics version 3.5a, and similar programs utilizing FEM, have been used successfully to simulate a wide variety of processes including surface analysis through scanning electrochemical microscopy,^{15,37} human neural response to an applied electric field for research into the treatment of Parkinson's disease,³⁸ two-dimensional bipolar electrochemistry,³⁹ solid oxide fuel cells,⁴⁰ and IT at an ITIES.^{15,31-34,41,42} Owing to the incorporation of geometry within the simulation environment, the results take on new meaning beyond those possible with simple numerical computations. Indeed, these types of simulations have been used to predict possible changes in the current-potential response of IT processes brought about by varying geometries of a micro-ITIES held at the tip of a micropipette.^{31,33,42}

An advantage of COMSOL software is the ability to solve multiple equations, linear or non-linear, simultaneously, such that the diffusion of species through a solution can be coupled with heterogeneous or homogeneous chemical reactions as well as IT. This aspect is of considerable interest in complex, multi-step reactions where it is difficult to differentiate between possible mechanistic pathways. As an example, Kakiuchi *et al.*³² used this technique to elucidate the mechanism and kinetics/thermodynamics of interfacial complexation reactions between metal ions dissolved in an aqueous phase and ionophores placed in an ionic liquid; in that report,³² they compared experimentally obtained CVs with simulated ones. Herein, COMSOL is used to evaluate a possible ORR pathway at the w/DCE interface in a similar way, through comparison to features present in CV experimental data.

Figure 5-1A illustrates a typical large (centimeter scale) four electrode liquid/liquid electrolytic cell, including a blow-up of the ITIES with the two dimensional simulation geometry marked using a red box. Figure 5-1B displays the details of the simulation environment which constituted a radial cross-section of the circular ITIES including the subdomains 1 and 2 used to represent the organic (o) and water (w) phases, respectively. These subdomains are enclosed by ten external boundaries and divided by one internal boundary such that the geometry is a two-dimensional cross-section of the area surrounding the ITIES; in order to reduce computational time further it was recognized that a radial axis-of-symmetry remained, perpendicular to the interface and the simulation environment was reduced by half. A detailed description of the simulation boundary conditions have been given in the caption of Figure 5-1; however, boundary 5 is significant as it was the w/o interface and was used to describe the flux of species – its boundary condition was set as 'flux'. IT at boundary 5, of the form:

$$i_w^{z_i} \rightleftharpoons i_o^{z_i} \quad (5-2)$$

where ion i of charge z_i transfers from w to o, was approximated using Butler-Volmer kinetics which describe the forward (k_f) and reverse (k_b) rate constants through the following, facile potential dependent equations:

$$k_f = k^0 \exp\left[-\alpha f(\Delta_o^w \phi - \Delta_o^w \phi^{0'})\right] \quad (5-3)$$

$$k_b = k^0 \exp\left[(1-\alpha) f(\Delta_o^w \phi - \Delta_o^w \phi^{0'})\right] \quad (5-4)$$

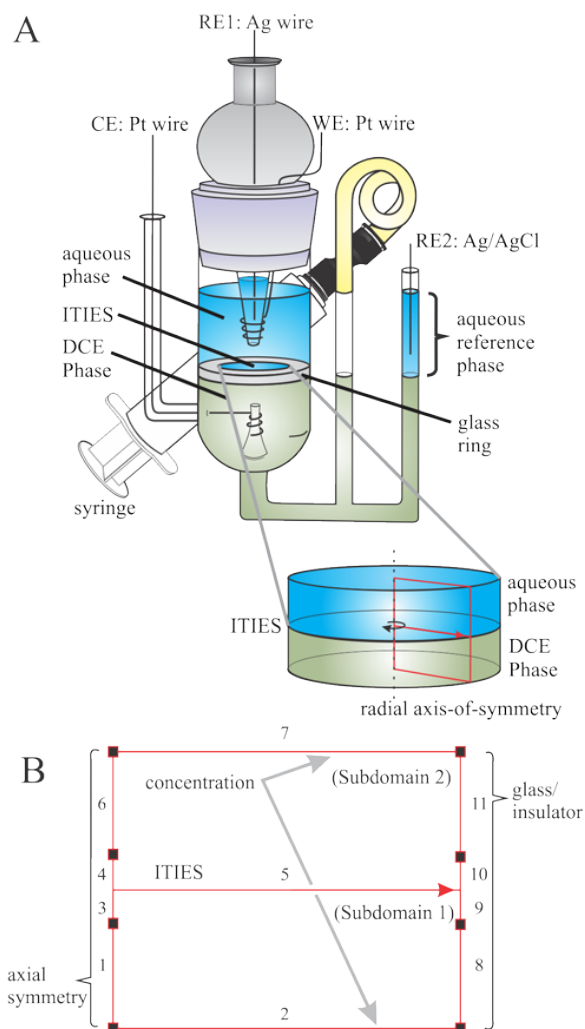


Figure 5-1. A, a typical large (centimeter) four electrode, glass electrolytic cell that is open to the atmosphere (*i.e.* not air-tight) used for liquid/liquid electrochemical experiments. Also shown is a blow-up of the interface with the 2-D area representing the geometry of the simulation marked in red. B, Illustrates the 2-D radial cross-

section of the large ITIES used as the simulation geometry and drawn in COMSOL Multiphysics. The geometry was composed of subdomains 1 and 2 for the organic and aqueous phases, respectively, along with 10 external and one internal boundary. The boundary condition ‘axis-of-symmetry’ was chosen for boundaries 1, 3, 4, and 6, as this was the center of rotation for the radial geometry, while boundaries 8, 9, 10, and 11 were designated as glass/insulator. Boundaries 2 and 7 were given the condition ‘concentration’ as to represent the semi-infinite (on the time scale of the simulation) concentration of species available from the bulk two phases, while boundary 5 described the w/o interface and was given the condition ‘flux’. These boundary conditions have been noted within the diagram.

In equations 5-3 and 5-4, k^0 is the standard rate constant, α is the transfer coefficient (assumed to be 0.5 unless otherwise stated), and $f_i = z_i F/RT$; such that F , R , and T are Faraday’s constant, the universal gas constant, and temperature in Kelvin, respectively. $\Delta_o^w \phi$ was applied in the simulation through the use of a triangular waveform⁴² implemented directly into equations 5-3 and 5-4; thus, generating a potential sweep with time analogous to the scanning programs found in CV. Finally, $\Delta_o^w \phi^{o'}$ is the formal IT potential, which is a constant and property individual to each species and biphasic system.

Mass transport within each phase was handled using Fick’s laws of diffusion and this is given below for the cylindrical coordinate system employed herein:

$$\frac{\partial c_{i,w}(r, z, t)}{\partial t} = D_{i,w} \left(\frac{\partial^2 c_{i,w}(r, z, t)}{\partial r^2} + \frac{1}{r} \frac{\partial c_{i,w}(r, z, t)}{\partial r} + \frac{\partial^2 c_{i,w}(r, z, t)}{\partial z^2} \right) \quad (5-5)$$

$$= D_{i,w} \nabla^2 c_{i,w}(r, z, t)$$

where $D_{i,w}$ and $c_{i,w}$ are the diffusion coefficient and concentration of species i in phase w and ∇ is the gradient operator; an analogous equation can be written for species in the organic phase.

The current response with respect to charge transfer across the ITIES at boundary 5, was calculated as the integral of the flux of ions at the interface as given below:

$$I = 2\pi z_i F \int \left(-D_{i,w} \nabla c_{i,w}(r, z, t) \right) r dr \quad (5-6)$$

Figure 5-2A shows the CV obtained for simple IT using this system with a scan rate (ν) of $0.020 \text{ V}\cdot\text{s}^{-1}$, a potential range from 0.000 to 0.500 V, $D_{i,w} = D_{i,o} = 1 \times 10^{-5} \text{ cm}^2\cdot\text{s}^{-1}$, $c_{i,w}$ of $5 \text{ mmol}\cdot\text{L}^{-1}$, $c_{i,o}$ of $0 \text{ mmol}\cdot\text{L}^{-1}$, k^0 of $1 \text{ cm}\cdot\text{s}^{-1}$, and $\Delta_o^w \phi^{o'}$ equal to 0.250 V. During the forward scan, a peak-shaped wave was observed at 0.280 V and is indicative of ion transfer from w to o , while on the reverse scan, another peak-shaped wave was observed at 0.220 V and this is representative of the ions transferring back from o to w . The half-wave potential calculated from the simulated CV was then 0.250 V, which is in excellent agreement with the defined parameters.

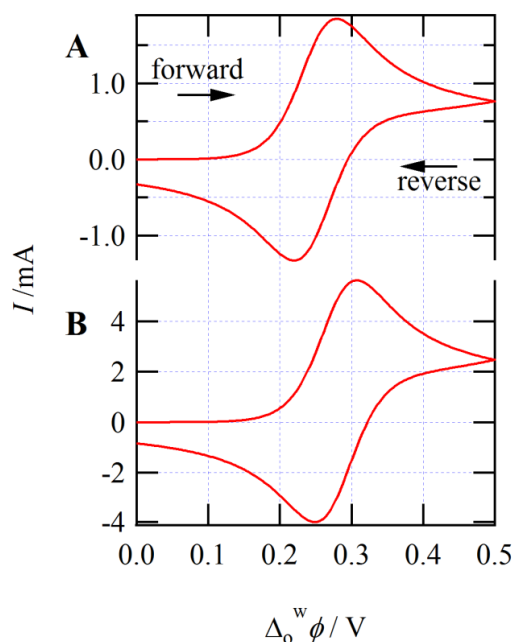


Figure 5-2. Simulated cyclic voltammograms of simple ion transfer of ion i of charge +1 transferring from w to o with initial concentrations $c_{i,w}$ and $c_{i,o}$ of 10 and 0 mol·m⁻³, respectively; the scan rate, $\Delta_0^w \phi_i^{o'}$, k^o , and α were set equal to 0.020 V·s⁻¹, 0.250 V, 1 cm·s⁻¹, and 0.5, respectively. $D_{i,w}$ and $D_{i,o}$ were both equal to 1×10^{-5} cm²·s⁻¹ in A, while in B, $D_{i,w}$ was changed to 9.3×10^{-5} cm²·s⁻¹ to better reflect proton mass transport.

The shape of the simulated CV is in good agreement with the expected current-potential response at a large ITIES;^{13,14} this is owing to semi-infinite linear diffusion. The peak-current is dependent on the scan rate through the Randles-Sevcik equation:

$$i_p = 0.4463 \left(\frac{F^3}{RT} \right)^{1/2} z_i^{3/2} D_{i,w}^{1/2} A c_{i,w} \nu^{1/2} \quad (5-7)$$

where A is the electrode area. Equation 5-7 was used to validate the simulation mesh in that the mesh was refined until the peak-current did not change and agreed well with the calculated value; the expected value was 1.84 mA and that obtained from the simulated curve in Figure 5-2A was 1.84 mA and, therefore, are in excellent agreement.

Next, the diffusion coefficient in the aqueous phase was changed to 9.3×10^{-5} cm²·s⁻¹ to reflect the fast mass transport associated with protons moving through water and the obtained CV was displayed in Figure 5-2B.^{43,44} In this case, the IT half-wave potential can be predicted using a modified Nernst equation as shown below:

$$\Delta_o^w \phi_{1/2} = \Delta_o^w \phi^{o'} - \frac{RT}{z_i F} \ln \xi \quad (5-8)$$

$$\xi = \sqrt{D_{i,o} / D_{o,w}}$$

The value calculated using the parameters designated in the simulation along with equation 5-8 and that garnered from the simulated CV itself were both 0.279 V. The excellent agreement of these two values demonstrates the robustness of the simulation.

5.4. Results and discussion

5.4.1. Chemical kinetics of homogeneous reactions

5.4.1.1. Acid in constant concentration but with various concentrations of DMFc

Firstly, real-time monitoring of DMFc^+ produced during oxygen reduction reaction was investigated under conditions of constant acid concentration but with variation of DMFc concentration in mono-phasic solutions. The results were shown in Figure 5-3 and Table 5-1.

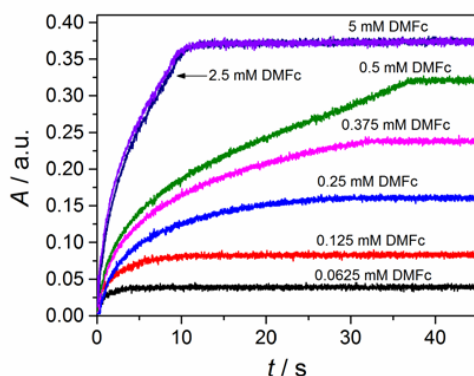


Figure 5-3. UV/Vis time profile of the oxygen reduction reaction by DMFc in DCE phase by monitoring DMFc^+ at 779 nm, where absorption at 900 nm as the reference value. Conditions: 1.5 mL of 1mM HTB solution was added into 1.5 mL of DMFc solutions of various concentrations labeled in the legend. The legend in this figure shows the initial DMFc concentration for each mixed solution with HTB in 0.5 mM.

Table 5-1. The DMFc^+ concentration after reaction.

System	$[\text{DMFc}^+] / \text{mM}$ after reaction ^[a]
0.5 mM HTB/0.0625 mM DMFc	0.0586

System	[DMFc ⁺] / mM after reaction ^[a]
0.5 mM HTB/0.125 mM DMFc	0.125
0.5 mM HTB/0.25 mM DMFc	0.2468
0.5 mM HTB/0.375 mM DMFc	0.3655
0.5 mM HTB/0.5 mM DMFc	0.4937
0.5 mM HTB/2.5 mM DMFc	0.60
0.5 mM HTB/5 mM DMFc	0.60

^aConcentration was calculated based on the ε of DMFc⁺ of $0.632 \text{ mM}^{-1} \cdot \text{cm}^{-1}$ at 779 nm.

It can be seen from Figure 5-3 and Table 5-1 that DMFc has been completely converted to DMFc⁺ at the point where the absorption of DMFc⁺ reaches its steady-state value when DMFc was equal or smaller than HTB in concentration. However, more DMFc⁺ was produced when DMFc is in excess (in the case of 2.5 or 5 mM) with respect to HTB. It is caused by the fact that the produced H₂O₂ can oxidize the remaining DMFc in DCE.⁴⁵ So the reaction may occur *via* the following steps in series:



For the case in Equation 5-10, OH[−] will be hydrated by the water clusters dispersed in the DCE phase, while DMFc⁺ will be solvated by the DCE molecules. This is similar to the case of LiTB dissolved in DCE that will be discussed in Chapter 7. The abrupt change in the slope in Figure 5-3 at higher concentrations of DMFc can be ascribed to the instrumental non-ideality. It would also be seen in Figures 5-5 and 5-6. To investigate further the aspects of kinetics and mechanism, the reaction was assumed to be a pseudo-second-order reaction, namely $v = k[\text{DMFc}][\text{H}^+]$. Hence the integrated rate law can be expressed as⁴⁶

$$kt = \frac{1}{[\text{H}^+]_0 - [\text{DMFc}]_0} \ln \frac{[\text{DMFc}]_0([\text{H}^+]_0 - [\text{DMFc}^+])}{([\text{DMFc}]_0 - [\text{DMFc}^+])[\text{H}^+]_0} \quad (5-11)$$

Plot of the rate law in a case of an elementary reaction gives a straight line with a slope of k which is constant at different concentrations of reactants. Another method to extract the rate

constant is to use the initial rate. A straight line can be fitted on the first experimental data points, and k is estimated from Equation 5-12.

$$k = v_0 / ([\text{DMFc}]_0 [\text{H}^+]_0) \quad (5-12)$$

where $[\text{DMFc}]_0$ and $[\text{H}^+]_0$ represent the initial concentrations of DMFc and HTB respectively, in addition to $[\text{DMFc}^+]$ representing the product concentration at real time. The results treated with the integrated rate law were demonstrated in Figure 5-4 and tabulated in Table 5-2. The data in Figure 5-3 was also treated with the methodology of the initial rate but not shown here. Only the obtained initial rate v_0 and the corresponding rate constant k were listed in Table 5-2.

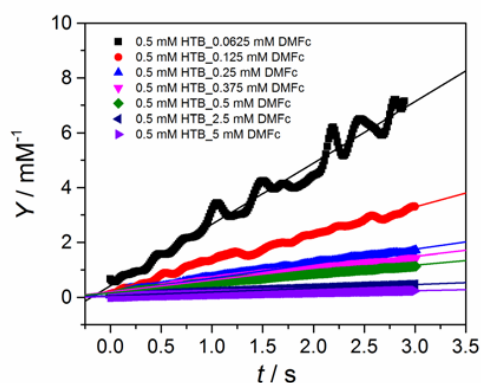


Figure 5-4. Experimental (thick line) and theoretical (thin line) curves of the integrated rate law, see Equation 5-11, for a pseudo-second-order reaction. Note that the duration used for fitting for all the systems is *ca.* 3 s for comparative reasons, and the ordinate Y represents the right-hand side of Equation 5-11 for clarity.

Table 5-2. Pseudo-second-order rate constants k obtained from Figure 5-4 and initial rates (data not shown).

System	$k / \text{mM}^{-1}\text{s}^{-1}$ (from rate law)	$v_0 / \text{mM s}^{-1}$	$k / \text{mM}^{-1}\text{s}^{-1}$ (from v_0)
0.5 mM HTB/0.0625 mM DMFc	2.24	0.038	1.22
0.5 mM HTB/0.125 mM DMFc	1.01	0.062	0.99
0.5 mM HTB/0.25 mM DMFc	0.53	0.079	0.63
0.5 mM HTB/0.375 mM DMFc	0.43	0.11	0.61

System	$k / \text{mM}^{-1}\text{s}^{-1}$ (from rate law)	$v_0 / \text{mM s}^{-1}$	$k / \text{mM}^{-1}\text{s}^{-1}$ (from v_0)
0.5 mM HTB/0.5 mM DMFc	0.34	0.16	0.62
0.5 mM HTB/2.5 mM DMFc	0.14	0.30	0.24
0.5 mM HTB/5 mM DMFc	0.07	0.33	0.13

It can be seen from Table 5-2 that the determined rate constant k is not constant under different concentrations for reactants employing both methods. It implies that the ORR in the bulk DCE phase is not a simple elementary reaction but composed of multiple steps. This was further evidenced by the experiments under conditions of constant DMFc concentration but with variation of acid concentration (*vide infra*).

5.4.1.2. DMFc in constant concentration but with various concentrations of acid

The effect of acid concentration at constant DMFc concentration was investigated and shown in Figure 5-5. The kinetic rate constants were obtained from the integrated rate law and the initial rate and only some accessible results were tabulated in Table 5-3.

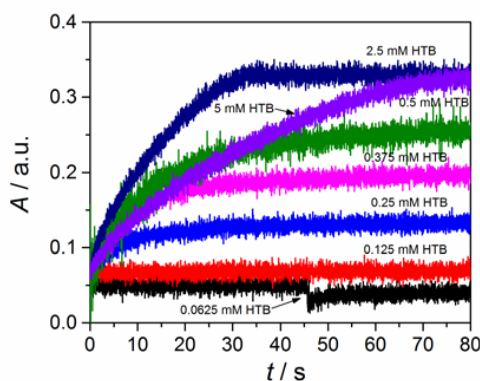


Figure 5-5. UV/Vis time profile of the oxygen reduction reaction by DMFc in DCE phase by monitoring DMFc^+ at 779 nm, where absorption at 900 nm as the reference value. Conditions: 1.5 mL of HTB solutions of various concentrations were added into 1.5 mL of 1 mM DMFc solution. The legend in this figure shows the initial HTB concentration for each mixed solution with DMFc in 0.5 mM.

Table 5-3. Pseudo-second-order rate constants k obtained from Figure 5-5 and initial rates (data not shown), in addition to the H_2O concentration in the reactant mixture.

System	$k / \text{mM}^{-1} \text{s}^{-1}$ (from rate law)	$v_0 / \text{mM s}^{-1}$	$k / \text{mM}^{-1} \text{s}^{-1}$ (from v_0)	$[\text{H}_2\text{O}] / \text{mM}^{[a]}$
0.5 mM DMFc/0.0625 mM HTB	0.31	0.018	0.588	0.79
0.5 mM DMFc/0.25 mM HTB	0.37	0.045	0.585	3.2
0.5 mM DMFc/0.375 mM HTB	0.26	0.037	0.235	4.8
0.5 mM DMFc/2.5 mM HTB	0.033	0.024	0.022	32
0.5 mM DMFc/5 mM HTB	0.007	0.023	0.010	64

^aConcentration was calculated based on the solubility of H_2O of 127 mM^{35} in DCE with respect to the commercial DCE.

It can be seen from Table 5-3 that the agreement of rate constants obtained by the integrated rate law and the initial rate is better than that in Table 5-2. But again the determined rate constant k is not constant under different concentrations for reactants using both methods. Another effect is the k value decreases with the increase in concentration of HTB, which is somewhat reverse to the trend obtained in Table 5-2. It implies that counter-anion TB^- has an inhibitive effect on the kinetics, which is in reasonable agreement with the observations made by Samec *et al.*^{35,47} in the study of homogeneous oxygen reduction catalyzed by a metal-free porphyrin. In their work^{35,47} they found TB^- can form ion pair with the protonated porphyrin in competition with the binding of O_2 on the protonated porphyrin. Herein it can be explained similarly as the ion-pair formation between the protonated DMFc and TB^- which is in competition with the reaction between the protonated DMFc and O_2 . The data in Table 5-3 also implies that water molecules (H_2O) inhibit the reaction kinetics, while in Table 5-2, H_2O concentration is fixed at *ca.* 6.35 mM with respect to the commercial DCE. It should be stressed that the commercial DCE also has a considerable amount of H_2O which will be addressed in Chapter 7. The effect of counter-anions, including TB^- and ClO_4^- , and H_2O , on the kinetics of oxygen reduction was investigated further and shown in Figure 5-6 and Table 5-4.

5.4.1.3. Effect of counter-anions and water on the ORR kinetics

From Figure 5-6 and Table 5-4, TB^- has much smaller influence on the ORR kinetics compared to that from ClO_4^- and H_2O . Specifically, the kinetic hindrance from ClO_4^- and

H₂O is 6.88, and 6.5 times slower, compared to that of the system of 0.5 mM HTB/0.5 mM DMFc. ClO₄[−] is a coordinating anion⁴⁸ which can bind with the protonated DMFc more effectively with respect to that of TB[−]. H₂O, acting as a ligand, will compete with O₂ in the interaction with the protonated DMFc.³⁵

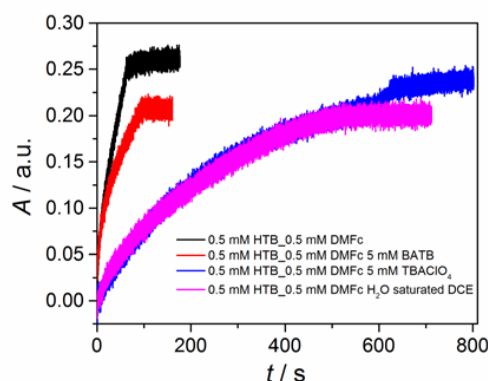


Figure 5-6. Effect of counter-anions (TB[−] and ClO₄[−]) and H₂O content on the kinetics of oxygen reduction reaction in the DCE phase by monitoring DMFc⁺ at 779 nm, where absorption at 900 nm as the reference value.

Table 5-4. Effect of Counter-anions and water on the kinetics.

System	$k / \text{mM}^{-1}\text{s}^{-1}$ (from rate law)	$v_0 / \text{mM s}^{-1}$	$k / \text{mM}^{-1}\text{s}^{-1}$ (from v_0)
0.5 mM HTB/0.5 mM DMFc	0.15	0.033	0.13
0.5 mM HTB/0.5 mM DMFc 5 mM BATB	0.16	0.026	0.104
0.5 mM HTB/0.5 mM DMFc 5 mM TBAClO ₄	0.023	0.004	0.016
0.5 mM HTB/0.5 mM DMFc 5 mM (H ₂ O saturated DCE)	0.028	0.005	0.02

In brief, The ORR in the DCE phase is not an elementary reaction but composed of multiple steps. It is evidenced from the fact that the determined pseudo-second-order rate constant k is not constant under different concentrations of reactants. Besides, counter-anions such as ClO₄[−] have significant effect on the ORR kinetics due to ion-pair formation, so does H₂O concentration.

The complexity in terms of the mechanism in ORR indicates that another way needs to be found. As mentioned in the introduction, comparison between FEM simulations and experimental CVs at the ITIES will be employed to clarify the ORR mechanism, discussed

below. Compared to the bulk phase methodology developed by Fukuzumi *et al.*,⁴⁹ the method developed in this work will be more intuitive.

5.4.2. Mechanism elucidation by FEM simulations of electrochemical measurements (*carried out by T. Jane Stockmann*)

The bold curve drawn in Figure 5-7 shows an experimentally obtained CV using Cell 5-1 with 0.5 mM H₂SO₄ in the aqueous phase under aerobic conditions, but with no Fc derivative present; essentially a ‘blank’ CV. The CV was swept from 0.000 V at a rate of 0.050 V·s⁻¹ with a potential range of approximately +/-0.500 V; this range constitutes the polarizable potential window (PPW) available at the liquid/liquid interface. As the potential increased from 0.000 to 0.500 V, a rise in current can be observed at 0.500 V, at which point the scan direction was switched towards more negative potentials. Similarly, as the potential reaches -0.500 V a decrease in current was observed and the CV was then scanned in the positive direction until a return to the initial potential of 0.000 V was reached. The rise in current at positive potentials and the decrease in current at negative potentials represent the limit of the PPW and these are indicative of the transfer of ions constituting the supporting electrolyte.

At positive potentials this is the transfer of protons from w to o as well as tetrakis(pentafluorophenyl)borate (TB⁻) anions from o to w, while at negative potentials this is the transfer of sulfate anions from w to o and bis(triphenylphosphoranylidine)ammonium (BA⁺) cations from o to w. However, the organic phase supporting electrolytes, BA⁺ and TB⁻, are so hydrophobic^{20,50} that they are likely minor contributors, such that H⁺ and HSO₄⁻ and/or SO₄²⁻ (depending on the concentration of H₂SO₄) are the dominant limiting ions. The potential scale of the blank – and all experimental CVs unless otherwise noted – have been calibrated by addition of an internal standard of known IT potential in conjunction with an extra-thermodynamic assumption known as the tetraphenylarsonium-tetraphenylborate (TATB) or Parker’s assumption.^{51,52} Herein, tetraethylammonium (TEA⁺) was used as the internal standard with a standard IT potential, $\Delta_o^w \phi_{\text{TEA}^+}^o$, of 0.019 V.⁵³

The blank CV in Figure 5-7 highlights another curve feature of interest: after the switching potential, during the reverse scan from 0.500 to -0.500 V, a return peak can be observed at 0.490 V. This corresponds to the transfer of protons back across the ITIES from o to w. An opposite intensity but analogous return peak was recorded during the final forward scan segment at -0.466 V and represents the return of sulfate, from o to w, back across the ITIES.

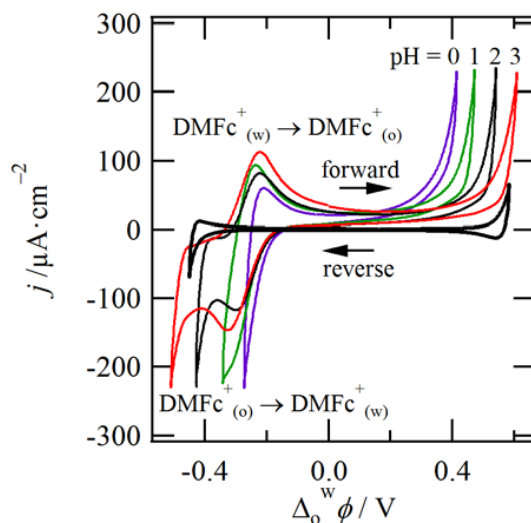


Figure 5-7. Cyclic voltammograms (CVs) acquired using Cell 5-1 with 5 mM of DMFc in the DCE phase and 0.5, 5, 50, and 500 mM of H_2SO_4 in the aqueous phase such that the pH was roughly 3, 2, 1, and 0, respectively, as indicated. Instrument parameters included a scan rate of $0.050 \text{ V}\cdot\text{s}^{-1}$, with an initial potential of 0.000 V. The bold, black curve shows the system with no DMFc added to the DCE phase. The displayed CVs have been calibrated using the TATB assumption and TEA^+ as an internal standard with $\Delta_o^w \phi_{\text{TEA}^+}^o = 0.019 \text{ V}$.⁵³

The significance of the H^+ return peak is made clear through comparison to the other CVs, overlaid in Figure 5-7, acquired using Cell 5-1 with 0.5, 5, 50, and 500 mM of H_2SO_4 – indicated as pH 3, 2, 1, and 0, respectively – and 5 mM of DMFc dissolved in the DCE phase. It is recognized that, owing to sulfuric acids two pK_a 's⁵⁴ (–6.62 and 1.99 for H_2SO_4 and HSO_4^- , respectively), that the pH of the aqueous solutions will vary from these values slightly. The pH of the aqueous phase was measured using a pH meter and found to be, for example, 1.55, 2.09, and 3.30 for 0.5, 5, and 50 mM of H_2SO_4 , respectively. Similar instrumental parameters as those described for the blank experiment were used to obtain these CVs and can be exemplified by the trace at pH 3.

Here the rise in current marking the edge of the PPW was reached at 0.608 V and subsequently the potential was swept in the reverse direction towards negative potentials. During the reverse scan, from 0.608 to –0.509 V, the return peak of H^+ transfer back across the ITIES is noticeably absent; however, a peak has emerged at –0.333 V which is indicative of DMFc^+ transfer²⁰ from o to w. The edge of the PPW was reached at –0.509 V and the CV was subsequently scanned back in the positive direction until 0.000 V. During this last segment, a peak-shaped wave at –0.223 V was recorded and is representative of DMFc^+ transfer back across the ITIES, from w to o. The approximate formal IT potential for DMFc^+ , $\Delta_o^w \phi_{\text{DMFc}^+}^{o'}$, was calculated as an average between the four CVs from the midpoint between forward and reverse IT peaks to be –0.250 V; iR -compensation was used during signal acquisition and so this value should be treated as an estimate.

Put simply, with the addition of DMFc to the organic phase, two major changes to the CV have been noted: the appearance of DMFc^+ transfer and the lack of any signal for H^+

returning from o to w; therefore, protons must have been consumed in the organic phase in a process that generates DMFc^+ . This is in good agreement with previous biphasic reports utilizing CV.^{24,55,56}

With increasing proton concentration in the aqueous phase from pH 3 to 2, 1, and 0 the limiting positive potential of the PPW decreases from 0.608 V to 0.540, 0.470, and 0.413 V, respectively, as shown in Figure 5-7, with a current limit – set in the instrumental parameters – of $\sim 230 \mu\text{A}\cdot\text{cm}^{-2}$. This may be owing simply to the increasing supporting electrolyte concentration that has been known to limit the PPW;⁵⁷ however, it may also be the result of proton consumption in the DCE phase facilitating H^+ transfer and thus decreasing the amount of applied potential, or Galvani potential difference across the ITIES, necessary to elicit IT.

The CVs displayed in Figure 5-7 are in good agreement with previous results by our group for the study of the ORR by DMFc^{20} and 1,2-diferrocenylethane (DFcE^{22}) in which DMFc^+ and DFcE^+ transfer were similarly observed. Additionally, other biphasic studies²¹ have utilized UV-Vis spectroscopy to monitor the reaction progress in homogeneous DCE through the use of the DMFc^+ absorption peak in the visible range.

The electroactive species dimethylferrocene (DFc) and ferrocene (Fc) were also dissolved in the DCE phase and utilized in Cell 5-1 at 5 mM concentrations with 0.5 mM H_2SO_4 in the aqueous phase. The CVs for the DFc and Fc experiments are shown in Figures 5-8A and B, respectively, where the H^+ return peak is still present indicating that any oxygen reduction is occurring more slowly. IT peaks for the oxidized forms of DFc and Fc were also in evidence suggesting that ORR is still taking place; however, with cathodic peak current densities of roughly $-2.0 \mu\text{A}\cdot\text{cm}^{-2}$ each, it is likely, owing to the reduced reaction rate, that only a modicum of material has reacted. The formal IT potentials for DFc^+ and Fc^+ were determined to be -0.078 and -0.016 V, respectively.

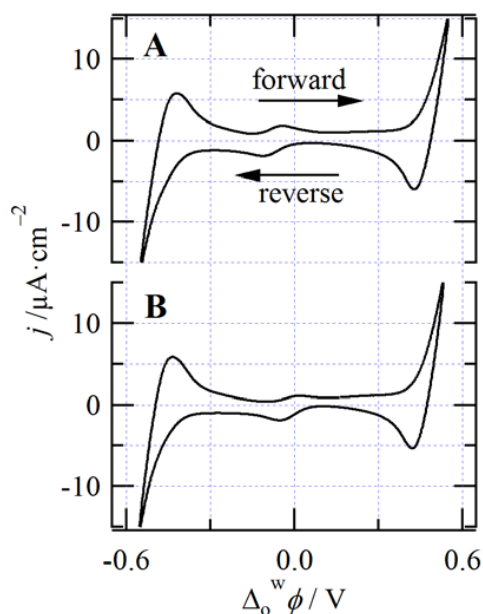


Figure 5-8. Cyclic voltammograms acquired using Cell 5-1 with 0.5 mM of H_2SO_4 in the aqueous phase as well as 5 mM of DFC (A) and Fc (B) in the organic phase. Instrument parameters were similar to those described for Figure 5-7 except a scan rate of $0.020 \text{ V}\cdot\text{s}^{-1}$ was utilized.

In order to elucidate these processes further, COMSOL was used to generate simulated CVs through the geometry drawn in Figure 5-1B, by altering the kinetic parameters. Figure 5-9 illustrates the proposed reaction pathways including a potential-dependent reversible proton and DMFc^+ transfer steps across the ITIES along with five subsequent homogeneous reactions taking place in the organic or DCE phase.

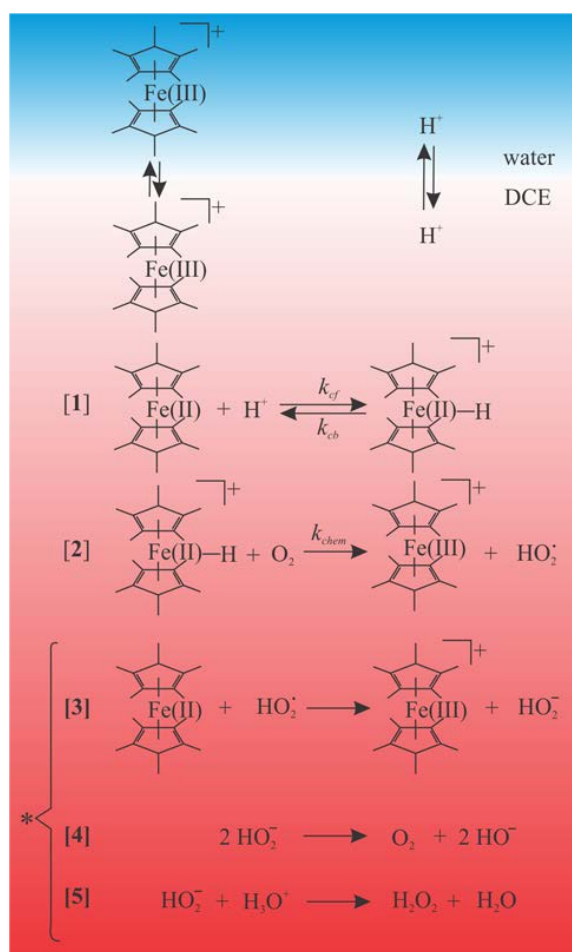


Figure 5-9. Proposed mechanism for oxygen reduction at the w/DCE interface. The two potential dependent ion transfer reactions, for DMFc^+ and H^+ , are shown at the top between the water (blue box) and the organic (red box) phases, while step-wise ORRs occurring in the organic phase are numbered and drawn in the red box. Reaction 1 is the DMFc-H^+ formation, 2 is the reaction of DMFc-H^+ with O_2 to form DMFc^+ and HO_2^\bullet , 3 is the one electron oxidation of DMFc by the hydroxyl radical species, 4 is the disproportionation of HO_2^- to oxygen and two equivalents of OH^- , and 5 is the reaction of HO_2^- with an acid to form hydrogen peroxide and water. Reactions marked with an asterisk were assumed to be fast and irreversible.

The first homogeneous reaction, reaction **1** from Figure 5-9, is the formation of DMFc-H⁺, as also given in equation 5-13:



Previous DFT studies²¹ suggest that a proton will first coordinate to the metal center in DMFc; however, while oxygen may coordinate⁵⁸ it is energetically unfavourable and likely a small contributor.^{20,21} The latter is owing to the highly methylated cyclopentadienyl rings structurally inhibiting access to the metal center. Hydrogen is small enough to pass through, but molecular oxygen coordination requires too great a distortion, or tilting, of the cyclopentadienyl rings that is energetically prohibitive.²⁰ It has been shown that highly methylated cyclopentadienyl rings enhance the electron donor performance of ferrocene derivatives in ORRs;²⁴ in this way, the experimental results, using DFc and Fc, are in good agreement with the literature and, therefore, formation of protonated ferrocene derivatives was considered the logical first step in the mechanism.

The second reaction in the bulk DCE phase was the reaction of DMFc-H⁺ with dissolved molecular oxygen that leads to the formation of DMFc⁺ and the hydrogen peroxy radical species HO₂[•]; this is given in reaction **2** of Figure 5-9 and in equation 5-14, below:



This radical species is thought to react rapidly with DMFc to form HO₂⁻ and DMFc⁺, shown as reaction **3** in Figure 5-9. HO₂⁻ can either disproportionate forming oxygen and two equivalents of OH⁻ as drawn in reaction **4** of Figure 5-9, or generate hydrogen peroxide, H₂O₂, by reaction with dissolved water/protons, illustrated in reaction **5** of Figure 5-9. A concerted reaction involving either two DMFc-H⁺ molecules with diatomic oxygen was also considered possible for the generation of hydrogen peroxide, but deemed unlikely in the sense that a third-order reaction would be kinetically unfavourable – or at the very least a minor contributor. Instead, the chosen simulation consisted of only reactions **1** and **2** of Figure 5-9, since the subsequent reactions from HO₂[•] to HO₂⁻ and finally H₂O₂ were considered extremely fast. Regardless, all that was required of the system was an effective, so-called ‘proton-sink’. Reaction **2** in Figure 5-9 served this purpose by being irreversible, which is more a reflection of the kinetics and favourability of reactions **3-5** than the reversibility of **2**. This also had the benefit of limiting the number of dependent variables within the simulation and thus, reducing computational time. However, it should be noted that while one DMFc⁺ molecule is generated through **1** and **2**, the second DMFc⁺ generated in **3** was not included. If hydrogen peroxide is further reduced to water, then two more DMFc⁺ molecules will be produced. This means that the peak current densities for DMFc⁺ transfer can be multiplied by as much as a factor of two.

Moving forward, the simulation described in section 5.3 was adapted to include the homogeneous and heterogeneous reactions outlined in Figure 5-9. First, the effect of changing the rate of **2** was investigated.

Figure 5-10 illustrates the simulated CVs obtained using this system, such that the simulation parameters were set to closely approximate those employed experimentally. These included a scan rate of $0.050 \text{ V}\cdot\text{s}^{-1}$, an initial aqueous H^+ concentration of $0.010 \text{ mol}\cdot\text{L}^{-1}$, $0.005 \text{ mol}\cdot\text{L}^{-1}$ of DMFc in the organic phase, $0.001 \text{ mol}\cdot\text{L}^{-1}$ of O_2 ,^{59,60} and a potential range of $\pm 0.540 \text{ V}$. Kinetic parameters included D_{O_2} , $D_{\text{DMFc}^+,o}$, $D_{\text{H}^+,w}$, $D_{\text{H}^+,o}$, k_{cf} , and k_{cb} , that were maintained at $2.8 \times 10^{-5} \text{ cm}^2\cdot\text{s}^{-1}$,⁶¹ $7.3 \times 10^{-6} \text{ cm}^2\cdot\text{s}^{-1}$, $9.3 \times 10^{-5} \text{ cm}^2\cdot\text{s}^{-1}$,^{43,44} $1 \times 10^{-5} \text{ cm}^2\cdot\text{s}^{-1}$, $1 \times 10^3 \text{ L}\cdot\text{mol}^{-1}\cdot\text{s}^{-1}$, and 1 s^{-1} , respectively. The diffusion coefficient of DMFc^+ was assumed to be equal in both phases and was determined using a Pt-disk microelectrode immersed in a DCE solution of 5 mM DMFcTB with 5 mM BATB as supporting electrolyte (data not shown). The formal IT potentials, $\Delta_o^w \phi_{\text{H}^+}^{o'}$, and $\Delta_o^w \phi_{\text{DMFc}^+}^{o'}$, were set equal to 0.580 V ⁵⁰ and -0.250 V , respectively. The rate of **2**, k_{chem} in Figure 5-9, was varied from $1 \times 10^1 \text{ L}\cdot\text{mol}^{-1}\cdot\text{s}^{-1}$ to 1×10^2 , 1×10^4 , and finally $1 \times 10^{10} \text{ L}\cdot\text{mol}^{-1}\cdot\text{s}^{-1}$.

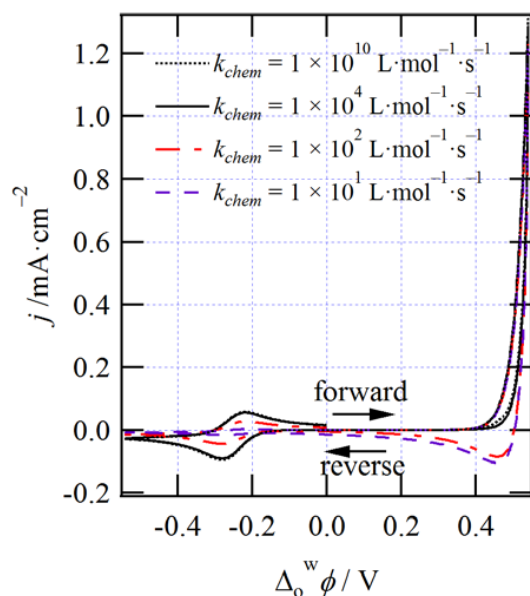


Figure 5-10. Simulated cyclic voltammograms generated using the geometry shown in Figure 5-1B and the mechanism illustrated in Figure 5-9. The following coefficients were used: $k_{cf} = 1 \times 10^3 \text{ L}\cdot\text{mol}^{-1}\cdot\text{s}^{-1}$, $k_{cb} = 1 \text{ s}^{-1}$, $\Delta_o^w \phi_{\text{H}^+}^{o'} = 0.580 \text{ V}$, $\Delta_o^w \phi_{\text{DMFc}^+}^{o'} = -0.250 \text{ V}$, $k^0 = 1 \text{ cm}^2\cdot\text{s}^{-1}$ (for both H^+ and DMFc^+ ion transfers), $\nu = 0.050 \text{ V}\cdot\text{s}^{-1}$, a potential range of $\pm 0.540 \text{ V}$, $c_{\text{H}^+,w} = 0.010 \text{ mol}\cdot\text{L}^{-1}$, $c_{\text{DMFc},o} = 0.005 \text{ mol}\cdot\text{L}^{-1}$, $c_{\text{O}_2,o} = 0.001 \text{ mol}\cdot\text{L}^{-1}$, $D_{\text{H}^+,w} = 9.3 \times 10^{-5} \text{ cm}^2\cdot\text{s}^{-1}$, $D_{\text{H}^+,o} = 1.0 \times 10^{-5} \text{ cm}^2\cdot\text{s}^{-1}$, $D_{\text{DMFc},o} = D_{\text{DMFc}^+,o} = D_{\text{DMFc}^+,w} = 0.7 \times 10^{-5} \text{ cm}^2\cdot\text{s}^{-1}$, and k_{chem} as indicated.

When k_{chem} is equal to 1×10^1 and $1 \times 10^2 \text{ L}\cdot\text{mol}^{-1}\cdot\text{s}^{-1}$ reaction **2** becomes the rate-determining or rate-limiting step. This results in large H^+ return peaks at $\sim 0.455 \text{ V}$ with magnitudes of -104 and $-85 \mu\text{A}\cdot\text{cm}^{-2}$ as well as DMFc^+ ion transfer peaks with cathodic intensities of -15 and $-44 \mu\text{A}\cdot\text{cm}^{-2}$ for the former and latter k_{chem} values, respectively.

Therefore, even at low orders of magnitude for k_{chem} relative to k_{cf} , an electrochemically observable amount of $DMFc^+$ and thus, H_2O_2 is being produced. As k_{chem} increases the H^+ return peak decreases significantly and once it exceeds k_{cf} the curve feature is essentially absent, as can be seen with k_{chem} equal to 1×10^4 and $1 \times 10^{10} \text{ L}\cdot\text{mol}^{-1}\cdot\text{s}^{-1}$ in Figure 5-10. Likewise, as k_{chem} increases the concentration of $DMFc^+$ generated also increases, that in turn increases the $DMFc^+$ transfer peak intensity; the cathodic currents for both 1×10^4 and $1 \times 10^{10} \text{ L}\cdot\text{mol}^{-1}\cdot\text{s}^{-1}$ were observed to be -182 and $-202 \mu\text{A}\cdot\text{cm}^{-2}$, after the generation of the second $DMFc^+$ is considered. These peak current densities are in fair agreement with the experimental data for $DMFc$, which provided average $DMFc^+$ transfer peaks of roughly $-160 \mu\text{A}\cdot\text{cm}^{-2}$. This also demonstrates that even though reaction 1 is rate determining in these later two simulations, significant increases in the rate of reaction 2 can still produce appreciable changes in the CVs.

Next, k_{cf} was altered while k_{chem} was held equal to $1 \times 10^8 \text{ L}\cdot\text{mol}^{-1}\cdot\text{s}^{-1}$; the obtained, simulated CVs have been plotted in Figure 5-11 for k_{cf} equal to 1×10^4 , 1×10^5 , and $1 \times 10^6 \text{ L}\cdot\text{mol}^{-1}\cdot\text{s}^{-1}$, whereby reaction 1 is always rate determining. Owing to the fast $DMFc-H^+$ formation, there is no observable return peak for H^+ . The potential range was maintained at $\pm 0.540 \text{ V}$ in order to facilitated comparisons between the simulated and experimental CVs. An increase in the overall rate of the reactions shown in Figure 5-9 generates a significant change in the current-potential profile at the edge of the PPW. For k_{cf} equal to $1 \times 10^4 \text{ L}\cdot\text{mol}^{-1}\cdot\text{s}^{-1}$, this translates to an increase in the current at the edge-of-scan, I_{eos} , from $\sim 1 \text{ mA}\cdot\text{cm}^{-2}$ in Figure 5-10 to $\sim 1.5 \text{ mA}\cdot\text{cm}^{-2}$ in Figure 5-11.

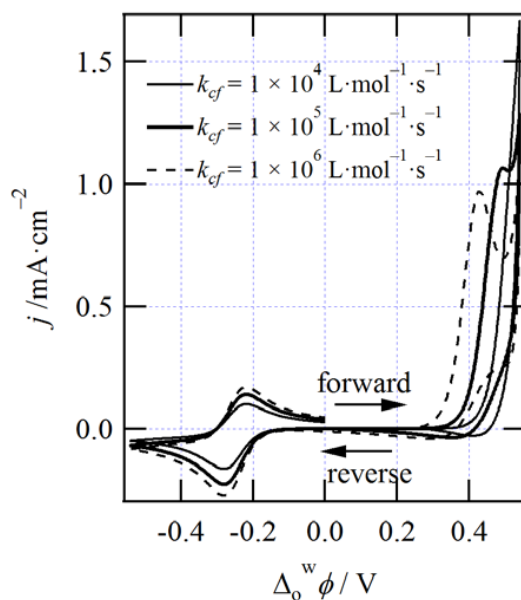


Figure 5-11. Simulated cyclic voltammograms using the same coefficients and geometry as detailed in Figure 5-10, except that k_{chem} was maintained at $1 \times 10^8 \text{ L}\cdot\text{mol}^{-1}\cdot\text{s}^{-1}$ while k_{cf} was varied as indicated.

The reaction scheme outlined in Figure 5-9 can be split into an electrochemical step, the potential dependent proton transfer, followed by two chemical steps, the homogeneous reactions taking place in the organic phase; an IT-C₁C₂ mechanism. As the rate of reaction **1** increases, protons in the organic phase are quickly consumed and this results in a shift in the potential of proton transfer. This phenomena can be seen in Figure 5-11 with k_{cf} equal to 1×10^5 and $1 \times 10^6 \text{ L}\cdot\text{mol}^{-1}\cdot\text{s}^{-1}$, such that during the forward scan, from 0.000 to 0.540 V, a peak-shaped wave was observed, for the two rates, at 0.493 and 0.430 V, respectively. The IT-C₁C₂ mechanism is similar in some respects to interfacial complexation reactions that have been studied extensively at liquid/liquid interfaces.⁶²⁻⁶⁵ The DMFc- H⁺ is, in essence, a metal-ligand complex and, in this way, the electrochemical mechanism described herein follows the classical interfacial complexation scheme, described by Shao *et al.*,⁶⁶ Koryta,⁶⁷ as well as recently by Molina *et al.*,⁶⁸ often abbreviated TOC: transfer of an ion followed by organic phase complexation. Thus, the peaks observed during the forward scan for higher values of k_{cf} in Figure 5-11 are the facilitated ion transfer of protons from the aqueous to organic phase; however, because k_{chem} is also high, this means that protons are consumed during the chemical step and are unavailable for return across the interface. This in turn generates an irreversible IT wave on the return scan.

Additionally, as k_{cf} increases the DMFc⁺ transfer peak intensity also increases, just as in the case of k_{chem} . In Figure 5-11 for k_{cf} equal to 1×10^{-4} , 1×10^{-5} , and 1×10^{-6} the negative peak current increases from $140 \mu\text{A}\cdot\text{cm}^{-2}$ to 226, and $272 \mu\text{A}\cdot\text{cm}^{-2}$ that becomes 280, 452, and $544 \mu\text{A}\cdot\text{cm}^{-2}$, respectively, if the generation of a second equivalent of DMFc⁺ is considered. This alludes to two critical findings. First, since the DMFc⁺ transfer peak current intensity has exceeded that found experimentally, it can be concluded that the ORR taking place in the DCE phase is not limited by the diffusion of DMFc at experimental concentrations. However, the simulated case plotted in Figure 5-11 is limited by the diffusion of DMFc in that the IT-C₁C₂ mechanistic peak (or essentially the FIT peak) is followed by conventional proton transfer. Secondly, this suggests that the rate of the reaction is in a range measureable by CV.

Moving forward, the simulated curves displayed in Figure 5-12 were generated in order to mirror, or recreate, the experimental CVs plotted in Figure 5-7. These traces were generated using the same simulation parameters as described for Figure 5-10 except that a k_{chem} and k_{cf} of 1×10^4 and $5 \times 10^2 \text{ L}\cdot\text{mol}^{-1}\cdot\text{s}^{-1}$, respectively, were utilized while the H⁺ concentration was varied. As the pH of the solution decreased, the potential at the edge of scan was also decreased from 0.601 V to 0.540, 0.467, and 0.413 V for pH 3, 2, 1, and 0, respectively, in an analogy of the experimental curves displayed in Figure 5-7. This is in good agreement with the IT-C₁C₂ mechanism, such that the IT of the protons, is concentration dependent.⁶⁴

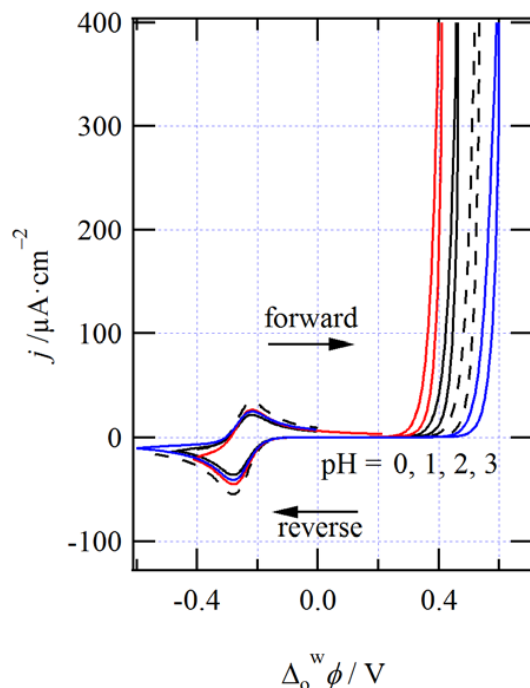


Figure 5-12. Simulated cyclic voltammograms generated using the same parameters as listed for Figure 5-10, save that the k_{chem} and k_{cf} were held equal to 1×10^{10} and $5 \times 10^2 \text{ L} \cdot \text{mol}^{-1} \cdot \text{s}^{-1}$, respectively, while $C_{H^+,w}$ was varied from 0.001 to 0.010, 0.100, and 1.000 $\text{mol} \cdot \text{L}^{-1}$ as indicated.

However, current density at the edge of scan, I_{eos} , was found to be 466, 846, 506, and 595 $\mu\text{A} \cdot \text{cm}^{-2}$ for pHs 3, 2, 1, and 0, respectively, where the experimental case for all proton concentrations was roughly 230 $\mu\text{A} \cdot \text{cm}^{-2}$ throughout. I_{eos} corresponds to the amount of protons transferred across the interface such that, the magnitude of the potential range, in conjunction with the I_{eos} , becomes a curve feature to be optimized. However, this optimization cannot be performed in isolation and the two other curve features, DMFc⁺ transfer and the proton return peak intensities, must be taken into account.

Curve matching the peak intensity of DMFc⁺ transfer between the actual and simulated CVs is complicated by two experimental factors. First, despite purifying *via* sublimation the commercial DMFc, some DMFc⁺ is present and can contribute to the signal intensity; however, this is often considered negligible. Secondly, while every attempt was made to acquire the first scan of the system during experimentation, it is often necessary to perform multiple (2 or 3) scans in order to establish the experimental potential range; this may generate a build-up of oxidized DMFc at the interface and increase the current response of its IT. Figure 5-13 illustrates the result of scanning the PPW 3 times with the traces overlaid and demonstrates an appreciable increase in the cathodic IT peak intensity for DMFc⁺ with values of -90, -136, and -172 $\mu\text{A} \cdot \text{cm}^{-2}$ (with 2 equivalents of DMFc⁺) for scans 1, 2, and 3, respectively, for the cathodic sweep. In this way, the peak intensity is in good agreement with that observed experimentally. The I_{eos} does not change appreciably with increasing scans and

this is owing to the high effective diffusion coefficient of protons in the aqueous phase that quickly replenish the H^+ concentration near the interface.

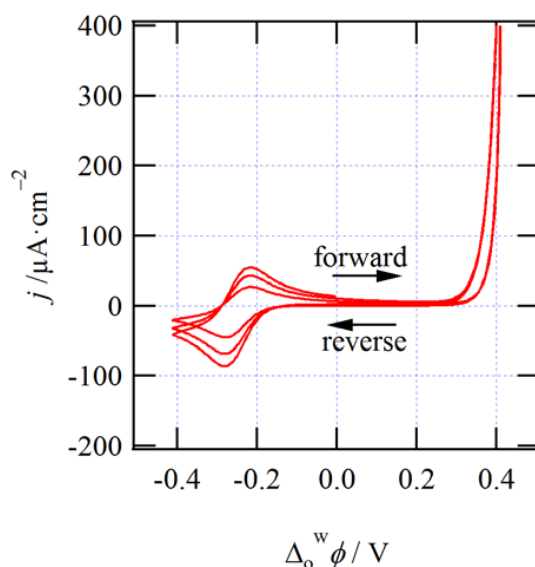


Figure 5-13. Simulated cyclic voltammogram obtained using the same simulation parameters described in Figure 5-12 except only $c_{\text{H}^+,w}$ equal to $1.000 \text{ mol}\cdot\text{L}^{-1}$ was utilized with a potential range of $\pm 0.413 \text{ V}$. Additionally the simulation run time was extended so that 3 forward/reverse sweeps were recorded.

A number of factors may affect the H^+ return peak and the I_{eos} . To explore proton transfer further a chronoamperometric (CA) potential step, from 0.000 to 0.540 V , was added to the simulation and using the same simulation parameters described for Figure 5-12, with $c_{\text{H}^+,w}$ equal to $0.010 \text{ mol}\cdot\text{L}^{-1}$, the CA curve drawn in Figure 5-14 was generated. This trace demonstrates the expected current density versus time progression, in that, as the potential is held, species steadily transfer (*i.e.* are consumed) and the response is a steady decay.

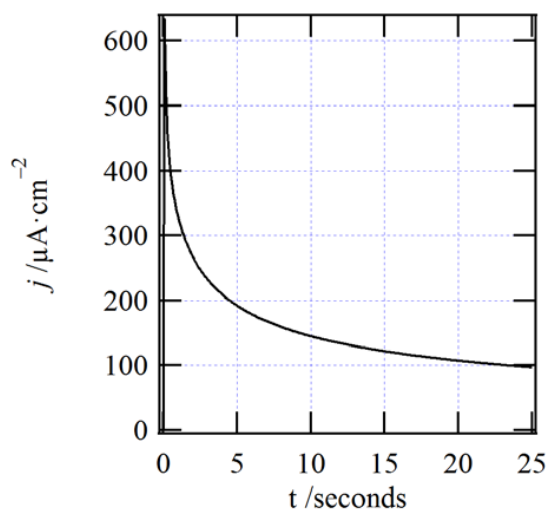


Figure 5-14. Chronoamperometric curve generated using FEM and the simulation described in Section 5.3. Simulation parameters are the same as those described for Figure 5-12.

The concentration profile of protons around the interface, without DMFc present, is displayed graphically in Figure 5-15 for five time intervals – 5, 10, 15, 20, and 25 seconds – such that $x = 0$ is the ITIES while positive and negative x , the left and right panels of Figure 5-15, correspond to the aqueous and organic phase, respectively. Inset in Figure 5-15 reveals the proton concentration profile on the organic phase with DMFc added along with k_{cf} and k_{chem} equal to 5×10^2 and $1 \times 10^4 \text{ L} \cdot \text{mol}^{-1} \cdot \text{s}^{-1}$, respectively.

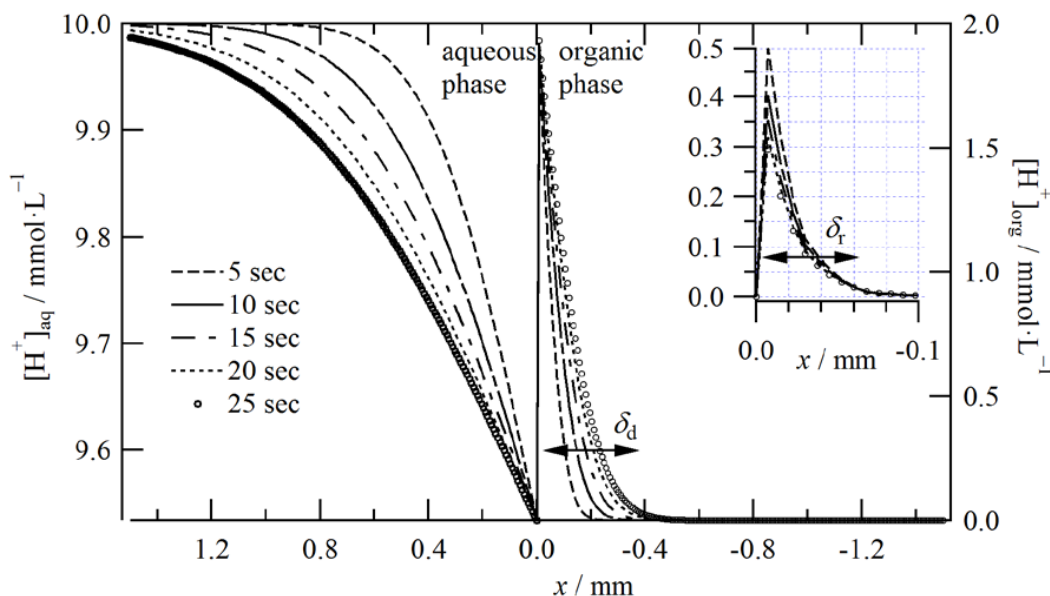


Figure 5-15. The proton $[H^+]$ concentration profile surrounding the interface ($x = 0.0 \text{ mm}$) between w (positive x) and o (negative x) during a potential step from 0.000 to 0.540 V. The following coefficients were used: $k_{cf} =$

$5 \times 10^2 \text{ L}\cdot\text{mol}^{-1}\cdot\text{s}^{-1}$, $k_{cb} = 1 \text{ s}^{-1}$, $k_{chem} = 1 \times 10^4 \text{ L}\cdot\text{mol}^{-1}\cdot\text{s}^{-1}$, and $C_{\text{DMFc},o} = 0.000 \text{ mol}\cdot\text{L}^{-1}$. Inset in the right-hand panel is the $[\text{H}^+]$ concentration profile of the organic phase with $C_{\text{DMFc},o} = 0.005 \text{ mol}\cdot\text{L}^{-1}$. The diffusion (δ_d) and reaction (δ_r) layer thickness have been indicated with double arrows for the organic side.

As time progresses the concentration of protons near the interface on the aqueous side decreased slightly, while the organic side observed a small increase. After 25 seconds – steady state conditions – protons have penetrated almost 0.40 mm into the organic phase for the system without DMFc added, whereas, for the system with DMFc, this depth is reduced to 0.06 mm. The former and latter are indicative of the diffusion (δ_d) and reaction (δ_r) layers, respectively. The latter is indicative of the rapid proton consumption through reactions **1** and **2** and may indicate that the IT- C_1C_2 mechanism is trending towards a more direct interfacial pathway; *i.e.* the proton/DMFc TOC route employed may be moving towards a transfer through interfacial complexation/decomplexation (TIC/TID) pathway. For convenience, the ITIES utilized here is an infinitely thin compact layer; however, the interface has been shown to most likely resemble a mixed solvent layer^{12,13,19} so that the system is changing from TOC to TIC/TID, and the reduction in the size of δ_r , may indicate a move towards this mixed solvent layer model. The criteria describing the trend from a IT- C_1C_2 mechanism (effectively TOC or EC mechanism) has been elucidated through rigorous treatment by Molina *et al.*,⁶⁸ in which they differentiate between three reaction conditions: a kinetic steady state, diffusive-kinetic steady state, and a total equilibrium condition.

Additionally, since FEM is a computational treatment of chemical species which views them as concentration in an abstract sense such that molecules do not have size or dimension, the number of surface active sites^{69,70} at the ITIES is effectively infinite in a TIC/TID mechanism. This may be true at higher pH, however, as the proton concentration increases the number of available DMFc molecules may diminish limiting these ‘effective’ active sites. However, this is likely a minor contributor to the disparity in the I_{eos} between the experimental and simulated results.

Another explanation for the deviation in the I_{eos} is the use of $\Delta_o^w\phi_{\text{H}^+}^{o'}$ equal to 0.580 V as previously determined by our group.⁵⁰ In that article,⁵⁰ the formal IT potential of protons at the w/DCE interface was determined using a microhole apparatus with minimal supporting electrolyte in the organic phase and only the analyte in the aqueous phase; the method also utilized a curve fitting algorithm – applied directly to the CVs – developed by Oldham⁷¹ and Wilke.⁷² While minimal supporting electrolyte was used in the organic phase,⁵⁰ it has been recently shown, by Mirkin *et al.*,⁷³ that even small amounts of supporting electrolyte can assist or facilitate the transfer of highly hydrophilic ions across the ITIES; essentially behaving as a ligand or complexing agent. It is also well known that increasing either the ligand or ion concentration will reduce the amount of applied potential necessary to induce FIT^{64,74,75} as is seen when moving from the microhole experiment⁵⁰ – performed to obtain the formal IT potential value – to the present case; therefore, a higher $\Delta_o^w\phi_{\text{H}^+}^{o'}$ may be indicated. However, since k_{cf} and k_{chem} have a marked influence on the onset potential for proton transfer

making their determination – as well as that of $\Delta_o^w \phi_{H^+}^{o'}$ – exceedingly complex and, therefore, beyond the scope of the present work.

In order to verify the final k_{cf} value of $5 \times 10^2 \text{ L} \cdot \text{mol}^{-1} \cdot \text{s}^{-1}$, two facile experiments were conducted. In the first, a blank CV was obtained using Cell 5-1 with 5 mM H_2SO_4 ($y = 5$) and no DMFc added in the DCE phase – the black, dashed trace in Figure 5-16. Next, the cell was de-aerated and transferred to the glovebox (no oxygen present) where 5 mM of DMFc was added to the organic phase – black, solid trace in Figure 5-16. Simulated CVs were generated using the same conditions and were plotted in Figure 5-16 as well, such that c_{O_2} and $c_{\text{DMFc},o}$ were set equal to 1.3 and 0 mM or 0 and 5 mM for the blue and red traces, respectively. All other conditions were the same as those described for Figure 5-15. The shift in onset potential for H^+ transfer is in good agreement between the two experimental and simulated CVs for the blank (no DMFc present), aerated (oxygen present) system and the 5 mM DMFc, anaerobic system. These two experiments provide evidence for the strength of the DMFc- H^+ formation effectively in the absence of any known homogeneous reactions – aside from the hydrogen evolution reaction that may be a minor contributor in this case.^{76,77}

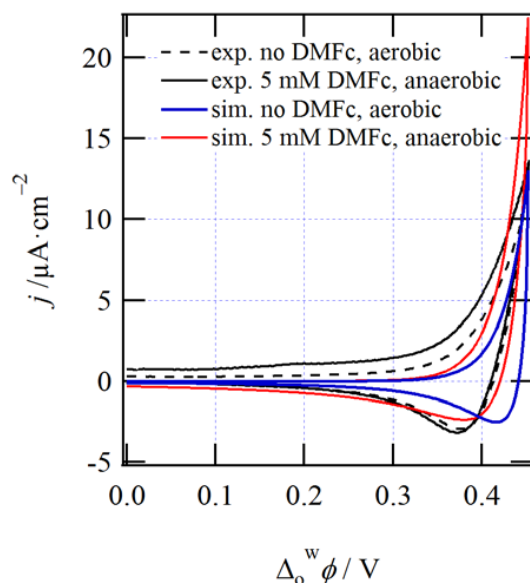


Figure 5-16. Experimental cyclic voltammograms (CVs) obtained using Cell 5-1 with 5 mM of H_2SO_4 in the aqueous phase with no DMFc under aerobic conditions (dashed curve) or 5 mM of DMFc in the DCE phase under anaerobic conditions (black, solid curve). Two simulated CVs with c_{O_2} and $c_{\text{DMFc},o}$ equal to 1.3 and 0 mM (blue curve) as well as c_{O_2} and $c_{\text{DMFc},o}$ equal to 0 and 5 mM (red curve), respectively.

Next, the formal IT potential for DMFc^+ in the simulation can be altered to reflect that of DFc^+ and Fc^+ , with these CVs shown in Figures 5-17A and B, such that $\Delta_o^w \phi_{\text{DFc}^+}^{o'}$ and $\Delta_o^w \phi_{\text{Fc}^+}^{o'}$ equal to -0.078 and -0.016 V, respectively, were utilized. For these CVs the focus was to

replicate the ratio of the H^+ return peak to the DFc^+/Fc^+ cathodic peak intensity; i_{rp}/i_{cp} . For both species i_{rp} was approximately $-6 \mu A \cdot cm^{-2}$ while i_{cp} equalled roughly $-2 \mu A \cdot cm^{-2}$, thus generating a i_{rp}/i_{cp} ratio of 3 with an I_{eos} of $\sim 15 \mu A \cdot cm^{-2}$. Rates for reactions **1** and **2**, k_{cf} and k_{chem} , were set equal to 1×10^2 and $5 \times 10^2 L \cdot mol^{-1} \cdot s^{-1}$, respectively, generating i_{rp}/i_{cp} of 3 with an I_{eos} of $\sim 40 \mu A \cdot cm^{-2}$. In this way, the simulated CVs plotted in Figures 5-17A and B are in fair agreement with the experimental ones displayed in Figure 5-8.

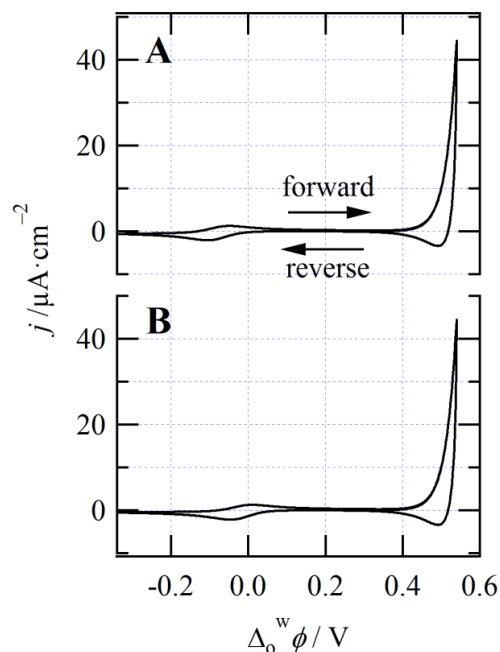


Figure 5-17. Simulated cyclic voltammograms with the same simulation parameters as those listed for Figure 5-15; however, with $\Delta_o^w \phi_{DFc^+}^{o'}$ and $\Delta_o^w \phi_{Fc^+}^{o'}$ equal to -0.078 and -0.016 V for A and B, respectively. k_{cf} and k_{chem} were set equal to 1×10^2 and $5 \times 10^2 L \cdot mol^{-1} \cdot s^{-1}$, respectively, and the initial H^+ concentration was set equal to $0.001 mol \cdot L^{-1}$.

For all three Fc derivatives the rate determining step was reaction **1** and is in good agreement with the result recently published by Trojáněk *et al.*,²⁴ in which a Fc derivative with six methyl substituents on the cyclopentadienyl rings was found to have a non-catalyzed rate of $4.7 \times 10^3 L \cdot mol^{-1} \cdot s^{-1}$.

A list of the simulation parameters can be found in Table 5-5, including the diffusion coefficients, initial concentrations of each species in either phase, standard/formal IT potentials with calculated partition coefficients, as well as the values of k_{cf} and k_{chem} determined for each of the reducing agents. The partition coefficient, shown in Table 5-5, is related to potential through the following,⁷⁸

$$\ln P_i = \ln \frac{c_{i,o}}{c_{i,w}} = \ln P_i^{o'} + \frac{z_i F}{RT} \Delta_o^w \phi \quad (5-15)$$

$$\text{where, } \ln P_i^{o'} = -\frac{z_i F}{RT} \Delta_o^w \phi_i^{o'}$$

Table 5-5. Parameters used in the simulation including the diffusion coefficients in either phase ($D_{i,w} / D_{i,o}$), the initial concentrations for either phase ($c_{i,w}^* / c_{i,o}^*$), the formal ion transfer potentials ($\Delta_o^w \phi_i^{o'}$), the partition coefficient ($P_i^{o'}$, from w to o), along with the final values of k_{cf} and k_{chem} for the associated electron donor species.

Species	$D_{i,w} / D_{i,o}$ ($\times 10^{-5} \text{ cm}^2 \cdot \text{s}^{-1}$)	$c_{i,w}^* / c_{i,o}^*$ ($\text{mmol} \cdot \text{L}^{-1}$)	$\Delta_o^w \phi_i^{o'}$ (V)	$P_i^{o'}$ (w to o)	k_{cf}	k_{chem}
					(L·mol ⁻¹ ·s ⁻¹)	
H ⁺	9.3/1.0	y (Cell 1)/0	0.580	1.57×10^{-10}		
SO ₄ ⁻	NA	NA	-0.540	7.44×10^{-10}		
DMFc ⁺	0.7/0.7	0/0	-0.250	1.68×10^4	5×10^2	1×10^4
DFc ⁺	0.7/0.7	0/5	-0.078	21	1×10^2	5×10^2
Fc ⁺	0.7/0.7	0/5	-0.016	2	1×10^2	5×10^2
O ₂	-/2.8	-/1	-	6		
BA	-	-	-0.699	6.55×10^{11}		
TB	-	-	0.718	1.37×10^{12}		

While ferrocenium demonstrates a moderate Gibbs energy of transfer, where $\Delta G_{tr, \text{Fc}^+}^{w \rightarrow o} = z_i F \Delta_o^w \phi_{\text{Fc}^+}^{o'}$ such that $-1.5 \text{ kJ} \cdot \text{mol}^{-1}$ for Fc⁺ is obtained. The Gibbs energy of transfer for the neutral Fc species has been determined to be $-24.5 \text{ kJ} \cdot \text{mol}^{-1}$,⁷⁹ from which the standard partition coefficient of Fc can be calculated through equation 5-15 to be 1.8×10^4 . It can be concluded, based on this value that, a negligible concentration of Fc would transfer to the aqueous phase at equilibrium on the experimental time scale. The open circuit potential of the system was calculated, as described recently,⁸⁰ using the initial experimental

concentrations and found to be 0.060 V. While protons are too hydrophilic to transfer, if the solution is left for a long enough period of time, then Fc may partition to the aqueous phase, as shown recently by Opallo *et al.*,²⁵ and subsequently react; however, this was found to be minor. Therefore, the IT-C₁C₂ mechanism involving strictly homogeneous organic phase ORR, as shown in Figure 5-9, is reasonable on the time scale of the CV experiment. In this way, these reactions are only induced when protons are transferred to the organic phase through an external, applied potential. To the best of our knowledge there is no published data for the partition coefficient of neutral DMFc or DFc at a w/DCE interface; however, it is reasonable to assume that these species are more hydrophobic than neutral Fc and would follow a similar mechanism of ORR – that being restricted, predominantly, to the organic phase.

Additionally, varying scan rates 0.010 to 0.100 V·s⁻¹ were performed both experimentally and using the simulation; the only appreciable change was an increase in the DMFc⁺ transfer peak as expected from the Randles-Sevcik equation with no significant change to the H⁺ return peak.

5.5. Conclusions

The ORR was firstly investigated in the bulk DCE phase using HTB as the proton source along with DMFc as the electron donor, employing *in-situ* absorption spectroscopy as the technique. Experimental conditions were varied to try to elucidate the mechanism of this reaction, while it was found that the ORR in the DCE phase is not a simple elementary reaction but composed of multiple steps. Another interesting effect arises: counter-anions such as TB⁻ or especially ClO₄⁻ have significant inhibitive effect on the ORR kinetics, so does H₂O. It was explained as the ion-pair formation between the protonated DMFc – DMFcH⁺ and counter-anions or H₂O (acting as a ligand). Due to the complexity in terms of the mechanism, FEM simulations were employed to clarify the specific steps in the reaction.

The ORR was then explored using facile electrochemistry at a biphasic interface between water and DCE, under aerobic conditions, using DMFc, DFc, and Fc, dissolved in the organic phase, as electron donors and sulfuric acid in the aqueous phase as a proton source. It should be stressed that now the bulk concentrations of TB⁻ and H₂O in the DCE phase were assumed to be constant. Two prominent curve features within the CV were noted: the absence of a return peak current for H⁺ at the edge of the PPW along with the emergence of an IT peak towards negative potentials that was later assigned to DMFc⁺ transfer. It was thereby concluded that protons were being consumed in the organic phase in a reaction oxidizing DMFc. This is in good agreement with previous reports.^{6,20,22-25,55,56,60}

With this evidence, a mechanism was proposed and tested using a two-dimensional FEM simulation, whereby oxygen was reduced by first proton transfer to the organic phase, followed by formation of a DMFc-H⁺, which would then react with dissolved oxygen to generate a peroxy radical species, HO₂[•]. It was also proposed that this radical would react quickly, with either DMFc-H⁺ or H₂O and a proton, to form hydrogen peroxide completing the reduction of oxygen. In this way, potential dependent proton transfer comprised the electrochemical (*i.e.* IT) step, while the two homogeneous reactions, DMFc-H⁺ formation and

oxygen reduction, constituted the chemical step in a reaction pathway reminiscent of classical EC-mechanisms. No further reactions were included as the formation of H_2O_2 was thought to be fast and irreversible, such that the HO_2^\cdot step was considered a ‘hydrogen-sink’ for the purposes of the simulation.

Through comparison of the simulated and experimental CVs several critical insights were garnered. First, the rate of the reaction (1) is measureable by CV and is likely between 1 and $5 \times 10^2 \text{ L}\cdot\text{mol}^{-1}\cdot\text{s}^{-1}$ for all three Fc derivatives and is the rate-determining step, based on the height of the $\text{DMFc}^+/\text{DFc}^+/\text{Fc}^+$ cathodic transfer peak along with the current at the edge of scan, I_{eos} , profile. The rate of the homogeneous reaction (2) was similarly discerned and found to be $1 \times 10^4 \text{ L}\cdot\text{mol}^{-1}\cdot\text{s}^{-1}$ for DMFc, but only $5 \times 10^2 \text{ L}\cdot\text{mol}^{-1}\cdot\text{s}^{-1}$ for DFC/Fc. However, based on the investigations on the inhibitive effect of TB^- and H_2O on the ORR kinetics in the bulk DCE phase, it can be deduced that the ORR near the ITIES in the DCE phase is actually slower than that under anhydrous conditions. Besides, as one of the products – H_2O_2 can be decomposed or further reduced to H_2O , this biphasic ORR is actually self-inhibiting. Second, biphasic ORR is not dependent on the diffusion of DMFc in the organic phase. Most importantly, the simulated CVs demonstrate the feasibility of the proposed mechanism through their comparison to experimental curve features.

5.6. References

- (1) O’Sullivan, S.; Arrigan, D. W. M. *Anal. Chem.* **2012**, 85, 1389.
- (2) Wikström, M. *Biochim. Biophys. Acta* **2012**, 1817, 468.
- (3) Yasuda, T.; Watanabe, M. *MRS Bull.* **2013**, 38, 560.
- (4) Pringle, J. M. *Phys. Chem. Chem. Phys.* **2013**, 15, 1339.
- (5) Wang, X.; Ahluwalia, R. K.; Steinbach, A. J. *J. Electrochem. Soc.* **2013**, 160, F251.
- (6) Peljo, P.; Rauhala, T.; Murtomäki, L.; Kallio, T.; Kontturi, K. *Int. J. Hydrogen Energy* **2011**, 36, 10033.
- (7) Otsuka, K.; Yamanaka, I. *Electrochim. Acta* **1990**, 35, 319.
- (8) Yamanaka, I.; Onizawa, T.; Takenaka, S.; Otsuka, K. *Angew. Chem., Int. Ed.* **2003**, 42, 3653.
- (9) Yamanaka, I.; Murayama, T. *Angew. Chem., Int. Ed.* **2008**, 47, 1900.
- (10) Khan, A.; Lu, X.; Aldous, L.; Zhao, C. *J. Phys. Chem. C* **2013**, 117, 18334.
- (11) Fukuzumi, S.; Kotani, H.; Lucas, H. R.; Doi, K.; Suenobu, T.; Peterson, R. L.; Karlin, K. D. *J. Am. Chem. Soc.* **2010**, 132, 6874.
- (12) Samec, Z.; Langmaier, J.; Kakiuchi, T. *Pure Appl. Chem.* **2009**, 81, 1473.
- (13) Girault, H. H. In *Electroanalytical Chemistry, Vol 23*; Bard, A. J., Zoski, C. G., Eds. 2010; Vol. 23, p 1.
- (14) Liu, S.; Li, Q.; Shao, Y. *Chem. Soc. Rev.* **2011**, 40, 2236.
- (15) Wang, Y.; Kececi, K.; Velmurugan, J.; Mirkin, M. V. *Chem. Sci.* **2013**, 4, 3606.
- (16) Scanlon, M. D. *ChemCatChem* **2013**, 5, 1696.
- (17) Méndez, M. A.; Partovi-Nia, R.; Hatay, I.; Su, B.; Ge, P.; Olaya, A.; Younan, N.; Hojeij, M.; Girault, H. H. *Phys. Chem. Chem. Phys.* **2010**, 12, 15163.
- (18) Ge, P.; Olaya, A. J.; Scanlon, M. D.; Hatay Patir, I.; Vrabel, H.; Girault, H. H. *ChemPhysChem* **2013**, 14, 2308.
- (19) Peljo, P.; Girault, H. H. In *Encyclopedia of Analytical Chemistry*; John Wiley & Sons, Ltd: 2012.

- (20) Su, B.; Nia, R. P.; Li, F.; Hojeij, M.; Prudent, M.; Corminboeuf, C.; Samec, Z.; Girault, H. H. *Angew. Chem., Int. Ed.* **2008**, *47*, 4675.
- (21) Su, B.; Hatay, I.; Ge, P. Y.; Mendez, M.; Corminboeuf, C.; Samec, Z.; Ersoz, M.; Girault, H. H. *Chem. Commun.* **2010**, *46*, 2918.
- (22) Deng, H.; Peljo, P.; Cortés-Salazar, F.; Ge, P.; Kontturi, K.; Girault, H. H. *J. Electroanal. Chem.* **2012**, *681*, 16.
- (23) Peljo, P.; Murtomäki, L.; Kallio, T.; Xu, H. J.; Meyer, M.; Gros, C. P.; Barbe, J. M.; Girault, H. H.; Laasonen, K.; Kontturi, K. *J. Am. Chem. Soc.* **2012**, *134*, 5974.
- (24) Trojánek, A.; Langmaier, J.; Samec, Z. *Electrochim. Acta* **2012**, *82*, 457.
- (25) Jedraszko, J.; Nogala, W.; Adamiak, W.; Rozniecka, E.; Lubarska-Radziejewska, I.; Girault, H. H.; Opallo, M. *J. Phys. Chem. C* **2013**, *117*, 20681.
- (26) Ohde, H.; Maeda, K.; Yoshida, Y.; Kihara, S. *J. Electroanal. Chem.* **2000**, *483*, 108.
- (27) Deng, H.; Peljo, P.; Stockmann, T. J.; Qiao, L.; Vainikka, T.; Kontturi, K.; Opallo, M.; Girault, H. H. *Chem. Commun.* **2014**, *50*, 5554.
- (28) Park, S. H.; Choi, C. H.; Koh, J. K.; Pak, C.; Jin, S.-a.; Woo, S. I. *ACS Comb. Sci.* **2013**, *15*, 572.
- (29) Kariuki, N. N.; Khudhayer, W. J.; Karabacak, T.; Myers, D. J. *ACS Catal.* **2013**, *3*, 3123.
- (30) Escaño, M. C. S.; Kasai, H. *J. Power Sources* **2014**, *247*, 562.
- (31) Nishi, N.; Imakura, S.; Kakiuchi, T. *J. Electroanal. Chem.* **2008**, *621*, 297.
- (32) Nishi, N.; Murakami, H.; Imakura, S.; Kakiuchi, T. *Anal. Chem.* **2006**, *78*, 5805.
- (33) Stockmann, T. J.; Ding, Z. *J. Electroanal. Chem.* **2010**, *649*, 23.
- (34) Stockmann, T. J.; Ding, Z. *J. Phys. Chem. B* **2012**, *116*, 12826.
- (35) Trojánek, A.; Langmaier, J.; Záliš, S.; Samec, Z. *Chem. Commun.* **2012**, *48*, 4094.
- (36) Hatay, I.; Ge, P. Y.; Vrabel, H.; Hu, X.; Girault, H. H. *Energy Environ. Sci.* **2011**, *4*, 4246.
- (37) Momotenko, D.; Qiao, L.; Cortés-Salazar, F.; Lesch, A.; Wittstock, G.; Girault, H. H. *Anal. Chem.* **2012**, *84*, 6630.
- (38) Chaturvedi, A.; Foutz, T. J.; McIntyre, C. C. *Brain Stimul.* **2012**, *5*, 369.
- (39) Fosdick, S. E.; Crooks, J. A.; Chang, B.-Y.; Crooks, R. M. *J. Am. Chem. Soc.* **2010**, *132*, 9226.
- (40) Khaleel, M. A.; Lin, Z.; Singh, P.; Surdoval, W.; Collin, D. *J. Power Sources* **2004**, *130*, 136.
- (41) Jossierand, J.; Morandini, J.; Lee, H. J.; Ferrigno, R.; Girault, H. H. *J. Electroanal. Chem.* **1999**, *468*, 42.
- (42) Rodgers, P. J.; Amemiya, S. *Anal. Chem.* **2007**, *79*, 9276.
- (43) Light, T. S.; Licht, S.; Bevilacqua, A. C.; Morash, K. R. *Electrochem. Solid-State Lett.* **2005**, *8*, E16.
- (44) Lee, S. H.; Rasaiah, J. C. *J. Chem. Phys.* **2011**, *135*, 1245051.
- (45) Karyakin, A. A. *Electroanalysis* **2001**, *13*, 813.
- (46) Atkins, P. W. *Physical Chemistry, 4th ed.*; Oxford University Press: Oxford, 1990.
- (47) Trojánek, A.; Langmaier, J.; Ebera, J.; Záli, S.; Barbe, J. M.; Girault, H. H.; Samec, Z. *Chem. Commun.* **2011**, *47*, 5446.
- (48) Nowicka, A. M.; Stojek, Z.; Ciszewska, M. *Anal. Lett.* **2004**, *37*, 979.
- (49) Fukuzumi, S.; Okamoto, K.; Gros, C. P.; Guillard, R. *J. Am. Chem. Soc.* **2004**, *126*, 10441.
- (50) Olaya, A. J.; Méndez, M. A.; Cortes-Salazar, F.; Girault, H. H. *J. Electroanal. Chem.* **2010**, *644*, 60.
- (51) Parker, A. J. *Electrochim. Acta* **1976**, *21*, 671.
- (52) Zhurov, K.; Dickinson, E. J. F.; Compton, R. G. *J. Phys. Chem. B* **2011**, *115*, 6909.

- (53) Wandlowski, T.; Mareček, V.; Samec, Z. *Electrochim. Acta* **1990**, *35*, 1173.
- (54) *CRC Handbook of Chemistry and Physics*; 94th ed.; Haynes, W. M., Ed.; CRC Press: Boca Raton, 2013.
- (55) Trojánek, A.; Mareček, V.; Jänchenová, H.; Samec, Z. *Electrochem. Commun.* **2007**, *9*, 2185.
- (56) Trojánek, A.; Langmaier, J.; Su, B.; Girault, H. H.; Samec, Z. *Electrochem. Commun.* **2009**, *11*, 1940.
- (57) Langmaier, J.; Samec, Z. *Anal. Chem.* **2009**, *81*, 6382.
- (58) Fomin, V. M. *Russ. J. Gen. Chem.* **2007**, *77*, 954.
- (59) Luehring, P.; Schumpe, A. *J. Chem. Eng. Data* **1989**, *34*, 250.
- (60) Trojánek, A.; Langmaier, J.; Samec, Z. *Electrochem. Commun.* **2006**, *8*, 475.
- (61) Schumpe, A.; Luehring, P. *J. Chem. Eng. Data* **1990**, *35*, 24.
- (62) Stockmann, T. J.; Montgomery, A.-M.; Ding, Z. *Anal. Chem.* **2012**, *84*, 6143.
- (63) Qiao, Y.; Zhang, B.; Zhu, X.; Ji, T.; Li, B.; Li, Q.; Chen, E.; Shao, Y. *Electroanalysis* **2013**, *25*, 1080.
- (64) Reymond, F.; Lagger, G.; Carrupt, P.-A.; Girault, H. H. *J. Electroanal. Chem.* **1998**, *451*, 59.
- (65) Nestor, U.; Wen, H.; Girma, G.; Mei, Z.; Fei, W.; Yang, Y.; Zhang, C.; Zhan, D. *Chem. Commun.* **2014**, *50*, 1015.
- (66) Shao, Y.; Osborne, M. D.; Girault, H. H. *J. Electroanal. Chem.* **1991**, *318*, 101.
- (67) Koryta, J. *Electrochim. Acta* **1979**, *24*, 293.
- (68) Molina, Á.; Torralba, E.; Serna, C.; Ortuño, J. A. *J. Phys. Chem. A* **2012**, *116*, 6452.
- (69) Savéant, J. M. *J. Electroanal. Chem.* **1980**, *112*, 175.
- (70) Amatore, C.; M'Halla, F.; Savéant, J. M. *J. Electroanal. Chem.* **1981**, *123*, 219.
- (71) Oldham, K. B. *J. Electroanal. Chem.* **1988**, *250*, 1.
- (72) Wilke, S. *J. Electroanal. Chem.* **2001**, *504*, 184.
- (73) Sun, P.; Laforge, F. O.; Mirkin, M. V. *J. Am. Chem. Soc.* **2005**, *127*, 8596.
- (74) Kakiuchi, T.; Senda, M. *J. Electroanal. Chem.* **1991**, *300*, 431.
- (75) Samec, Z.; Homolka, D.; Mareček, V. *J. Electroanal. Chem.* **1982**, *135*, 265.
- (76) Hatay, I.; Su, B.; Li, F.; Partovi-Nia, R.; Vrubel, H.; Hu, X.; Ersoz, M.; Girault, H. H. *Angew. Chem., Int. Ed.* **2009**, *48*, 5139.
- (77) Scanlon, M. D.; Bian, X.; Vrubel, H.; Amstutz, V.; Schenk, K.; Hu, X.; Liu, B.; Girault, H. H. *Phys. Chem. Chem. Phys.* **2013**, *15*, 2847.
- (78) Girault, H. H. *Analytical and Physical Electrochemistry*; 1st ed.; EPFL Press: Lausanne, 2004.
- (79) Fermin, D. J.; Lahtinen, R. In *Liquid Interfaces in Chemical, Biological and Pharmaceutical Applications*; Volkov, A., G., Ed.; Marcel Dekker: New York, 2001; Vol. 95, p 213.
- (80) Li, Y.; Wu, S.; Su, B. *Chem. Eur. J.* **2012**, *18*, 7372.

Chapter 6

Kinetic Differentiation of Bulk/Interfacial Oxygen Reduction Mechanisms at/near Liquid/Liquid Interfaces using Scanning Electrochemical Microscopy

Based on J. Electroanal. Chem., in press, DOI: 10.1016/j.jelechem.2014.08.031.

6.1. Introduction

Oxygen reduction reaction (ORR) at the liquid/liquid interface that is normally composed of two phases between water (w) and an organic solvent (o, *e.g.*, 1,2-dichloroethane, DCE) has been introduced in Section 1.3 in Chapter 1 and also in Chapter 5. In the last chapter, the kinetics of biphasic ORR by ferrocene (Fc) and its derivatives such as decamethylferrocene (DMFc) as the lipophilic electron donors, along with sulfuric acid as the aqueous proton source, were investigated through comparison of experimentally observed voltammograms to simulated ones generated by COMSOL Multiphysics utilizing the finite element method (FEM).¹ The reaction pathway was shown to be composed of a potential dependent proton transfer step (*i.e.* ion transfer, IT) from the aqueous to organic phases along with two homogeneous chemical reactions (C_1C_2) occurring in the organic phase – an IT- C_1C_2 mechanism.¹ In that study, the reaction between DMFc and $H^+(o)$ to form $DMFc-H^+$ was considered the first step (C_1), while reaction of $DMFc-H^+$ with oxygen to form a hydrogen peroxy radical species (HO_2^\bullet) and $DMFc^+$ was recognized as the second step (C_2). The following reactions, between HO_2^\bullet and another DMFc and H^+ forming H_2O_2 and $DMFc^+$, were considered to be fast and irreversible.

In this chapter, an alternative methodology employing scanning electrochemical microscopy (SECM) in the feedback mode was developed to study the mechanism and kinetics of the ORR at the ITIES. It should be mentioned that an earlier work surrounding *in situ* SECM detection of H_2O_2 produced in a w/DCE biphasic reaction has been reported;² however, no kinetic/thermodynamic information was obtained, while the work presented here will address this missing component and provide new physical, mechanistic insights. SECM in the feedback mode implements a microelectrode probe approaching or scanning over an interface, while recording the current generated by a redox mediator. Depending on the capability of the interface to regenerate the initial redox species, a current change monitored at the

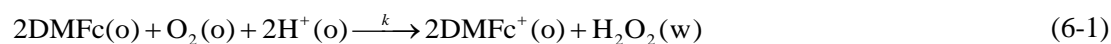
microelectrode allows the extraction of kinetic information by taking into account the balance between rates of electron transfer and mass transport processes. Therefore, SECM is an excellent tool to study interfacial phenomena,^{3,4} such as electron transfer at liquid/liquid interfaces,^{5,6} as well as homogeneous chemical reactions involving redox species generated at the SECM probe.⁷⁻¹¹ For instance, Bard and co-workers have employed SECM for rapid screening of metallic catalysts deposited on a solid substrate in acidic media for oxygen reduction.^{12,13}

Specifically, a decamethylferrocenium (DMFc⁺) solution was prepared firstly by a biphasic reaction.¹⁴ Then DMFc⁺ is reduced to DMFc at the tip of a microelectrode in DCE and the electrogenerated DMFc reacts with protons (either from aqueous in a liquid/liquid interface system or from an organic acid) and dissolved oxygen to be re-oxidized in a EC' scheme.¹⁵ Steady-state microelectrode voltammetry has been previously employed to measure the kinetics of a catalytic EC' process,¹⁶ but SECM feedback measurements offer some further advantages featured with the tunable kinetic and mass transfer regimes;¹⁷ therefore, this methodology has been adopted for this work.

6.2. Theory

6.2.1. Mechanism of oxygen reduction by DMFc

The overall oxygen reduction by DMFc at the liquid/liquid interface is described by reaction (6-1),¹⁴ in which H⁺ in the organic phase (o = DCE) is transferred from aqueous phase (w) by either an external electrical polarization or by phase transfer catalysis with an addition of extremely lipophilic counter-anion.



Reaction 6-1 is composed of the individual steps shown in reactions 6-2 to 6-4, occurring in the oil phase.



The rate determining step has been found to be the protonation of DMFc to form DMFc-H⁺ (equation 6-2).^{1,18} The DMFc-H⁺ can then react with oxygen to produce DMFc⁺ and the hydrogen peroxy radical (equation 6-3) that then reacts quickly with a proton and an equivalent of DMFc to produce H₂O₂ (reaction 6-4).^{1,18} It has been shown by FEM simulations that reaction 6-3 can still influence the kinetics of the overall reaction (equation 6-1) appreciably, even though the reaction described in equation 6-2 is the rate determining step.¹ The H₂O₂ produced then partitions into the aqueous phase. Hence the total rate of DMFc consumption or DMFc⁺ formation can be estimated by taking the steady-state

assumption for the intermediate species – DMFcH^+ and HO_2^\bullet and assuming fast diffusing O_2 can be replenished during the course of the reaction. It reads:

$$\begin{aligned}\frac{d[\text{DMFcH}^+]}{dt} &= k_1[\text{DMFc}][\text{H}^+] - k_2[\text{DMFcH}^+] = 0 \\ \frac{d[\text{HO}_2^\bullet]}{dt} &= k_2[\text{DMFcH}^+] - k_3[\text{HO}_2^\bullet][\text{DMFc}][\text{H}^+] = 0\end{aligned}\quad (6-5)$$

From equation 6-5, we can obtain:

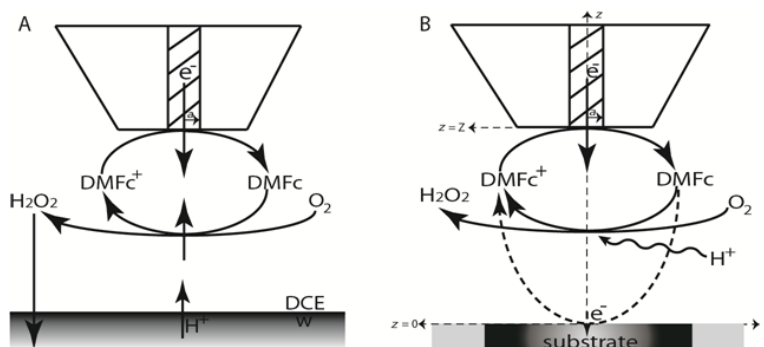
$$k_2[\text{DMFcH}^+] = k_3[\text{HO}_2^\bullet][\text{DMFc}][\text{H}^+] = k_1[\text{DMFc}][\text{H}^+] \quad (6-6)$$

Finally, the rate of the DMFc^+ formation in the overall reaction (in combination with equation 6-6) can be expressed approximately as

$$\begin{aligned}\frac{d[\text{DMFc}^+]}{dt} &= -\frac{d[\text{H}^+]}{dt} = -\frac{d[\text{DMFc}]}{dt} \\ &\approx k_2[\text{DMFcH}^+] + k_3[\text{HO}_2^\bullet][\text{DMFc}][\text{H}^+] \\ &= k_1[\text{DMFc}][\text{H}^+] + k_1[\text{DMFc}][\text{H}^+] \\ &= 2k_1[\text{DMFc}][\text{H}^+]\end{aligned}\quad (6-7)$$

where k_1 is the rate constant of DMFcH^+ formation (equation 6-2).

To study the kinetics of this process, DMFc^+ was reduced to DMFc at the SECM tip, thus the electrogenerated DMFc can then react with oxygen and protons according to the equation 6-1, regenerating the starting material, DMFc^+ (Scheme 6-1). The protons were introduced into the DCE phase either by positively polarizing the liquid/liquid interface to such an extent that protons can be transferred from the aqueous to the oil phase (Scheme 6-1A) or by direct addition of an organic acid into the DCE phase (in this case, the w/DCE interface is replaced by a solid conductive substrate, see Scheme 6-1B). Under these conditions, regeneration of DMFc^+ takes place by the overall homogeneous reaction (equation 6-1), with the interfacial reaction as a minor contributor; Scheme 6-1A only shows the major contributor for clarity. Hence, the system can be studied either with the w/DCE interface as the proton source or in the homogeneous phase by adding an organic acid directly into the solution.



Scheme 6-1. Schematic of the catalytic EC' process for oxygen reduction by electrogenerated DMFc studied with SECM in feedback mode (not to the scale). Panel A shows the biphasic system where the polarized w/DCE interface acts as the proton source and panel B illustrates the homogeneous phase system with organic acid as the proton source, respectively. The thin dashed lines with arrows indicate the coordinate axes in panel B. These two systems are detailed in Figure 6-1 A and B, respectively.

6.2.2. Simulations (*carried out by Pekka Peljo*)

The ORR kinetics can be studied more conveniently in a homogeneous phase by adding an organic acid directly into the solution. The experimental evidence will be addressed in Section 6.4.2; however, to extract the kinetic rate constants of the homogeneous ORR quantitatively, a simulation model, employing COMSOL Multiphysics software and incorporating a solid conductive substrate in place of the liquid/liquid interface, along with an organic acid as the proton source, was built (see Scheme 6-1B). The merit of this strategy is the number of independent variables in this model is less than that in a model built on liquid/liquid interfacial design, simplifying the simulation drastically. DMFc⁺ is reduced at the microelectrode tip, producing DMFc (reaction 6-8). DMFc will react homogeneously with protons and oxygen, and is oxidized back to DMFc⁺ by means of bulk (equation 6-1) and heterogeneous (substrate, equation 6-9) reactions. The rate of reaction 6-1 can be estimated as shown in equation 6-7, where $k = 2k_1$. O₂ is assumed to be in excess during the homogeneous reaction; the system under consideration is deemed open, such that O₂ is continually replenished. In this way, the current profile of the tip approaching the conductive substrate is different between the cases with and without the homogeneous ORR. In the absence of homogeneous reactions ($k = 0$), DMFc was oxidized back to DMFc⁺ directly on the solid substrate (equation 6-9) in a close tip/substrate separation. While, less DMFc will be oxidized directly on the solid substrate due to a compressed current (concentration) profile of DMFc close to the tip surface in the presence of the competitive homogeneous ORR ($k \neq 0$).¹⁹ The approach curves recorded at the tip are highly sensitive to the rate constant of the homogeneous chemical reaction and comparison and fitting between theoretical and experimental approach curves form the basis of the methodology described here.



Migration effects are assumed to be negligible in the presence of a large excess of a supporting electrolyte, so that mass transport mainly occurs by diffusion and can be described using Fick's laws with the corresponding equations in axial-symmetric, cylindrical coordinates (r , radial, and z , normal, coordinates with the origin at the center of the substrate disk). These can be written as the following equations (6-10)-(6-12) in a steady-state mode.

$$\frac{\partial c_{\text{DMFc}^+}}{\partial t} = D_{\text{DMFc}^+} \left(\frac{\partial^2 c_{\text{DMFc}^+}}{\partial z^2} + \frac{\partial^2 c_{\text{DMFc}^+}}{\partial r^2} + \frac{1}{r} \frac{\partial c_{\text{DMFc}^+}}{\partial r} \right) + k c_{\text{DMFc}} c_{\text{H}^+} = 0 \quad (6-10)$$

$$\frac{\partial c_{\text{DMFc}}}{\partial t} = D_{\text{DMFc}} \left(\frac{\partial^2 c_{\text{DMFc}}}{\partial z^2} + \frac{\partial^2 c_{\text{DMFc}}}{\partial r^2} + \frac{1}{r} \frac{\partial c_{\text{DMFc}}}{\partial r} \right) - k c_{\text{DMFc}} c_{\text{H}^+} = 0 \quad (6-11)$$

$$\frac{\partial c_{\text{H}^+}}{\partial t} = D_{\text{H}^+} \left(\frac{\partial^2 c_{\text{H}^+}}{\partial z^2} + \frac{\partial^2 c_{\text{H}^+}}{\partial r^2} + \frac{1}{r} \frac{\partial c_{\text{H}^+}}{\partial r} \right) - k c_{\text{DMFc}} c_{\text{H}^+} = 0 \quad (6-12)$$

where c_i and D_i are the concentration and diffusion coefficient of species i and k is the rate constant of the homogeneous chemical reaction in the organic solution (equation 6-1).

The boundary conditions are:

$$D_{\text{DMFc}^+} \frac{\partial c_{\text{DMFc}^+}}{\partial z} = k_{f,T} c_{\text{DMFc}^+} - k_{b,T} c_{\text{DMFc}} = -D_{\text{DMFc}} \frac{\partial c_{\text{DMFc}}}{\partial z}, D_{\text{H}^+} \frac{\partial c_{\text{H}^+}}{\partial z} = 0$$

(tip electrode surface, $z = Z$) (6-13)

$$D_{\text{DMFc}^+} \frac{\partial c_{\text{DMFc}^+}}{\partial z} = D_{\text{DMFc}} \frac{\partial c_{\text{DMFc}}}{\partial z} = D_{\text{H}^+} \frac{\partial c_{\text{H}^+}}{\partial z} = 0 \quad (\text{glass insulating sheath}) \quad (6-14)$$

$$D_{\text{DMFc}} \frac{\partial c_{\text{DMFc}}}{\partial z} = k_{f,S} c_{\text{DMFc}} - k_{b,S} c_{\text{DMFc}^+} = -D_{\text{DMFc}^+} \frac{\partial c_{\text{DMFc}^+}}{\partial z}, D_{\text{H}^+} \frac{\partial c_{\text{H}^+}}{\partial z} = 0$$

(solid substrate, $z = 0$) (6-15)

$$c_{\text{DMFc}^+} = c_{\text{DMFc}^+}^*, c_{\text{DMFc}} = 0, c_{\text{H}^+} = c_{\text{H}^+}^* \quad (\text{open boundaries far from the tip}) \quad (6-16)$$

Equations (6-13) and (6-15) indicate that protons are inert at the microelectrode tip and at the substrate. $k_{f,T}$ and $k_{b,T}$ are the rate constants of the forward and backward reactions at the tip (reaction 6-8), and $k_{f,S}$ and $k_{b,S}$ are the rate constants of the forward and backward reactions at the substrate (equation 6-9). The reaction kinetics at the electrodes are set so that $c_{\text{DMFc}^+}(z = Z, r, t \neq 0) = 0$ at the surface of the tip, and $c_{\text{DMFc}}(z = 0, r, t \neq 0) = 0$ at the surface of the substrate. Here $k_{b,T}$ is set to zero, $k_{f,T} = 1 \times 10^6$, $k_{b,S}$ is set to zero, and $k_{f,S} = 1 \times 10^6$. Far from the electrode the concentrations reach the bulk values. The initial conditions over all space (all r , all z) are

$$c_{\text{DMFc}^+}(z, r, t = 0) = c_{\text{DMFc}^+}^*, c_{\text{DMFc}}(z, r, t = 0) = 0, c_{\text{H}^+}(z, r, t = 0) = c_{\text{H}^+}^* \quad (6-17)$$

Equation (6-17) describes that initially there is only DMFc^+ and protons present in the system. Computational approach curves were obtained by varying the position of the tip in the simulations, while a series of working curves were obtained for different values of k . To compare the computational and experimental results, experimentally obtained normalized currents were calculated as follows.

$$I = \frac{i_{\text{UME}}}{i_{\text{UME},\infty}} \quad (6-18)$$

$$i_{\text{UME}} = \frac{\pi}{2} \int_0^a \frac{\partial c}{\partial z} r dr, \text{ at } z = Z \quad (6-19)$$

$$i_{\text{UME},\infty} = \frac{\pi}{2} \int_0^a \frac{\partial c}{\partial z} r dr, \text{ at } z = Z, Z \rightarrow \infty \quad (6-20)$$

where $i_{\text{UME},\infty}$ is the steady-state diffusion-limited tip current for reduction of DMFc^+ when the tip is far from the substrate. This approach allows for better comparison of simulated and experimental data, as $i_{\text{UME},\infty}$ can always be measured and used for current normalization. In the absence of protons or without a homogenous reaction ($k = 0$)

$$i_{\text{UME},\infty} = 4FaD_{\text{DMFc}^+} c_{\text{DMFc}^+}^* \quad (6-21)$$

where a is the radius of the carbon or glassy-carbon microelectrode.

The model was validated by simulating approach curves without any homogeneous reactions ($k = 0$) and comparing the results with the analytical expressions for positive feedback.²⁰ The obtained approach curve differs from the analytical solution by less than 2.5%.

6.3. Experimental section

6.3.1. Chemicals

The common chemicals used throughout this Chapter have been summarized in Section 2.2 in Chapter 2. The organic acid HTB was prepared by shaking x mM LiTB and y mM H_2SO_4 ($x \ll y$) in aqueous phase with pure DCE for 1 h, followed by the isolation of the DCE phase.¹⁸ The obtained DCE solution is assumed to contain only HTB in x mM, considering the extreme lipophilicity of TB^- as phase transfer catalyst for H^+ . 5 mM DMFc^+TB^- with 5 mM BATB as supporting electrolyte in DCE was prepared by two-phase shake flask reactions between an aqueous phase containing 5 mM LiTB along with 50 mM H_2SO_4 and a DCE phase containing 5 mM BATB and 5 mM DMFc. The biphasic mixture was stirred for 1 h, followed by isolation of the DCE phase.¹⁴

6.3.2. Electrochemical measurements

All the electrochemical measurements were performed at ambient temperature (20 ± 2 °C) under aerobic conditions in a Faraday cage with a CHI900 electrochemical workstation (CH Instruments, Austin, USA) or an Autolab PGSTAT 30 potentiostat (Metrohm, Switzerland). The electrochemical cells are described in Figure 6-1, including the setup for the liquid/liquid interface system as illustrated in Figure 6-1A and that for homogeneous phase system drawn in Figure 6-1B. For the liquid/liquid interface system, the reference electrode was a Ag/AgTB

wire (diameter = 0.5 mm) inserted into a fine-tip glass capillary (outer/inner diameter = 591/130 μm)²¹ immersed in the test solution. An Ag/AgCl electrode (diameter = 0.5 mm) sealed in glass (2 mm in overall diameter) was used as a substrate electrode for supporting the aqueous droplet (5 μL , 1 M HCl). A home-made glass-insulated carbon fiber microelectrode (diameter = 10 μm , RG = 5.5) or a commercial glassy carbon microelectrode (Princeton Applied, diameter = 10 μm , RG = 5.5) was used as the SECM probe in the DCE phase (0.5 mM DMFc⁺TB⁻ and 50 or 5 mM BATB). Carbon electrodes were used since they have a sufficiently high overpotential for hydrogen evolution²² to allow the selective separation of proton and DMFc⁺ reduction current waves, simplifying the kinetic studies. A Pt wire was used as a counter electrode. The DCE phase and aqueous phase were saturated with each other before SECM studies. A set of approach curves were obtained by approaching the microelectrode (biased at a potential where a diffusion-limited steady-state current for the reduction of DMFc⁺ is achieved) toward the DCE/w interface, while at the same time polarizing the interface at different Galvani potentials. All the approach curves started from a point far away from the interface and were stopped after the probe touched the aqueous phase. After each approach curve, the tip was cleaned to avoid any contamination that may have occurred through possible contact with the interface. The Galvani potential difference at the liquid/liquid interface was obtained by correcting the applied potential with respect to the standard ion transfer potential of tetraethylammonium (TEA⁺), $\Delta_o^w \phi_{\text{TEA}^+}^{\circ} = 0.019 \text{ V}$ or tetramethylammonium (TMA⁺), $\Delta_o^w \phi_{\text{TMA}^+}^{\circ} = 0.160 \text{ V}$.²³

To clarify the reaction site for the ORR at the liquid/liquid interface, SECM studies on a soft interface were complemented with studies on a solid glassy carbon surface (diameter = 3 mm), where another set of approach curves were conducted with a Pt microelectrode tip (diameter = 10 μm , RG = 5.5) over the glassy carbon surface (Figure 6-1B). All other conditions were the same as those for the SECM experiments for the liquid/liquid interface. Fabrication of the Pt (diameter = 10 or 25 μm) and carbon fiber (diameter = 10 μm) microelectrodes has been described in Section 2.3.4.2 in Chapter 2.^{22,24}

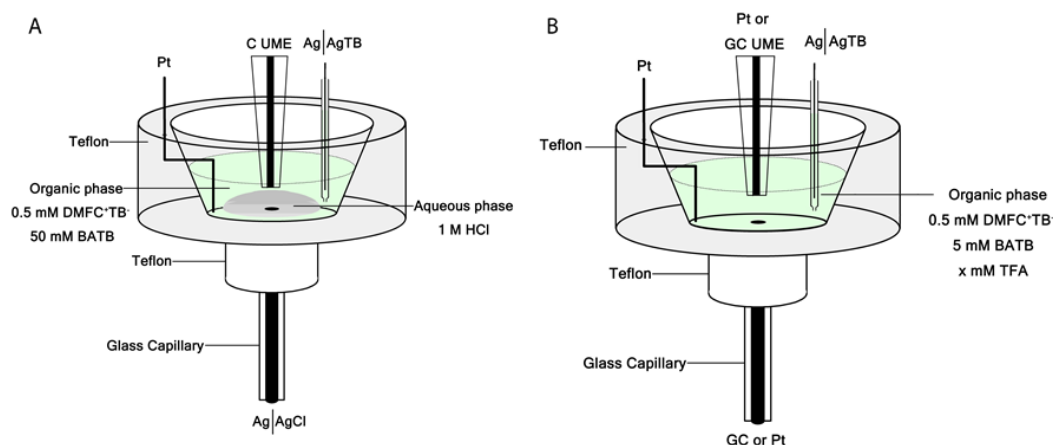


Figure 6-1. (A) Experimental arrangement used for polarizing the liquid/liquid interface during SECM studies, in which a carbon microelectrode (diameter = 10 μm , RG = 5.5) was used as the tip. (B) Electrolytic cell for studying the homogeneous reaction such that the aqueous droplet has been removed and the Ag/AgCl substrate

was replaced with a glassy carbon (3 mm diameter) or Pt (500 μm diameter) disk electrode, paired with a Pt (diameter = 10 μm , RG = 5.5) or a glassy carbon (diameter = 10 μm , RG = 8.6) microelectrode, respectively.

For a quantitative determination of the kinetic constants in the homogeneous chemical reaction, a series of approach curves with the GC microelectrode (diameter = 10 μm , RG = 8.6) on a Pt substrate (500 μm diameter) were performed, employing the setup shown in Figure 6-1B. The tip was firstly centered over the middle of the substrate by filling the cell with 2 mM FcMeOH solution in 100 mM KNO_3 and measuring the x and y scans over the substrate in the feedback mode. The angle of the substrate was then adjusted with the tilt table so that both x and y scans were reasonably flat. Afterwards, the cell was emptied and washed with pure DCE solvent before introducing the test solution of *ca.* 0.5 mM DMFc^+TB^- with 2 equivalents of trifluoroacetic acid (TFA) as the organic acid into the cell. The tip was set to a potential for DMFc^+ reduction at a diffusion-limited rate, while the substrate was biased at a potential for diffusion-limited oxidation of DMFc to DMFc^+ . Then the approach curve was recorded at a speed of 0.5 $\mu\text{m/s}$ and a step of 0.5 μm . The procedure was also repeated for 4 and 10 equivalents of TFA. For comparison of the experimental data with the simulated results, the tip current was normalized with the tip current in the bulk, and the distance at the end of the approach was adjusted to get the best possible correspondence with the experimental data. These experiments were conducted employing a custom-built SECM setup controlled by SECMx software²⁵ and with an IVIUM Compactstat (IVIUM Technologies, The Netherlands).

6.4. Results and discussion

6.4.1. Characterization by UV-Vis spectroscopy and voltammetry

Careful examination of reaction kinetics requires that H^+ be inactive at the microelectrode tip over the same potential range for DMFc^+ reduction. The standard redox potentials for $\text{DMFc}^+/\text{DMFc}$ and H^+/H_2 in DCE phase are 0.07 and 0.55 V, respectively.²⁶ To minimize the interference from the proton reduction at the tip electrode, electrode materials with high overpotential for this reaction should be used. Earlier studies have demonstrated that carbon has a high overpotential for hydrogen evolution in DCE;²² hence, the use of a carbon electrode allows the selective separation of proton and DMFc^+ reduction. Additionally, interference from O_2 reduction was investigated under both aerobic and anaerobic conditions, such that the presence of O_2 had no influence on the voltammetry at a carbon microelectrode for $\text{DMFc}^+/\text{DMFc}$ oxidation/reduction (data not shown). This was also the case for the study of ORR by 1,2-diferrocenylethane (DFcE) at a liquid/liquid interface.²²

Figure 6-2 compares the voltammetric profile obtained at a Pt and a carbon disk microelectrode in a DCE solution containing both HTB and DMFc^+TB^- . This illustrates that proton reduction occurs before DMFc^+ at a Pt surface, as the wave at *ca.* 0.32 V *vs.* $\text{DMFc}^+/\text{DMFc}$, which has been assigned to hydrogen evolution, increases with increasing proton/acid concentration (solid line *vs.* dotted line). Linear sweep voltammetry (LSV) rather than CV was employed to avoid a severely distorted signal during the reverse potential scan due to the large amount of H_2 evolved. As shown in Figure 6-2, the high overpotential for H^+

reduction on carbon shifts its reduction to more negative potentials, allowing a clear separation of the DMFc^+ and proton cathodic waves, with the difference in the half-wave potentials of more than 300 mV (dashed line). This is in agreement with earlier results (see Figure 3, in reference²²); therefore, biasing the carbon microelectrode at -0.15 V vs. $\text{DMFc}^+/\text{DMFc}$ allows the selective reduction of DMFc^+ at a diffusion-controlled steady state rate.

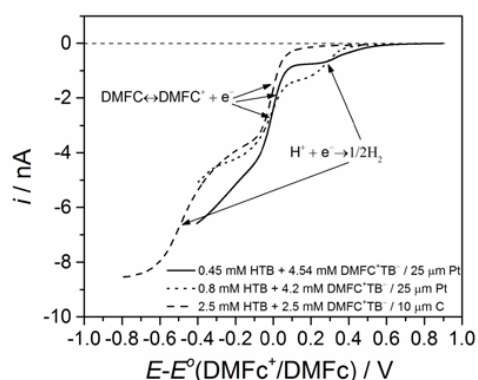


Figure 6-2. Linear sweep voltammograms of 0.45 mM HTB + 4.54 mM DMFc^+TB^- (solid line) and 0.8 mM HTB + 4.2 mM DMFc^+TB^- (dotted line) in DCE on a Pt microelectrode (diameter = 25 μm) and of 2.5 mM DMFc^+TB^- + 2.5 mM HTB (dashed line) in DCE on a carbon fiber microelectrode (diameter = 10 μm). For both conditions, 5 mM BATB is added as the supporting electrolyte in the DCE phase. Scan rate was 20 mV s^{-1} , with a Ag/AgTB reference electrode and a Pt wire as the counter electrode.

The produced DMFc^+TB^- in DCE solution was characterized by UV-Vis measurements and cyclic voltammetry with a carbon microelectrode, as illustrated in Figure 6-3, to confirm that a 100% yield for DMFc^+TB^- was obtained. Normally, a fresh yellow solution of DMFc in DCE displays an absorption band in the UV-Vis spectrum at $\lambda_{\text{max}} = 425$ nm (dashed line). However, after a two-phase shake flask experiment, using LiTB and H_2SO_4 , the DCE phase turned green and displayed a new absorption band in the UV-Vis spectrum with a $\lambda_{\text{max}} = 779$ nm, indicating the presence of DMFc^+ (solid line in Figure 6-3). Since the absorption band of DMFc at $\lambda_{\text{max}} = 425$ nm disappeared completely, it can be assumed that the reaction was quantitative (*i.e.* 100%). This assumption was confirmed by cyclic voltammetry in the DCE phase at a carbon microelectrode, where only a pure steady-state cathodic current wave was observed during the forward scan (*i.e.* reduction of DMFc^+), while the reverse scan superimposed exactly with the forward scan, showed a signal without any appreciable anodic component (see inset in Figure 6-3). This voltammetric result also indicates that the formed DMFc^+ is very stable and no decomposition takes place in the time-scale of the experiment.

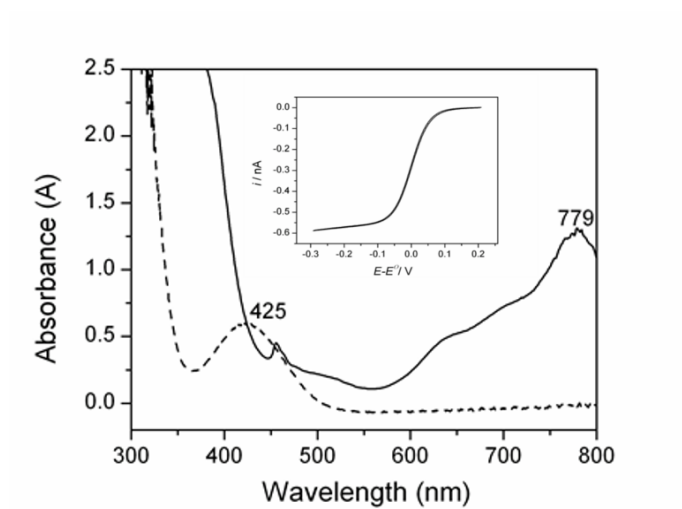


Figure 6-3. UV-Vis spectrum of the prepared solution of 5 mM DMFc^+TB^- in DCE (solid line), supporting electrolyte is BATB. For the purpose of comparison, the spectrum of freshly prepared 5 mM DMFc in DCE (dashed line) is also included. Inset: Cyclic voltammogram of 0.5 mM DMFc^+TB^- and 10 mM BATB at a carbon microelectrode (diameter = 10 μm) in DCE, with a scan rate of 20 mV s^{-1} .

Figure 6-4 shows the cyclic voltammograms obtained at the droplet w/DCE interface in the three-electrode setup (see Figure 6-1A) and at the conventional planar w/DCE interface (0.159 cm^2) in the four-electrode setup.²⁷ The similarity inherent in these two voltammograms confirms the applicability of the three-electrode setup to polarize the liquid/liquid interface. The only difference is that the CV obtained in the four-electrode setup is sharper at the negative and positive potential limits, mostly due to iR drop compensation. As discussed previously,^{2,28-30} the potential window in the droplet case is limited by the transfer of H^+ and Cl^- from water to DCE at positive and negative potentials, respectively. The voltammetric wave of DMFc^+ transfer cannot be observed under the present conditions as it is outside the negative limit of the potential window. By replacing HCl with H_2SO_4 as the aqueous electrolyte, the DMFc^+ signal can be observed owing to the more negative transfer potential of $\text{HSO}_4^-/\text{SO}_4^{2-}$.² The vertical dashed lines on the 3-electrode cell CV (solid line) in Figure 6-4 represent the different Galvani potential values employed for polarizing the interface during SECM feedback mode experiments (*i.e.* approach curves).

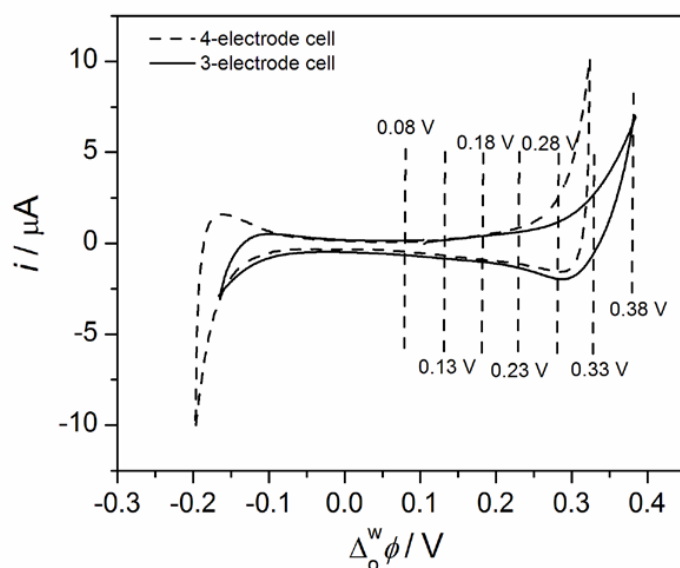


Figure 6-4. Cyclic voltammograms of the w/DCE interface with a three-electrode (solid line) and four-electrode setup²⁷ (dashed line; the same cell composition as the three-electrode setup, but in addition a Ref. water solution of 1 mM BACl + 10 mM LiCl was used for the DCE phase, and iR drop was compensated). The vertical dashed lines represent the substrate Galvani potentials employed for the set of approach curves. The scan rate was $50 \text{ mV} \cdot \text{s}^{-1}$, while other conditions were the same as those described for Figure 6-1.

6.4.2. SECM feedback mode in biphasic system

Figure 6-5A shows the experimental approach curves performed *via* approaching the microelectrode probe towards the DCE/w interface biased at the Galvani potentials highlighted in Figure 6-4. A trend in the approach curves evolving from negative to positive feedback can be observed as the Galvani potential difference at the ITIES was gradually increased. The positive feedback can be explained as the regeneration of the initial species – DMFc^+ according to equation 6-1. The increase in the current starts from normalized distances higher than 50, when the interfacial potential difference was higher than 0.23 V in the Galvani potential scale. This is not in agreement with the typical approach curves obtained for interfacial processes studied by SECM (as seen from a series of approach curves obtained over the glassy-carbon substrate biased at different applied potentials, Figure 6-5B). Typically, the normalized current is mainly perturbed at normalized distances smaller than 2 in the SECM approach curves obtained at the electrolyte/solid substrate interface. The fact that an increase in the recorded current is observed at much longer distances can be explained by the homogeneous reaction between the electrogenerated DMFc with protons diffusing into the bulk DCE phase from the liquid/liquid interface and dissolved oxygen in DCE. This is in agreement with the $\text{IT-C}_1\text{C}_2$ mechanism proposed in Chapter 5.¹ As it has been well recognized that the ion transfer across the ITIES is fast ($0.5\text{--}1 \text{ cm s}^{-1}$),³¹ the polarization of the liquid/liquid interface fixes the interfacial proton concentration at the oil side to the value

dictated by the Nernst equation (6-22), and then the protons start to diffuse into the bulk phase.

$$\Delta_o^w \phi = \Delta_o^w \phi_{H^+}^{\circ'} + \frac{RT}{F} \ln \left(\frac{c_{H^+}^o}{c_{H^+}^w} \right) \quad (6-22)$$

where $\Delta_o^w \phi_{H^+}^{\circ'}$ is the formal transfer potential of H^+ and equals to 0.55 V,²⁶ $c_{H^+}^o$ and $c_{H^+}^w$ are the proton concentrations in the organic and aqueous sides of the liquid/liquid interface, respectively. $c_{H^+}^w$ is assumed to be the same as the bulk value due to the high diffusion coefficient of H^+ in aqueous phase ($9.3 \times 10^{-5} \text{ cm}^2 \cdot \text{s}^{-1}$).³² R , T , and F have their usual meanings. Once the proton diffusion layer meets the tip, the tip current increases as described by the catalytic EC' process (reactions 6-2 to 6-4).

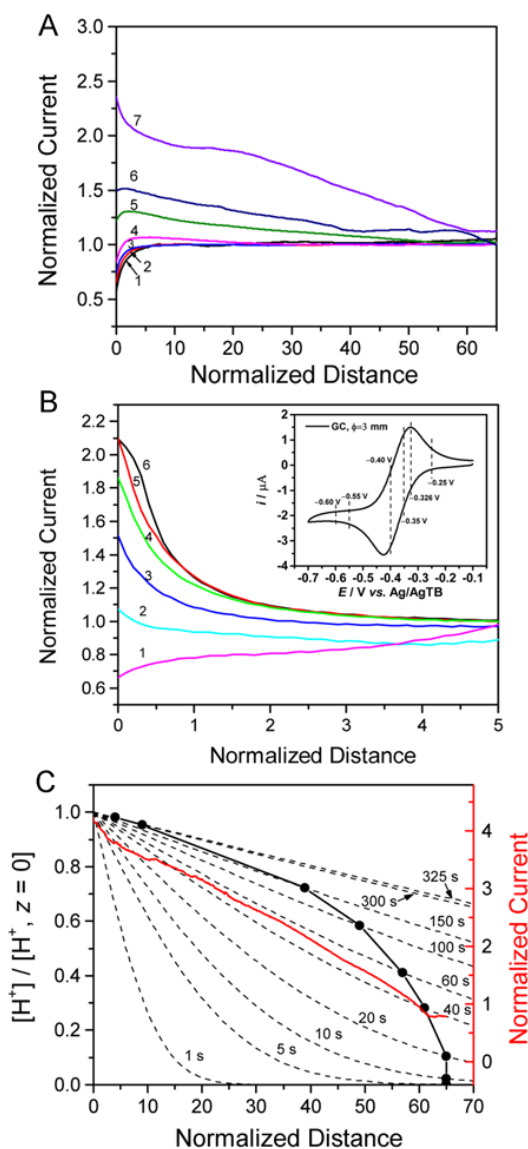


Figure 6-5. (A) Experimental SECM approach curves obtained by biasing the w/DCE interface at different Galvani potentials, 0.08 (1), 0.13 (2), 0.18 (3), 0.23 (4), 0.28 (5), 0.33 (6), and 0.38 V (7), respectively, while keeping the potential at -0.15 V (vs. $DMFc^+/DMFc$) for the mass transport controlled reduction of $DMFc^+$ at the carbon microelectrode tip (diameter = $10\ \mu m$, $RG = 5.5$). Approach rate was $1\ \mu m\ s^{-1}$. (B) Experimental SECM approach curves obtained by approaching a Pt disk microelectrode (diameter = $10\ \mu m$, $RG = 5.5$) biased at a potential (-0.8 V vs. $Ag/AgTB$) for diffusion-limited reduction of $DMFc^+$ towards the glassy carbon substrate biased at different potentials between -0.6 to -0.25 V (vs. $Ag/AgTB$) from down to top: -0.60 (1), -0.55 (2), -0.40 (3), -0.35 (4), -0.326 (5), and -0.25 V (6) with an approach rate of $1\ \mu m\ s^{-1}$. Other conditions are the same as those in Figure 6-1. Inset: Cyclic voltammogram at a glassy carbon electrode (diameter = $3\ mm$, substrate) immersed into a solution of $0.5\ mM\ DMFc^+TB^-$ and $50\ mM\ BATB$ in DCE, with a scan rate of $50\ mV\cdot s^{-1}$. (C) The normalized H^+ concentration profiles for different times (dashed lines, left ordinate axis) and the H^+ concentration profile at the tip moving towards the DCE/w interface at specific times shown on the dashed lines (solid line, left ordinate axis), built based on the equation 6-23 and the approach curve (red line, right ordinate axis) obtained at a Galvani potential difference of 0.38 V in Figure 6-4. Instrumental parameters: The quiet time was $20\ s$ before the approach curve experiment and the initial tip position was at $325\ \mu m$ from the DCE/w interface.

The concentration profile of H^+ at the tip can be built based on the proton concentration at the oil side ($c_{H^+}^o$) from the Nernst equation 6-22 and the approach curves such as those drawn in Figure 6-5A. The concentration profile equation derived from the Laplace transform is as follows:

$$c_{H^+}(x, t) = c_{H^+}^o \operatorname{erfc} \left[\frac{x}{2\sqrt{D_{H^+}^o t}} \right] \quad (6-23)$$

where $c_{H^+}(x, t)$ is the H^+ concentration in DCE at the tip located at a distance x from the interface and at time t , erfc is the complementary error function, $x = \text{initial tip position} - vt$, in which v is the approach rate ($1 \mu\text{m s}^{-1}$) of the SECM tip, and $D_{H^+}^o$ is the diffusion coefficient of H^+ in DCE, taken to be approximately $1 \times 10^{-5} \text{ cm}^2 \cdot \text{s}^{-1}$.¹

Figure 6-5C shows a normalized H^+ concentration profiles in the DCE phase at different times (dashed lines, left ordinate axis) and the H^+ concentration profile at the tip (solid line, left ordinate axis) at an applied Galvani potential difference of 0.38 V in Figure 6-4, built based on equation 6-23 and the approach curve in Figure 6-5C (red line, right ordinate axis). It can be seen from Figure 6-5C that the H^+ concentration is noticeable even at a normalized distance of more than 50 in only 20 s, in agreement with the observations from Figure 6-5A. Additionally, the shapes of the H^+ concentration profile at the tip and the approach curve are in fair agreement. This provides evidence that the ORR mainly occurs in the bulk DCE phase, corroborating earlier findings.¹ Nevertheless, it should be stressed that the reproducibility between approach curves was poor as can be seen from comparison between the approach curve obtained at a Galvani potential difference of 0.38 V in Figure 6-5A and Figure 6-5C. The current signal obtained at the tip was not always stable; this likely due to some surface contamination. This was confirmed by slow addition of HTB into the DMFc solution and consecutive measurements of microelectrode voltammograms after each addition. The steady-state current decreased upon addition of HTB, but could be recovered by polishing the tip surface. So, another strategy, illustrated in Scheme 6-1B and Figure 6-1B, was employed to extract the kinetic rate constant of the ORR, which will be discussed in Section 6.4.3.

Figure 6-5A also shows a slight increase in the tip current close to the interface, when the Galvani potential difference was less than 0.23 V. This can be explained by the interfacial oxygen reduction when the electrogenerated DMFc reaches the DCE/w interface. Recently, SECM measurements using perchlorate as the common ion to polarize the liquid-liquid interface have shown that the driving force for oxygen reduction is high enough so that protons are not needed to transfer into the oil phase to trigger the reaction.³³ However, the heterogeneous reaction is much slower than the homogeneous reaction. Very recently, four-electrode cell measurements under anaerobic conditions in combination with finite element method simulations¹ have shown that DMFc can only slightly facilitate proton transfer (DMFcH^+ formation constant of *ca.* $0.5 \text{ m}^3 \text{ mol}^{-1} \text{ s}^{-1}$ in DCE) across the polarized liquid/liquid interface. Hence, an additional reason for the slight increase in the tip current close to the interface, while keeping interfacial Galvani potential difference at values that

cannot transfer protons into the DCE phase, can be explained by a homogeneous reaction mechanism.³⁴ In that case, the electrogenerated DMFc diffuses into the water droplet and reacts with O_2 and H^+ at the aqueous side of the interface, forming $DMFc^+$ that is transferred back to the organic phase at potentials higher than the observed half-wave potential for $DMFc^+$ transfer (*ca.* -0.3 V in Galvani potential scale). Subsequently, $DMFc^+$ is available for reduction at the SECM tip, forming a feedback loop. The superiority of homogeneous over heterogeneous regeneration of $DMFc^+$ can be ascribed to the drastic difference in the reaction field thickness between these two conditions.³⁴ The fact that a third order reaction is kinetically unfavorable also accounts for the small possibility of a heterogeneous reaction. This phenomenon has been observed previously for studies of ORR at the liquid/liquid interface by DMFc³⁵ and DFcE.²²

The same methodology developed here was also used to try to determine the kinetics of oxygen reduction by tetrathiafulvalene at the ITIES, but the results showed that the reaction between oxygen and TTF was too slow to show any significant changes in the current. This was not unexpected, as the completion of the reaction between 1 mM TTF, 10 mM HCl, and 10 mM LiTB was reported to take more than 80 hours.³⁶

6.4.3. SECM feedback mode in the homogeneous phase

As shown in the previous section, oxygen reduction by DMFc occurs mostly homogeneously in the DCE phase. Simulations of the system described in the previous section are difficult to compare with the experimental results due to the complexity of the system that involves both the moving tip and macro-scale diffusion of transferred protons into the bulk DCE towards the approaching tip. For the sake of simplicity, the reaction was studied in the homogeneous phase. A 500 μm diameter Pt electrode was used as the substrate and a GC microelectrode of 10 μm diameter used as the tip. This procedure was also repeated with addition of 4 and 10 equivalents of TFA. TFA was used since a more stable current was obtained in comparison with HTB, that lead to considerable fouling of the tip and thus fluctuations of the signal.

The recorded curves were compared to the simulated ones to estimate the kinetic rate constant for the homogeneous reaction as shown in Figure 6-6.

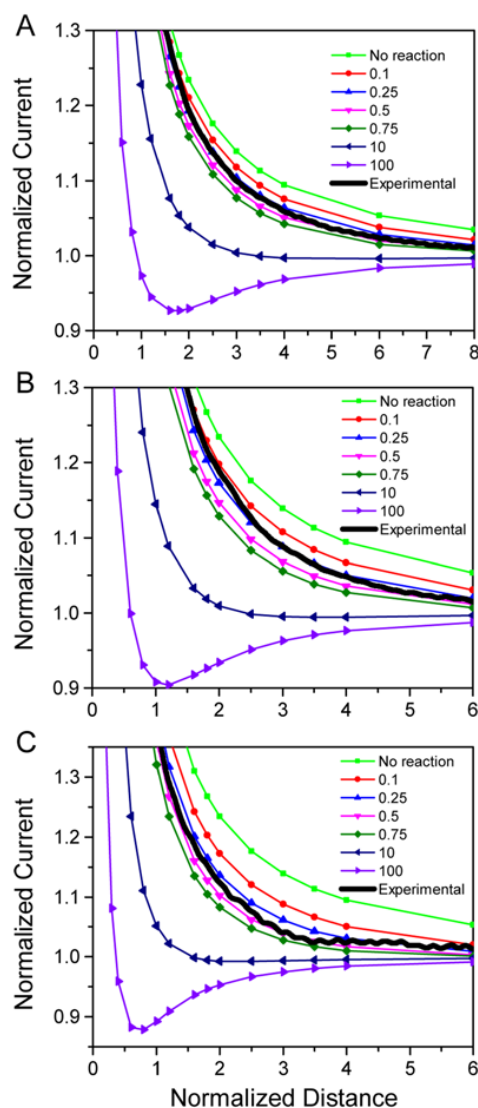


Figure 6-6. Comparison of the measured approach curves (thick black lines) to the simulated ones for the EC' mechanism ($k = 0, 0.1, 0.25, 0.5, 0.75, 10, 100 \text{ m}^3 \text{ mol}^{-1} \text{ s}^{-1}$, $\text{RG} = 8.6$), in positive feedback mode. Experimental conditions: $10 \text{ }\mu\text{m}$ diameter GC microelectrode with a RG of 8.6 as the SECM tip and $500 \text{ }\mu\text{m}$ diameter Pt disk as the substrate. $0.5 \text{ mM DMFc}^+\text{TB}^-$ and TFA acid with the concentration from top to bottom: 1 mM (panel A), 2 mM (panel B) and 5 mM (panel C) in DCE, was used as the test solution, plus 5 mM BATB added as the supporting electrolyte.

Figure 6-6 shows that the apparent rate constant for all the TFA concentrations seems to be quite similar, such that the apparent reaction rate constant $-k$ can be estimated as *ca.* $0.2\text{--}0.5 \text{ m}^3 \text{ mol}^{-1} \text{ s}^{-1}$. More accurate determination of the rate is not possible with this method, as the differences between simulated curves are quite small in this kinetics range. The simulations in Figure 6-6 were done for the simple second-order reaction mechanism where DMFc and protons (and O_2) react in the bulk phase generating DMFc^+ and other products. For ORR, the rate determining step has been identified as protonation of DMFc to form DMFc-H^+ .¹ The rate

constant k_1 for the DMFc-H⁺ formation can be related to k simply by dividing it by a factor of two. This gives an estimate for k_1 as *ca.* 0.1-0.25 m³ mol⁻¹ s⁻¹, which further corroborates the value of 0.5 m³ mol⁻¹ s⁻¹ estimated from finite element simulations of the cyclic voltammetry at ITIES.¹ This shows that COMSOL simulations can be very good tools for analyzing reaction rates for complicated chemical reactions. The slightly smaller value obtained by the present experiments could be explained by the lower acidity of TFA compared to HTB present in the previous cyclic voltammetry experiments.¹ However, simulations show that this method would be more sensitive for even faster reactions and that the sensitivity can be increased by increasing concentration of protons.

6.5. Conclusions

It has been demonstrated that the combination of conventional electrochemistry at a liquid/liquid interface (enabled by the three-electrode strategy) with SECM in a feedback mode can be used to study the complicated kinetics of the oxygen reduction reaction at a biphasic system (*i.e.* catalytic EC' process). The present results confirmed that the liquid/liquid interface works as a proton pump controlled by the interfacial potential difference. The protons in the organic phase then participate in the reduction of dissolved oxygen by DMFc in DCE. Moreover, it was shown experimentally that the ORR mainly takes place in the bulk DCE phase when sufficient Galvani potential at the interface is applied. The kinetic rate constant for the chemical reaction between DMFc and H⁺ was estimated as *ca.* 0.1-0.25 m³ mol⁻¹ s⁻¹, further confirming the voltammetric data analyzed by FEM through COMSOL.¹ The developed methodology can be used as a screening tool to characterize other electron donors or catalysts used for the oxygen reduction reaction or other energy-related reactions at the liquid/liquid interface.

6.6. References

- (1) Jane Stockmann, T.; Deng, H.; Peljo, P.; Kontturi, K.; Opallo, M.; Girault, H. H. *J. Electroanal. Chem.* **2014**, 729, 43.
- (2) Li, F.; Su, B.; Salazar, F. C.; Nia, R. P.; Girault, H. H. *Electrochem. Commun.* **2009**, 11, 473.
- (3) Bard, A. J.; Fan, F. R. F.; Kwak, J.; Lev, O. *Anal. Chem.* **1989**, 61, 132.
- (4) Bard, A. J.; Fan, F. R. F.; Pierce, D. T.; Unwin, P. R.; Wipf, D. O.; Zhou, F. *Science* **1991**, 254, 68.
- (5) Wei, C.; Bard, A. J.; Mirkin, M. V. *J. Phys. Chem.* **1995**, 99, 16033.
- (6) Mirkin, M. V.; Tsionsky, M. In *Scanning Electrochemical Microscopy*; 2nd ed.; Bard, A. J., Mirkin, M. V., Eds.; Marcel Dekker: New York, 2001, p 299.
- (7) Unwin, P. R.; Bard, A. J. *J. Phys. Chem.* **1991**, 95, 7814.
- (8) Zhou, F.; Unwin, P. R.; Bard, A. J. *J. Phys. Chem.* **1992**, 96, 4917.
- (9) Martin, R. D.; Unwin, P. R. *J. Chem. Soc., Faraday Trans.* **1998**, 94, 753.
- (10) Unwin, P. R. In *Scanning Electrochemical Microscopy*; 2nd ed.; Bard, A. J., Mirkin, M. V., Eds.; Marcel Dekker: New York, 2001, p 241.
- (11) Wittstock, G.; Burchardt, M.; Pust, S. E.; Shen, Y.; Zhao, C. *Angew. Chem., Int. Ed.* **2007**, 46, 1584.
- (12) Fernández, J. L.; Bard, A. J. *Anal. Chem.* **2003**, 75, 2967.

- (13) Fernández, J. L.; Walsh, D. A.; Bard, A. J. *J. Am. Chem. Soc.* **2005**, *127*, 357.
- (14) Su, B.; Nia, R. P.; Li, F.; Hojeij, M.; Prudent, M.; Corminboeuf, C.; Samec, Z.; Girault, H. H. *Angew. Chem., Int. Ed.* **2008**, *47*, 4675.
- (15) Bard, A. J.; Faulkner, L. R. *Electrochemical Methods*; 2nd ed.; John Wiley & Sons: New York, 2001.
- (16) Fleischmann, M.; Lasserre, F.; Robinson, J.; Swan, D. *J. Electroanal. Chem. Interfacial Electrochem.* **1984**, *177*, 97.
- (17) Cannan, S.; Cervera, J.; Steliaros, R. J.; Bitziou, E.; Whitworth, A. L.; Unwin, P. R. *Phys. Chem. Chem. Phys.* **2011**, *13*, 5403.
- (18) Su, B.; Hatay, I.; Ge, P. Y.; Mendez, M.; Corminboeuf, C.; Samec, Z.; Ersoz, M.; Girault, H. H. *Chem. Commun.* **2010**, *46*, 2918.
- (19) Galceran, J.; Taylor, S. L.; Bartlett, P. N. *J. Electroanal. Chem.* **2001**, *506*, 65.
- (20) Cornut, R.; Lefrou, C. *J. Electroanal. Chem.* **2008**, *621*, 178.
- (21) Smith, T. J.; Stevenson, K. J. In *Handbook of Electrochemistry*; Zoski, C. G., Ed.; Elsevier: Amsterdam, 2007, p 73.
- (22) Deng, H.; Peljo, P.; Cortés-Salazar, F.; Ge, P.; Kontturi, K.; Girault, H. H. *J. Electroanal. Chem.* **2012**, *681*, 16.
- (23) Wandlowski, T.; Mareček, V.; Samec, Z. *Electrochim. Acta* **1990**, *35*, 1173.
- (24) Gao, F.; Yang, Y.; Liu, J.; Shao, H. *Ionics* **2010**, *16*, 45.
- (25) Kirchner, C. N.; Hallmeier, K. H.; Szargan, R.; Raschke, T.; Radehaus, C.; Wittstock, G. *Electroanalysis* **2007**, *19*, 1023.
- (26) Hatay, I.; Su, B.; Li, F.; Partovi-Nia, R.; Vrubel, H.; Hu, X.; Ersoz, M.; Girault, H. H. *Angew. Chem., Int. Ed.* **2009**, *48*, 5139.
- (27) Peljo, P.; Murtomäki, L.; Kallio, T.; Xu, H. J.; Meyer, M.; Gros, C. P.; Barbe, J. M.; Girault, H. H.; Laasonen, K.; Kontturi, K. *J. Am. Chem. Soc.* **2012**, *134*, 5974.
- (28) Hatay, I.; Su, B.; Li, F.; Méndez, M. A.; Khoury, T.; Gros, C. P.; Barbe, J. M.; Ersoz, M.; Samec, Z.; Girault, H. H. *J. Am. Chem. Soc.* **2009**, *131*, 13453.
- (29) Hatay, I.; Su, B.; Méndez, M. A.; Corminboeuf, C.; Khoury, T.; Gros, C. P.; Bourdillon, M.; Meyer, M.; Barbe, J. M.; Ersoz, M.; Zališ, S.; Samec, Z.; Girault, H. H. *J. Am. Chem. Soc.* **2010**, *132*, 13733.
- (30) Su, B.; Hatay, I.; Trojánek, A.; Samec, Z.; Khoury, T.; Gros, C. P.; Barbe, J. M.; Daina, A.; Carrupt, P. A.; Girault, H. H. *J. Am. Chem. Soc.* **2010**, *132*, 2655.
- (31) Samec, Z. *Electrochim. Acta* **2012**, *84*, 21.
- (32) Lee, S. H.; Rasaiah, J. C. *J. Chem. Phys.* **2011**, *135*, 1245051.
- (33) Jedraszko, J.; Nogala, W.; Adamiak, W.; Rozniecka, E.; Lubarska-Radziejewska, I.; Girault, H. H.; Opallo, M. *J. Phys. Chem. C* **2013**, *117*, 20681.
- (34) Hotta, H.; Ichikawa, S.; Sugihara, T.; Osakai, T. *J. Phys. Chem. B* **2003**, *107*, 9717.
- (35) Su, B.; Hatay, I.; Li, F.; Partovi-Nia, R.; Méndez, M. A.; Samec, Z.; Ersoz, M.; Girault, H. H. *J. Electroanal. Chem.* **2010**, *639*, 102.
- (36) Olaya, A. J.; Ge, P.; Gonthier, J. F.; Pechy, P.; Corminboeuf, C.; Girault, H. H. *J. Am. Chem. Soc.* **2011**, *133*, 12115.

Chapter 7

Lewis Acidity of Hydrated Alkali/Alkaline Earth Metal Cations in Biphasic Systems: Effect on Oxygen and Proton Reduction and S_N1 Reactions

Based on Chem. Commun. 2014, 50, 5554 and J. Electroanal. Chem. 2014, 731, 28.

7.1. Introduction

The alkali metal cations, such as lithium, sodium, and potassium ions, and alkaline-earth metal cations, such as magnesium and calcium ions, are among the most important metal ions in life science¹ and in industry.^{2,3} These ions (except lithium) are present in considerable concentrations in living systems and their distribution inside and outside the living cells is regulated by the intricate ion channels or pumps embedded within the biomembranes of the cells.¹ In aqueous solutions, cations interact strongly with water molecules having a large dipole moment and unshared electron pairs on their oxygen atoms.⁴ Specifically, cations approach the oxygen atoms of the water molecules due to the ion-dipole interaction. In industry, metal ions, such as many lanthanide and transition metal salts, have been employed as Lewis acids to catalyze organic reactions; the catalytic activity has been found to correlate with the hydrolysis constant and water exchange rate constant.⁵ Transition metals have also been used to catalyze synthetic reactions with significant architectures⁶ or stereochemistry.⁷ Additionally, alkali metal cations have been demonstrated to have appreciable impact in the electrode reactions on platinum in an alkaline fuel cell.²

The oxygen reduction reaction (ORR) occurring as the cathodic reaction plays a crucial role in the performance of a fuel cell. The major hurdle that needs to be overcome for developing high efficient fuel cells is the design and synthesis of good ORR electrocatalysts that will not degrade in both acidic and alkaline media. Three model systems have been employed to characterize the performance of the catalysts, as has been detailed in Section 1.3 in Chapter 1. In this chapter, ORR will still be investigated in the third model system – the liquid/liquid interface, just as those in previous chapters. The state-of-the-art on the ORR at the liquid/liquid interface has been reviewed in Section 1.3 in Chapter 1. In Chapters 5 and 6, ORR at the liquid/liquid interface is proved to proceed *via* an IT-C₁C₂ mechanism: a potential

dependent proton transfer step (*i.e.* ion transfer, IT) from the aqueous to organic phases along with two homogeneous chemical reactions (C_1C_2) occurring in the organic phase.

In this chapter, a novel mechanism, utilizing alkali/alkaline earth metals in the absence of an acid, will be evidenced here, in which water – dissolved in the organic phase – becomes the proton source in a Lewis acid catalyzed reaction. This work shows firstly the surprising effect of lithium hydrolysis in organic solvents for the catalysis of oxygen and proton reduction by decamethylferrocene (DMFc), as well as for catalysis of a S_N1 reaction. Then, the thermodynamics, kinetics and mechanism of the electrochemical ORR at soft interfaces catalyzed by the transfer of hydrated lithium cation were studied *via* comparison between the experimental obtained voltammograms and those simulated using finite element methods. Furthermore, ORR at soft interfaces catalyzed by other cations has also been investigated briefly and a catalytic trend is shown to be correlated to the hydration energy of the cations. Finally, the biphasic ORR can be enhanced further in the presence of a cation carrier such as a crown ether in the organic phase. Regardless of the reactions investigated, they can proceed mainly *via* the surprising Lewis acidity of the alkali/alkaline earth metal cations in the organic phase, while in aqueous these cations are normally neutral or slightly alkaline.

7.2. Experimental methods

7.2.1. Chemicals

All chemicals used throughout this chapter have been summarized in Section 2.2 in Chapter 2.

7.2.2. Two-phase shake flask reactions

The details for performing UV/Vis spectroscopy to analyze the products after the two- or single-phase shake flask reactions for oxygen/proton reduction have been described in Sections 2.4.1 and 2.4.2 in Chapter 2. Initial compositions shown in Scheme 7-1 were used for hydrogen evolution reactions under anaerobic conditions.

100 μ L H_2O 10 mM LiTB 10 mM DMFc 5 mg Mo_2C 3 mL DCE a	100 μ L H_2O 10 mM DMFc 3 mL DCE b	100 μ L H_2O 10 mM DMFc 5 mg Mo_2C 3 mL DCE c	100 μ L H_2O 10 mM LiTB 5 mg Mo_2C 3 mL DCE d
---	---	---	---

Scheme 7-1. Schematic representation of the initial compositions for shake-flask experiments under anaerobic conditions. Duration: 16 h.

To estimate the extent of the oxidized electron donor after the shake flask reactions, microelectrode voltammetry measurements were also performed with a CHI-900 electrochemical workstation (CH Instruments, Austin, USA) in the traditional three-electrode

setup employing a commercial glassy carbon microelectrode (13.7 μm diameter, Princeton Applied Research) as the working electrode, plus a platinum wire and a silver wire as the counter, and quasi-reference electrodes, respectively. The potential scale was referred to the redox couple itself.

7.2.3. Electrospray ionization mass spectrometry (ESI-MS)

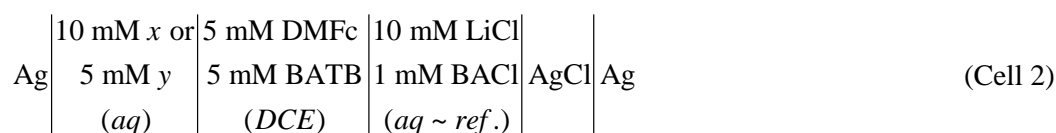
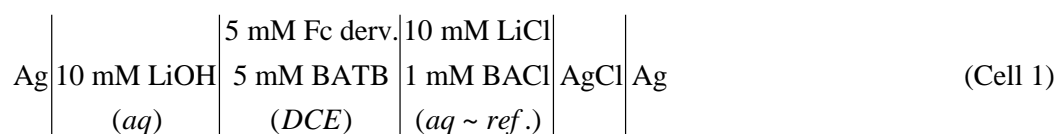
To analyze the products in the alkali metal catalyzed biphasic $\text{S}_{\text{N}}1$ reaction, a two-channel microchip illustrated in Figure 2-10 in Chapter 2 was used as an emitter to interface with the electrospray ionization mass spectrometry (ESI-MS). More details can be found in Section 2.4.3 in the Chapter 2.

7.2.4. Water determination by Karl Fischer titration

The water content in the commercial DCE solvent was analyzed using the Karl Fischer titration method that has been described in Section 2.5 in Chapter 2.

7.2.5. Four-electrode liquid/liquid interface voltammetry

CV measurements were recorded through the use of a PGSTAT30 potentiostat (Metrohm, CH) at the w/DCE interface (geometric area of 1.53 cm^2) *via* three-compartment, four-electrode glass cell, as those illustrated in Figure 1-1 and Figure 1-7 in Chapter 1.⁸⁻¹⁰ The following electrochemical cells were used:



In Cell 1, LiOH was employed as the supporting electrolyte/analyte in aqueous phase, while bis(triphenylphosphoranylidene) ammonium tetrakis(pentafluorophenyl)borate (BATB) served as the supporting electrolyte in the organic phase. 'Fc deriv.' refers to the three ferrocene derivatives evaluated individually; Fc, DFc, and DMFc. In Cell 2, x is LiOH, NaOH, or MgSO_4 , and y is TMA_2SO_4 . The potential scale was calibrated through the use of the tetraphenylarsonium-tetraphenylborate (TATB),⁸⁻¹⁰ or Parker's^{11,12} assumption and the addition of an ion of known standard IT potential; in this case, tetramethylammonium (TMA^+ , $\Delta_o^w \phi_{\text{TMA}^+}^{o'} = 0.160 \text{ V}$) or tetraethylammonium (TEA^+ , $\Delta_o^w \phi_{\text{TEA}^+}^{o'} = 0.019 \text{ V}$) ion transfer was used.¹³

All experiments were performed under aerobic – open bench-top – conditions, such that any oxygen consumed by reactions in either phase could be readily replenished.

7.2.6. Computations

All simulations were performed using a MacIntosh computer with 4 Intel Xeon(R) 5150 processors operating at 2.66 GHz and using the Ubuntu 12.04 LTS operating system; runtimes ranged from 15 to 18 minutes.

7.3. Simulations (*carried out by T. Jane Stockmann*)

Simulation software, like COMSOL Multi-physics, which employs the finite element method, has been used to evaluate a broad spectrum of phenomenon including nanocrystalline phase change memory cells,¹⁴ the thickness of methanol fuel cell cathode catalyst layers,¹⁵ hydrogen storage tanks,¹⁶ nuclear fuel bundles,¹⁷ and a host of electrochemical phenomenon;¹⁸⁻²⁰ the latter has been subject to a recent mini-review concerning electrochemical analysis.²¹ Herein, this versatile software was used to explore the mechanism and kinetics of O₂ reduction in the biphasic systems. The model, comprised of a facile 1-dimensional geometry depicted in Figure 7-1, contained two subdomains to represent either phase and three boundaries. The boundaries at the terminal ends of the geometry in Figure 7-1 were given the designation ‘concentration’ in the software, which is used to describe the bulk concentration of species unaffected during the time scale of the experiment. Mass transport, for the fully supported electrolyte solution, was described within each phase using Fick’s laws as per the following equation,

$$\frac{\partial c_{i,w}(x,t)}{\partial t} = D_{i,w} \nabla^2 c_{i,w}(x,t) = D_{i,w} \left(\frac{\partial^2 c_{i,w}(x,t)}{\partial x^2} \right) \quad (7-1)$$

for a 1-dimensional system, such that $c_{i,w}$ and $D_{i,w}$ are the concentration and diffusion coefficient of species i in water (w); an analogous equation can be written for the organic (o) phase.

Potential dependent ion transfer (IT) across the central boundary (Figure 7-1) of an ion, with a charge z_i , can be written as:

$$i_w^{z_i} \rightleftharpoons i_o^{z_i} \quad (7-2)$$

IT was controlled using Butler-Volmer kinetics described by the forward and reverse, k_f and k_b , rate constants, respectively, through the following:

$$k_f = k^o \exp\left(-\alpha f (\Delta_o^w \phi - \Delta_o^o \phi^{o'})\right) \quad (7-3)$$

$$k_b = k^o \exp\left((1-\alpha) f (\Delta_o^w \phi - \Delta_o^o \phi^{o'})\right) \quad (7-4)$$

where k^o is the standard rate constant (a value of $1 \text{ cm} \cdot \text{s}^{-1}$ was used unless otherwise noted for fully reversible IT), α is the transfer coefficient (0.5 was used throughout), and f is F/RT , where F is Faraday’s constant, R is the universal gas constant, and T is the thermodynamic

temperature. $\Delta_o^w \phi$ is the Galvani potential difference across the interface, $\phi_w - \phi_o = \Delta_o^w \phi$, and was approximated using a triangular waveform^{20,22} in order to mirror the CV experiments. A formal IT potential, $\Delta_o^w \phi_i^{o'}$, of 0.696 V, described for lithium cations²³ at the w/DCE interface, was used throughout unless otherwise stated.

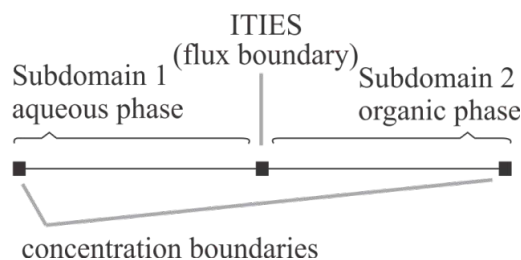


Figure 7-1. The 1-dimensional simulation geometry (thin back line) with three boundaries (squares) as drawn in COMSOL Multi-physics software. The geometry was split into subdomains 1 and 2 representing the aqueous and organic phases, respectively, within which mass transport was governed by Fick's laws of diffusion. The outer boundaries were given the designation 'concentration' in the software, representing the bulk solution beyond which point the solution concentration profile is not expected to change on the time scale of the experiment. The interface between two immiscible electrolytic solutions (ITIES) shown at center and was given the boundary condition 'flux', such that species could cross the interface either through ascribed partition coefficients or through potential dependent ion transfer described by Butler-Volmer kinetics.

The current was taken to be the sum of the flux of charged species across the ITIES *via*:²⁴

$$J(x, t) = -FA \sum_i z_i D_{i,w} \nabla c_{i,w}(x, t) \quad (7-5)$$

where A is the electrode area as defined by a circle of radius 0.7 cm. The simulation mesh was validated using simple IT and comparison of the peak current to the Randles-Sevcik equation^{24,25} as demonstrated recently.²⁶

7.4. Results and Discussion

7.4.1. Two-phase shake flask reactions

7.4.1.1. Oxygen reduction

Biphasic oxygen reduction by DMFc was studied in so called shake flask experiments, where DCE containing DMFc was mixed with an equal volume of aqueous phase. The mixtures in Figure 7-2 were stirred rigorously for 140 min and subsequently analyzed using UV-Vis spectroscopy as well as electrochemically by voltammetry using a glassy carbon microelectrode.

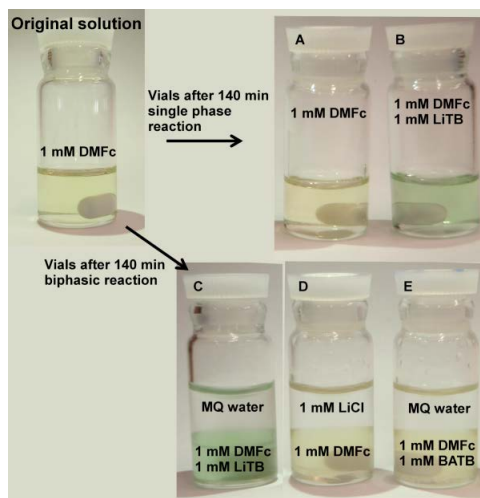


Figure 7-2. The 1 mM DMFc solution and the different shake flask experiments after 140 min of reaction.

A solution of DMFc in DCE has a yellow color with an absorption peak at 425 nm; however, when DMFc is oxidized to DMFc^+ , the solution turns green and the UV-Vis spectrum has a peak at 779 nm. When the DCE phase contained LiTB and DMFc in contact with a neat water phase (*i.e.* no electrolyte, flask “C” in Figure 7-2), both voltammetry and UV-Vis spectroscopy indicate that a significant amount of DMFc was oxidized after the shake flask experiment (red line, Figure 7-3). Only minimal changes were observed in the control experiments without LiTB (Figure 7-2E, and black line in Figure 7-3). If the reaction with LiTB was repeated in an anaerobic atmosphere, almost no changes were observed. This confirms that DMFc is oxidized by oxygen, and the presence of Li^+ cations in the organic phase is essential for oxygen reduction to take place.

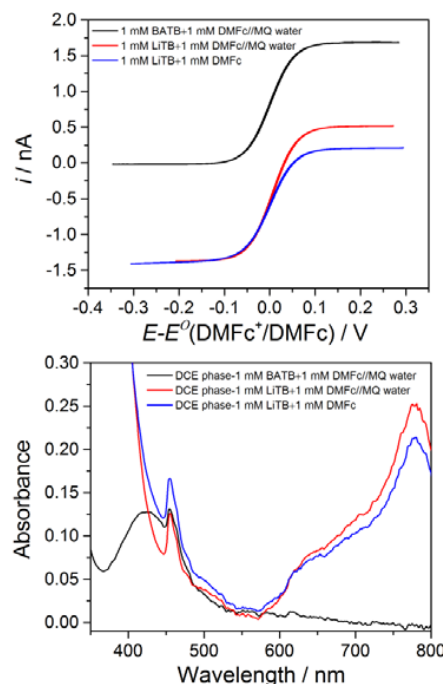


Figure 7-3. Microelectrode voltammetry and UV-Vis spectra of the organic phase before and after the reactions.

The pH of the aqueous phase increased from 6.80 to 9.95, indicating that *ca.* 0.1 mM of OH^- was produced; however, almost no hydrogen peroxide was observed in the aqueous phase by NaI method (red line in the lower panel of Figure 7-4).²⁷ Hydrogen peroxide may be further reduced or decomposed during more than 2 hours' reaction. Based on the products and the available active reactants – oxygen and DMFc in the system, the total reaction can be deduced as the oxygen reduction by DMFc under neutral or alkaline conditions



followed by either the further reduction reaction²⁸⁻³⁰



or the decomposition reaction^{28,30}



pK_a of H_2O_2 is 11.62;³¹ therefore, below this pH hydrogen peroxide is mostly in a protonated neutral form – H_2O_2 .

Curiously, flask “B” in Figure 7-2 containing only DMFc and LiTB in DCE, without any intentionally added water, also turned green during the reaction. However, the water content of a commercial DCE solvent used in the experiments was determined as 26 mM by Karl-

Fischer method. This indicates that the amount of residual water in the solvent is enough for oxygen reduction to take place.

In the typical shake flask experiments performed with DMFc in the organic phase and LiTB with an inorganic acid like HCl or H_2SO_4 in the aqueous phase^{32,33}, *i.e.* in the presence of protons located in the organic phase, oxygen reduction by DMFc is thought to proceed by protonation of the electron donor at the iron core, forming the activated $[DMFc-H]^+$.³⁴ Subsequently, the molecular oxygen dissolved in the bulk DCE binds to the $[DMFc-H]^+$ *via* a delocalized triplet transition state $[DMFc\cdots H\cdots OO]^+$, finally resulting in the oxidation of DMFc to form $DMFc^+$ and the generation of hydrogen peroxy radical species HO_2^\bullet .³⁴ The HO_2^\bullet will then react rapidly with another DMFc and proton to form H_2O_2 .³⁵⁻³⁷

It was noticed that the oxygen reduction reaction does not occur in the absence of alkali metal cation in the organic phase. If 1 mM of DMFc in DCE (flask “A” in Figure 7-2) was stirred for 2h 20 min, no changes were observed (black line and green line in the upper and lower panels of Figure 7-4, respectively). Thus far, oxygen reduction has been demonstrated to take place also in the absence of protons, but only in the presence of LiTB. If LiTB was replaced with BATB, then no changes were observed (Figure 7-2E, black line in Figure 7-3, and black line in the lower panel of Figure 7-4). Besides, if organic LiTB was replaced with aqueous LiCl (flask “D” of Figure 7-2), no changes were observed from both CV (blue line in the upper panel of Figure 7-4) and UV/Vis results (blue and navy lines in the lower panel of Figure 7-4). This implies that the lithium cation must be located in the DCE phase to drive the reaction. For comparison, the CV and UV/Vis results of a fresh DMFc solution were also included (black line and pink line in the upper and lower panels of Figure 7-4, respectively).

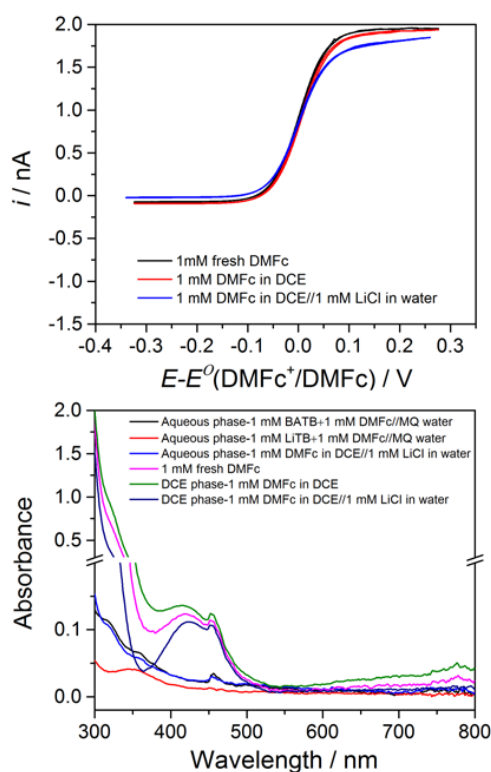


Figure 7-4. The glassy carbon UME (13.7 μm diameter) CVs (10 mV s^{-1}) for the DCE phases and the UV/Vis spectra for aqueous (treated by 0.1 M NaI beforehand) and DCE phases specified in the Figure 7-2 after shake-flask reactions.

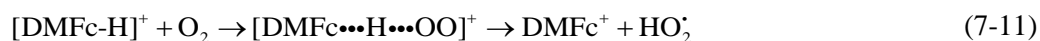
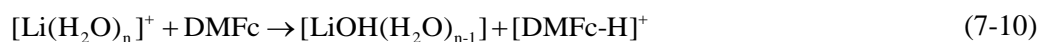
It has been shown that small alkali metal cations like Li^+ and Na^+ transfer into the organic phase either along with their hydration shell or that they firstly shed their hydration shell partially and then transfer into a water cluster inside the DCE phase; however, hydrophobic cations like BA^+ shed the hydration shell and are instead solvated predominately by DCE molecules.³⁸⁻⁴⁰ It has been demonstrated using molecular dynamics simulations by Benjamin⁴¹ that water molecules interact more strongly with cations than with anions of an alkali halide ion pair hydrated in a hydrophobic media, when the cation is smaller than the anion. This was elucidated through a hydration asymmetry parameter “ HA ” that is related with the size asymmetry between the cation and the anion.

$$HA = \frac{\langle U_+ \rangle - \langle U_- \rangle}{\langle U_+ \rangle + \langle U_- \rangle} \quad (7-9)$$

in which U_+ denotes the cation-water electrostatic interaction energy and U_- represents the anion-water electrostatic interaction energy. Equation 7-9 implies that “ HA ” will be zero if the cation and anion of an ion pair are hydrated by water equally; while “ HA ” is approaching 1 if the hydration on cation is much more favorable and it goes to -1 in the reverse case. This is the case of LiTB in DCE employed in the shake flask reactions, flasks “B” and “C” in Figure 7-2. While BA^+ and TB^- are large ions and have the symmetrical size, so it implies that “ HA ” is almost zero in the case of flask “E” in Figure 7-2 in the shake flask experiments. Conversely, a shake flask experiment with 1 mM BACl and 1 mM DMFc in DCE in contact with a neat aqueous phase was also performed in the same duration (not shown) and no reaction happens. The reason lies in that H^+ cannot be dissociated from water molecules in the hydration shell of Cl^- .

These results indicate that highly hydrophilic cations, surrounded by a hydration shell, are essential components for catalyzing oxygen reduction in an organic phase. Hence, we can propose that interactions between the positively charged ion and the water molecules in the surrounding hydration layer make the protons more acidic. Essentially, the alkali metal cations catalyze water dissociation by an inductive effect, possibly with the help of hydrogen bonding to adjacent water molecules that aid in weakening the O–H bond. This is a well-known property of metal ions in solution; for example, many metal ions with higher charges, like aluminum(III) or zinc(II), are strong enough to dissociate water;^{42,43} while hydrated Li^+ has a $\text{p}K_a$ of 13.8.³¹ So the surprising acidity of Li^+ is caused by the hydration asymmetry between Li^+ and TB^- that is in turn the consequence of dramatic size difference between Li^+ and TB^- , implied from equation 7-9.

Most likely the mechanism is that the hydrolysis of cation allows the formation of the $[\text{DMFc-H}]^+$, and the oxygen reduction can proceed similarly as in the presence of protons.





All the reactions 7-10 to 7-12 take place in the DCE phase; however, in the presence of a separated aqueous phase, the produced LiOH and H₂O₂ will transfer into the aqueous phase. In the absence of a separated aqueous phase, LiOH will precipitate as it is not soluble in DCE (for calculation of the solubility product, see equation 7-28 in the “Thermodynamic calculations” shown below). The total Gibbs energy for reactions 7-10 to 7-12, when LiOH is transferred into the aqueous phase, is $-111 \text{ kJ}\cdot\text{mol}^{-1}$ and $-78.9 \text{ kJ}\cdot\text{mol}^{-1}$ for the case where LiOH precipitates in the DCE phase; therefore, both reactions are clearly thermodynamically favorable. The Gibbs free energy in the absence of Li⁺ in the organic phase is $+57.3 \text{ kJ}\cdot\text{mol}^{-1}$ (see equation 7-27); these calculations confirm that the presence of Li⁺ is essential for these reactions to proceed.

7.4.1.1.1. Thermodynamic calculations

7.4.1.1.1.1. Standard redox potentials of oxygen reduction in organic phase

The standard redox potentials of the reactions in DCE can be estimated by the thermodynamic cycle.⁴⁴ Generally, a half reaction for the reduction of O to R in phase α can be expressed as:



With the standard redox potential in the Standard Hydrogen Electrode scale expressed as:

$$[E_{\text{O/R}}^\circ]_{\text{SHE}}^\alpha = \frac{\Delta G^\circ}{-nF} = \frac{1}{nF} \left[\mu_{\text{O}}^{\circ,\alpha} - \mu_{\text{R}}^{\circ,\alpha} - n \left(\mu_{\text{H}^+}^{\circ,\text{w}} - \frac{1}{2} \mu_{\text{H}_2}^{\circ,\text{w}} \right) \right] \quad (7-14)$$

Where F is the Faraday constant. The standard redox potentials of the reaction in DCE and water are:

$$[E_{\text{O/R}}^\circ]_{\text{SHE}}^{\text{DCE}} = \frac{1}{nF} \left[\mu_{\text{O}}^{\circ,\text{DCE}} - \mu_{\text{R}}^{\circ,\text{DCE}} - n \left(\mu_{\text{H}^+}^{\circ,\text{w}} - \frac{1}{2} \mu_{\text{H}_2}^{\circ,\text{w}} \right) \right] \quad (7-15)$$

$$[E_{\text{O/R}}^\circ]_{\text{SHE}}^{\text{w}} = \frac{1}{nF} \left[\mu_{\text{O}}^{\circ,\text{w}} - \mu_{\text{R}}^{\circ,\text{w}} - n \left(\mu_{\text{H}^+}^{\circ,\text{w}} - \frac{1}{2} \mu_{\text{H}_2}^{\circ,\text{w}} \right) \right] \quad (7-16)$$

If equation 7-15 is subtracted from equation 7-16, then we can obtain equation 7-17 shown below:

$$\begin{aligned} [E_{\text{O/R}}^\circ]_{\text{SHE}}^{\text{DCE}} &= [E_{\text{O/R}}^\circ]_{\text{SHE}}^{\text{w}} + \frac{1}{nF} \left[\mu_{\text{O}}^{\circ,\text{DCE}} - \mu_{\text{O}}^{\circ,\text{w}} + \mu_{\text{R}}^{\circ,\text{w}} - \mu_{\text{R}}^{\circ,\text{DCE}} \right] \\ &= [E_{\text{O/R}}^\circ]_{\text{SHE}}^{\text{w}} + \frac{1}{nF} \left(\Delta G_{\text{O}}^{\circ,\text{w} \rightarrow \text{DCE}} - \Delta G_{\text{R}}^{\circ,\text{w} \rightarrow \text{DCE}} \right) \end{aligned} \quad (7-17)$$

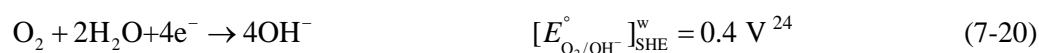
Where $\Delta G_i^{\circ, w \rightarrow \text{DCE}}$ is the standard Gibbs transfer energy of species i from the aqueous to DCE phase. For the case of the two-electron oxygen reduction:



$$\left[E_{\text{O}_2/\text{H}_2\text{O}_2, \text{OH}^-}^{\circ} \right]_{\text{SHE}}^{\text{DCE}} = \left[E_{\text{O}_2/\text{H}_2\text{O}_2, \text{OH}^-}^{\circ} \right]_{\text{SHE}}^{\text{w}} + \frac{1}{2F} (\Delta G_{\text{O}_2}^{\circ, w \rightarrow \text{DCE}} + 2\Delta G_{\text{H}_2\text{O}}^{\circ, w \rightarrow \text{DCE}} - \Delta G_{\text{H}_2\text{O}_2}^{\circ, w \rightarrow \text{DCE}} - 2\Delta G_{\text{OH}^-}^{\circ, w \rightarrow \text{DCE}}) \quad (7-19)$$

$\Delta G_{\text{O}_2}^{\circ, w \rightarrow \text{DCE}}$ was calculated as $-3.99 \text{ kJ mol}^{-1}$ based on solubility of oxygen in water (0.27 mM)⁴⁵ and DCE (1.4 mM),⁴⁶ $\Delta G_{\text{H}_2\text{O}}^{\circ, w \rightarrow \text{DCE}}$ was calculated as $15.42 \text{ kJ mol}^{-1}$ based on solubility of water in DCE (1846 ppm)³⁶ and the same value was used for $\Delta G_{\text{H}_2\text{O}_2}^{\circ, w \rightarrow \text{DCE}}$ as an approximation, as described previously.⁴⁴ The standard Gibbs transfer energy of OH^- from water to DCE ($G_{\text{OH}^-}^{\circ, w \rightarrow \text{DCE}}$) is 63.3 kJ mol^{-1} .⁴⁷ Finally, this calculations gives a standard redox potential of $\left[E_{\text{O}_2/\text{H}_2\text{O}_2, \text{OH}^-}^{\circ} \right]_{\text{SHE}}^{\text{DCE}} = -0.74 \text{ V}$.

For the four-electron oxygen reduction, we have:

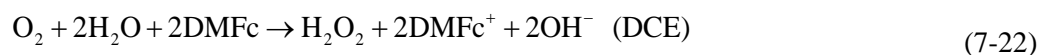


$$\left[E_{\text{O}_2/\text{OH}^-}^{\circ} \right]_{\text{SHE}}^{\text{DCE}} = \left[E_{\text{O}_2/\text{OH}^-}^{\circ} \right]_{\text{SHE}}^{\text{w}} + \frac{1}{4F} (\Delta G_{\text{O}_2}^{\circ, w \rightarrow \text{DCE}} + 2\Delta G_{\text{H}_2\text{O}}^{\circ, w \rightarrow \text{DCE}} - 4\Delta G_{\text{OH}^-}^{\circ, w \rightarrow \text{DCE}}) \quad (7-21)$$

Using the same values as previously, the result is $\left[E_{\text{O}_2/\text{OH}^-}^{\circ} \right]_{\text{SHE}}^{\text{DCE}} = -0.185 \text{ V}$.

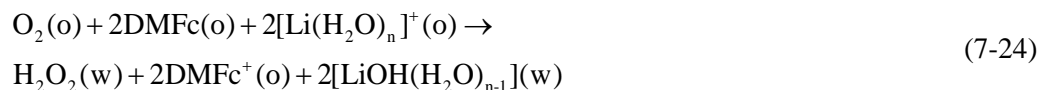
7.4.1.1.2. Two-electron oxygen reduction by DMFc in organic phase

If DMFc was used as the reducing agent, the standard Gibbs energy change of electron transfer $\Delta G_{\text{et}}^{\circ}$ of the chemical reaction 7-22 is given by equation 7-23, where $\left[E_{\text{DMFc}^+/\text{DMFc}}^{\circ} \right]_{\text{SHE}}^{\text{DCE}}$ is 0.04 V ,⁴⁸



$$\Delta G_{\text{et}}^{\circ} = -2F \left(\left[E_{\text{O}_2/\text{H}_2\text{O}_2, \text{OH}^-}^{\circ} \right]_{\text{SHE}}^{\text{DCE}} - \left[E_{\text{DMFc}^+/\text{DMFc}}^{\circ} \right]_{\text{SHE}}^{\text{DCE}} \right) = 151 \text{ kJ mol}^{-1} \quad (7-23)$$

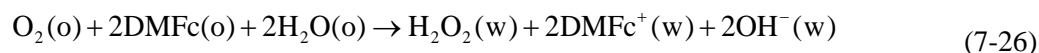
In the case of the two-electron reduction, the overall reaction described by equations from 7-10 to 7-12 is:



The total Gibbs free energy change for oxygen reduction by DMFc (equation 7-24) is then (the transfer energies of Li⁺ and OH⁻ were taken as 59.8 kJ mol⁻¹ and 63.3 kJ mol⁻¹, and these experimental values include the transfer of the “n” water molecules on the hydration shell of the ion)⁴⁷

$$\Delta G_{\text{tot}}^\circ = \Delta G_{\text{et}}^\circ - \Delta G_{\text{H}_2\text{O}_2}^{\circ, \text{w} \rightarrow \text{DCE}} - 2\Delta G_{\text{Li}^+}^{\circ, \text{w} \rightarrow \text{DCE}} - 2\Delta G_{\text{OH}^-}^{\circ, \text{w} \rightarrow \text{DCE}} = -110.6 \text{ kJ mol}^{-1} \quad (7-25)$$

If no lithium is present in the oil phase, the produced DMFcOH will transfer into the aqueous phase ($\Delta G_{\text{DMFc}^+}^{\circ, \text{w} \rightarrow \text{DCE}} = 24.1 \text{ kJ mol}^{-1}$):

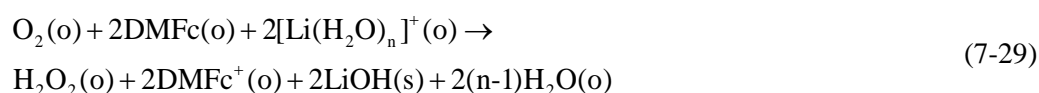


$$\Delta G_{\text{tot}}^\circ = \Delta G_{\text{et}}^\circ - \Delta G_{\text{H}_2\text{O}_2}^{\circ, \text{w} \rightarrow \text{DCE}} - 2\Delta G_{\text{DMFc}^+}^{\circ, \text{w} \rightarrow \text{DCE}} - 2\Delta G_{\text{OH}^-}^{\circ, \text{w} \rightarrow \text{DCE}} = +57.3 \text{ kJ mol}^{-1} \quad (7-27)$$

In the case where there is no separate aqueous phase LiOH formed in the reaction will precipitate. The Gibbs free energy of solvation of LiOH in DCE was calculated from a thermodynamic cycle by the following procedure:

$$\Delta G_{\text{sol, LiOH}}^{\text{DCE}} = \Delta G_{\text{sol, LiOH}}^{\text{w}} + \Delta G_{\text{Li}^+}^{\circ, \text{w} \rightarrow \text{DCE}} + \Delta G_{\text{OH}^-}^{\circ, \text{w} \rightarrow \text{DCE}} \quad (7-28)$$

$\Delta G_{\text{sol, LiOH}}^{\text{w}}$ was calculated from the solubility product ($\ln K_{\text{sp}}$ at 293.15 K = 3.312)⁴⁹ as -8.07 kJ mol⁻¹, and hence $\Delta G_{\text{sol, LiOH}}^{\text{DCE}} = 115 \text{ kJ mol}^{-1}$. The total Gibbs free energy for the reaction (7-29) is then



$$\Delta G_{\text{tot}}^\circ = \Delta G_{\text{et}}^\circ - 2\Delta G_{\text{sol, LiOH}}^{\text{DCE}} = -78.9 \text{ kJ mol}^{-1} \quad (7-30)$$

The results summarized in Table 7-1 indicate that oxygen reduction to hydrogen peroxide in the DCE phase followed by transfer of DMFcOH into the aqueous phase is not thermodynamically favorable, but all the other reactions are significantly exergonic.

Table 7-1. Summary of the thermodynamic calculations of the oxygen reduction by DMFc in the DCE phase under different conditions.

Conditions	$\Delta G_{\text{tot}}^\circ$, kJ mol ⁻¹
------------	--

Li ⁺ in oil phase, LiOH transfers	-111
Li ⁺ in oil phase, LiOH precipitates	-78.9
No Li ⁺ in oil phase, DMFcOH transfers	57.3

7.4.1.2. Hydrogen evolution

As the hydrophilic cation with high charge density can dissociate water molecules dispersed in DCE and donate H⁺ under aerobic conditions, in principle H₂ should be obtained with shake-flask experiments performed anaerobically. If a well-known catalyst Mo₂C⁵⁰ was added to the mixture (1.7 g L⁻¹), very small amounts of hydrogen was detected after the shake flask reaction with 10 mM DMFc and LiTB in DCE phase (Scheme 7-1a) after 16 h of reaction (black line and flask “a” in the inset of Figure 7-5). This confirms that cation facilitated water hydrolysis can provide a source of protons for hydrogen evolution in the organic phase. However, the reaction is very slow even in the presence of the catalyst. Otherwise the generated hydrogen has time to diffuse out through the septum. The blank experiments without LiTB and catalyst (b in Figure 7-5), without LiTB (c in Figure 7-5), and without DMFc (d in Figure 7-5) did not show any traces of hydrogen, using the initial chemical compositions described in Scheme 7-1.

From the mechanistic point of view, the H₂ evolution can proceed *via* a concerted pathway involving two [DMFc-H]⁺. The second order nature and steric effect of this concerted bimolecular reaction would be kinetically slow, which has been confirmed by the experimental results herein and DFT calculations before.³⁴ The reaction can be summarized through equation 7-31:



where [DMFc-H]⁺ is from equation 7-10.

However, Volmer-Heyrovski and Volmer-Tafel mechanisms are probably the major contributors for the H₂ evolution on the Mo₂C surface in acidic microenvironments (lithium hydrolysis) in the DCE phase.⁵¹ But it is difficult to discriminate between these two mechanisms at the moment.

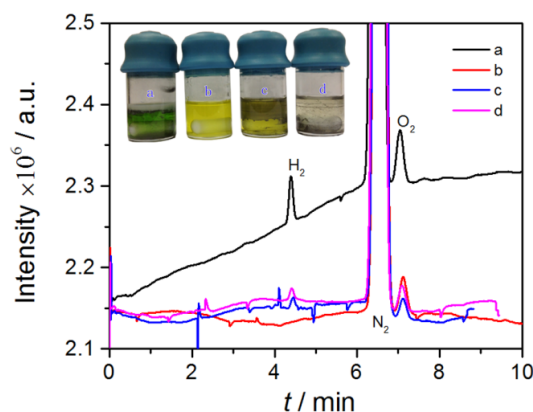


Figure 7-5. Gas chromatograms of the headspaces for shake-flask reactions after 16 h stirring under anaerobic conditions. Inset shows the corresponding photographs of the shake-flask glass vials after reaction. a) 10 mM DMFc + 10 mM LiTB with Mo_2C . b) no LiTB and catalyst, c) no LiTB, d) no DMFc.

7.4.1.3. S_N1 substitution reaction

Further confirmation of the significance of cation catalyzed hydrolysis in organic solvents was obtained by using LiTB in the S_N1 substitution of an indole to ferrocene methanol (FcMeOH).⁵² This demonstrates that lithium cations can be used as Brønsted acids to catalyze what are typically acid catalyzed reactions. This reaction happens fast in the presence of HTB at room temperature;⁵² however, when equal amounts of LiTB, indole and ferrocene methanol in DCE were left to react for 30 min at 60 °C, the reaction product could be detected by electrospray ionization mass spectrometry (ESI-MS) at $m/z = 315$ (Figure 7-6). This reaction was slow at room temperature.

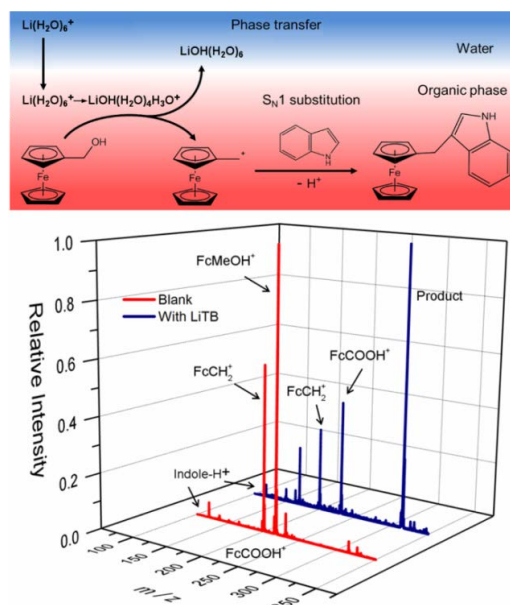


Figure 7-6. The comparison of the ESI-MS spectra of the blank (5 mM FcMeOH and indole in DCE) and the LiTB catalyzed reaction (3.33 mM FcMeOH, indole and LiTB in DCE), both after 30 min reaction at 60 °C. Indole- H^+ , protonated indole ion; FcCH_2^+ , α -ferrocenyl carbocation; FcMeOH^+ , oxidized FcMeOH ion with Fe^{3+} ; FcCOOH^+ , oxidized FcCOOH ion with Fe^{3+} .

Figure 7-6 shows that the sample containing only FcMeOH and indole has the peaks corresponding to the protonated indole ($m/z = 118$), carbocation FcCH_2^+ ($m/z = 199$), FcMeOH^+ ($m/z = 216$) and small amounts of ferrocene carboxylic acid FcCOOH^+ ($m/z = 230$), while the corresponding spectra of the solution containing LiTB shows a significant increase of the peaks of the reaction product with indole (3-(ferrocenylmethyl)-1H-indole, $m/z = 315$) and FcCOOH^+ . Also, the peak for FcMeOH is almost absent.

As discussed previously,⁵² stable α -ferrocenyl carbocations can be generated from ferrocenyl alcohols in the presence of acids. These carbocations can then react with oxygen to produce FcCOOH, or with indole. The results indicate that both of these reactions can proceed in the absence of acids at elevated temperatures, but even mild acids like Li^+ can significantly increase the reaction rate. However, better selectivity is obtained by proton catalysis, as in that case no FcCOOH was observed.⁵²

7.4.2. ORR mechanism elucidation by FEM simulations of four-electrode electrochemical measurements

The discussions above have demonstrated the hydrated lithium cation in the DCE can catalyze the oxygen/hydrogen reduction as well as a $\text{S}_{\text{N}}1$ reaction. In this part, more details will be given to elucidate the ORR mechanism at a liquid/liquid interface that mimics the respiration process at cellular membrane in nature, which is of fundamental importance.

Figure 7-7 illustrates CVs obtained using Cell 1 with (solid trace) or without (dashed curve) 5 mM of DMFc in the organic phase. The polarizable potential window (PPW) was swept at $0.050 \text{ V}\cdot\text{s}^{-1}$ with a potential range of *ca.* $\pm 0.530 \text{ V}$.

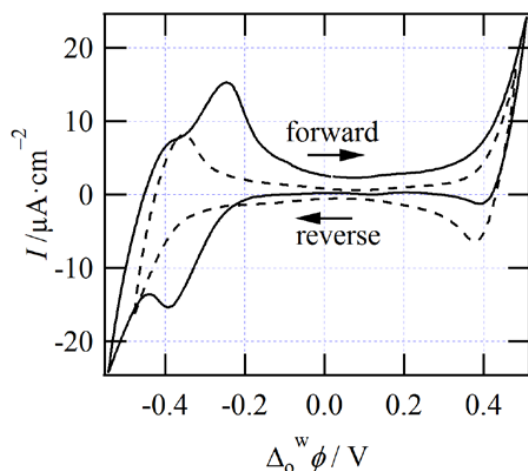


Figure 7-7. Experimental cyclic voltammograms obtained using Cell 1 under aerobic conditions with (solid trace) and without (dashed curve) 5 mM of DMFc added to the organic phase. Instrument parameters included a scan rate of $0.050 \text{ V}\cdot\text{s}^{-1}$ with a potential range of approximately $\pm 0.530 \text{ V}$.

To obtain the blank CV in Figure 7-7, the potential was initially swept from 0.000 to 0.480 V at a scan rate of $0.050 \text{ V}\cdot\text{s}^{-1}$ until a sharp rise in the current density was reached at 0.480 V; at which point the scan direction was reversed and proceeded towards more negative potentials. The sharp increasing current is owing to the transfer of the supporting electrolyte ions, Li^+ (from w to o) and TB^- (from o to w) and represents the positive limit of the polarizable potential window (PPW). Next, the potential was swept from 0.480 to -0.500 V ; initially the current density decreases rapidly followed by a negative peak-shaped wave at $\sim -0.380 \text{ V}$ that is indicative of the return of Li^+ from o to w and TB^- from w to o. The scan was continued until roughly -0.500 V when a sharp decrease in the current density was observed. This is representative of IT of the other supporting electrolyte components; specifically, the transfer of OH^- (from w to o) and BA^+ (from o to w) – the transfer of these ions constitutes the negative potential limit of the PPW. Similar to Li^+ and TB^- , a positive return peak was recorded, when the potential was swept from -0.500 to 0.000 V , and represents the transfer of OH^- and BA^+ back across the interface. It is likely, however, that TB^- and BA^+ are minor contributors to the current signal at the PPW limit owing to their high hydrophobicity^{23,53}.

The solid trace in Figure 7-7 describes the system after addition of DMFc to the organic phase; an IT wave was recorded with a half-wave potential of -0.338 V that is indicative of the transfer of DMFc^+ , and its transfer potential is in fair agreement with previous reports.^{26,54-56} The appearance of the DMFc^+ transfer wave is somewhat surprising at first glance and the signal intensity is beyond that expected from simple contamination of the stock DMFc, which is common in commercial sources of this reagent.²⁶ The oxidation of DMFc has been known

to take place in acidic media through the ORR;^{27,28,30,55,57,58} however, as just demonstrated above,⁵⁴ DMFc oxidation *via* ORR can take place even with alkaline aqueous solutions but in polarized biphasic systems, albeit at reduced rates of reaction. Additionally, comparing the blank (dashed) curve without DMFc and the solid curve with DMFc added, a decrease in the Li^+ return peak intensity, from -6.393 to $-1.3 \mu\text{A}\cdot\text{cm}^{-2}$, was observed. This suggests that metal ions may be either “sequestered or consumed” in a process that generates DMFc^+ .

It has been demonstrated in Chapter 5²⁶ in CV experiments obtained at the liquid/liquid interface, where H_2SO_4 was employed as electrolyte, that the current density-potential profile at the positive end of the PPW, along with the peak intensity of the DMFc^+ transfer wave (or other oxidized Fc derivative) could be used as measures towards the kinetics of ORR. In that work,²⁶ a correlation between a decrease in the H^+ return-peak intensity and increase in IT wave intensity of the oxidation product of an electron donor in the organic phase (*e.g.* a Fc derivative) was recognized. In this way, a mechanism was tested²⁶ wherein protons were consumed in a series of reactions that reduced dioxygen to hydrogen peroxide, or water, while oxidizing DMFc.

In a similar manner, the mechanism drawn in Figure 7-8 has been proposed, such that a metal ion crosses the ITIES – owing to the applied Galvani potential difference – but because of its hydrophilicity, the metal ion retains some of its hydration sphere, or is transferred into hydration pockets within the organic phase as observed by Mirkin *et al.*³⁸ In this way, the metal ion is closely associated with H_2O in the organic phase and can behave as a Lewis acid through coordination of the metal ion to the oxygen atoms within the surrounding water molecules. The metal ion can then weaken the O-H bond and, thus, water becomes the proton source for oxygen reduction – similarly to oxygen reduction in alkaline conditions.

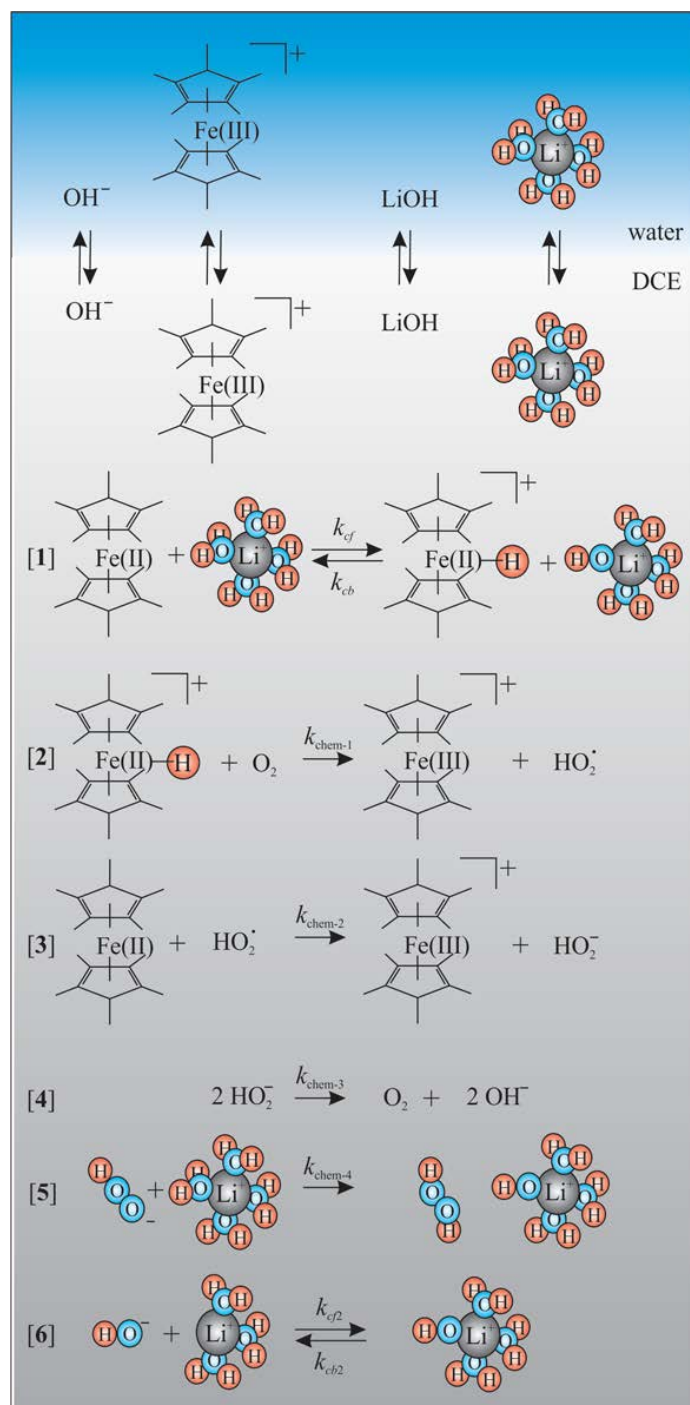
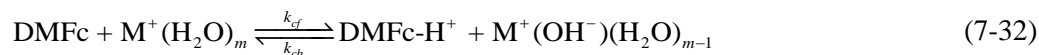


Figure 7-8. Proposed mechanism of Li^+ Lewis acidity at a w/DCE interface.

The homogeneous reactions outlined in Figure 7-8 were incorporated into the simulation model described in section 7.3. In this system interfacial reactions included the potential dependent IT of Li^+ , OH^- , and DMFc^+ , as described through Butler-Volmer kinetics, along with the non-potential dependent partition of the neutral ion pair MOH , in which M represents

the metal cation. These were coupled with the bulk organic phase reactions **1** to **6** in Figure 7-8. For simplicity, this study has limited itself to these six reactions. In reaction **1** of Figure 7-8, as also shown below in equation 7-32, DMFc abstracts a proton from water in the hydration sphere of the metal ion.



The equilibrium constant, K , can be related to the forward and reverse rate constants, k_{cf} and k_{cb} , respectively, through the following:

$$\frac{k_{cf}}{k_{cb}} = K = \frac{c_{[\text{M}^+\text{OH}^-]} c_{\text{DMFc-H}^+}}{c_{\text{M}^+} c_{\text{DMFc}}} \quad (7-33)$$

The number of water molecules within the inner metal ion hydration sphere, m , is highly dependent on the ion under consideration; it has been shown to be as much as $m = 8$ for Rb^+ and Cs^+ , while Li^+ and Na^+ exhibit values of 4 and 5 to 6, respectively, such that m is highly correlated to the ionic radius of the metal ion.⁵⁹ DMFc has been shown to form DMFc-H^+ in acidic media^{27,34,36,54,55} and is an electron donor for O_2 reduction and hydrogen evolution reactions. Reaction 7-32 is an equilibrium reaction where the forward and reverse reactions are described by the rate constants designated in the simulation as k_{cf} and k_{cb} , respectively, and related by equilibrium constant K at equilibrium condition.

In acidic conditions, the proton has been found to coordinate to the DMFc metal center, which is then available for reaction with O_2 to ultimately produce hydrogen peroxide through a series of reactions,³⁴ this mechanism is supported by density functional theory calculations. With this in mind, reaction **2** in Figure 7-8 was chosen, as also detailed in equation 7-34, such that O_2 reacts with DMFc-H^+ to form DMFc^+ and the hydrogen peroxy radical, HO_2^\bullet .



Reactions **3** and **4** in Figure 7-8, described by the rate constants $k_{\text{chem-2}}$ and $k_{\text{chem-3}}$, respectively, and also given below in equations 7-35 and 7-36, illustrate one possible fate for HO_2^\bullet , in that it reacts with one equivalent of DMFc to generate DMFc^+ and HO_2^- . The latter subsequently disproportionates to oxygen and OH^- , or alternatively, HO_2^- can react in a similar manner as DMFc and abstract a proton from the hydration sphere of the metal ion forming hydrogen peroxide; this pathway was included through reaction **5** in Figure 7-8 and in equation 7-37 and governed by the rate constant $k_{\text{chem-4}}$.



The final bulk reaction under consideration was the formation of the metal ion-hydroxide ion-pair as given through reaction **6** in Figure 7-8 and in equation 7-38 shown below:



The association constant, K_f , can be related to the forward and reverse rate constants, k_{cf2} and k_{cb2} , respectively, through the following:

$$\frac{k_{cf2}}{k_{cb2}} = K_f = \frac{c_{[M^+OH^-]}}{c_{M^+}c_{OH^-}} \quad (7-39)$$

Reaction **6** in Figure 7-8 was active in both aqueous and organic phases, such that the ion-pair formation is favoured (high k_{cf2}) and disfavoured (high k_{cb2}) in o and w, respectively. This is in keeping with the Bjerrum and Fuoss models which describe the association constant for ion-pair formation as decreasing with increasing dielectric constant.⁶⁰ In this case, the high and low dielectric constant in water and DCE, 78.4 and 10.2,³¹ discourage and promote ion-pair formation, respectively. The organic phase ion-pair association constant was an additional parameter investigated through the simulation.

Moving forward, the simulation was performed using the parameters given in Table 7-2, while varying the rates of reaction **1** to **6** in Figure 7-8.

Table 7-2. COMSOL simulation parameters.

Parameter	Value	Description
ν	0.050 V·s ⁻¹	Scan rate
$\Delta_o^w \phi_i$	0.000 V	Initial potential
$\Delta_o^w \phi_f$	0.550 V	Upper potential
$\Delta_o^w \phi_{Li^+}^{o'}$	0.696 V	Formal Li ⁺ transfer potential ²³
$\Delta_o^w \phi_{OH^-}^{o'}$	-0.696 V	Formal OH ⁻ transfer potential*
$\Delta_o^w \phi_{DMFc^+}^{o'}$	-0.250 V	Formal DMFc ⁺ transfer potential
k^o	0.01 m·s ⁻¹	Standard rate constant
α	0.5	Transfer coefficient
$c_{M^+,w} / c_{M^+,o}$	10 mmol·L ⁻¹ /0 mmol·L ⁻¹	Initial metal ion concentration
$c_{DMFc,w} / c_{DMFc,o}$	0 mmol·L ⁻¹ /5 mmol·L ⁻¹	Initial concentration of DMFc
$c_{OH^-,w} / c_{OH^-,o}$	10 mmol·L ⁻¹ /0 mmol·L ⁻¹	Initial hydroxide concentration
$c_{O_2,o}$	1.6 mmol·L ⁻¹	Initial oxygen concentration ^{46,61,62}
D_{DMFc}	7.26 × 10 ⁻⁶ cm·s ⁻¹	Diffusion coefficient of DMFc and DMFc ⁺²⁶
D_{O_2}	2.76 × 10 ⁻⁵ cm·s ⁻¹	Diffusion coefficient of O ₂ ⁶¹
D_{M^+}	1.0 × 10 ⁻⁵ cm·s ⁻¹	Diffusion coefficient of M ⁺

Parameter	Value	Description
D_{OH^-}	$1.0 \times 10^{-5} \text{ cm} \cdot \text{s}^{-1}$	Diffusion coefficient of OH^-
$k_{cf2} / k_{cb2}(\text{org})$	$5000 \text{ L} \cdot \text{mol}^{-1} \cdot \text{s}^{-1} / 1 \text{ s}^{-1}$	Rate of ion-pair formation in the organic phase
$k_{cf2} / k_{cb2}(\text{aq})$	$1 \text{ L} \cdot \text{mol}^{-1} \cdot \text{s}^{-1} / 1 \times 10^5 \text{ s}^{-1}$	Rate of ion-pair formation in the aqueous phase
r_d	0.7 cm	Radius of the ITIES

*A value of -0.656 V is described in the literature (ref.⁴⁷) for $\Delta_o^w \phi_{\text{OH}^-}^{o'}$; however, to make the simulated CVs symmetric, and for the sake of convenience, -0.696 V was employed.

Figure 7-9 contains plots of simulated CVs where $k_{\text{chem-1}}$, $k_{\text{chem-2}}$, $k_{\text{chem-3}}$, and $k_{\text{chem-4}}$ were all maintained at $1 \times 10^4 \text{ L} \cdot \text{mol}^{-1} \cdot \text{s}^{-1}$, k_{cb} was set equal to 1 s^{-1} , and k_{cf} was varied from $1 \times 10^2 \text{ L} \cdot \text{mol}^{-1} \cdot \text{s}^{-1}$ to 1×10^5 and $1 \times 10^8 \text{ L} \cdot \text{mol}^{-1} \cdot \text{s}^{-1}$ for Figure 7-9 A, B, and C, respectively.

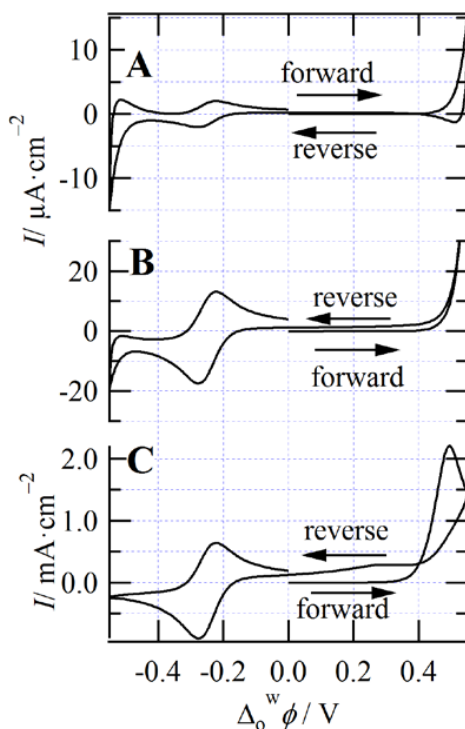


Figure 7-9. Simulated cyclic voltammograms generated using COMSOL Multi-physics using the 1-dimensional geometry illustrated in **Figure 7-1** and the simulation parameters listed in **Table 7-2**; however, with $k_{\text{chem-1}}$, $k_{\text{chem-2}}$, $k_{\text{chem-3}}$, and $k_{\text{chem-4}}$ all set equal to $1 \times 10^4 \text{ L} \cdot \text{mol}^{-1} \cdot \text{s}^{-1}$, while k_{cb} was set equal to 1 s^{-1} . k_{cf} was varied from 1×10^2 to 1×10^5 and $1 \times 10^8 \text{ L} \cdot \text{mol}^{-1} \cdot \text{s}^{-1}$ for panels A, B, and C, respectively.

As the rate of reaction **1** in Figure 7-8 increases through A, B, and C, the peak current density for the transfer of DMFc^+ increases from $-2.06 \mu\text{A} \cdot \text{cm}^{-2}$ to -17.5 and $-905 \mu\text{A} \cdot \text{cm}^{-2}$,

respectively. Simultaneously, the return peak for metal IT at 0.510 V in panel A of Figure 7-9 was $-1.3 \mu\text{A}\cdot\text{cm}^{-2}$, but is not present in traces B or C. Indeed, in Figure 7-9C a peak-shaped wave has emerged on the forward scan at 0.470 V with a peak current density of $2200 \mu\text{A}\cdot\text{cm}^{-2}$. This peak is similar to the voltammetric response for facilitated IT using ligands, or ionophores, through a conventional EC (electrochemical-chemical) or TOC (transfer of the metal ion, followed by organic phase complexation) mechanism as described recently by Molina *et al.*⁶³ and classically by Mareček *et al.*⁶⁴ as well as Girault *et al.*⁶⁵ In the present model, IT serves as the electrochemical step, whilst proton transfer to the metal center of DMFc – to form DMFc-H^+ – is the chemical step. The latter is analogous to a complexation reaction; however, here the metal ion is acting as a Lewis acid – essentially behaving as a catalyst for hydride formation. In traditional complexation reactions across the ITIES with an increasing complexation constant, the transfer potential of a metal cation (transferring from w to o) decreases, or shifts towards more negative potentials.⁶³ In this way, the model is in good agreement with the present understanding of facilitated IT⁶³⁻⁶⁵ at liquid/liquid interfaces.

In Figure 7-9B, the current density during the forward scan is lower than that observed during the reverse scan, while normally, and in Figure 7-9A, this is reversed. For Figure 7-9C, this effect is more exaggerated and a positive peak current density response was even observed at 0.295 V. By examining the concentration profiles (data not shown) it was found that the flux of OH^- , from o to w, was responsible. It was also found that the facilitated IT of the metal ion, through the TOC mechanism, was not limited by the diffusion of either the metal ion or DMFc, but rather was sequestered as an ion-pair in the organic phase. In the present model, MOH is not catalytic; therefore, the ion-pair formation would block any further O_2 reduction. The rate constants used in Figures 7-9B and 7-9C are highly relative to other ORR rate constants reported in the literature³⁶ and have been used here to demonstrate an extreme case. The CV response plotted in Figure 7-9A is more similar to the experimental data given in Figure 7-7; however, the peak current density for DMFc^+ is much lower (by a factor of 5) in the simulated results. This discrepancy between the experimental and simulated peak current density for the IT wave of DMFc^+ may be owing to a number of factors arising from the experiment. For example, when conducting the experiment often multiple voltammetric scans are necessary to establish a potential window and this would result in a buildup of DMFc^+ near the interface – artificially enhancing its IT response. Besides, multiple trials need to be made to get a good-shaped CV due to the strong Marangoni effect⁶⁶ especially when DMFc is used as the lipophilic electron donor, resulting in an apparently higher IT current of DMFc^+ . Additionally, if the experiment is allowed to stand for a period of time the reaction may proceed; however, owing to the high hydrophilicity of Li^+ this can be considered a minor contributor.

Subsequently, the rate of reaction 2 in Figure 7-8, the formation of DMFc^+ , was examined. At this stage, a k_{cf} equal to $1 \times 10^3 \text{ L}\cdot\text{mol}^{-1}\cdot\text{s}^{-1}$ was used and $k_{\text{chem-1}}$ was varied from $1 \times 10^2 \text{ L}\cdot\text{mol}^{-1}\cdot\text{s}^{-1}$ to 1×10^4 and $1 \times 10^8 \text{ L}\cdot\text{mol}^{-1}\cdot\text{s}^{-1}$, as shown in Figure 7-10, such that the resultant cathodic peak current density for the DMFc^+ transfer wave was observed to be -7.5 , -25.7 , and $-25.9 \mu\text{A}\cdot\text{cm}^{-2}$, respectively. This indicates that, despite reaction 1 in Figure 7-8 being rate limiting, increasing the rate of 2 in Figure 7-8 can still elicit an increase in product formation; however, large rate increases are necessary with depreciating returns in the DMFc^+

generation. During the forward sweep of the simulated CVs where $k_{\text{chem-1}}$ was 1×10^4 and $1 \times 10^8 \text{ L}\cdot\text{mol}^{-1}\cdot\text{s}^{-1}$, the current density remains close to baseline until the edge of the PPW was reached and a sharp increase, associated with the transfer of Li^+ from w to o, was recorded. However, upon reversal of the scan direction (from 0.550 to -0.550 V) the rapid decrease in the current density seen experimentally was not observed. Instead, a gradual decline in the current density was obtained; this was associated with the flux of OH^- , generated through reaction 4 or 6 in Figure 7-8, from o to w. This current density offset was observed but not reproducible experimentally but may be the cause of slight positive potential shift observed across the entire CV in Figure 7-7 after addition of DMFc; however, $k_{\text{chem-1}}$ values greater than $1 \times 10^4 \text{ L}\cdot\text{mol}^{-1}\cdot\text{s}^{-1}$ should not be considered.

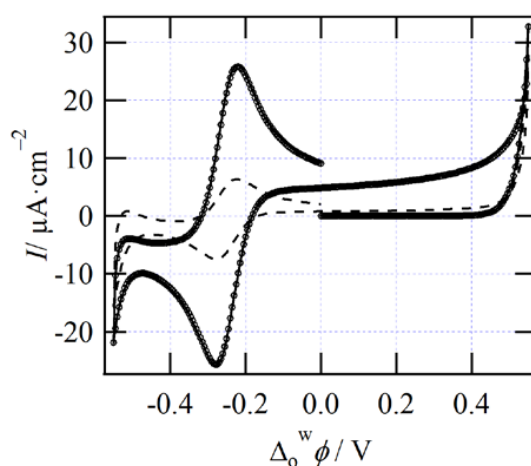


Figure 7-10. Cyclic voltammograms obtained *via* simulation using similar conditions as described for **Figure 7-9**; however, $k_{cf} = 1 \times 10^3 \text{ L}\cdot\text{mol}^{-1}\cdot\text{s}^{-1}$ was employed whilst varying $k_{\text{chem-1}}$ to 1×10^2 (dashed line), 1×10^4 (\circ), and $1 \times 10^8 \text{ L}\cdot\text{mol}^{-1}\cdot\text{s}^{-1}$ (solid line).

Subsequently Figure 7-11 was generated and illustrates the investigation of the metal-ion-hydroxide ion-pair formation in the organic phase on the CV response using the parameters given in Table 7-2. k_{cf2} was set equal to $5000 \text{ L}\cdot\text{mol}^{-1}\cdot\text{s}^{-1}$, while k_{cb2} was changed to 1, 100, 500, and 5000 s^{-1} for the black, dotted, dashed, and sphere-marker traces, respectively. As k_{cb2} increases, the magnitude of the cathodic peak current density for DMFc^+ transfer increases from $-48 \mu\text{A}\cdot\text{cm}^{-2}$, at a k_{cb2} of 1 s^{-1} , to $-880 \mu\text{A}\cdot\text{cm}^{-2}$, at k_{cb2} equal to 5000 s^{-1} . This is owing to the increased availability of the metal ion to catalyze the DMFc-H^+ formation. However, similar to the effect observed in Figure 7-9C and Figure 7-10, during the reverse scan, from roughly 0.550 to -0.200 V , the current density decays gradually owing to the flux of OH^- across the interface. Figure 7-11 serves to demonstrate the importance of ion-pair formation to the catalytic behavior of the metal ion, as well as its impact on the overall mechanism.

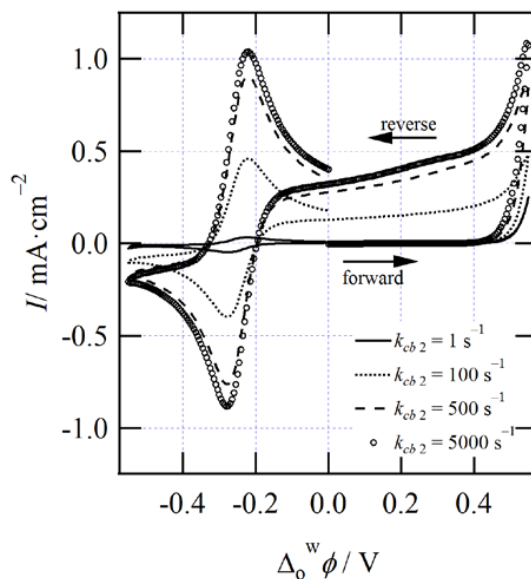


Figure 7-11. Simulated cyclic voltammograms generated using the same parameters as those described for **Figure 7-9**; however, $k_{cf} = 1 \times 10^2 \text{ L} \cdot \text{mol}^{-1} \cdot \text{s}^{-1}$ and $k_{cf2} = 5000 \text{ L} \cdot \text{mol}^{-1} \cdot \text{s}^{-1}$, were employed whilst varying k_{cb2} as indicated, inset.

Figure 7-12 illustrates the simulated CVs obtained through iterative changes in $k_{\text{chem-2}}$, such that the $k_{\text{chem-2}}$ equal to $1 \times 10^2 \text{ L} \cdot \text{mol}^{-1} \cdot \text{s}^{-1}$ (solid trace) and $1 \times 10^8 \text{ L} \cdot \text{mol}^{-1} \cdot \text{s}^{-1}$ (spherical marker trace) demonstrates only a minute change in the DMFc⁺ transfer peak intensity, from -2.03 to $-2.06 \mu\text{A} \cdot \text{cm}^{-2}$. Analogously, the rates of $k_{\text{chem-3}}$ and $k_{\text{chem-4}}$ were also varied systematically (data not shown) and elicited similar results to those found for $k_{\text{chem-2}}$. This seems to suggest that reaction **1** (k_{cf}/k_{cb}) and **2** ($k_{\text{chem-1}}$) in Figure 7-8 have the largest influence on the CV profile, with further reactions having less impact on the response.

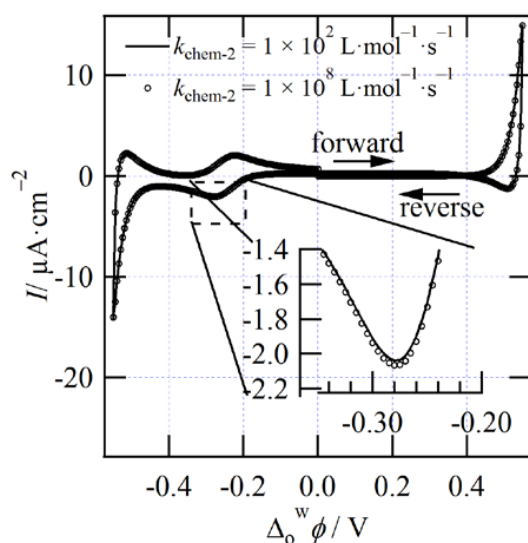


Figure 7-12. Cyclic voltammograms generated using the simulation outlined in section 7.3 comprised of similar parameters as those described for **Figure 7-9**; however, $k_{cf} = 1 \times 10^2 \text{ L}\cdot\text{mol}^{-1}\cdot\text{s}^{-1}$, $k_{\text{chem-1}} = 1 \times 10^4 \text{ L}\cdot\text{mol}^{-1}\cdot\text{s}^{-1}$, along with $k_{\text{chem-3}}$ and $k_{\text{chem-4}} = 1 \times 10^2 \text{ L}\cdot\text{mol}^{-1}\cdot\text{s}^{-1}$, were used while $k_{\text{chem-2}}$ was changed as listed, inset. The inset graph displays a magnified region of the two traces for the DMFc⁺ transfer cathodic waves.

Equation 7-33 offers another parameter for optimization in that the ratio of the forward and reverse rate constants of reaction **1** in Figure 7-8 can be altered while keeping the overall equilibrium constant the same. In this way, K was maintained at 1×10^4 and the ratios of k_{cf}/k_{cb} were set equal to $1 \times 10^2/1 \times 10^{-2}$, $1 \times 10^4/1$, $1 \times 10^8/1 \times 10^4 \text{ L}\cdot\text{mol}^{-1}\cdot\text{s}^{-1}$ for Figure 7-13 panels A, B, and C, respectively. The homogeneous rate constants of reactions **2** to **5** in Figure 7-8 were maintained at $1 \times 10^4 \text{ L}\cdot\text{mol}^{-1}\cdot\text{s}^{-1}$. The response is similar to that observed in Figure 7-9; this is likely owing to the general consumption of species through the latter reactions, thereby facilitating the forward directional dominance of reaction **1**.

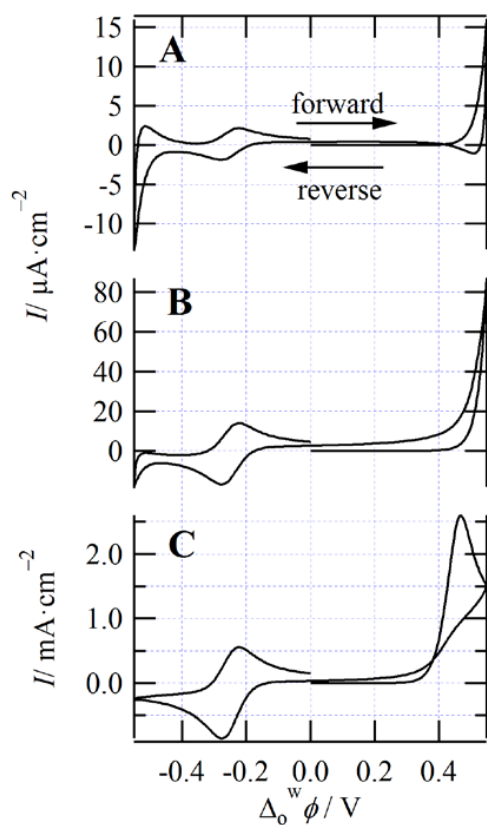


Figure 7-13. Simulated cyclic voltammograms compiled using the simulation outlined in section 7.3 with similar parameters as provided for Figure 7-9, such that $k_{\text{chem-1}}$, $k_{\text{chem-2}}$, $k_{\text{chem-3}}$, and $k_{\text{chem-4}}$ equal to $1 \times 10^4 \text{ L}\cdot\text{mol}^{-1}\cdot\text{s}^{-1}$, while k_{cf}/k_{cb} were changed to $1 \times 10^2/1 \times 10^{-2}$, $1 \times 10^4/1$, $1 \times 10^8/1 \times 10^4 \text{ L}\cdot\text{mol}^{-1}\cdot\text{s}^{-1}$ for panels A, B, and C, respectively.

DFc and Fc were also explored as possible electron donors and compared to DMFc using Cell 1 with 10 mM of LiOH in the aqueous; experimental CVs are shown in Figure 7-14. The half-wave IT potentials for DFc^+ and Fc^+ were determined to be roughly -0.065 and 0.000 V, respectively. Based on the rate constants evaluated thus far, it is possible to estimate the rates of reactions **1** and **2** for the three electron donor species. DMFc and DFc elicit comparable $DMFc^+/DFc^+$ cathodic IT peak current densities, at roughly $-15.4/-13.8 \mu A \cdot cm^{-2}$, along with similar Li^+ return peak intensities, at $-1.3/-2.2 \mu A \cdot cm^{-2}$; therefore, k_{cf} and k_{chem-1} were both approximated to be $100 L \cdot mol^{-1} \cdot s^{-1}$. In the case of Fc, if the diffusion coefficients of these three species are considered to be roughly equivalent, then amount of Fc^+ is half that of DMFc or DFc. Based on this, Fc was considered to yield between 50 and $100 L \cdot mol^{-1} \cdot s^{-1}$ for reaction **1** and $100 L \cdot mol^{-1} \cdot s^{-1}$ for **2**. In this way, a general trend in reactivity for these ferrocene derivatives can be proposed to be $DMFc > DFc > Fc$, that is in good agreement with the recent results reported by Samec *et al.*³⁶ In that work,³⁶ the authors demonstrate an increasing rate of both the catalyzed and Fc derivative only mediated O_2 reduction with increasing methyl substitution on the cyclopentadienyl rings. Additionally, the rates estimated here are in good agreement with those found by Samec *et al.*³⁶ using stopped-flow kinetic measurements.

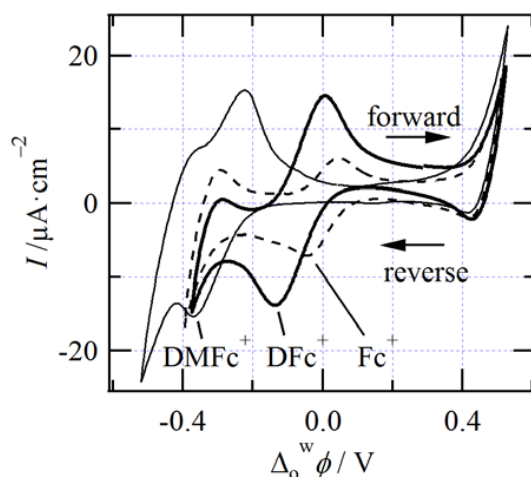


Figure 7-14. Cyclic voltammograms measured using Cell 1 with ‘Fc deriv.’ as DMFc, DFc, and Fc for the thin, thick, and dashed curves, respectively; the ion transfer peaks for the oxidized forms of the electron donor species are indicated. Similar instrument parameters as those detailed for **Figure 7-7** have been used in the acquisition of these CVs.

7.4.3. Effect of the charge density of the cations

Aqueous electrolytes with different cations were investigated under aerobic conditions using the Cell 2 and the results were shown in Figure 7-15. By comparison with the amount of $DMFc^+$ formed in Figure 7-15, it was found that the reactivity trend in the ORR is proportional to the charge densities of the cations ($Mg^{2+} > Li^+ > Na^+ > TMA^+$)⁶⁷ in the corresponding electrolytes. $DMFc^+$ observed in the case of TMA^+ is mostly expected to arise from the residual $DMFc^+$ in commercial DMFc,²⁶ as currents of the same magnitude were also

observed under anaerobic conditions (not shown). Equation 7-40 indicates that the hydration enthalpy (H) is proportional to the charge density of the ion in a given solvent:⁴

$$H = -\frac{ze^2}{2r} \left(1 - \frac{1}{\varepsilon} \right) \quad (7-40)$$

where z is the charge on the ion, r is its radius, e is the elementary charge, and ε is the dielectric constant of the solvent. With cations of high charge density, they interact with the centers of negative charge (oxygen atoms) of the water molecules in their hydration shells strongly, resulting in higher rate of cation hydrolysis. This facilitates the DMFc-H⁺ formation that can be used further in the following ORR steps producing DMFc⁺. The anomalous current fluctuation near DMFc⁺ transfer, from roughly -0.300 to -0.100 V, when Mg²⁺ was the aqueous cation is thought to be due to the potential dependent adsorption of ions at the ITIES – this has been known to generate convective turbulence brought about by abrupt changes in the interfacial surface tension; this phenomena is sometimes referred to as the Marangoni convection or effect.⁶⁶ Large amount of DMFc⁺ transfer across the interface maybe induce this Marangoni convection.

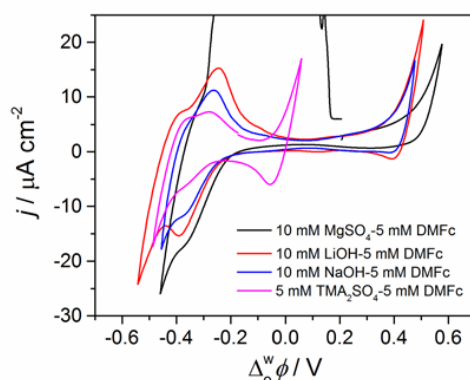


Figure 7-15. Cyclic voltammograms obtained using Cell 2 described in Section 7.2.5 under aerobic conditions with 10 mM of MgSO₄ (black line), LiOH (red line), and NaOH (blue line), or 5 mM TMA₂SO₄ (pink line) dissolved in the aqueous phase. Instrument parameters included a scan rate of 0.050 V s⁻¹ and a potential range of approximately ± 0.550 V.

7.4.4. Effect of the crown ether

Since the discovery of crown ethers made by Petersen at du Pont in 1967,⁶⁸ studies on the facilitated ion transfer at the liquid/liquid interface using this kind of ionophores has burst. The effect of crown ethers on the CV profile for the hydrophilic cation catalyzed biphasic ORR was investigated using the Cell 2 but with additional 5 mM DB18C6 in the DCE phase and 5 mM Na₂SO₄ as the aqueous phase and the results were shown in Figure 7-16.

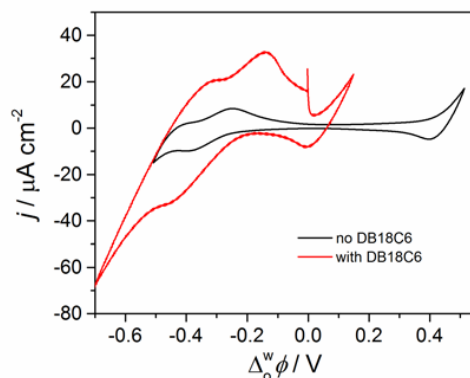


Figure 7-16. Cyclic voltammograms obtained using Cell 2 described in Section 7.2.5 under aerobic conditions with 5 mM of Na_2SO_4 in aqueous (black line), and 5 mM of Na_2SO_4 in aqueous and 5 mM of additional DB18C6 in DCE (red line). Instrument parameters: scan rate of 0.050 V s^{-1} .

It can be seen from Figure 7-16 that with DB18C6 the reaction rate was enhanced dramatically. The reasons can be ascribed to: 1) DB18C6 facilitates the transfer of Na^+ *via* the coordinate bond formation between the Na^+ and the oxygen atoms around the macro-ring of this compound, increasing the available amount of Na^+ for the catalyzed ORR in DCE, producing more DMFc^+ ; 2) binding of Na^+ into the macrocycle of DB18C6 will increase the acidity of water molecules in the hydration shell. Maybe this effect will be more evident when K^+ is used as the cation. This can be termed as “ligand-mediated hydrophilic-cation catalyzed ORR”.

7.5. Conclusions

Firstly, oxygen reduction by DMFc can take place in the absence of acids, as hydrolysis of alkali metal cations in the organic phase will provide protons for the reaction. Hydrophilic cations polarize the water molecules in their solvation shell, making the protons more acidic. These slightly acidic protons can be utilized in both oxygen reduction and hydrogen evolution by DMFc, as well as Brønsted acids as catalysts of organic reactions. This new type of catalysis based on mildly acidic protons in the solvation shell of metal cations would be useful for acid catalyzed reactions, for example, in organic synthesis. A very positive “HA” is responsible for this phenomenon.

Secondly, the mechanism of oxygen reduction in a biphasic – between water and an organic solvent, in this case DCE – was investigated by voltammetry employing only lithium hydroxide as analyte/supporting electrolyte in the aqueous phase, along with DMFc, DFc, or Fc as an electron donor in DCE. Simulated voltammograms, generated using COMSOL Multi-physics software, were used to investigate the impact of different reaction rates within a proposed mechanism on the CV curve features and then compared to those seen experimentally. The proposed mechanism included the potential dependent IT of Li^+ , OH^- , and DMFc^+ , along with six homogeneous organic phase reactions. Reaction 1 involved a proton abstraction by DMFc from the hydration sphere of the metal ion forming DMFc-H^+

and the metal ion-hydroxide ion-pair. It was proposed that the metal ion would transfer either with some of its hydration sphere intact or it would transfer into hydration ‘pockets’ already present in the DCE phase as has been previously shown.^{38,54} In this way, the metal ion behaves as a Lewis acid, weakening the O-H bonds of the water molecules surrounding it and, thus, water becomes the proton source.

Reactions **2** to **6** follow the typical pathway,^{27,30,36,54} such that the DMFc-H⁺ then reacts with one equivalent of oxygen to form DMFc⁺ and a hydrogen peroxy radical species. This radical can then oxidize DMFc and form HO₂⁻, which can either disproportionate or, similar to reaction **1**, abstract a proton from a water molecule in the metal ions hydration shells to form H₂O₂.

By systematically varying the rates of these reactions it has been demonstrated herein, that reactions **1** and **2** play the dominant role. The rates of these two reactions were estimated to be *ca.* 100 L·mol⁻¹·s⁻¹ for both **1** and **2** for DMFc and DFc electron donors, while for Fc these were estimated to be between 50 and 100 L·mol⁻¹·s⁻¹ for **1** and 100 L·mol⁻¹·s⁻¹ for **2**. Because **1** and **2** were found to exert the greatest influence on the CV profile it is not possible to establish a clear estimate of the rates of reactions **3** to **6**; however, it is generally accepted that radical reactions are fast (reaction **3**) and it has been shown here that the ion-pair formation can have a dramatic influence.

The method presented herein offers a new avenue with which to explore the Lewis acid properties of various metal ions. This approach could offer critical insight into the development of new catalysts for hydrogen fuel cells, whose presence has been shown to enhance performance,⁶⁹ as well as offer routes to investigate their reactivity of novel synthetic methodologies.⁵⁴

Lastly, effect of different cations and crown ether on the biphasic ORR was investigated. A correlation was built between the catalytic activities of these cations with their charge densities. Crown ether can enhance the reaction activity further by either facilitating the cation transfer or increasing the acidity of water molecules in the hydration shells of the cations.

7.6. References

- (1) Gouaux, E.; MacKinnon, R. *Science* **2005**, *310*, 1461.
- (2) Strmcnik, D.; Kodama, K.; van der Vliet, D.; Greeley, J.; Stamenkovic, V. R.; Markovic, N. M. *Nature Chem.* **2009**, *1*, 466.
- (3) Goodenough, J. B.; Park, K.-S. *J. Am. Chem. Soc.* **2013**, *135*, 1167.
- (4) House, J. E. *Inorganic Chemistry*; 1st ed.; Academic Press, 2008.
- (5) Kobayashi, S.; Manabe, K. *Acc. Chem. Res.* **2002**, *35*, 209.
- (6) Xie, Y.-X.; Tang, R.-Y.; Song, R.-J.; Xiang, J.-N.; Li, J.-H. *J. Org. Chem.* **2013**, *79*, 686.
- (7) Deng, Y.; Kumar, S.; Wang, H. *Chem. Commun.* **2014**, *50*, 4272.
- (8) Girault, H. H. In *Electroanalytical Chemistry*, Vol 23; Bard, A. J., Zoski, C. G., Eds. 2010; Vol. 23, p 1.
- (9) Peljo, P.; Girault, H. H. In *Encyclopedia of Analytical Chemistry*; John Wiley & Sons, Ltd: 2012.
- (10) Samec, Z.; Langmaier, J.; Kakiuchi, T. *Pure Appl. Chem.* **2009**, *81*, 1473.

- (11) Zhurov, K.; Dickinson, E. J. F.; Compton, R. G. *J. Phys. Chem. B* **2011**, *115*, 6909.
- (12) Parker, A. J. *Electrochim. Acta* **1976**, *21*, 671.
- (13) Wandlowski, T.; Mareček, V.; Samec, Z. *Electrochim. Acta* **1990**, *35*, 1173.
- (14) Trombetta, M.; Williams, N. E.; Fischer, S.; Gokirmak, A.; Silva, H. *Electron. Lett.* **2014**, *50*, 100.
- (15) Matar, S.; Ge, J.; Liu, H. *J. Power Sources* **2013**, *243*, 195.
- (16) Xiao, J.; Hu, M.; Bénard, P.; Chahine, R. *Int. J. Hydrogen Energy* **2013**, *38*, 13000.
- (17) Bell, J. S.; Lewis, B. J. *Nucl. Eng. Des.* **2012**, *250*, 134.
- (18) Zigah, D.; Wang, A.; Lagrost, C.; Hapiot, P. *J. Phys. Chem. B* **2009**, *113*, 2019.
- (19) Stockmann, T. J.; Ding, Z. *Phys. Chem. Chem. Phys.* **2012**, *14*, 13949.
- (20) Stockmann, T. J.; Ding, Z. *J. Phys. Chem. B* **2012**, *116*, 12826.
- (21) Dickinson, E. J. F.; Ekström, H.; Fontes, E. *Electrochem. Commun.* **2014**, *40*, 71.
- (22) Rodgers, P. J.; Amemiya, S. *Anal. Chem.* **2007**, *79*, 9276.
- (23) Stockmann, T. J.; Montgomery, A.-M.; Ding, Z. *J. Electroanal. Chem.* **2012**, *684*, 6.
- (24) Bard, A. J.; Faulkner, L. R. *Electrochemical Methods*; 2nd ed.; John Wiley & Sons: New York, 2001.
- (25) Randles, J. E. B. *Trans. Faraday Soc.* **1948**, *44*, 327.
- (26) Stockmann, T. J.; Deng, H.; Peljo, P.; Kontturi, K.; Opallo, M.; Girault, H. H. *J. Electroanal. Chem.* **2014**, *accepted*.
- (27) Su, B.; Nia, R. P.; Li, F.; Hojeij, M.; Prudent, M.; Corminboeuf, C.; Samec, Z.; Girault, H. H. *Angew. Chem., Int. Ed.* **2008**, *47*, 4675.
- (28) Deng, H.; Peljo, P.; Cortés-Salazar, F.; Ge, P.; Kontturi, K.; Girault, H. H. *J. Electroanal. Chem.* **2012**, *681*, 16.
- (29) Fomin, V. M.; Terekhina, A. A.; Zaitseva, K. S. *Russ. J. Gen. Chem.* **2013**, *83*, 2324.
- (30) Peljo, P.; Murtomäki, L.; Kallio, T.; Xu, H. J.; Meyer, M.; Gros, C. P.; Barbe, J. M.; Girault, H. H.; Laasonen, K.; Kontturi, K. *J. Am. Chem. Soc.* **2012**, *134*, 5974.
- (31) *CRC Handbook of Chemistry and Physics*; 94th ed.; Haynes, W. M., Ed.; CRC Press: Boca Raton, 2013.
- (32) Méndez, M. A.; Partovi-Nia, R.; Hatay, I.; Su, B.; Ge, P.; Olaya, A.; Younan, N.; Hojeij, M.; Girault, H. H. *Phys. Chem. Chem. Phys.* **2010**, *12*, 15163.
- (33) Su, B.; Girault, H. H.; Samec, Z. In *Catalysis in Electrochemistry*; John Wiley & Sons, Inc.: 2011, p 427.
- (34) Su, B.; Hatay, I.; Ge, P. Y.; Mendez, M.; Corminboeuf, C.; Samec, Z.; Ersoz, M.; Girault, H. H. *Chem. Commun.* **2010**, *46*, 2918.
- (35) Hatay, I.; Su, B.; Méndez, M. A.; Corminboeuf, C.; Khoury, T.; Gros, C. P.; Bourdillon, M.; Meyer, M.; Barbe, J. M.; Ersoz, M.; Zališ, S.; Samec, Z.; Girault, H. H. *J. Am. Chem. Soc.* **2010**, *132*, 13733.
- (36) Trojánek, A.; Langmaier, J.; Samec, Z. *Electrochim. Acta* **2012**, *82*, 457.
- (37) Trojánek, A.; Langmaier, J.; Zališ, S.; Samec, Z. *Electrochim. Acta* **2013**, *110*, 816.
- (38) Sun, P.; Laforge, F. O.; Mirkin, M. V. *J. Am. Chem. Soc.* **2007**, *129*, 12410.
- (39) Rose, D.; Benjamin, I. *J. Phys. Chem. B* **2009**, *113*, 9296.
- (40) Murakami, W.; Eda, K.; Yamamoto, M.; Osakai, T. *J. Electroanal. Chem.* **2013**, *704*, 38.
- (41) Benjamin, I. *J. Phys. Chem. B* **2010**, *114*, 13358.
- (42) Barthomeuf, D. *J. Phys. Chem.* **1979**, *83*, 249.
- (43) Barnum, D. W. *Inorg. Chem.* **1983**, *22*, 2297.
- (44) Hatay, I.; Su, B.; Li, F.; Méndez, M. A.; Khoury, T.; Gros, C. P.; Barbe, J. M.; Ersoz, M.; Samec, Z.; Girault, H. H. *J. Am. Chem. Soc.* **2009**, *131*, 13453.
- (45) Battino, R.; Rettich, T. R.; Tominaga, T. *J. Phys. Chem. Ref. Data* **1983**, *12*, 163.
- (46) Luehring, P.; Schumpe, A. *J. Chem. Eng. Data* **1989**, *34*, 250.

- (47) Zhou, M.; Gan, S.; Zhong, L.; Dong, X.; Ulstrup, J.; Han, D.; Niu, L. *Phys. Chem. Chem. Phys.* **2012**, *14*, 3659.
- (48) Hatay, I.; Su, B.; Li, F.; Partovi-Nia, R.; Vrubel, H.; Hu, X.; Ersoz, M.; Girault, H. H. *Angew. Chem., Int. Ed.* **2009**, *48*, 5139.
- (49) Monnin, C.; Dubois, M. *J. Chem. Eng. Data* **2005**, *50*, 1109.
- (50) Scanlon, M. D.; Bian, X.; Vrubel, H.; Amstutz, V.; Schenk, K.; Hu, X.; Liu, B.; Girault, H. H. *Phys. Chem. Chem. Phys.* **2013**, *15*, 2847.
- (51) Morales-Guio, C. G.; Stern, L.-A.; Hu, X. *Chem. Soc. Rev.* **2014**.
- (52) Peljo, P.; Qiao, L.; Murtomäki, L.; Johans, C.; Girault, H. H.; Kontturi, K. *ChemPhysChem* **2013**, *14*, 311.
- (53) Olaya, A. J.; Méndez, M. A.; Cortes-Salazar, F.; Girault, H. H. *J. Electroanal. Chem.* **2010**, *644*, 60.
- (54) Deng, H.; Peljo, P.; Stockmann, T. J.; Qiao, L.; Vainikka, T.; Kontturi, K.; Opallo, M.; Girault, H. H. *Chem. Commun.* **2014**, *50*, 5554.
- (55) Su, B.; Hatay, I.; Li, F.; Partovi-Nia, R.; Méndez, M. A.; Samec, Z.; Ersoz, M.; Girault, H. H. *J. Electroanal. Chem.* **2010**, *639*, 102.
- (56) Trojánek, A.; Langmaier, J.; Su, B.; Girault, H. H.; Samec, Z. *Electrochem. Commun.* **2009**, *11*, 1940.
- (57) Peljo, P.; Rauhala, T.; Murtomäki, L.; Kallio, T.; Kontturi, K. *Int. J. Hydrogen Energy* **2011**, *36*, 10033.
- (58) Trojánek, A.; Langmaier, J.; Kvapilová, H.; Zális, S.; Samec, Z. *J. Phys. Chem. A* **2014**, *118*, 2018.
- (59) Mähler, J.; Persson, I. *Inorg. Chem.* **2012**, *51*, 425.
- (60) Girault, H. H. *Analytical and Physical Electrochemistry*; 1st ed.; EPFL Press: Lausanne, 2004.
- (61) Schumpe, A.; Luehring, P. *J. Chem. Eng. Data* **1990**, *35*, 24.
- (62) Trojánek, A.; Langmaier, J.; Samec, Z. *Electrochem. Commun.* **2006**, *8*, 475.
- (63) Molina, A.; Torralba, E.; Serna, C.; Ortuño, J. A. *Electrochim. Acta* **2013**, *106*, 244.
- (64) Samec, Z.; Homolka, D.; Mareček, V. *J. Electroanal. Chem.* **1982**, *135*, 265.
- (65) Shao, Y.; Osborne, M. D.; Girault, H. H. *J. Electroanal. Chem.* **1991**, *318*, 101.
- (66) Kitazumi, Y.; Kakiuchi, T. *Bull. Chem. Soc. Jpn.* **2011**, *84*, 1312.
- (67) Dietrich, B. *J. Chem. Educ.* **1985**, *62*, 954.
- (68) Pedersen, C. J. *J. Am. Chem. Soc.* **1967**, *89*, 7017.
- (69) Park, J.; Morimoto, Y.; Lee, Y.-M.; Nam, W.; Fukuzumi, S. *Inorg. Chem.* **2014**, *53*, 3618.

Appendix

Photoinduced Electron Transfer Reaction at the Liquid/Liquid Interface

A.1 Introduction

In natural photosynthesis, the light energy from the sun is used to facilitate the uphill reaction between carbon dioxide (CO_2) and water, finally resulting in its conversion into chemical energy that is stored in carbohydrate molecules. The proteins that participate in light harvesting and the following electron-transfer events are embedded within cell membranes. Due to the great success of natural photosynthesis in powering life for billions of years and the current global energy and environment crisis, a great deal of efforts has been made to mimic this process. The term of “artificial photosynthesis” is then coined and it mainly focuses on the realization of elementary function but not the complicated mechanism occurred in natural photosynthesis. Hence, designing efficient systems utilizing sunlight to make renewable fuels such as hydrogen (H_2) from water splitting and hydrocarbons from CO_2 reduction is one of the Holy Grails in chemistry.¹ The advantage of H_2 over hydrocarbons is that hydrogen can be burned either in a flame or in a fuel cell to produce only water.² However, storage and carriage of H_2 is a technological concern.

Hydrogen peroxide (H_2O_2) can be an energy carrier alternative to fossil fuels or H_2 , due to its potential to be used as a fuel in a direct H_2O_2 fuel cell.³ Currently 95% of world's H_2O_2 production is made through the biphasic anthrahydroquinone oxidation (AO) process *via* reduction of oxygen with hydrogen in a high yield.⁴ An electrocatalytic 2e^- reduction of O_2 to H_2O_2 powered by a photovoltaic solar cell has been demonstrated by Fukuzumi's group.³ Another methodology, utilizing (catalyzed) oxygen reduction reaction (ORR) at a liquid/liquid interface, or the interface between two immiscible electrolyte solutions (ITIES), that is normally composed of two phases between water (w) and an organic solvent (o) such as 1,2-dichloroethane (DCE), has been developed for *ca.* 20 years.^{5,6} Very recently, Rastgar *et al.* has developed a simple method for H_2O_2 production *via* ORR at the ITIES catalyzed by *in-situ* generated reduced graphene oxide (RGO), with a yield of *ca.* 43%.⁷ The non-ideal H_2O_2 yield from this protocol compared to the AO process lies in the fact that in the former case ORR mainly occurs in the bulk of the organic phase⁸ and some of the produced H_2O_2 will be either decomposed or reduced by the transition-metal complexes such as ferrocene (Fc) and its derivatives before its partition into the aqueous phase.^{9,10} A very recent work from Opallo's group¹¹ showed that H_2O_2 could be also generated from ORR at the liquid/liquid interface under conditions unfavorable for proton transfer, but the reaction is really slow. It should be noted that in 2004, Nagatani *et al.* Have suggested the photo-production of H_2 at the

ITIES employing 5,10,15,20-tetraphenylporphyrinato zinc (ZnTPP) as a lipophilic sensitizer in contact with an acidic aqueous phase to regenerate the photooxidized sensitizer,¹² but the product is more likely H₂O₂ from oxygen reduction than H₂, considering that oxygen reduction is much easier from the thermodynamic point of view. The yield of H₂O₂ in this experimental configuration should be higher, taking into account its heterogeneous nature.

Photoinduced heterogeneous electron transfer (ET) reactions between a sensitizer (S) and a quencher (Q) located at either side of the ITIES can mimic the photosynthesis process that leads to the facile charge/product separation from the intermediate ion pair (S⁺Q⁻) formed at the interface.¹³ Eugster *et al.* Investigated the heterogeneous ET between a series of Fc derivatives and a zinc porphyrin heterodimer at the polarized w/DCE interface and a quasi-square-wave shaped photocurrent response was observed when decamethylferrocene (DMFc) was used as the lipophilic quencher.¹⁴ They suggested that the back ET is slower compared to the product separation, as the driving force for the forward ET increases and the driving force for the back ET decreases, resulting from the more negative redox potential of the DMFc in comparison with the other ferrocene based donors.¹⁴ However, a detail was mentioned that the photocurrent transients in the presence of DMFc could last for hours of illumination, which has not been understood.

In the present chapter, photoinduced ET between a hydrophilic zinc meso-tetra(4-carboxyphenyl)porphyrin (ZnTPPC) and DMFc in DCE has been studied. The results show that the photocurrent intensity is dependent on the ET driving force and increases with the increase in the aqueous acidity. Biphasic shake-flask experiments has also been conducted to show that ZnTPPC is not degraded during *ca.* 2h illumination and a mechanism involving ZnTPPC regeneration *via* reducing O₂ to H₂O₂ by ZnTPPC⁻ is thus demonstrated. The yield of produced H₂O₂ is estimated to be 55.7% that is highest in the ITIES system up to date. To further improve the system, the electron donor could be regenerated photocatalytically for example by dark TiO₂,^{15,16} accomplishing the production of solar fuel sustainably.

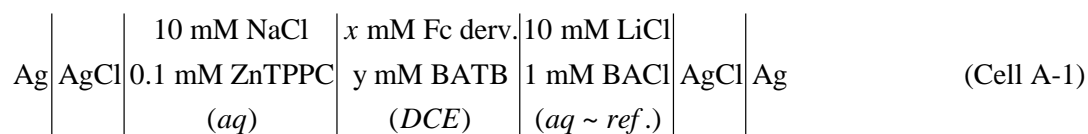
A.2 Experimental section

A.2.1 Chemicals

All chemicals used throughout this chapter have been summarized in Section 2.2 in Chapter 2.

A.2.2 Photoelectrochemical measurements

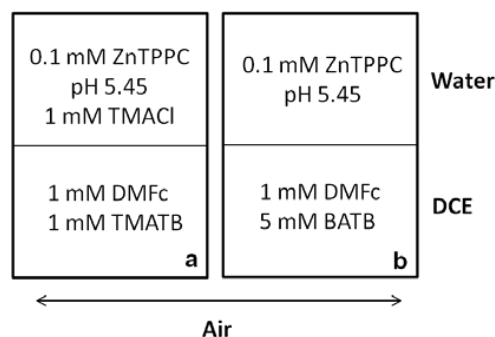
Cyclic voltammetry (CV) and photocurrent transient measurements were recorded at the w/DCE interface (1.53 cm²) in a normal three-compartment, four-electrode glass cell with a PGSTAT30 potentiostat (Metrohm, CH).¹³ Photocurrent measurements were achieved by illumination at the w/DCE interface by a blue InGaN LED light (peak wavelength at 450 nm, typical power output of 20 mW, GmbH, Austria) controlled by a wave-function generator. The following photoelectrochemical cells were used :



In Cell A-1, two quasi-reference electrodes, Ag/AgCl, were used to measure the potential/polarization of the interface; ‘Fc deriv.’ Refers to the two ferrocene derivatives evaluated individually – Fc and DMFc. It should be noted that the potential scale was not calibrated into the conventional Galvani potential scale ($\Delta_o^w\phi$), as here only preliminary results were shown. However, the cell potential, E , is related to $\Delta_o^w\phi$ by $E = \Delta_o^w\phi + \Delta E_{\text{ref}}$, in which ΔE_{ref} is dependent on the compositions of the two reference electrodes and the junction potential at the DCE-aqueous reference phase interface.¹⁷ Hence the non-calibrated potential scale E is still equivalent to $\Delta_o^w\phi$. All experiments were performed under aerobic conditions.

A.2.3 Two-phase shake flask reactions

Two-phase shake flask reactions were performed in a small flask under stirring (1000 rpm) and illumination (with a monochromatic high power LED of ~200 mW at 455 nm, Thorlabs, M455L2, USA) conditions to clarify the reaction mechanisms. For these experiments, equal volumes (2 mL) of DCE and aqueous solutions containing the reactants with the initial compositions shown in Scheme A-1 were employed. After reaction, the aqueous and organic phases were separated and the UV/Vis spectrum of the DCE phase was measured directly. The aqueous phase was firstly acidified by 1 M HCl to precipitate the ZnTPPC and then subject to ultracentrifugation for 1 min. The obtained supernatant was used to analyze the probable reaction product – H_2O_2 , following the methodology detailed in Section 2.4.1.1.1 in Chapter 2.¹⁸ At the same time, microelectrode voltammetry employing a commercial glassy carbon (GC) microelectrode (Princeton Applied, diameter 13.7 μm) was conducted in a three-electrode system with a CHI900 electrochemical workstation (CH Instruments, Austin, USA) to estimate the percentage of consumed DMFc. The quasi-reference electrode is an Ag wire and the counter electrode is a Pt wire. UV/visible (UV/Vis) spectra were obtained with an Ocean Optics CHEM2000 spectrophotometer with a quartz cuvette (path length : 10 mm).



Scheme A-1. Schematic representation of the initial compositions for shake-flask experiments under aerobic and illumination conditions. Stirring rate : 1000 rpm ; LED : 455 nm ; Duration : 2 h 13 min for (a) and 14 h for (b).

A.3 Results and discussion

A.3.1 Photoelectrochemical measurements

Figure A-1 shows the cyclic voltammograms of the w/DCE interface recorded in the dark, employing the electrochemical Cell A-1 with $x = 1$ Mm Fc and $y = 2$ (full line) and with $x = 5$ Mm DMFc and $y = 5$ (dashed line), respectively. In the case of Fc, the potential window of nearly 600 mV without any evident Faradaic signal is observed, which is *ca.* 100 mV wider than that reported previously.¹⁹ This is probably because the iR drop was much larger in the cell used before.¹⁹ The absence of Faradaic signal in the potential window indicates that no ET event occurs across the w/DCE interface when ZnTPPC is at ground state. Interestingly, the potential window is much narrower featured with the dramatic shift of the positive limit to more negative potential, in the case of DMFc. This phenomenon can be caused by oxygen reduction in the organic phase catalyzed by hydrated alkali metal cation (here Na^+) transfer.²⁰ Nevertheless, it should be stressed that the CV recorded in the presence of DMFc ensues from illumination at the w/DCE interface over a period of time. This may produce some species that limit the positive potential window.

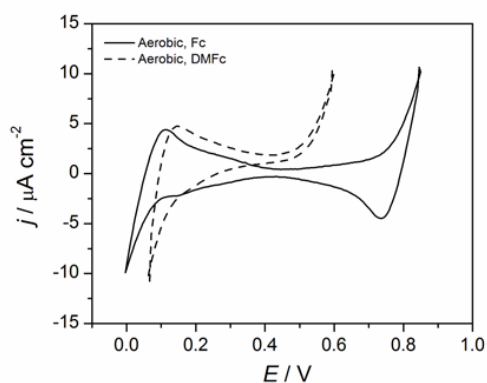


Figure A-1. CVs recorded at 50 mV s^{-1} using electrochemical Cell A-1 with $x = 1 \text{ mM Fc}$, and $y = 2$ (aerobic, full line) and $x = 5 \text{ mM DMFc}$, and $y = 5$ (aerobic, dashed line), respectively. Notes : LED at 450 nm has been turned on and off over a period of time before the dashed line is recorded, besides, the potential is not corrected in the Galvani scale.

Photocurrent transient responses obtained using electrochemical Cell A-1 with 5 mM DMFc as the quencher in DCE and 0.1 mM ZnTPPC as the photosensitizer in aqueous are shown in Figure A-2, at different interfacial potential differences.

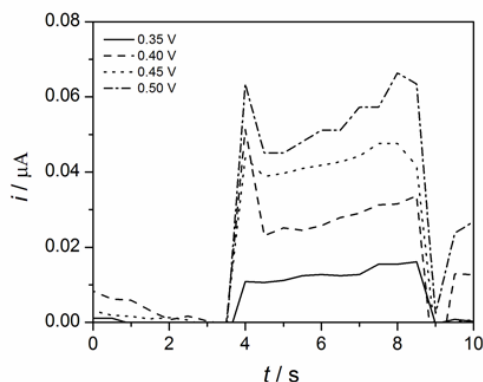


Figure A-2. Photocurrent transient measurements at different interfacial potentials obtained using the electrochemical Cell A-1 with $x = 5$ mM DMFc, and $y = 5$. Notes : The employed potential for photocurrent measurement is not corrected in the Galvani scale, and the current value recorded in the dark is set to zero.

It can be seen that positive photocurrent responses are observed at all potentials, indicating the heterogeneous photoinduced electron transfer is directed from DMFc to excited ZnTPPC, marked as ZnTPPC*. Besides, photocurrent intensity increases with the increase in the interfacial potential differences. The quasi-square-wave photocurrent response also reflects the absence of the back electron transfer. The photocurrent transients in the case of Fc as a function of the interfacial potential were also investigated (not shown), showing that the photocurrent also increases with increasing the applied interfacial potentials. However, in the presence of Fc, the photocurrent relaxes after the initial illumination and then a negative overshoot is observed upon interruption of the illumination, indicating a back electron-transfer process. The driving force or the standard Gibbs free energy ($\Delta G_{\text{et}}^{\circ}$) for this heterogeneous electron transfer can be expressed as

$$\Delta G_{\text{et}}^{\circ} = -F \left([E_{\text{P}^{*}/\text{P}^{-}}^{\circ}]_{\text{SHE}}^{\text{w}} - [E_{\text{Q}^{+}/\text{Q}}^{\circ}]_{\text{SHE}}^{\text{DCE}} + \Delta_{\text{o}}^{\text{w}} \phi \right) \quad (\text{A-1})$$

where $[E_{\text{P}^{*}/\text{P}^{-}}^{\circ}]_{\text{SHE}}^{\text{w}}$ and $[E_{\text{Q}^{+}/\text{Q}}^{\circ}]_{\text{SHE}}^{\text{DCE}}$ are the standard redox potentials (vs. SHE) for the excited sensitizer/porphyrin and quencher in aqueous and DCE, respectively, and F is Faraday constant. The specific potential values are shown in Figure A-3 – energy level diagram. Equation A-1 and Figure A-3 explain the different behavior between Fc and DMFc in the photocurrent transients.

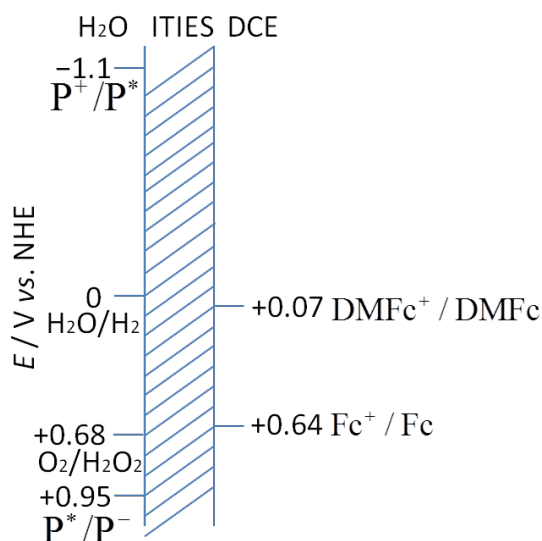
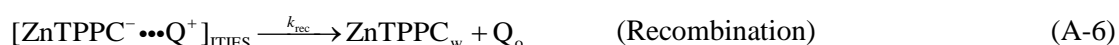
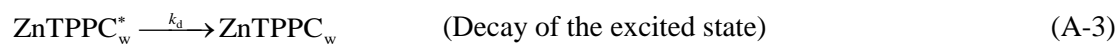
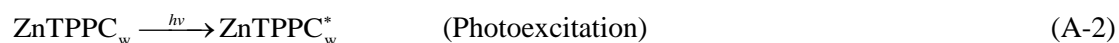


Figure A-3. Energy level diagram of the participated species during the photoelectrochemical reaction. Notes : P denotes ZnTPPC, ITIES means the interface between two immiscible electrolyte solutions.

Then, the mechanism behind this photocurrent can be generally described by :¹⁹



where $[\text{ZnTPPC}^- \cdots \text{Q}^+]_{\text{ITIES}}$ is the photoinduced intermediate ion pair formed at the ITIES.

Interestingly, the photocurrent transients in the presence of DMFc under a given interfacial potential increase dramatically with the dropwise addition of acid (0.1 M HCl) into the aqueous phase, seen from Figure A-4. Besides, the photocurrent increases with time after the addition of acid, probably caused by diffusion of H^+ towards the interfacial site thus providing more H^+ for reaction. Considering the redox species available in the aqueous phase, the water or oxygen will be the electron acceptor from the reduced ZnTPPC, resulting in the regeneration of ZnTPPC. But it cannot exclude the possibility of increased concentration in ZnTPPC adsorbed at the ITIES upon acidification,²¹ considering the pK_{a1} of the carboxylic group of ZnTPPC is 4.2.²²

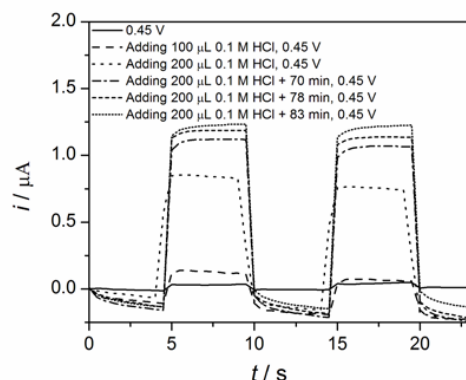


Figure A-4. Effect of acid (0.1 M HCl) added in the aqueous phase and its diffusion with time on photocurrent response. Notes : The employed potential for photocurrent measurement is not corrected in the Galvani scale, and the current value recorded in the dark is set to zero.

Figure A-5 shows the time profile of the photocurrent transients with and without the addition of HCl in aqueous phase. The photocurrent is stable without any degradation during this period and even lasts for hours. Comparing the results in Figures A-4 and A-5, it implies that ZnTPPC is recycled.

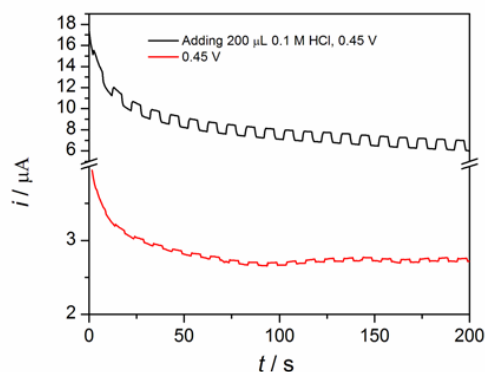


Figure A-5. Time profile of the photocurrent transients with and without additional HCl in aqueous phase.

A.3.2 Two-phase shake flask reactions

To confirm further the claims made above, biphasic shake-flask experiments employing the initial composition described in Scheme A-1 “a” under illumination (455 nm) were conducted, shown in Figure A-6. It can be seen that ZnTPPC is not degraded and DMFc is oxidized to DMFc^+ featured with the green color, after *ca.* 2 h of reaction.

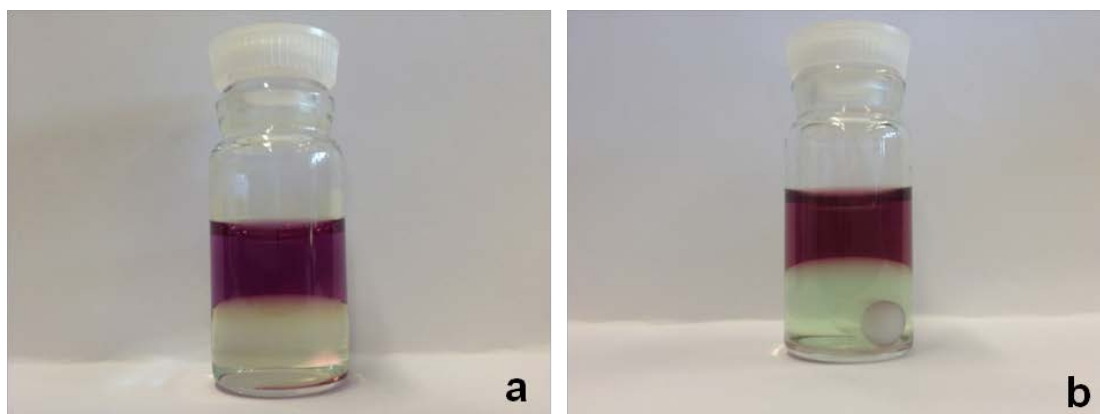


Figure A-6. Photographic illustrations of photocatalytic biphasic reactions employing the initial compositions described in Scheme A-1 “a” at the beginning (a) and after 2 h 13 min (b).

The UV/Vis spectra of DCE and aqueous phases were also analyzed and shown in Figure A-7. It can be seen in Figure A-7 (red line) that DCE solution after biphasic reaction shows an absorption band with the maximum located at 779 nm corresponding to DMFc^+ , whereas the characteristic absorption peak for DMFc at 425 nm disappeared. Formation of DMFc^+ was also confirmed by microelectrode voltammetry, as illustrated in the inset of Figure A-7. Aqueous phase was firstly acidified to precipitate out ZnTPPC , and then analyzed for H_2O_2 by NaI method. The color of the aqueous after addition of NaI changed from colorless to deep yellow immediately, indicating the formation of a large amount of I_3^- . I_3^- has absorption bands located at 286 and 352 nm, as seen in Figure A-7. So it can be deduced that H_2O_2 is formed from oxygen reduction by ZnTPPC^- to recycle the ZnTPPC . Additionally, no reaction occurred with the initial composition described in Scheme A-1 “b”. It indicates that chemical polarization of the liquid/liquid interface to a slightly positive potential is essential for this biphasic photocatalytic reaction to proceed.

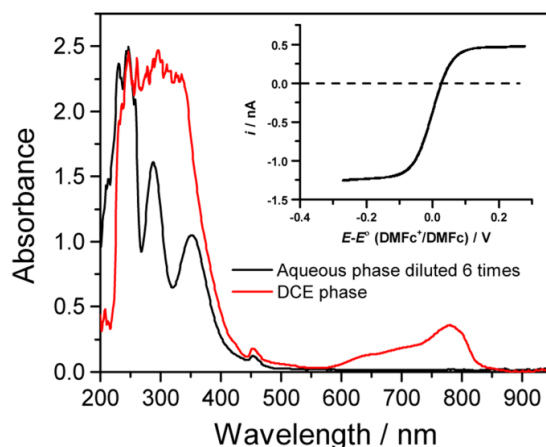


Figure A-7. UV/Vis spectra of the aqueous phase (diluted 6 times, black line) after treatment with 0.1 M NaI for 0.5 h and organic phase (red line) after the biphasic photocatalytic reaction using the composition in Scheme A-1

“a”. Inset shows the microelectrode (glassy carbon, diameter 13.7 μm) voltammetry in the DCE phase after the biphasic photocatalytic reactions.

The percentage of DMFc oxidized and the H_2O_2 yield are summarized in Table A-1. It is promising to have 55.7% yield of H_2O_2 that is highest in the ITIES system reported up to date.⁷ This is because ZnTPPC works as a photocatalyst mediating vectorial electron transfer from lipophilic DMFc to aqueous O_2 in this novel strategy, minimizing the decomposition and further reduction of H_2O_2 by DMFc in the strategy reported before.^{9,10}

Table A-1. The percentage of oxidized DMFc and H_2O_2 yield.

Electron donor	Conversion / %	Detected H_2O_2 / Mm	Theoretical H_2O_2 / Mm	H_2O_2 yield / %
DMFc	72.7	0.2024	0.3635	55.7

A.3.3 Mechanism

Based on the discussions above, the biphasic photocatalytic reaction goes *via* the mechanism depicted in Figure A-8. Upon illumination, ZnTPPC is excited to ZnTPPC^* and then electron exchange between DMFc and ZnTPPC^* occurs with the formation of ZnTPPC^- and DMFc^+ in aqueous and DCE, respectively. Simultaneously a TMA^+ ion will transfer from DCE to aqueous phase to keep the charge neutrality in each phase. Aqueous O_2 works as the final electron acceptor from ZnTPPC^- to regenerate ZnTPPC and produce H_2O_2 .

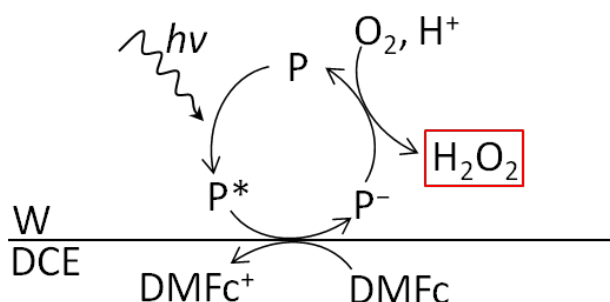


Figure A-8. The proposed mechanism for this photocatalytic biphasic reaction, in which P denotes ZnTPPC.

A.4 Conclusions

Photoinduced heterogeneous electron transfer from lipophilic DMFc to aqueous ZnTPPC was demonstrated at the w/DCE interface. Photocurrent increases dramatically with the acidity increase in aqueous, due to either the regeneration of ZnTPPC *via* oxygen reduction or

increase in concentration of ZnTPPC adsorbed at the ITIES upon acidification. Acidification also makes oxygen reduction easier; this might be one reason for the increasing photocurrents. The quasi-square-wave shaped photocurrent response can be explained by both the increase in driving force for the electron transfer and ZnTPPC recycling. A photocatalytically heterogeneous H_2O_2 production strategy with a relatively high yield can be developed if the lipophilic electron donor can be recycled by *e.g.* water oxidation photocatalytically. In principle, H_2 can be also obtained using this system under anaerobic conditions, implied by the energy level diagram of Figure A-3. Then an indirect water splitting system can be envisaged.

A.5 References

- (1) Dempsey, J. L.; Brunschwig, B. S.; Winkler, J. R.; Gray, H. B. *Acc. Chem. Res.* **2009**, *42*, 1995.
- (2) Fukuzumi, S.; Yamada, Y.; Karlin, K. D. *Electrochim. Acta* **2012**, *82*, 493.
- (3) Yamada, Y.; Fukunishi, Y.; Yamazaki, S.-i.; Fukuzumi, S. *Chem. Commun.* **2010**, *46*, 7334.
- (4) Campos-Martin, J. M.; Blanco-Brieva, G.; Fierro, J. L. G. *Angew. Chem., Int. Ed.* **2006**, *45*, 6962.
- (5) Cunnane, V. J.; Geblewicz, G.; Schiffrin, D. J. *Electrochim. Acta* **1995**, *40*, 3005.
- (6) Su, B.; Girault, H. H.; Samec, Z. In *Catalysis in Electrochemistry*; John Wiley & Sons, Inc.: 2011, p 427.
- (7) Rastgar, S.; Deng, H.; Cortés-Salazar, F.; Scanlon, M. D.; Pribil, M.; Amstutz, V.; Karyakin, A. A.; Shahrokhian, S.; Girault, H. H. *ChemElectroChem* **2014**, *1*, 59.
- (8) Stockmann, T. J.; Deng, H.; Peljo, P.; Kontturi, K.; Opallo, M.; Girault, H. H. *J. Electroanal. Chem.* **2014**, *accepted*.
- (9) Deng, H.; Peljo, P.; Cortés-Salazar, F.; Ge, P.; Kontturi, K.; Girault, H. H. *J. Electroanal. Chem.* **2012**, *681*, 16.
- (10) Peljo, P.; Murtomäki, L.; Kallio, T.; Xu, H. J.; Meyer, M.; Gros, C. P.; Barbe, J. M.; Girault, H. H.; Laasonen, K.; Kontturi, K. *J. Am. Chem. Soc.* **2012**, *134*, 5974.
- (11) Jedraszko, J.; Nogala, W.; Adamiak, W.; Rozniecka, E.; Lubarska-Radziejewska, I.; Girault, H. H.; Opallo, M. *J. Phys. Chem. C* **2013**, *117*, 20681.
- (12) Nagatani, H.; Dejima, S.; Hotta, H.; Ozeki, T.; Osakai, T. *Anal. Sci.* **2004**, *20*, 1575.
- (13) Girault, H. H. In *Electroanalytical Chemistry, Vol 23*; Bard, A. J., Zoski, C. G., Eds. 2010; Vol. 23, p 1.
- (14) Eugster, N.; Fermín, D. J.; Girault, H. H. *J. Phys. Chem. B* **2002**, *106*, 3428.
- (15) Chen, X.; Liu, L.; Yu, P. Y.; Mao, S. S. *Science* **2011**, *331*, 746.
- (16) Wang, G.; Wang, H.; Ling, Y.; Tang, Y.; Yang, X.; Fitzmorris, R. C.; Wang, C.; Zhang, J. Z.; Li, Y. *Nano Lett.* **2011**, *11*, 3026.
- (17) Senda, M.; Kakiuchi, T.; Osaka, T. *Electrochim. Acta* **1991**, *36*, 253.
- (18) Su, B.; Nia, R. P.; Li, F.; Hojeij, M.; Prudent, M.; Corminboeuf, C.; Samec, Z.; Girault, H. H. *Angew. Chem., Int. Ed.* **2008**, *47*, 4675.
- (19) Schaming, D.; Hojeij, M.; Younan, N.; Nagatani, H.; Lee, H. J.; Girault, H. H. *Phys. Chem. Chem. Phys.* **2011**, *13*, 17704.
- (20) Deng, H.; Peljo, P.; Stockmann, T. J.; Qiao, L.; Vainikka, T.; Kontturi, K.; Opallo, M.; Girault, H. H. *Chem. Commun.* **2014**, *50*, 5554.
- (21) Fermín, D. J.; Ding, Z.; Duong, H. D.; Brevet, P. F.; Girault, H. H. *J. Phys. Chem. B* **1998**, *102*, 10334.

- (22) Sobczyk, J.; Tønnesen, H. H.; Kristensen, S. *Pharmazie* **2013**, 68, 100.

Chapter 8

Conclusions and Perspective

Chapter 1 of this thesis gives a comprehensive review of the state-of-the-art of the research on liquid/liquid interface electrochemistry. Chapter 2 summarizes the experimental and instrumentation details employed in conducting the research throughout this thesis.

Chapter 3 to 7 in this thesis is dedicated to elucidation of the mechanism, thermodynamics/kinetics of oxygen reduction reaction (ORR) at the liquid/liquid interface, which is fundamentally important to both biology (*i.e.* respiration) and practical applications such as in catalysts screening for fuel cells. The methods employed are UV/Vis spectroscopy, microelectrode voltammetry, four- and three-electrode liquid/liquid interface voltammetry, scanning electrochemical microscopy (SECM), as well as finite element method (FEM) simulations. The ORR can be initiated by either the transfer of protons or hydrophilic metallic cations from aqueous to organic phase controlled by either an external power source or a phase transfer catalyst, and the reaction requires the presence of an electron donor in the organic phase. With ferrocene derivatives used as the lipophilic electron donors, the ORR mainly goes *via* the $2e^-/2H^+$ pathway with H_2O_2 as the product even though the yield is not so high due to the further reduction and decomposition of H_2O_2 by these transition metal complexes. Specifically, the overall biphasic reaction is composed of a potential dependent proton/cation transfer (*i.e.* ion transfer, IT) followed by two homogeneous chemical reactions (C_1C_2) occurring in the organic phase – an IT- C_1C_2 mechanism.

In Chapter 3, when 1,2-diferrocenylethane (DFcE), a multiferrocenyl compound, is used as the lipophilic electron donor, the ORR in the organic phase proceeds *via* oxidation of one ferrocenyl side to form $DFcE^+$ until all DFcE is converted. $DFcE^+$ can be further oxidized by oxygen to produce $DFcE^{2+}$, but at much slower rate due to the lower thermodynamic driving force. Depending on the published results (by others) and the investigations herein, it implies that the supporting electrolyte and solvent can have significant influence on the reaction pathway. Besides, H_2O_2 can be reduced by DFcE at a rate that is even faster than that for ORR by DFcE.

In Chapter 4, a novel method – H_2O_2 production *via* ORR catalyzed by *in-situ* generated reduced graphene oxide (RGO) at the liquid/liquid interface is developed. RGO is formed by heterogeneous reduction of GO in aqueous by ferrocene derivatives in the organic phase. The H_2O_2 yield with decamethylferrocene (DMFc) as the lipophilic electron donor is *ca.* 43%. This simple approach could be an alternative method for H_2O_2 production, instead of the traditional, ungreen anthraquinone oxidation (AO) process.¹ While, the AO process involves the use of the expensive palladium catalyst, sequential hydrogenation and oxidation of the anthraquinone in an organic phase, and the liquid/liquid extraction of H_2O_2 .

Chapters 5 and 6 provide new physical insights into the mechanistic details of this biphasic ORR by comparison of the cyclic voltammetry (CV) and SECM experiments with the FEM simulations through COMSOL Multiphysics software. Kinetic rate constants for the rate-determining step – protonated electron donor formation (**1**) and the following HO_2^\bullet formation step (**2**) during the ORR are determined and the reaction is recognized to occur mainly in the bulk organic phase. In the CV strategy, the rates of **1** and **2** were determined to be 5×10^2 and $1 \times 10^4 \text{ L}\cdot\text{mol}^{-1}\cdot\text{s}^{-1}$, respectively, for DMFc as the electron donor. In the SECM approach, the rate of **1** was estimated as *ca.* $1\text{--}2.5 \times 10^2 \text{ L}\cdot\text{mol}^{-1}\cdot\text{s}^{-1}$. This implies a good agreement between these two methods. Besides, counter-anions such as ClO_4^- can inhibit the ORR kinetics significantly due to ion-pair formation, so does H_2O concentration.

Chapter 7 shows that ORR can also occur without any pre-existing protons but in the presence of hydrophilic metallic cations in the organic phase, proving that hydrophilic ion transfer is an activated rather than a simple diffusive process – interaction between a protruding water finger and the transferred ion at the interface plays an important role for the successful transfer.² These small cations either are re-hydrated by the pre-existing water clusters dispersed inside the organic phase after transfer or just keep their hydration shells inert during the transfer process. Hydrophilic cations polarize the water molecules in their solvation shells due to electrostatic interactions between the ions and the water dipoles and with the help of hydrogen bonding from adjacent water molecules, making the protons more acidic. Now the mechanism of oxygen reduction mirrors the mechanism under proton conditions, with the difference that now the proton source is water from the solvation shell of the cation. Additionally, hydrogen evolution and $\text{S}_{\text{N}}1$ reaction are also demonstrated in the presence of hydrophilic metal cations. A hydration asymmetry parameter “*HA*” can interpret the salt (*e.g.* LiTB) case. Besides, crown ether can enhance either the transferred cation amount in the organic phase or the acidity of water molecules surrounded over the cations entrapped in the macrocycles of crown ether, speeding up the reaction.

The Appendix chapter was focused on the photoinduced electron transfer across the liquid/liquid interface with some preliminary results. The hydrophilic sensitizer is proven to be recycled upon relaying electrons to oxygen to produce H_2O_2 directly in the aqueous phase, minimizing the encounter between H_2O_2 and lipophilic quencher. 55.7% in H_2O_2 yield in this heterogeneous photocatalyzed system implies a promising future if lipophilic quencher can be recycled for example by photocatalytic water oxidation.

In the future, some works need to be considered:

1. [1.1]ferrocenophane, a multiferrocenyl compound, could be employed as the lipophilic electron donor for ORR and hydrogen evolution at the liquid/liquid interface. Some interesting phenomena in terms of reaction mechanism, such as generation of sandwich-kind of complex intermediates, are expected. If so, the efficiency and kinetics of the reactions could be promising. Besides, methylation on the cyclopentadienyl rings will lower the redox potential of this compound to enhance the rate of ORR and hydrogen evolution.

2. Effect of different metal cations with varied charge densities and the corresponding crown ethers or other kinds of complexing agents could be investigated for ORR and hydrogen evolution at the liquid/liquid interface. It would also be interesting to search for ligands that can inhibit the cation hydrolysis in the organic phase, as this would give more information about the solvation of cations and complexed cations.

3. Further work on photocatalyzed H_2O_2 production in the liquid/liquid interface system should be conducted, such as SECM studies on the kinetic and mechanistic aspects. H_2 should be obtained under anaerobic conditions from the viewpoint of thermodynamics. It is proposed to regenerate the electron donor at the expense of water oxidation photocatalytically by such as dark TiO_2 , accomplishing the production of solar fuel sustainably.

References

- (1) Campos-Martin, J. M.; Blanco-Brieva, G.; Fierro, J. L. G. *Angew. Chem., Int. Ed.* **2006**, *45*, 6962.
- (2) Benjamin, I. *Science* **1993**, *261*, 1558.

CURRICULUM VITAE

HAIQIANG DENG

Male, 25th October 1984, China

Address: Ch. du Bochet 18, CH-1024
Ecublens, VD, Switzerland
Mobile: (0041) 78 897 62 08
E-mail: Haiqiang.deng@epfl.ch

Education:

- | | |
|-----------------|--|
| 09/2010-Present | École Polytechnique Fédérale de Lausanne (EPFL), Lausanne, Switzerland <ul style="list-style-type: none">• PhD candidate in the Laboratory of physical and analytical electrochemistry (LEPA) |
| 09/2007-07/2010 | South China University of Technology, Guangzhou, China <ul style="list-style-type: none">• Master degree in Environmental Science• Admitted with qualification exam exempted |
| 09/2003-07/2007 | Northwest A & F University, Yangling, China <ul style="list-style-type: none">• Bachelor degree in Environmental Science |

Research Experience:

- | | |
|-----------------|---|
| 09/2010-Present | Laboratory of physical and analytical electrochemistry (LEPA), Lausanne <ul style="list-style-type: none">• Under supervision of Prof. Hubert H. Girault.• Investigate energy-related reactions at the polarizable liquid/liquid interface: oxygen reduction reaction, hydrogen evolution reaction, nucleophilic substitution, as well as photo-induced electron transfer reactions;• Mainly focus on the thermodynamics and kinetics of these reactions, clarifying the reaction mechanisms that were not understood correctly before;• Collaborate with colleagues to study such as gold mirrors at the liquid/liquid interface and scanning electrochemical microscopy (SECM) related studies. |
| 09/2007-07/2010 | Electroanalytical chemistry lab in South China University of Technology, Guangzhou <ul style="list-style-type: none">• Under supervision of Prof. Lishi Wang.• Develop a novel methodology – Fourier transformed large-amplitude square-wave voltammetry at thin-film or three-phase electrode to study the thermodynamics and kinetics of the ion transfer across the liquid/liquid interface. |
| 09/2006-07/2007 | Northwest A & F University, Yangling <ul style="list-style-type: none">• Under supervision of Lecturer Hui Mao.• Deacidification studies on the hydrolyzed wastewater of acidated food oil;• Optimum process conditions have been recognized. |

Honors:

- | | |
|------|---|
| 2007 | Outstanding diploma thesis (college level), Northwest A & F University |
| 2010 | Outstanding diploma thesis (college level), South China University of Technology |

Publications:

1. **Deng, H.**; Peljo, P.; Stockmann, T. J.; Qiao, L.; Vainikka, T.; Kontturi, K.; Opallo, M.; Girault, H. H. *Chem. Commun.* **2014**, 50, 5554.
2. Rastgar, S.; **Deng, H.**; Cortés-Salazar, F.; Scanlon, M. D.; Pribil, M.; Amstutz, V.; Karyakin, A. A.; Shahrokhian, S.; Girault, H. H. *ChemElectroChem* **2014**, 1, 59.
3. Stockmann, T. J.; **Deng, H.**; Peljo, P.; Kontturi, K.; Opallo, M.; Girault, H. H. *J. Electroanal. Chem.* **2014**, 729, 43.
4. **Deng, H.**; Peljo, P.; Momotenko, D.; Cortés-Salazar, F.; Stockmann, T. J.; Kontturi, K.; Opallo, M.; Girault, H. H. *J. Electroanal. Chem.*, in press, DOI: 10.1016/j.jelechem.2014.08.031.

5. **Deng, H.**; Stockmann, T. J.; Peljo, P.; Opallo, M.; Girault, H. H. *J. Electroanal. Chem.* 2014, 731, 28.
6. Huang, X.; **Deng, H.**; Fang, Y.; Chen, W.; Wang, L. submitted to *J. Electroanal. Chem.*, 2014.
7. Fang, P.-P.; Chen, S.; **Deng, H.**; Scanlon, M. D.; Gummy, F.; Lee, H. J.; Momotenko, D.; Amstutz, V.; Cortés-Salazar, F.; Pereira, C. M.; Yang, Z.; Girault, H. H. *ACS Nano* 2013, 7, 9241.
8. Cortés-Salazar, F.; **Deng, H.**; Peljo, P.; Pereira, C. M.; Kontturi, K.; Girault, H. H. *Electrochim. Acta* 2013, 110, 22.
9. **Deng, H.**; Peljo, P.; Cortés-Salazar, F.; Ge, P.; Kontturi, K.; Girault, H. H. *J. Electroanal. Chem.* 2012, 681, 16.
10. Schaming, D.; Hatay, I.; Cortez, F.; Olaya, A.; Méndez, M. A.; Ge, P. Y.; **Deng, H.**; Voyame, P.; Nazemi, Z.; Girault, H. *CHIMIA International Journal for Chemistry* 2011, 65, 356.
11. Huang, X.; Chen, H.; **Deng, H.**; Wang, L.; Liao, S.; Tang, A. *J. Electroanal. Chem.* 2011, 657, 158.
12. Li, W.; Huang, X.; **Deng, H.**; Wang, L. *Anal. Lett.* 2011, 44, 1217.
13. **Deng, H.**; Huang, X.; Wang, L. *Langmuir* 2010, 26, 19209.
14. **Deng, H.**; Huang, X.; Chen, H.; Wang, L.; Luo, H. *Chemistry (in Chinese)* 2010, 73, 724.
15. Li, W.; Huang, X.; **Deng, H.**; Wang, L. *Journal of Shanghai Normal University (Natural Sciences, in Chinese)* 2010, 39, 284.
16. **Deng, H.**; Huang, X.; Wang, L.; Tang, A. *Electrochem. Commun.* 2009, 11, 1333.
17. **Deng, H.**; Mao, H.; Wang, L. *Environ. Eng. (in Chinese)* 2009, 27, 51.

Patents:

Wang, L.; Huang, X.; **Deng, H.** Arbitrary function waveform voltammeter, Patent Number: CN101871908 B

Posters and Seminars:

1. "Oxygen reduction by decamethylferrocene at a liquid/liquid interface: a kinetic study by scanning electrochemical microscopy" in the 63rd annual meeting of the International Society of Electrochemistry, 19-24 August, 2012, Prague, Czech Republic.
2. "Oxygen and hydrogen peroxide reduction by 1,2-diferrocenylethane at a liquid/liquid interface" in the 6th European Summer School on Electrochemical Engineering (ESSEE6) in Zadar, Croatia, from 16th to 21st, September 2012.
3. "Autolab" user meeting, 4th September, 2012, Zofingen, Switzerland.

Hobbies:

Hiking, Skiing, Swimming, Jogging, Pingpong, and so on.

